Co-funded by the European Union

SEamless integratioN of efficient 6G WirelesS tEchnologies for Communication and Sensing

D3.1 Initial report on the development of 6G-SENSES infrastructure building blocks

January 2025

6G-SENSES project has received funding from the Smart Networks and Services Joint Undertaking (SNS JU) under the European Union's Horizon Europe research and innovation programme under Grant Agreement 101139282

Project Start Date: 2024-01-01 **Duration**: 30 months

Call: HORIZON-JU-SNS-2023 **Date of delivery**: 2025-01-15

Topic: HORIZON-JU-SNS-2023-STREAM-B-01-02 **Version**: 1.0

Co-Funded by the European Union. Views and opinions expressed are however those of the author(s) only and do not necessarily reflect those of the European Union or the European Commission (granting authority). Neither the European Union nor the granting authority can be held responsible for them.

Type: Report (R)

Grant Agreement Number:	101139282
Project Name:	SEamless integratioN of efficient 6G WirelesS tEchnologies for Communication and Sensing
Project Acronym:	6G-SENSES
Document Number:	**D3.1**
Document Title:	Initial report on the development of 6G-SENSES infrastructure building blocks
Version:	1.0
Delivery Date:	2024-12-31 (**2025-01-15**)
Responsible:	*Barkhausen Institut* (**BI**)
Editor(s):	Muhammad Umar (**BI**)
Authors:	Muhammad Umar, Sajjad Ahmad, Padmanava Sen (**BI**), Vladica Sark, Mert Özates, Batuhan Sütbas, Arzu Ergintav, Jesús Gutiérrez (**IHP**), Ilias Floudas, Markos Anastasopoulos, Anna Tzanakaki (**IASA**), Jesús Ibáñez, Mikel Gutiérrez, Ignacio Santamaría, Luis Díez, Ramón Agüero (**UC**), Xi Ding, Nils Hildebrandt, Eduard Jorswieck (**TUBS**), Mikel Irazabal, Navid Nikaein (**BR**), Yazhou Zhu, Jessica Sanson, Valerio Frascolla (**INT**), Muhammad Saadi, Shahid Mumtaz (**NTU**).
Keywords:	Wireless Access Technologies (WATs), Integrated Sensing and Communication (ISAC), Software Defined Radio (SDR), Cell-Free massive MIMO (CF-mMIMO), ISAC Analog Front-End (AFE), Programmable Platforms, Open RAN (O-RAN), Reconfigurable Intelligent Surfaces (RIS).
Status:	Final
Dissemination Level	Public (PU)
Project URL:	https://www.6g-senses.eu

Revision History

Rev. N	Description	Author	Date
0.0	Draft Table of Contents (ToC)	Muhammad Umar (BI), Jesús Gutiérrez (IHP)	2024-08-27
0.1	Added contributions to section 5.1	Muhammad Umar (BI), Batuhan Sütbas (IHP)	2024-10-15
0.2	Added contributions to sections 3.1 and 3.3.2	Jesús Gutiérrez (IHP)	2024-10-17
0.3	Added contributions to section 4.3.3	Ignacio Santamaría, Jesús Ibáñez, Mikel Gutiérrez (UC)	2024-11-05
0.4	Added contributions to section 4.1	Xi Ding, Eduard Jorswieck (TUBS)	2024-11-15
0.5	Added contributions to Chapter 2 and sections 3.1, 3.2, and 3.3	Jesús Gutiérrez, Vladica Sark (IHP)	2024-11-18
0.6	Added contributions to section 4.3.4	Mert Özates (IHP)	2024-11-20
0.7	Added contributions to sections 4.2 and 5.2	Xi Ding, Eduard Jorswieck (TUBS) Ignacio Santamaría (UC), Jesús Gutiérrez (IHP)	2024-11-21
0.8	Added contributions to sections 3.2 and 3.3	Markos Anastasopoulos, Anna Tzanakaki (IASA), Mikel Irazabal, Navid Nikaein (BR), Vladica Sark, Nebojsa Maletic, Jesús Gutiérrez (IHP), Luis Díez, Ramón Agüero (UC)	2024-11-29
0.85	Added contributions to sections 3.2.1 and 3.3.1	Yazhou Zou, Jessica Sanson, Valerio Frascolla (INT)	2024-11-29
0.9	Revised Chapter 4	Eduard Jorswieck (TUBS), Ignacio Santamaría (UC), Simon Pryor (ACC)	2024-12-20
0.91	Revised Chapter 3	Shahid Mumtaz, Muhammad Saadi (NTU)	2024-12-20
0.92	Revised Chapter 5	Padmanava Sen (BI)	2024-12-25
0.93	Revised Chapter 2	Anna Tzanakaki (IASA)	2024-12-28
0.94	Full revision of the document	Shahid Mumtaz (NTU)	2025-01-09
0.95	Full revision of the document	Valerio Frascolla (INT)	2025-01-14
1.0	Last revision and submission of the document	Jesús Gutiérrez (IHP)	2025-01-15

Table of Contents

List of Figures

List of Tables

Executive Summary

6G-SENSES provides a detailed exploration of innovations in the forthcoming sixth generation (6G) wireless systems, focusing on their dual role in communication and sensing. It introduces the architecture and objectives of the 6G-SENSES proposition, which aims to revolutionize wireless technologies by integrating these capabilities seamlessly. Below is a summary of the key points of this deliverable:

Chapter 1 outlines the structure of the deliverable and its key terminology, providing readers with a foundation to understand the technical and innovative aspects of 6G-SENSES. This part also emphasizes the importance of defining common concepts to ensure that consistency and clarity throughout the project documentation is maintained.

Chapter 2 highlights the role of Work Package 3 (WP3). WP3 is central to defining the 6G-SENSES configurable wireless infrastructure technologies and interfaces at the data plane, integrated in an Open Radio Access Network (O-RAN) / the 3rd Generation Partnership Project (3GPP) framework. It introduces the Integrated Sensing and Communication (ISAC) framework, proposing architectural designs that unify communication and sensing within the 6G ecosystem. Chapter 2 also highlights the synergies between ISAC and the broader 6G framework, emphasizing the need for efficient signal processing, data fusion, and interoperability among diverse components of the system.

Chapter 3 examines advancements in the field of ISAC, including use cases, reference signals (RSs), and analog millimetre wave (mmWave) front-ends. It reviews State-of-the-Art (SotA) implementations and provides a detailed description of existing and emerging platforms, such as Wi-Fi, Sub-6 GHz, and mmWave systems. Additionally, it outlines planned integration activities for the 6G-SENSES Proofs of Concept (PoCs), focusing on Sub-6 GHz, 5GNR, Wi-Fi and mmWave platforms, and introduces innovative techniques like Orthogonal Time Frequency Space (OTFS)-based ISAC. This section also explores how ISAC can enable new applications, such as precise location tracking and environmental monitoring, by leveraging enhanced sensing capabilities.

Chapter 4 reviews Cell-Free Massive MIMO (CF-mMIMO), which is considered a cornerstone technology for 6G, its applications, testbed implementations, and advancements in platform development. The work in this field addresses distributed and scalable signal processing techniques and algorithms to support efficient CF-mMIMO operation, its associated practical challenges, and comprehensive studies such as energy consumption analyses, reciprocity calibration, and unsourced random access (URA). The proposed implementations aim to optimize multiple access techniques and improve system efficiency. Moreover, novel approaches to reduce latency and enhance scalability are discussed, to ensure that CF-mMIMO can meet the demands of next-generation wireless networks.

Chapter 5 highlights the exploration of human-centric radio systems and the role of Reconfigurable Intelligent Surfaces (RISs) in enhancing 6G capabilities. It discusses advancements in 60 GHz front-end modules, including antenna-in-package designs, and investigates RIS applications in ISAC and CF-mMIMO systems. These technologies promise to make 6G systems more adaptive, efficient, and environmentally friendly. Specific attention is given to the potential of RIS to dynamically shape wireless propagation environments, improving signal strength and coverage while reducing energy consumption. 6G-SENSES adopts a holistic approach to next-generation wireless technologies, addressing both technical and societal challenges, and by integrating communication and sensing, leveraging CF-mMIMO, and incorporating RIS. 6G-SENSES lays the groundwork for transformative advancements in wireless systems.

Finally, this deliverable defines the data plane activities to be assessed in the next WP3 deliverable release (D3.2), and sketches the wireless infrastructure devised in 6G-SENSES, which will turn into the testbeds and prototypes working together to assess the full 6G-SENSES framework end-to-end (E2E).

1 Introduction

Wireless communications are essential to achieve the expected performance of future generations of mobile communication systems. Despite increased efforts in enabling mmWave regions for 5G New Radio (NR) communications, still the spectrum is scarce, leading to the need of increasing spectral efficiency (SE). Given the practical implementation problems encountered with an increasing number of antennas for a centralized system and the interference problems encountered with cell splitting, the SE of 5G systems is not sustainable. Therefore, further innovations in the architecture of cellular networks are required.

6G is expected to bring paradigm changes, such as the elimination of the traditional “cell-like” deployment of mobile communications infrastructure, enabled by the introduction of CF-mMIMO [1]. This is considered a major technical asset to improve the performance of wireless networks. When all access points (APs) deployed in a system collaborate to serve a fixed number of users, as the number of APs increases, the cell boundary effect of traditional cells can be eliminated. As a result, a “cell-free” system is formed and the capacity and performance of the communication system can be significantly improved. CF-mMIMO not only increases the spectral and energy efficiency (EE) but also reduces latencies and improves the system reliability with diversity and multiplexing trade-offs, thus supporting hyper-reliable low-latency transmission. Extending CF-mMIMO to high-frequency bands can increase the system capacity and effectively solve the link robustness problem. However, the practicalities of the technology are hindering its broad implementation and deployment, which makes necessary to study the implementation architecture of the new CF-mMIMO, taking both performance and implementation complexity into account. The major challenge in the practical implementation of CF-mMIMO systems is the overhead in terms of signalling and coordination for pre- and de-coding of the transmitting and receive data, the data itself, and the required control signals for synchronization or scheduling.

We notice that the architecture of wireless systems for sensing resemble that for communications in terms of system architectures, channel characteristics, and the use of signal processing methods. Nowadays, sensing is considered to be a key functionality in future 6G wireless networks, with a plethora of applications that are supposed to benefit from it [2]. Fortunately, the wide deployment of MIMO communication systems and the use of higher frequency bands for communication, have undoubtedly benefited the use of sensing functionalities in those devices initially devised only for communication purposes [3]. In addition, recent investigations demonstrate the potential to exploit RIS technology in Integrated Sensing and Communication (ISAC) systems such as to optimize the ISAC system in terms of accuracy and coverage. We are witnessing that the architecture of wireless systems for sensing resemble that for communications in terms of system architectures, channel characteristics, and the use of signal processing methods.

The O-RAN paradigm has emerged as a way to better organise mobile networks, and proves to be interesting for practical deployments of CF-mMIMO networks [4], [5], [6], [7], [8] for two reasons. First, the physical (PHY) layer is split between the O-RAN Distributed Units (O-DUs) and Radio Units (O-RUs). Second, extra functional blocks are introduced, enabling Artificial Intelligence (AI) and containerized service orchestration on the network. These include the Near-Real Time RAN Intelligent Controller (Near-RT RIC), the Non-RT RIC, and the Service Management and Orchestration (SMO) framework. The new interfaces and options for network-wide control can be exploited to achieve cooperation amongst O-RUs, even beyond the borders of the O-DUs.

6G-SENSES proposes integrating novel 6G RAN technologies such as CF-mMIMO and ISAC to support the 6G vision that is sustained by the current (and future) architectural framework based on 3GPP and O-RAN. The project considers a multi-technology RAN ecosystem with technologies that are able to offer sensing functionalities (3GPP and non-3GPP). These technologies are Sub-6, Wi-Fi, mmWave and 5G NR, which will coexist in an ISAC framework whose goal is to obtain a faithful representation of the surrounding environment. This framework will make use of new PHY layer technologies to increase the cooperation between technologies and their inherent capabilities to improve the precision/accuracy of the sensing capabilities. To further strengthen communication and sensing functionalities, 6G-SENSES leverages RIS and works on designing, optimizing, and modelling the surfaces. Sensing information stemming from these technologies will be pushed to the O-RAN framework for optimization purposes and to build up a so-called network twin.

This deliverable presents the initial work carried out in the context of 6G-SENSES WP3, where the main PHY layer building blocks are described and first results are shown, and proposes the first specifications of those technologies. These specifications will be revised according to the ongoing work among the three parallel tasks 3.1, 3.2 and 3.3 of WP3. These blocks will all have a role in the project architectural concept, being built in the framework of the WP2 deliverable D2.2. The revised and definitive detailed description of the 6G-SENSES PHY layer and infrastructure components will be provided in deliverable D3.2.

1.1 Organisation of the document

This document comprises six (6) chapters. Following the Executive Summary and Introduction sections:

Chapter 2 introduces the role of WP3 activities in the context of the 6G-SENSES architectural framework and how the developments in this WP can be integrated with the rest of the developed components.

Chapter 3 provides an overview of the ISAC SotA and current challenges to then describe the ISAC platforms that will be used in the context of the project and the target implementations to be incorporated to 6G-SENSES PoC#1 and PoC#3.

Chapter 4 discusses the literature about CF-mMIMO and its role in the project, analysing in detail the target platforms for the implementation of PoC#2 and the ongoing work towards the incorporation of the algorithms and methods in the CF-mMIMO testbeds.

Chapter 5 presents the work carried out related to analogue systems such as ISAC front-end and RISs that, on the one hand, complement ISAC solutions and, on the other hand, serve as complementary solutions to enhance the ISAC capabilities of the network and improve EE.

Finally, Chapter 6 summarises the document.

1.2 Nomenclature & useful concepts

The following concepts will be used throughout the text:

- **Base Station (BS)**: is a fixed radio station consisting of radio frequency (RF) equipment (transceivers and antenna interface equipment), a baseband processing unit, controllers and power supply.
- **gNB**: The gNB serves as the BS in a 5G network, connecting mobile devices to the core network and facilitating the transfer of data between devices and the internet.
- **O-RAN**: The O-RAN architecture disaggregates traditional BS (gNB) functions into modular components, allowing for greater flexibility, cost-effectiveness, and scalability.
- **Access Point (AP)**: serves as the BS within a WLAN, terminating the air interface on the network side.
- **Radio Unit (RU):** aka O-RU (O-RAN radio unit), processes the RF and lower part of the PHY layer (Low-PHY) in an O-RAN disaggregated gNB.
- **Domain**: A group of entities that belong to a certain infrastructure that follow common rules and procedures. Examples are network, administrative or technology domains.
- **Platform**: A platform is any hardware (HW) or software (SW) used to host an application or service.

- **Testbed:** Platform for conducting rigorous, transparent, and replicable testing of scientific theories, computing tools, and new technologies.
- **Demonstrator**: is a prototype, rough example or otherwise incomplete version of a conceivable product or future system, put together as PoC with the primary purpose of showcasing the possible applications, feasibility, performance and method of an idea for a new technology.
- **Proof of Concept (PoC)**: set of actions meant to assess the feasibility of an idea or concept, typically through an experiment or a pilot.
- **Scenario**: includes information which is related to network, service and environment configurations and it is specific to the selected technologies and the target system.
- **Measurement system**: One or more measurement devices plus any other elements / components interconnected to perform a complete measurement from the first experiment operation to the end result [9], [10].
- **Device under test (DUT)**: The device or component to be placed in a test fixture (measurement system) and tested [9]. Usually, a single device being tested [10].
- **System under test (SUT)**: A system of devices / components, i.e., a specific combination of DUTs, being tested at the same time [10]. A SUT may – especially for virtualized network environments or software – include the computer system HW and SW on top of which the implementation under test operates [9].
- **Metric**: A generic high-level definition of a target quality factor (attribute) to be evaluated, i.e., a definition independent of the underlying system, the reference protocol layer, or the tool used for the measurement. Examples are capacity, latency, reliability, etc.

2 Role of WP3 in the 6G-SENSES Architecture

6G-SENSES proposes integrating novel 6G RAN technologies to support the 6G vision that is sustained by the current (and future) architectural framework based on 3GPP and O-RAN [1]. The project considers a multi-technology RAN ecosystem comprising a number of wireless access technologies (WATs), that are able to offer sensing functionalities. The resulting sensing data can be then conveyed to a 3GPP/O-RAN system.

6G technologies are relying on paradigm shifts compared to previous technology generations, such as the elimination of traditional "cell-based" deployment of mobile communications infrastructures, enabled by the introduction of CF-mMIMO [4]. This is considered a major technical advancement that can potentially improve the performance of wireless networks taking advantage of new PHY layer technologies and increasing cooperation between them. It is important to point out that the definition of CF-mMIMO does not restrict the deployment architecture to a specific topology. Regarding its benefits, CF-mMIMO is expected to foster its inherent capabilities to improve some of the most important Key Performance Indicators (KPIs) that the R&D community has acknowledged as vital, i.e., high coverage probability, EE, SE, etc. Moreover, CF-mMIMO is a networking architecture compatible with the RAN functional split adopted by O-RAN systems [4], [6], making clear its applicability in future 6G RANs.

ISAC applications in such novel network deployments advance promising opportunities, where the network can simultaneously provide communication services and perform environmental sensing. To further strengthen communication and sensing functionalities, 6G-SENSES will leverage RIS technologies and work on designing, optimizing, and modelling these surfaces.

This chapter provides an initial overview of the role of 6G-SENSES WP3 components in the preliminary 6G-SENSES architectural view. A detailed description of the architecture and the full definition of its functionality is described in 6G-SENSES deliverable D2.2 [11], while a more precise presentation of the WP3 building blocks and a full set of performance evaluation results will be provided in deliverable D3.2.

2.1 6G-SENSES overall architecture description

Dense deployment of 5G BSs is currently the most dominant approach to achieve massive connectivity and seamless coverage for the forthcoming 6G wireless sensing [12] and communication networks [13], [14]. A promising approach to achieve this goal is the CF-mMIMO paradigm [13], which consists of a large number of distributed APs connected to one or more central processing units (CPUs) to cooperatively serve all users in a given area without cell boundaries via joint signal encoding/decoding, based on the users' channel state information (CSI) that is locally estimated at individual APs or globally shared with the CPU.

CF-mMIMO, in the currently ongoing 6G RANs specifications, faces a variety of challenges: realization of distributed signal processing, calibration and "consensus" among APs, managing interference, and minimizing data exchange between APs and the CPU, while ensuring EE. These challenges appear even more relevant in practical implementations.

In addition to the initial adoption of CF-mMIMO, the O-RAN paradigm has gained significant attention by defining open interfaces between RUs and distributed baseband processing units (DUs). O-RAN enables multi-vendor interoperability and the implementation of the PHY layer as a SW-defined virtual network function (VNF) running on general-purpose HW such as CPUs and GPUs, and it is ideally suited (although not strictly necessary) for the implementation of CF-mMIMO (see, e.g., [6], [7], [15]).

O-RAN has emerged as an approach that facilitates improved organisation of mobile networks [6], and appears to be a promising way forward in practical deployments of CF-mMIMO networks for two reasons. First, the PHY layer is split between the O-DUs and O-RUs. Second, extra functional blocks are introduced, enabling AI and containerized service orchestration of the network. These include the Near-RT RIC, the Non-

RT RIC, and the SMO framework. The new interfaces and options for network-wide control can be exploited to achieve cooperation among O-RUs, even beyond the borders of the O-DUs.

6G-SENSES considers the O-RAN / 3GPP framework given that disaggregation, virtualisation and network and service management capabilities inherent in O-RAN, provide the mechanisms to realise many of the infrastructure control capabilities and to support the optimization strategies. The disaggregation of network functionalities promoted by O-RAN raises special interest in the development and deployment of CF-mMIMO in real-world distributed networks. A new network segment in-between the WATs and the UEs is envisioned in order to enable control of the such the elements of the RISs the parameters of which can be optimized to address the specific requirements of the use case under consideration. The ultimate RT-RIC controller additionally provides shorter timescales that those achieved to date by the two RIC controllers defined in O-RAN. Taking a high-level view, the proposed system architecture combining all network components along with the SMO are depicted in Figure 2-1.

6G-SENSES considers a RAN populated with WATs that are able to provide CF-mMIMO and ISAC functionalities depending on the capabilities of the HW, and on the requirements of the network that may make necessary the use of a certain technology depending on its performance and availability. This is shown in Figure 2-2. These WATs including Sub-6 GHz (non-3GPP and non-Wi-Fi), Wi-Fi 6, mmWave (60 GHz) and 5G NR, will coexist in the ISAC framework.

2.2 ISAC architectural proposal

6G services will be able to support a wide spectrum of vertical applications with greatly varying requirements and will offer advanced features beyond connectivity spanning from sensing to monitoring and positioning. To address these requirements, 6G will feature ISAC capabilities, performing sensing through the mobile communication infrastructure [17]. In this context, the network acts as a “radar” sensor, exploiting its own radio signals to sense and comprehend the surrounding physical world. The echoes (reflections) and scattering of wireless signals predominately transmitted for communication purposes, provide information related to the characteristics of the environment and/or objects therein [18].

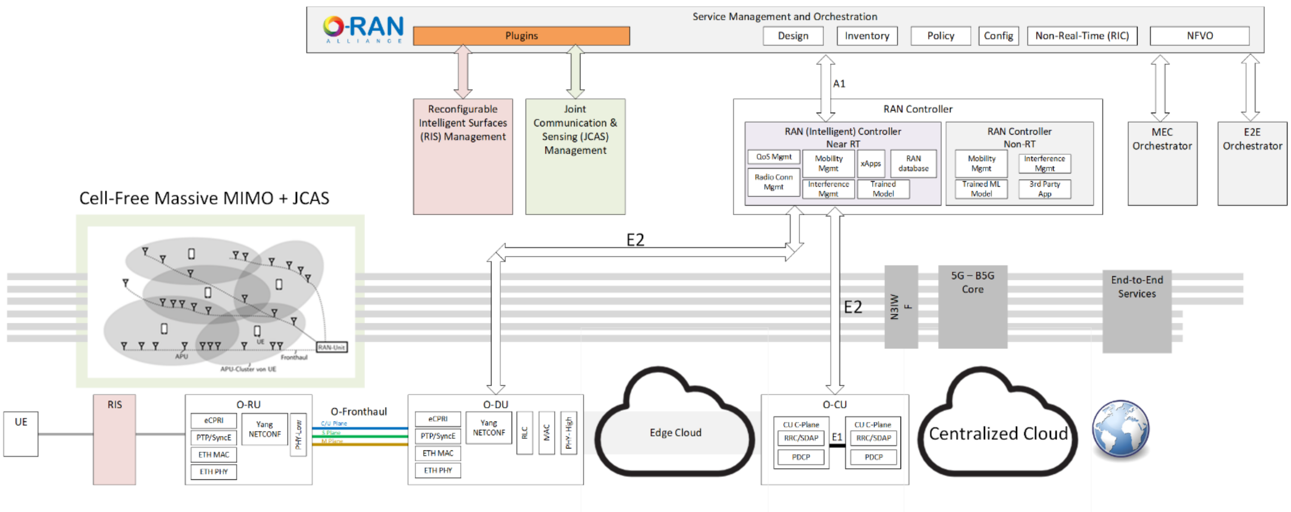

Figure 2-1 6G-SENSES architecture and building blocks

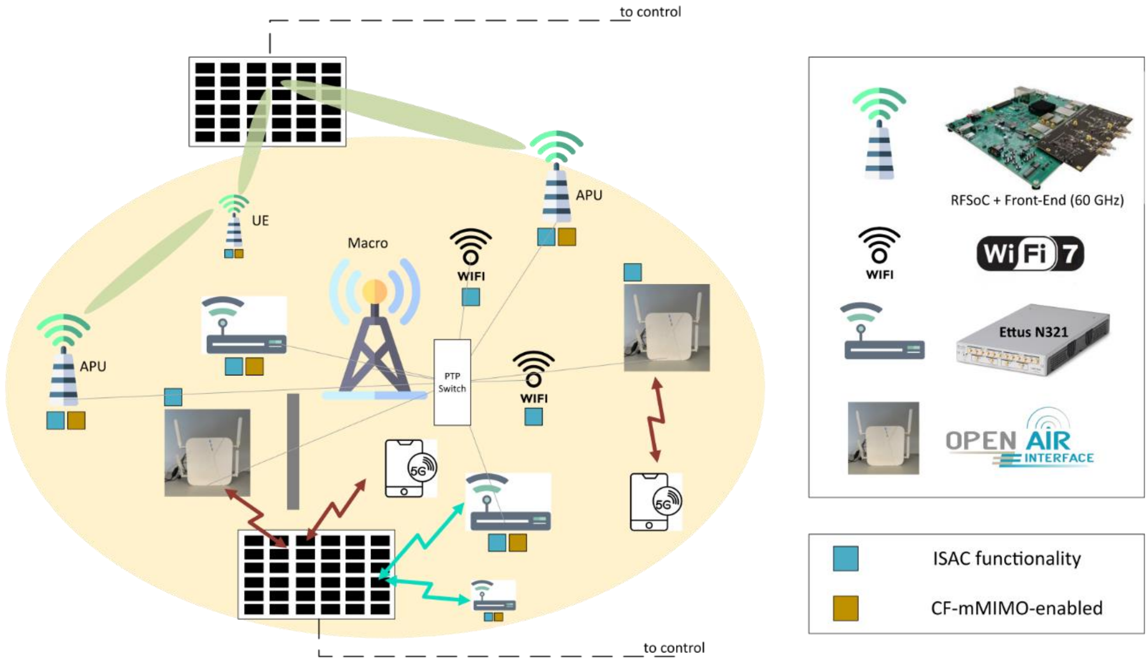

Figure 2-2 6G-SENSES data plane wireless technologies

To date, research on ISAC systems has mainly focused on monostatic sensing. However, the employment of monostatic sensing requires the co-located sensing transmitters and receivers to be full-duplex. Hence, multi-static sensing ISAC systems, in which there are multiple non-colocated transmitters and receivers for sensing, can provide diversity gain while avoiding the need for full-duplex nodes [19].

The sensing data collected and processed by the network can then be leveraged to enhance its operations, augment existing services such as extended reality (XR) and digital twinning, and enable new services, such as object detection and tracking, along with imaging and environment reconstruction. This potential has already attracted a lot of attention from 3GPP, which has initiated a preliminary study on use cases and ISAC requirements, making it a promising candidate to optimize both communications and sensing systems [18].

Sensing and communication functions can be performed taking different approaches: (a) adopting separate and dedicated infrastructures for sensing and communications, where information acquired from one infrastructure is used to assist the other; (b) sensing and communication capabilities are supported by common HW sharing the available spectrum, with the constraint that sensing and communication signals are transmitted over different timeslots; and (c) adopting integrated systems fully sharing both spectrum and time domains.

Although some early prototypes are available validating concepts (a) and (b), implementations of 3GPP-compliant ISAC systems (c) are still at a very early stage. These systems demand additional complexity in signal processing but require the collection and aggregation of huge volumes of synchronized in-phase and quadrature (IQ) reflected (echo) streams that need to be processed to extract information on the sensed environment. This processing can only be performed at edge servers, introducing the need to transport the IQ streams over flexible high-capacity transport networks.

Within 6G-SENSES, the know-how on CF architectures and implementation capabilities from the partners, provides the basis to develop ISAC services that exploit the distributed antenna and sensing environment from CF and distributed MIMO architectures. The CF-mMIMO ISAC system that will be built in the context of 6G-SENSES will enable the following key target outcomes: cm-level accuracy localization, extremely high reliability, and extreme energy and spectrum efficiency. This is achieved by smart deployment of distributed

RUs (or APs) with several distributed massive antennas which allow high sensing accuracy and very high reliability (zero outages), as well as low energy consumption.

The 6G-SENSES platform will support ISAC services through: (1) use of sensing information to optimize the configuration and parameters of the system, i.e., beamforming, handovers, bandwidth allocation, security; and (2) providing sensing data to end-user services e.g., immersive AR/VR services.

3 ISAC activities

Large bandwidth availability and WATs featuring massive arrays together with network densification enable additional services, such as radio-based positioning and sensing, which are beyond data transmission, with minimal cost by using the same infrastructure and spectrum [20].

Positioning of active communication devices has become an integral part of the recent and ongoing standards, e.g. 3GPP and IEEE [18]. As announced by the International Telecommunication Union (ITU) Recommendation on International Mobile Telecommunications 2030 ("IMT-2030 Framework") [21], three additional usage scenarios of integrated AI and communications, ISAC, and ubiquitous connectivity, will be fostered in 6G. In addition, three enhanced usage scenarios that extend the capabilities of 5G will be supported, which are: 1) immersive communication, 2) massive communication, and 3) hyper reliable and low-latency communication.

There exist a variety of technologies that are able to offer localization capabilities. New releases of Wi-Fi and Ultra-Wideband (UWB) are examples of non-3GPP technologies that are ready to play a major role in 6G mobile communications. The fact that 3GPP-based localization capabilities are lagging behind in terms of maturity, availability and precision performance, makes the interoperability of the 3GPP system with non-3GPP technologies needed to enhance the desired performance to support 6G use cases. Technologies like Sub-6, Wi-Fi (8/9), and mmWave (e.g. IEEE-based) have been subject of research for localization over the last years. Each of these technology options does not offer the same level of maturity in terms of controllability and integrability in frameworks like 3GPP/O-RAN. Nevertheless, when these technologies are available and sensing information can be extracted from them, particularly for the mmWave case, the combined performance of these can be increased. Building on earlier work, a digital twin (DT) of the environment is to be created using the HW-inherent sensory capabilities of the communication systems. For this purpose, the channel impulse responses (CIRs) of the individual wireless nodes will be generated and processed jointly. After a suitable pre-processing of the CIRs, these are transferred to an AI unit via interfaces yet to be defined. This can be implemented centrally or as an "edge" solution. The AI, trained with the help of real and partly synthetic CIRs, then generates a DT of the environment. This DT in turn serves to optimize the communication network and can also be used, for example, to control hybrid beamforming processes.

3.1 State-of-the-Art in ISAC activities

In the era of advanced wireless communication technologies, the integration of sensing and data transmission has become a pivotal research area to enhance resource utilization and efficiency. One promising technology in this domain is ISAC, which seeks to share HW and spectrum resources for data transmission and target sensing and improving the SE [22]. This can lead to improved network quality and to an increased number of service scenarios [16], [17], reduces HW costs, and lowers system power consumption, positioning ISAC as a promising technology for the forthcoming 6G wireless communication.

Due to the wide deployment of communication infrastructures, integrating passive wireless sensing in communication system gains great interests in enabling device-free applications. To implement passive sensing function into communication systems, full-duplex radio is an ideal option. With a full-duplex radio, the transmitter and sensing receiver can be the same node and share the same HW components. Thus, there is no carrier frequency offset and the sampling synchronization can be also perfectly controlled. Therefore, many ISAC studies are based on full-duplex sensing assumptions, e.g., [23], [24], or enable a full-duplex like sensing [27]. There are also a few experimental full-duplex ISAC studies [27], [28]. Although full-duplex ISAC design shows great potentials, the self-interference cancellation suffers severe complexity. In addition, many current devices are half-duplex radios. Thus, the passive bistatic sensing based on half-duplex radios is still of great interest.

The study and design communication-assisted sensing by leveraging the existing 5G communication signals remains an interesting open research problem. Few recent studies that investigate the feasibility and suitability of using current 5GNR OFDM-based communication signal for sensing purposes [25]. For example, Liu et al. in [3] demonstrates that pilot signals possess unique benefits over data signals, primarily due to their strong auto-correlation characteristics.

MmWave signals provide attractive opportunities for sensing due to their inherent geometrical connections to physical propagation channels. Two common modalities used in mmWave sensing are monostatic and bistatic sensing, which are usually considered separately [29].

3.1.1 Use Cases and applications

From a technical perspective, in the use case category of ISAC [1], 6G-SENSES envisions RAN sensing used as a means to obtain information on environmental conditions, density of people or machines (e.g., robots), speed of mobility of objects residing in the coverage of an access node, etc. To this end, the edge segment plays a key role in capturing and intelligently processing the sensing information streams that are parallel to the data communication ones.

In the research community, many use cases for future ISAC systems are currently under discussion and evaluation. Some of them are presented in [30]. 3GPP has identified 32 different use cases for the spatial location of humans, animals, vehicles and drones [18]. The growing number of robots and autonomous vehicles require advanced tools to map their surroundings with real-time data. ISAC can provide tremendous benefits compared with SotA systems (cameras, etc.) not only range-wise but also in poor weather conditions.

Nowadays, Mobile Network Operators (MNOs) are essentially the dominant stakeholders operating mobile networks serving large numbers of devices. 5G solutions usually aim at exploiting 5G network information captured by gNBs or UEs and processed by networks planning applications, towards optimising network deployments. Links toward communicating devices need to be established, no matter which propagation effects arise, and such technical challenges in low quality communication need to be overcome. It is certain that the accuracy is limited by the location, the availability of Line-of-Sight (LoS) connectivity and the available number of APs. An alternative to deploying additional APs is to deploy RIS, being more flexible and with reduced cost, but still the integration needs to be performed to reap the higher spatial resolution and positioning accuracy. A combination of ISAC and RIS can offer a solution for the above-mentioned problem.

Ultimately, an automated sensing of the environment, both related to traffic demands and to physical structures, is key to optimize the performance of the network towards the delivery of high-quality services. Machine Learning (ML) and AI are ready to play a role in enhancing the performance and capabilities of ISAC networks in the 6G era. The integration of AI enables smarter, more adaptive systems that can efficiently process vast amounts of data generated by sensing and communication functions. One of the major applications of AI in ISAC is edge intelligence [31], which allows local data processing and decision-making near the network edge. AI techniques, particularly federated learning, allow for distributed learning models that process data locally on devices (e.g., UEs) and then update global models through interaction with BSs and the cloud. This approach enhances privacy and reduces transmission delay, while improving overall network efficiency. AI-driven ISAC networks also leverage deep neural networks (DNNs) to optimize key tasks like interference management, beamforming, and resource allocation. DNNs help mitigate challenges like self-interference and mutual interference in full-duplex communication by predicting and cancelling non-linear distortions that traditional methods struggle to handle. Additionally, deep reinforcement learning is used for mobility management, enabling UEs to seamlessly transition between BSs while minimizing handover issues. By employing AI-based algorithms, ISAC networks can dynamically adapt to changing environments, optimize spectrum use, and improve the accuracy of both sensing and communication functions [32].

3.1.2 Reference signals

In general, conventional waveform designs are divided into three categories: 1) communication-centric designs [33], which aim to incorporate the sensing function into the existing communication waveform without significant modification; 2) sensing-centric designs [34], which focus on embedding communication data into the primary sensing waveform, which may cause limited communication performance; and 3) joint waveform designs [35], whose goal is to create an ISAC waveform from the ground-up, instead of relying on existing waveforms. The design of appropriate waveforms is crucial for achieving an efficient ISAC system. Research in this area can be generally categorized into three approaches [36]:

- **Communication-Centric Waveform Design (CCWD)**: modifies traditional communication waveforms, such as Orthogonal Frequency Division Multiplexing (OFDM) and single-carrier waveforms, to extract sensing information from signal echoes while preserving communication performance. OFDM is widely used due to its SE and robustness, allowing for dual functionality in radar and communication systems with high flexibility in time and frequency allocation.
- **Sensing-Centric Waveform Design (SCWD)**: primarily focuses on radar sensing functionality and embeds communication information within radar waveforms, such as chirp signals. By modulating communication data onto these waveforms, this design prioritizes sensing but enables communication in parallel. It often involves methods like chirp modulation and spatial diversity techniques, allowing radar and communication to coexist with minimal interference.
- **Joint Waveform Optimization and Design (JWOD)**: jointly optimizes both sensing and communication performance using advanced optimization techniques. This approach provides a better trade-off between the two functionalities, utilizing metrics like Signal-to-Interference-plus-Noise Ratio (SINR) and Cramér-Rao bounds (CRB) to balance the performance. It also explores spatial beamforming and hybrid beamforming for enhanced performance [37].

The RS-based waveform design is highly compatible with the PHY layer of current communication systems and facilitates a smooth transition toward 6G [38]. The RS is known in the modulation domain and is inserted in the OFDM signal for channel estimation, which exhibits good autocorrelation [39]. Consequently, the RS exhibits significant potential for application in radar sensing.

For 5G NR, the signals available for radar sensing can be divided into RSs used for channel estimation, non-channel estimation signals and data payload signals [40]. According to 3GPP standard [18], RSs mainly include the Demodulation Reference Signal (DMRS) associated with Physical Downlink Shared Channel (PDSCH) and Physical Uplink Shared Channel (PUSCH), CSI Reference Signals (CSI-RS) for downlink and Sounding Reference Signals (SRS) for uplink. Most of them have comb-type structures and adopt orthogonal codes for different users. Specifically, the authors in [41] analyze the sensing performance of SS and DMRS by self-ambiguity and cross-ambiguity functions. On the other hand, the authors in [42] demonstrate the feasibility and superiority of PRS by comparing with the SS, DMRS and CSI-RS. The authors in [43] fill the gaps in the research of OFDM-based ISAC systems by exploring the design of RS-based waveform strategies to enable simultaneous sensing and communications.

At the same time, there are optional configurations in time-frequency domains to support different requirements. Non-channel estimation signals, including Synchronization Signal (SS) and Physical Broadcast Channel (PBCH), are typically transmitted periodically and can be used to estimate the Doppler shift. However, the resolution of distance estimation is limited due to the limited number of occupied subcarriers. In terms of data payload signals such as PDSCH and PUSCH, the transmitted data is always random for specific users. This randomness will cause the sensing ambiguity and increased complexity for signal processing. Moreover, the unknown data payloads in a bi-static setup are a major challenge for the acquisition of sensing parameters. It can be concluded that the OFDM-based radar processing algorithm should be designed reasonably according to the transmission and mapping characteristics of different physical signals.

Regarding the interfaces for providing the sensing information, there is still a step to take towards the full integration of sensing in the architecture. As an example, 3GPP radio access technology supports location-based services for positioning, but the specifications do not have the built-in capability to detect objects unconnected to the RAN.

3.1.3 Analogue mmWave Front-End for ISAC

mmWave bands are considered as a key enabler for data-intensive wireless communications due to the large fractional bandwidth. The bandwidth serves as the backbone for the ultra-high data rate with extremely low latency. It can support target detection with refined resolutions and data transfer rate of several giga bits per second. High-resolution sensing is made possible through wideband and multicarrier waveforms, for which mmWave bands become relevant due to their large relative bandwidth compared to conventional Sub-6 GHz bands [44]. The device size shrinks at higher frequencies due to miniaturized free space wavelength, which on the one hand complicates the design and manufacturing process, on the other hand in return it provides the opportunities of realizing large antenna arrays useful for focused and narrow radiation beams. Pointed beams make refined lateral resolution and accurate spatial-mapping possible for various applications, e.g., 3D mapping for digital twinning, gesture recognition, surveillance and autonomous driving, which otherwise were dependent on optical technologies, which are vulnerable to atmospheric conditions [45]. The directional beams are also mandatory to counteract the high propagation losses by boosting signal-to-noise ratio (SNR) at mmWave frequencies, to maintain high throughput communications. It opens the opportunities of sharing the HW among radar and telecommunication resulting an ISAC system [46].

Advanced beamforming networks and array designs, supported by semiconductor and packaging innovations, make pencil beams possible at mmWave and sub-THz frequencies. However, the shorter wavelengths and larger arrays also make HW more prone to design and manufacturing flaws, with issues like mutual coupling, near-field coupling, beam squint, grating lobes and other beam-pointing errors, potentially compromising system performance due to the narrow beamwidths. Passive beamformers avoid several of these issues due to their simple and true-time-delay based design, however they provide fixed and limited beam pointing. Advanced techniques with active beamformer have been reported to mitigate these issues on the cost of increased design and manufacturing complications [47], [48]. Digital beamformers have been successful in avoiding these problems by precoding and compensating the artifacts digitally. However, digital beamforming required a complete dedicated RF chain for each antenna, operated by a dedicated baseband processor. In return, each antenna element becomes independent which supports MIMO communication [49]. MIMO capabilities are not only proven to enhance the communication throughput but also the sensing capabilities for a sensing system referred as MIMO radars.

The rapid progress in semiconductor technologies has resulted in miniaturization and increasing the device-count in a single die which has put a strict burden on the device packaging. Specially for RF die packaging, particular electrical performance criteria are to be met, e.g., impedance matching, which otherwise may not have importance in other type of devices. Particularly for mmWave chip packaging the problem intensifies as the interconnect becomes a significant fraction of the wavelength. In this case, the interconnect itself becomes a distributive component and does not obey the ohmic law, it instead should be dealt with transmission line approach [50]. Bondwire interconnects and flipchip approach have extensively been used in the microwave industry; with bondwire being more popular due to its simplicity and repeatability. However, for high-frequency operation, a bondwire has a strong parasitic inductance that needs to be compensated out and the matching network design depends on the chip, carrier substrate, frequency and application [51], [52], [53]. Apart from the interconnect design, modular integration of the chipset is also not straightforward at mmWave frequencies. The modular integration requires redesigning passive circuits for specific applications, e.g., baluns, as simple frequency scaling from low-frequency components is often impractical. Additionally, the lack of available lumped surface mount devices (SMDs) and sensitivity to manufacturing process variations add to the complexity. As a result, building a modular mmWave front-end demands significantly more effort compared to legacy chip-on-board methods used for sub-6 GHz frequencies [54] [55].

3.1.4 ISAC testbed implementations

To date, several works have presented prototyping platforms for ISAC where they assess their sensing performance.

A SW radio mmWave massive MIMO experimental platform at 60 GHz is presented in [56]. Using commodity 802.11ad RF chipsets from Qualcomm together with Ettus radios for signal processing, the design supports up to 8 RF chains with 256 antenna elements in total. The authors demonstrate its use for communications and radar experiments. The authors in [57] present a communication system prototype at 28 GHz that supports monostatic sensing. For communication and sensing, OFDM signaling with a bandwidth of 100 MHz is used. It supports transmission rates of up to 160 Mb/s and no sensing performance is reported. In [58] the SW Defined Radio (SDR)-capable mmWave system is extended with a radar receiver operating in the 71-76 GHz band to enable sensing. The system uses different HW resources to implement communication and sensing, so it is not an ISAC system in the true sense. In [59][60] two SDR prototyping platforms are presented.

In [40] the authors explore different properties of signals available for radar sensing and aim to combine the ISAC technology with the cellular network by optimizing the multi-dimensional resource scheduling. In the developed simulation platform, different mapping patterns of RSs are exploited to realize the performance trade-off between communication and sensing functions. Finally, the ISAC-enabled cooperative perception HW testbed has been designed and implemented, which can decrease the positioning error by 61% compared to a single ISAC system.

The authors in [61] present a high-bandwidth, real-time ISAC platform operating in the upper D-band at 160 GHz. The platform comprises a SW-defined intermediate frequency transceiver and a D-band RF module. Its flexible SW design allows for rapid integration of signal processing algorithms.

Recently, the authors in [62] have presented the design of a mmWave system for integrated communication and sensing based on SDR. Operating in the 60 GHz band, it supports signal bandwidths up to 2 GHz, a sampling frequency of up to 4 GSps, and one-dimensional (1D) sequential beam scanning within a Field of View (FoV) of 90 degrees. This HW can support two stream MIMO communication, mono- and bi-static radar-like sensing.

The problem with OFDM-based ISAC systems is that the bandwidth required for high-range resolution cannot be obtained. This problem can be overcome by using a stepped-carrier method, where the carrier frequency of each OFDM signal increases linearly to achieve wide overall RF bandwidth. In [63], for the first time, the authors present a PoC for OFDM-based ISAC system utilizing both stepped-carrier and time-division multiplexing (TDM) MIMO schemes.

3.2 Description of selected ISAC platforms

This section provides an insight of the different WATs that can serve as ISAC platforms for assessing the developments carried out in 6G-SENSES and for running the PoCs.

3.2.1 Wi-Fi

Wi-F) is a technology that allows electronic devices to connect to a wireless local area network (WLAN). It is based on the IEEE 802.11 standards and is widely used for Internet access, data transfer, and communication between devices. In the context of ISAC, Wi-Fi can be utilized not only for data communication but also for sensing applications such as motion detection, localization, and environmental monitoring. The dual functionality of Wi-Fi in ISAC systems leverages its widespread deployment and existing infrastructure to provide both connectivity and sensing capabilities.

Wi-Fi active sensing technology represents a significant leap forward in the realm of wireless communication, offering a multifaceted approach to real-time data analysis and environmental interaction. By utilizing one antenna to transmit signals and the remaining antennas to receive, Wi-Fi enables a device to engage in duplex communication, effectively 'listening' while it 'speaks.' This dual capability is the cornerstone of a PoC (PoC#1) that aims to demonstrate the practicality and efficiency of active sensing in a Wi-Fi context (for more details see section 4.4 in deliverable D2.1 [1]).

The algorithms developed for this purpose are designed to refine the process of delay and Doppler estimation, which are critical parameters in determining the relative motion and distance of objects in the vicinity of sensors. These advancements pave the way for a host of applications, particularly in the burgeoning fields of augmented reality (AR), virtual reality (VR), and extended reality (XR). The implications for these technologies are profound, as they rely heavily on seamless and intuitive interaction with virtual environments.

3.2.1.1 Functional definition

Passive sensing: This mode involves at least 2 devices (see Figure 3-1), similar to a bi/multi-static mode. In this operation mode the Wi-Fi devices do not have a global synchronization. As a result, the CSI information presents frequency and timing errors such as carrier frequency offset (CFO), carrier phase offset (CPO), sampling frequency offset (SFO) and sampling time offset (STO). Because of that, the passive sensing can mostly be used for larger-scale motion detection applications.

Active sensing: This mode operates in monostatic mode utilizing one Tx antenna and one Rx antenna (see Figure 3-2), and the transceivers are co-located and globally synchronized.

Active sensing adds an operation mode similar to radar, where range and Doppler estimation are enabled (not only monitoring/channel change). The expected performance of the Wi-Fi platform is related to the waveform configuration. The Wi-Fi platform, based on OFDM signals has the complex envelope of the transmitted Wi-Fi Long Training Field (LTF) signal that can be expressed as [64]:

$$x(t) = \sum_{m=0}^{M-1} \sum_{n=0}^{N-1} S(m,n) e^{j2\pi n \Delta f t} \mathrm{rect}\left(\frac{t - mT}{T}\right) \tag{3-1}$$

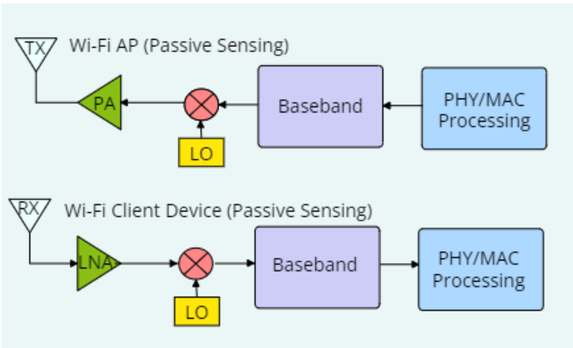

Figure 3-1 Wi-Fi transceiver architecture – Passive sensing

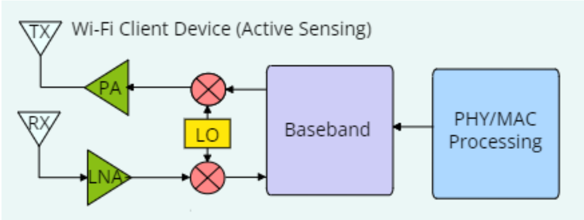

Figure 3-2 Wi-Fi transceiver architecture – Active sensing

where:

- N is the number of subcarriers,
- M is the number of LTF frames,
- Δf is the subcarrier spacing,
- T is the LTF frames interval,
- S(m, n) is the transmitted data/pilot at subcarrier (n) and of LTF frame (m).

Before reaching the receiver, the OFDM signal transmitted by the Wi-Fi system is reflected by K targets. For target k, the signal experiences a delay τ_k , which is proportional to the range of the target r_k, and a Doppler frequency shift, $f_{D,k}$, which is proportional to the velocity, v_k, of the target.

$$\tau_k = \frac{2r_k}{c} \qquad f_{D,k} = \frac{2v_k f_c}{c} \tag{3-2}$$

The received signal is given by [1]:

$$y(t) = \sum_{k=1}^{K} x(t-\tau_k) e^{j2\pi f_{D,k} t} \tag{3-3}$$

$$y(t) = \sum_{k=1}^{K} \sum_{m=0}^{M-1} \sum_{n=0}^{N-1} S(m,n) e^{j2\pi(n\Delta f + f_{D,k})(t-\tau_k)} + \tilde{\eta}(t) \tag{3-4}$$

The received signal can be defined as:

$$\hat{S}(m,n) = S(m,n) \sum_{k=1}^{K} a_k e^{j2\pi T f_{D,k} m} e^{-j2\pi n \Delta f \tau_k} + \tilde{\eta} \tag{3-5}$$

where:

- $\hat{S}(m,n)$ is the received OFDM symbol at subcarrier n and LTF frame m ,
- $S(m,n)$ is the transmitted data at subcarrier n and LTF frame m,
- K is the number of targets,
- a_k is the gain for target k ,
- $f_{D,k}$is the Doppler frequency shift for target k ,
- τ_k the delay for target k ,
- $\tilde{\eta}$ is the Additive White Gaussian Noise (AWGN).

We can observe that the distortions due to the channel are entirely contained in the received modulation symbol. By comparing the transmitted signal with the received signal and disregarding the noise, we can generate the following frequency domain channel matrix:

$$D_r(m,n) = \frac{\hat{S}(m,n)}{S(m,n)} = \sum_{k=1}^{K} e^{j2\pi T f_{D,k} m} e^{-j2\pi n \Delta f \tau_k} \tag{3-6}$$

The estimation of the round-trip delay and the Doppler shift (and hence the distance and relative velocity of the targets) is transformed into a spectral estimation problem. The range and velocity parameters can be obtained from a two-dimensional Fourier Transform (2D-DFT/FFT).

Range and doppler resolution:

A key performance measure of a radar system is its resolution limit for critical parameters such as range and velocity. The range resolution, Δr, is determined solely by the total bandwidth of the transmitted signal, B, and it is given by [65]:

$$\Delta r = \frac{c}{2B} = \frac{c}{2N\Delta f} \tag{3-7}$$

where:

- N is the number of subcarriers,
- Δf is the subcarrier spacing.
- The Doppler resolution depends on the number of LTF frames, M, and the time interval between the frames (frame rate) given by [65]:

  $$\Delta v = \frac{c}{2Mf_cT} = \frac{c\Delta f}{2Mf_c} \tag{3-8}$$

  where f_c is the carrier frequency, T is the LTF frame interval (1/frame rate) and M is the number of frames.

Unambiguous range and velocity limitation

The Wi-Fi sensing system also suffers from maximum and unambiguous distance limitations, as the signal travels the distance twice, resulting in an unequivocal maximum measurement distance, given by [65]:

$$R_{\max} = \frac{cN}{2B} = \frac{c}{2\Delta f} \tag{3-9}$$

The Wi-Fi system also has a maximum unambiguous velocity given by:

$$V_{\max} = \frac{c}{2f_cT} \tag{3-10}$$

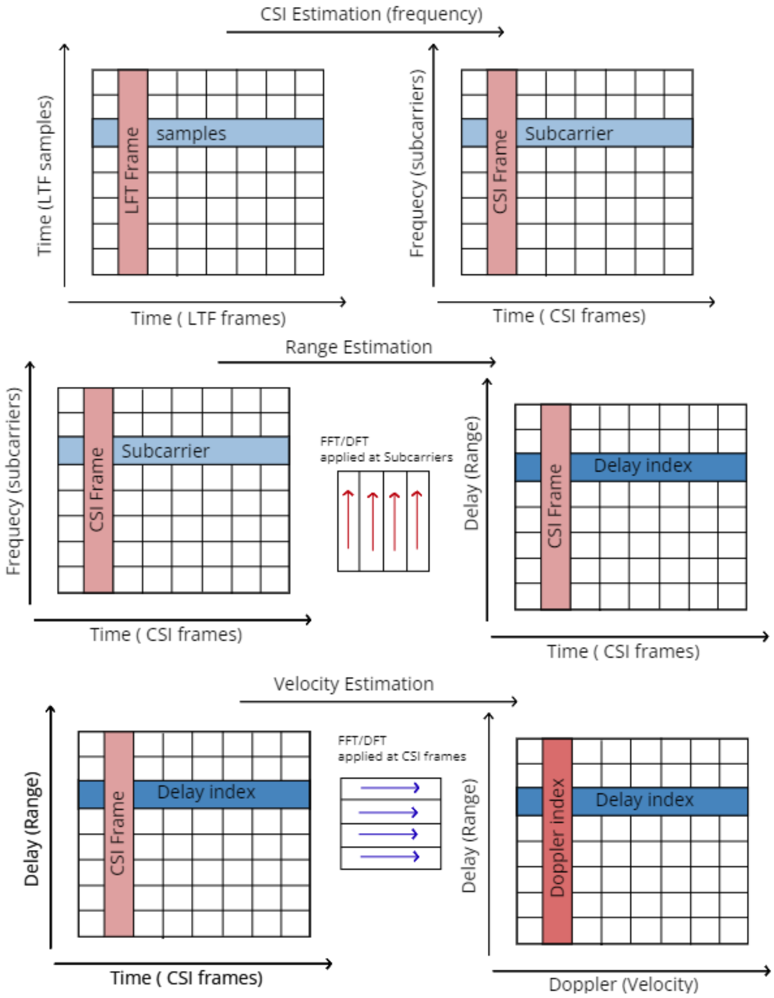

Figure 3-3 Range and Doppler estimation based on CSI

Radar Accuracy Estimation vs. Resolution

Radar resolution describes the ability of a radar to separate objects, whereas measurement accuracy indicates how precisely a parameter such as speed can be estimated. The accuracy of the distance measurement depends essentially on the noise, giving a specific power of the radar pulse: the noise power in relation to the pulse power. This quantity is described by the SNR. The size of the noise itself and the slope of the pulse edge depend on the bandwidth. For an SNR considerably higher than 1, the following relationship exists between these variables:

$$\delta R = \frac{c}{2B \cdot \sqrt{2\text{SNR}}}$$
$$\text{SNR} = 10log\left(\frac{\text{signal power}}{\text{noise power}}\right) = 10log\left(\frac{P_S}{P_R}\right) \tag{3-11}$$

where:

- δR is the measuring error.
- SNR is the signal-to-noise ratio.
- P_S is the signal power.
- P_R is the noise power.

Table 3-1 Wi-Fi Active sensing platform expected operational values

CSI Bandwidth	CSI frame interval	Range Resolution	Velocity Resolution (based on 8 frames and 6 GHz)	Unambiguous Range	Unambiguous velocity
160 MHz	0.025 s	0.94 m	0.12 m/s	480 m	1 m/s|+- 0.5m/s
20 MHz	0.02 s	7.5 m	0.15 m/s	3837 m	1.24 m/s|+- 0.62m/s

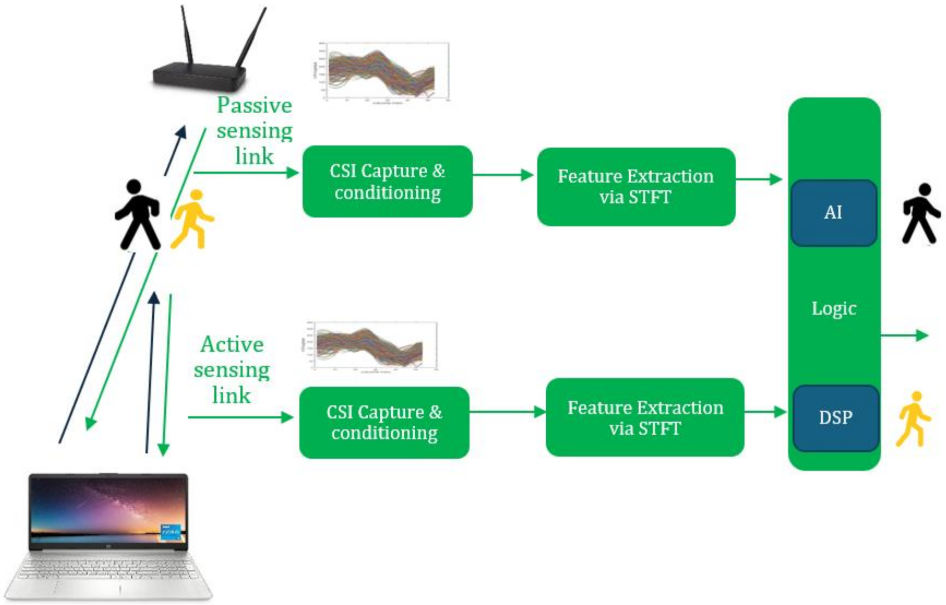

Figure 3-4 Block diagram of the Wi-Fi sensing signal processing

However, the bandwidth is also important to determine the range resolution of a radar. Thus, the maximum achievable accuracy can also be represented as a function of the range resolution of a radar:

$$\delta R = \frac{\Delta r}{\sqrt{2\mathrm{SNR}}} \tag{3-12}$$

In both active and passive sensing applications, data collection and processing are performed using Python, with Application Programming Interfaces (APIs) to communicate and control the Network Interface Card (NIC) Wi-Fi driver active in the client device. The bandwidth operation options include 20, 40, 80, and 160 MHz. The maximum frame rate for data collection depends on the selected bandwidth. For example, a frame rate of 50 Hz is expected for 20 MHz, and 40 Hz for 160 MHz data collection based on active sensing.

The range and Doppler resolution in active sensing are influenced by the number of CSI frames and the selected bandwidth. Table 3-1 provides operational values related to resolution and unambiguous values for the active sensing platform.

Regarding the ***Wi-Fi Human presence sensing PoC*** (PoC#1), the data is first acquired as a time-stream of complex IQ data. Then, CSI estimation is conducted based on the known legacy long training field (L-LTF). After preprocessing, the magnitude of the short-time Fourier transform (STFT) of the signal is then applied to generate a 2D time-frequency representation (spectrogram) of the signal. A block diagram summarizing the sensing signal processing steps is shown in Figure 3-4.

The CSI-based sensing algorithm makes use of the magnitude and phase of the channel estimates across the sub-carriers to reveal the multipath environment. The core algorithm makes use of the covariance matrix of multiple channel estimates obtained over time to determine motion in the link. In this work, **INT** will explore a novel sensing algorithm for human activity recognition, including:

- Determine the measured eigen-decomposition-metric values (E-metric values) of the multiple channel estimates over time for the different hypotheses as a function of time, to exemplify the impact of movement in the room to the link; that is: the key features of the CSI containing movement information can be extracted by conducting principal component analysis (PCA) over the multiple channel estimates over time.
- Develop statistical classifiers that take the calculated E-metric values over time and decide on the presence and motion of a subject, via appropriate pieces of training and calibrations.
- Fuse the decisions provided by each link, by using hybrid passive and active sensing links. By assuming that the hypotheses are equally likely and that the decisions made using each link are conditionally independent,

$$P(motion|active\ link, passive\ link) = \frac{P(active\ link|motion)P(passive\ link|motion)P(motion)}{P(active\ link, passive\ link)} \tag{3-13}$$

3.2.1.2 Hardware abstractions

The HW components of a Wi-Fi ISAC Sub-6 GHz platform system include the following:

- **APs:** act as the transmitter node for passive sensing in a Wi-Fi network. They transmit data packets that are used for sensing by analyzing the changes in the CSI received signal magnitude and phase.
- **Client Devices:** The client device used in this platform is a Lenovo TS / ThinkPad L / L14 G5 / Ultra 7 155U. This participates in sensing tasks by transmitting and receiving signals that can be analyzed for various sensing applications. In this study, client laptops/PCs operate in 'radar-like' mode for active sensing and in monitoring mode for passive sensing. The laptops with Intel® Wi-Fi solutions are proprietary to Intel® Wi-Fi 6/6E.
- **Antennas placements:** The design and placement of antennas can significantly impact the performance of both communication and sensing functions. In active sensing experiments a single station is considered where both Tx/Rx antennas are located in the same transceiver. For passive sensing two stations are considered: AP Tx and laptop Rx.
- **RF Modules:** The Intel® Wi-Fi 6E AX211 module handles the transmission and reception of RF signals for active sensing, and the reception mode for passive sensing. The Intel® Wi-Fi 6E AX211 is designed to support Wi-Fi 6 R2 features, supporting the 6 GHz band operation mode that includes 160 MHz of bandwidth channels. The operation frequency of the platform is Sub-6 GHz.
- **Processing Units:** These units, often embedded within APs and client devices, process the received signals for sensing purposes. They run algorithms for data decoding, signal processing, and sensing analysis based on Python. The notebook used for the platform data collection and processing is the Lenovo TS / ThinkPad L / L14 G5 / Ultra 7 155U (14", Intel Core Ultra 7 155U, 32 GB, 1 GB).

For the ***Wi-Fi Human presence sensing PoC***, both passive and active sensing mode are considered. Depending on whether there is an AP or not, there are two different modes of Wi-Fi sensing defined as follows:

Sensing Human Presence with Intel Wi-Fi PoC: Both active and passive Wi-Fi sensing models are deployed. The test setup is depicted in Figure 3-5:

- Wi-Fi networks that operate in co-channel (sub 7 GHz).
- A PC operates in 'radar-like' mode for active sensing and in monitoring mode for passive sensing.
- A PC with proprietary to Intel® Wi-Fi 6/6E.
- Brand name AP with chipsets coming from different vendors, instead of Intel.
- In active sensing experiments, the laptop detects human motion. In passive sensing experiments, two stations are considered: AP Tx and laptop Rx.

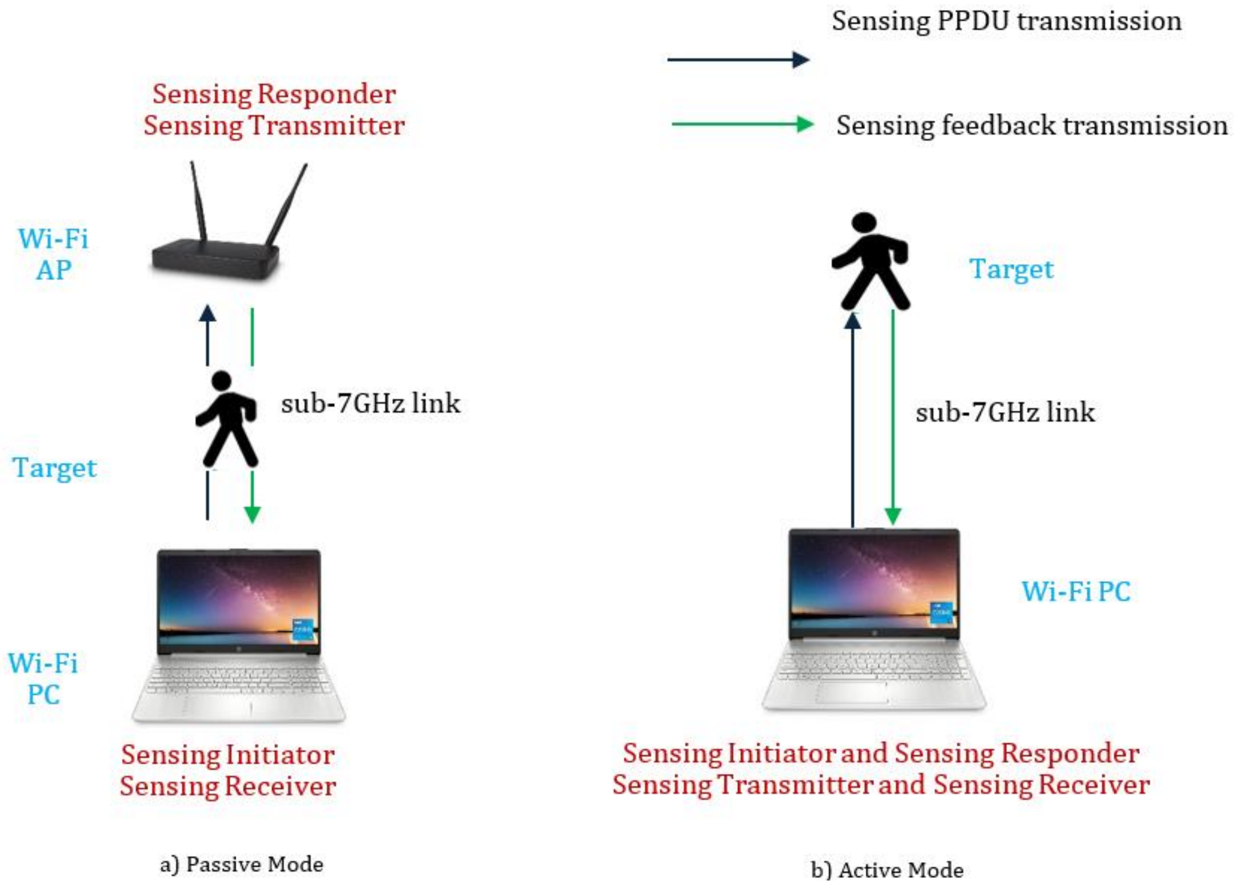

Figure 3-5 The illustration of the Wi-Fi sensing test setup

Experiments considered:

- Experiment 1: Active sensing, single subject.
- Experiment 2: Passive sensing, single subject.
- Experiment 3: Hybrid active and passive sensing, single subject.

The following hypotheses are considered:

- No human presence: nobody is in the room when sensing happens.
- Sensing human presence in the front of the PC, comprised of two sensing detection periods ***T1, T2*** and two notifications ***N1, N2*** in one loop:

  During a preset time T1: Gross motion activities detection is conducted, including subject walking, moving around, upper body motioning, sitting in front of the laptop. In this way, the laptop monitors the duration a person is sitting in front of a computer. Herein, respiration detection could be added for static person detection.

Notification N1: After ***T1,*** the laptop notifies the user to get up and move around.

During a preset time T2: As the person moves around, the laptop monitors the duration of the activity.

Notification N2: In case the user stops moving and sits down within ***T2***, the PC detects this and notifies the user to move a little longer.

The loop repeats.

Table 3-2 KPIs for Human Presence PoC

KPI	Value	Comments
Detection Distance	< 2 m (human presence detection)	-
Detection Probability	Missed detection ≤ 5%	Probability of correctness for (i) presence detection (ii) breathing rate (iii) distinguishing human target
Target number	>2	Expected number of simultaneous targets

3.2.1.3 Platform evaluation and preliminary results

Active Sensing sub 7 GHz Platform for Gesture Recognition and Presence Detection

Under 6G-SENSES, **INT** has developed an active sensing platform and advanced algorithms designed ISAC demonstrations, specifically focusing on gesture recognition and presence detection. This platform will be utilized to implement and validate new algorithms and waveforms for active sensing using real-world measurements. This subsection presents an evaluation of the current platform status and some preliminary results.

To demonstrate and assess the Wi-Fi sensing capabilities, preliminary tests were conducted on hand movement detection using active Wi-Fi sensing. A commercial radar system was used as a baseline to evaluate the accuracy of the platform and algorithms. Figure 3-6 illustrates the measurement setup, which includes a Wi-Fi AX211 module and a Frequency-Modulated Continuous Wave (FMCW) radar (BGT60TR13C).

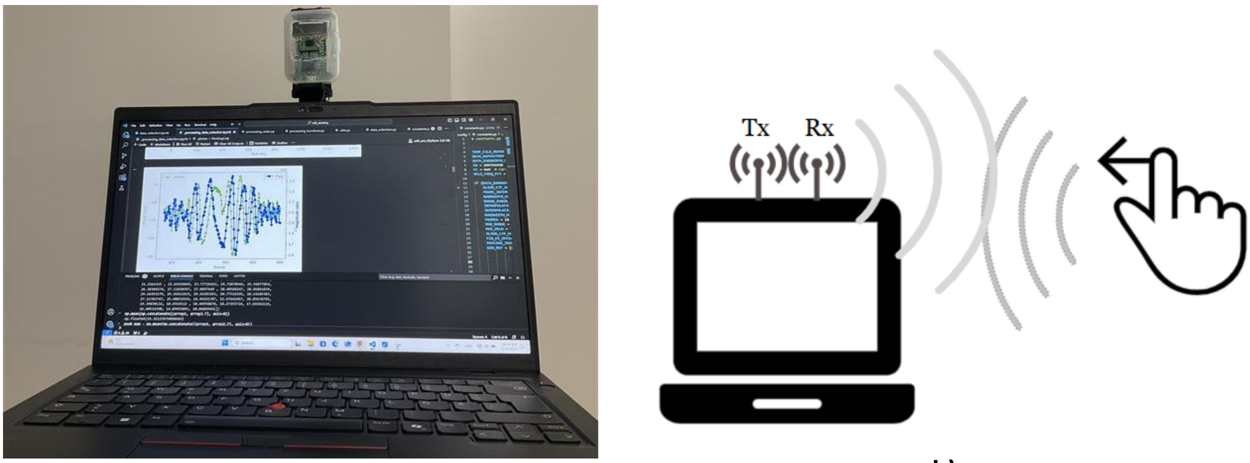

a) b)

Figure 3-6 Wi-Fi and Radar Measurement Setup (a) and Test Diagram Representation (b)

Table 3-3 System Parameter Configurations for Hand Movement Detection with Active Wi-Fi Sensing

System	Bandwidth	Frame/ Ramp Interval	Range Resolution	Velocity Resolution	Max. Range	Max. Velocity	Subcarriers /Samples	Frames/ Ramps
Wi-Fi	160 MHz	0.025 s	0.94 m	0.06 m/s	480 m	±0.5 m/s	512	16
Radar	4 GHz	0.0006 s	0.03 m	0.07 m/s	1 m	±2.24 m/s	64	64

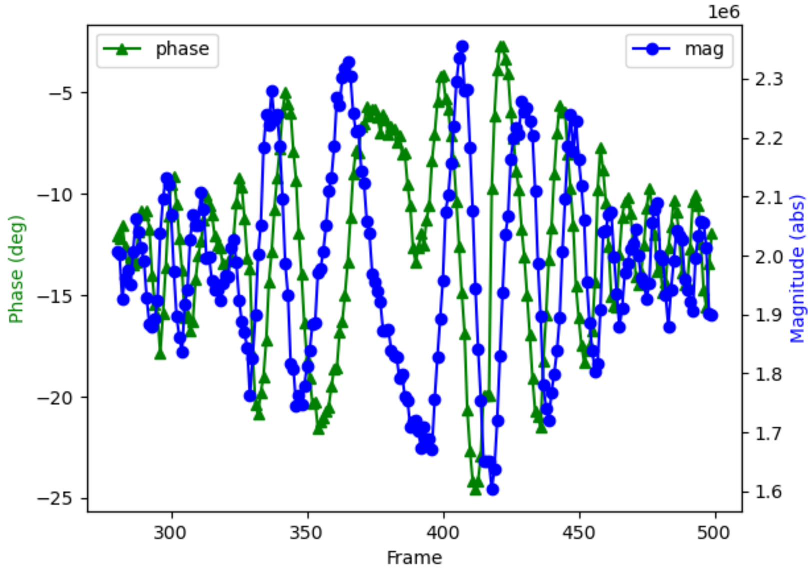

Figure 3-7 Wi-Fi CSI Active Sensing Magnitude and Phase vs. Frames

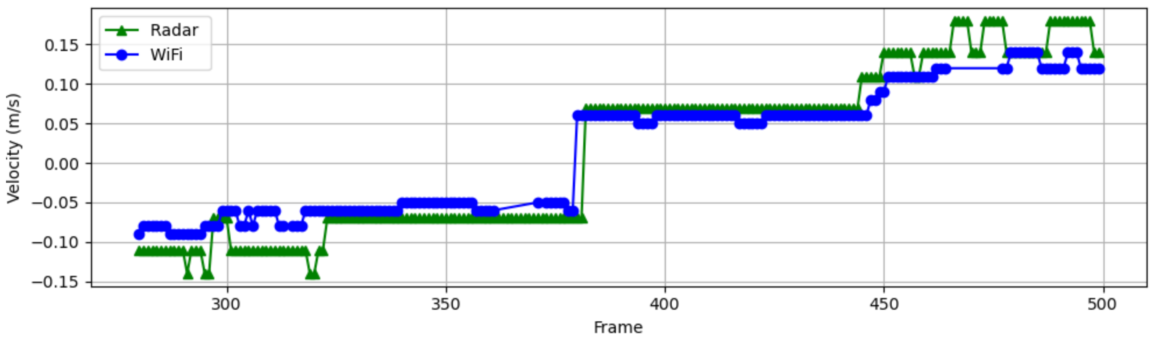

Figure 3-8 Wi-Fi vs. FMCW Radar Doppler Estimation for Hand Movement

Measurements were conducted simultaneously with both systems for a hand movement with an approximately constant velocity approaching and moving away from the Wi-Fi/radar setup at approximate 20/40 cm distance. The parameter configurations for both systems are shown in Table 3-3.

Figure 3-7 shows the CSI magnitude and phase plot by frame for the Wi-Fi signal, while Figure 3-8 compares the Doppler estimation between the radar and Wi-Fi systems. By comparing the estimations from both systems, we conclude that the Doppler estimation by the Wi-Fi system is accurate, with minor deviations due to the inherent accuracy limitations of both systems. The results indicate that the Wi-Fi platform provided by **INT** can accurately measure velocity. The range estimation and validation are ongoing investigations.

3.2.2 Sub-6

3.2.2.1 Functional definition

For testing and evaluation of the proposed ISAC approaches, a Sub-6 GHz sensing system has been developed in the context of the Smart Networks and Services Joint Undertaking (SNS JU) Phase 1 Project **BeGREEN** [66], [67]. The sensing system will be extended in the context of 6G-SENSES to a networking-based ISAC, to benefit from multi-node cooperative perception and sensing data sharing from multiple sensing nodes.

The sensing system implementation has been performed using a Universal Software Radio Peripheral (USRP) N321 SDRs. The developed system is shown in Figure 3-9. Four SDRs are used to obtain a total of 8 receive channels, given that each radio has only two receiver channels. All the SDRs share the same local oscillator (LO). This is achieved by generating the LO at one of the SDRs and using cables to distribute it to the other SDRs. It is necessary to calibrate the phases between the different SDRs, since they will have random phases due to tolerances of the electronic components built in them. This calibration will allow fully coherent operation of the SDRs, needed to perform beamforming.

The timing synchronization between the SDRs is achieved using the White Rabbit (WR) protocol, i.e. using a WR Ethernet switch model WRS-3/18[1]. With this approach, the SDRs time can be synchronized with precision of ±100 ps, which is sufficient for the current application.

The carrier frequency is in the 5 GHz Industrial, Scientific and Medical (ISM) radio band, since no explicit licence is needed for transmitting in this band. The lower 5 GHz ISM band is preferred, as it allows increasing the output power compared to the high 5 GHz band, resulting in an output power of not more than 10 dBm.

The ranging precision of the sensing system is proportional to the available bandwidth. In the 5 GHz ISM band, channel bandwidths of up to 160 MHz are available and bandwidths of 320 MHz are envisioned. These N321 SDRs are supporting bandwidths of up to 200 MHz and this value is used in the experiments. For sensing, different waveforms can be used. In this case a maximum length sequence, with length of 16383 bits, i.e. one symbol, was transmitted. This sequence is modulated using binary phase-shift keying (BPSK) modulation. An Uniform Linear Array (ULA) consisting of 8 patch antennas was designed and manufactured, being the distance between the antennas of $\lambda/2$.

[1] https://safran-navigation-timing.com/product/white-rabbit-switch-low-jitter/

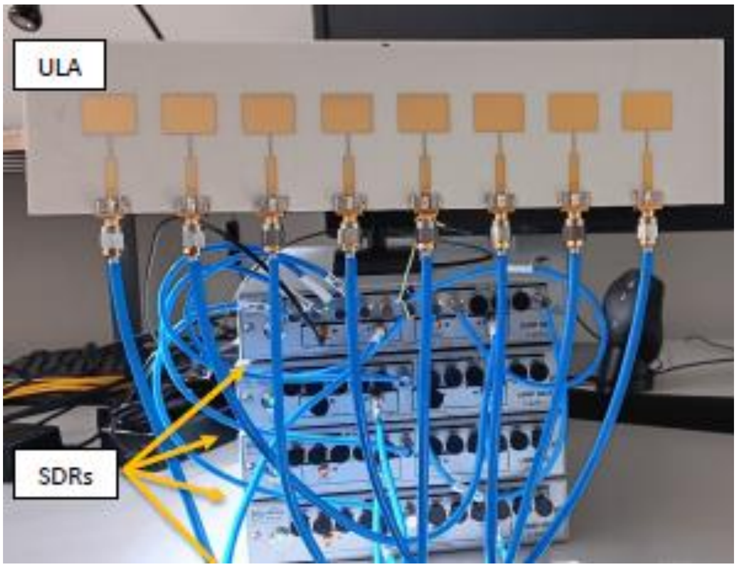

Figure 3-9 6G-SENSES Sub-6 ISAC system [67]

The system transmits a waveform that represents a data frame, but it only performs sensing and not data transmission, since the transmitted waveform is not received by another device. Even if there is no communication with another device, data transmission and sensing are performed simultaneously. We assume that the signal sent by the RU (AP) via a single antenna is reflected back from one or multiple targets, reaching the ULA as the superposition of delayed and attenuated copies of the transmitted signal.

The main objective of the sensing signal processing is to estimate the position of the obstacles from which the transmitted signal was reflected back and received by the receiver. This can be performed in a 3-dimensional (3D) space or in a 2D space. For both cases the required signal processing is similar. For the 3D case, the system and the required processing are slightly more complex compared to the 2D case. Namely, for a 3D case, a planar antenna array is needed where for the 2D case a linear antenna array is sufficient. Additionally, for a 3D case, an antenna array with larger number of antennas is required.

For many applications 2D sensing is sufficient and it is the starting point of 6G-SENSES, to then move to 3D sensing. In the former case, it is necessary to find the positions of the obstacles reflecting the signal back to the RU in a polar coordinate system. This means finding the distance from the RU to the obstacle, and the direction at which this reflected signal is returning to the RU.

The distance estimation is performed by estimating the round-trip time (RTT) of the received signal. The transmit time is known and the ToA needs to be estimated, which is usually obtained after carrying out the correlation between the received signal and that transmitted.

Estimation of the angle from which the reflected signal arrives at the receiver can be performed using different approaches, but always with an antenna array of at least two receive antennas. The larger the number of receive antennas is the better the sensing angular resolution will be. The receive antenna array, for 2D sensing is usually an ULA and for 3D sensing is usually a uniform planar array (UPA). The approaches to interconnect the antenna(s) and the RF chain can be: 1) each antenna is connected to a separate receive chain, offering the most flexible solution for sensing at a higher cost; 2) only analogue; and 3) hybrid beamforming.

In 6G-SENSES we have opted for the first approach for the Sub-6 sensing system, since many Sub-6 GHz devices are already designed as MIMO systems. This means that the necessary HW for the first approach described above is already available, and the sensing implementation will mainly require SW changes. This is a standard configuration used in digital beamforming systems and allows the implementation deployment of different direction-of-arrival (DoA) estimation approaches. Known methods that are usually implements are MUltiple SIgnal Classification (MUSIC), Matrix Pencil, Estimation of signal parameters via rotational invariant techniques (ESPRIT) or digital beamforming with multiple parallel beams. Despite its associated costs, it is becoming a preferred solution in commercial for Sub-6 GHz devices. For the case of mmWave systems, where larger channel bandwidths are used, this kind of solution is becoming expensive and is usually not implemented in commercial products.

3.2.2.2 Angle of arrival estimation

The current implementation of the AoA estimation uses digital beamforming to estimate the angle at which the signal is received at the receiver.

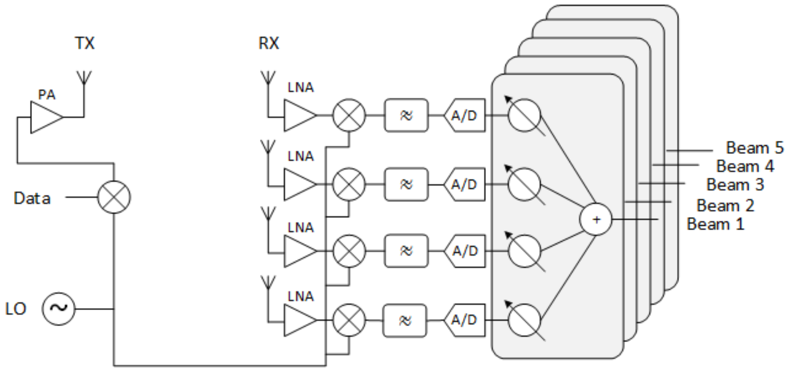

Figure 3-10 Digital beamforming capable transceiver

A simplified architecture of a transceiver capable of digital beamforming is given in Figure 3-10. This transceiver is a single-output-multiple-input system (SIMO), i.e., it has one transmit and multiple receiver chains. This architecture enables digital beam steering for the receiver only, which is necessary to obtain the DoA of the signal reflected from different obstacles. On the transmitter side, it is not necessary to have multiple transmit antennas.

To perform beamforming at the receiver, the signals from different antennas are multiplied by complex coefficients. A set of these complex coefficients for a single beam is called beamforming vector. The signal received from different beams can be calculated as:

$$s_B = B \cdot s, \tag{3-14}$$

Where s_B is a $m \times n$ matrix where n is the signal length and each row represents a signal coming from different direction, i.e. beam. The matrix B is a beam steering matrix where each row is a beamforming vector and has dimension of $m \times p$. Finally, the matrix s is a signal matrix where each row represents the signal received from each antenna and has a dimension of $p \times n$. Expanding (3-14), we obtain:

$$\begin{bmatrix} s_{B11} & \cdots & s_{B1n} \\ \vdots & \ddots & \vdots \\ s_{Bm1} & \cdots & s_{Bmn} \end{bmatrix}_{m\times n} = \begin{bmatrix} b_{11} & \cdots & b_{1p} \\ \vdots & \ddots & \vdots \\ b_{mp} & \cdots & b_{mp} \end{bmatrix}_{m\times p} \times \begin{bmatrix} s_{11} & \cdots & s_{1n} \\ \vdots & \ddots & \vdots \\ s_{p1} & \cdots & b_{pn} \end{bmatrix}_{p\times n}. \tag{3-15}$$

With this approach, a total of m different beams will be created. The number of beamforming vectors is also m, i.e. one beamforming vector for each beam. The number of antennas at the receiver is p and the signal length is n. The main advantage of using digital beamforming is that all of these beams can be formed at the same time in digital domain and larger environment can be sensed without additional spectrum usage.

3.2.2.3 ISAC assisted beam training

Beamforming and electronic beam steering are technologies that exist for more than a few decades. These technologies allow to have a high-gain antenna that can be electronically steered to a preferred direction.

The main advantage of having a high gain antenna is that lower output power can be used, leading to increased power efficiency of the system. The main disadvantage of high-gain antennas is that the antenna radiation pattern is relatively narrow, which significantly reduces the coverage area of such a system.

The main issue with the electronic beam steering approach is that beam training should be performed whenever an initial connection with the UEs needs to be established. This is needed to find the precise direction where a UE is located, i.e. direction to which pointing the beam. Additionally, if, for some reason, the connection between the two devices is lost, retraining must be performed.

Two main approaches for performing beam training are mainly used. The first one is called **exhaustive** search and the second one is called **hierarchical** search. In the first approach, all the possible directions are searched. Namely, if there are *n* directions in total, all of them will be searched. This means that the complexity of this approach will be $O(n)$ if only one of the transceivers in a communication scenario has electronic beam steering possibility, and $O(n^2)$ if both of the transceivers in a communication scenario have electronic beam steering possibility. In case of the hierarchical beam search, the complexities are $O(log(n))$ and $O(log^2(n))$ respectively. Nevertheless, despite the lower complexity of the hierarchical beam search, it has a disadvantage because it must electronically generate a wider radiation pattern of the phased array antenna, which means turning off some of the elements and transmitting less power, meaning less coverage. Both approaches are spectrum inefficient and relatively complex, therefore rarely used.

3.2.2.4 HW abstractions

The SW for sensing comprises two separate entities. The first part is written in C/C++ and is used to configure the SDRs and to acquire samples upon request. The second part is written in MATLAB and is used to perform the processing needed for the sensing part.

6G-SENSES plans to make this approach more convenient and more spectrum efficient, therefore being more attractive to be implemented in many devices. It is clear that this approach has good energy saving potential, if the above-mentioned disadvantages can be addressed. Namely, having the means to scan the environment help the beam training procedure to be optimized to be more spectrum efficient by searching more precisely the areas where more users are expected and less precise where no users are detected. This should improve the training procedure beyond the one of the hierarchical search and, at the same time, improve some of the disadvantages of this approach. This will make the approach more favourable in the future wireless system, leading to improvement of their EE.

This system is in the process of being integrated in an ISAC platform hosted at the University of Cantabria (**UC**), which is described in section 3.2.4.3.

3.2.3 mmWave

Unlike the previous work included in section 3.1.4, 6G-SENSES, and this section in particular, presents a mmWave ISAC system featuring all digital signal processing in a single System-on-Chip (SoC), thus minimizing the form factor. It is based on a COTS evaluation board (FPGA-based) and front-end modules.

The developed mmWave ISAC system is based on the mmWave SDR platform from [68], built using RFSoC Ultrascale+ FPGA ZCU111 (Gen1) from Xilinx and a dual module analog antenna frontend equipped with two Sivers BFM06005 60 GHz phased array beam-steering modules [70]. The system is depicted in Figure 3-11.

The extensions to support ISAC in the platform to be used in 6G-SENSES have been implemented in the context of the German-funded project Open6GHub [71]. The platform supports both SDR and real-time (RT) operation modes and it is fully described in [62]. HW-based processing is leveraged to reach several Gbit/s data throughputs and a short sensing time of below 0.5 ms.

3.2.3.1 System Components

The central element of the SDR platform is an AMD UltraScale+ RFSoC [72]. This SoC is made of a quad-core ARM Cortex-A53 processing system, 8 highspeed analogue-to-digital converters (ADCs) and 8 high-speed digital-to-analogue converters (DACs) as well as a huge amount of programmable logic resources (i.e. the FPGA part of the SoC). The data converters support sample rates up to around 6.5 GSps (DAC) and 4.1 GSps (ADC), respectively.

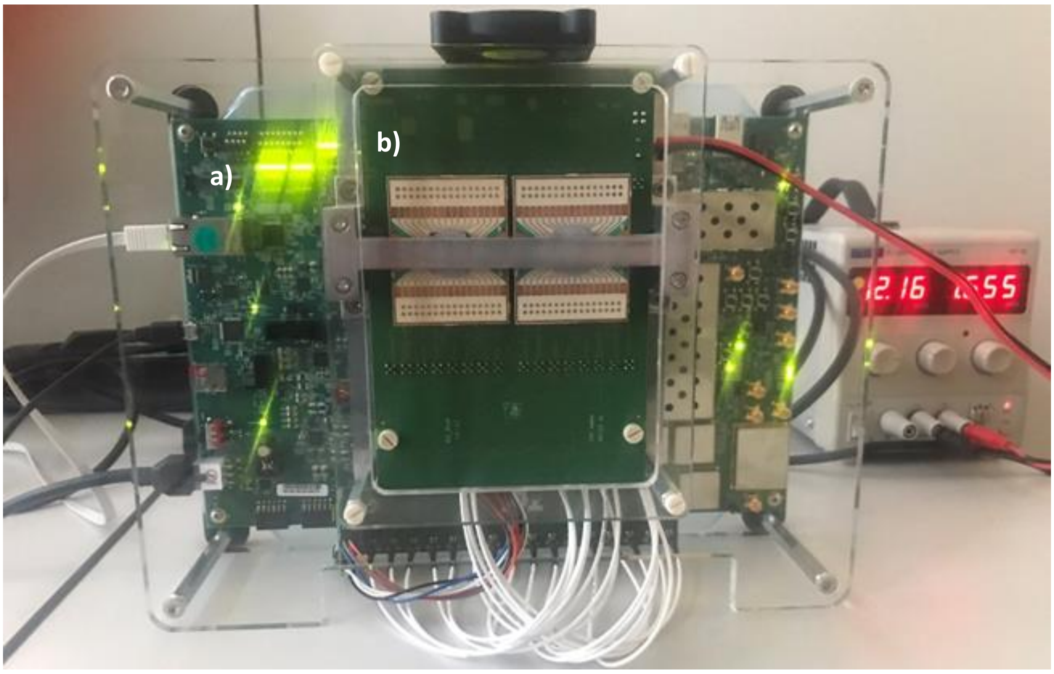

Figure 3-11 a) Xilinx RFSoC ZCU 111 board with SDR functionality and HW implemented real-time OFDM baseband processor, b) 60 GHz dual-module full-duplex RF frontend

3.2.3.1.1 RF data converters

The used AMD UltraScale+ RFSoC contains 16 high-speed data converters (8 ADCs, 8 DACs). The basic SDR design supports 4 ADCs and 4 DACs, which is sufficient for the dual-module beam-steering frontend with an IQ modulated baseband signal interface. Although the sampling clock of the data converters can be freely adjusted, the basic SDR design requires a sampling clock which is an integer multiple of 160 MHz. Otherwise, the sample synchronization of the data converters would not properly work, leading to a sample offset in the IQ signal. As a consequence, the target sampling frequency for the existing OFDM baseband processor (2.16 GSps) cannot be generated. Thus, the sample rate is slightly increased to 2.24 GSps. The AXI4-Stream interface of each data converter provides 8 samples in parallel and operates at a clock rate of 280 MHz.

3.2.3.1.2 SDR Module

The SDR module contains the memory to store the signal waveforms which is be sent out through the DACs and the signal waveforms which are sampled from the ADCs. Its current implementation supports 4 ADCs and 4 DACs. Furthermore, the SDR module contains trigger logic. One trigger input channel is connected to the OFDM baseband processor. Thus, it is possible to analyze the IQ signal generated by the OFDM baseband processor in a loopback mode.

3.2.3.1.3 Sensing controller

The implemented sensing controller consists of a finite state machine (FSM), a timestamp counter and a memory buffer structure to store the estimated channel coefficients.

3.2.3.2 Functional definition

There is a bare metal application on the ZynqMP running TCP server and firmware API. The application interacts with a PC running MATLAB over 1 GbE interface. Full control of the platform can be done from the PC using dedicated MATLAB control functions. In the SDR mode there are 2x4 dedicated memory channels for 4 DAC and ADC, which are set in the direct sampling mode. The sampling frequency of the DACs and ADCs is adjustable in the range from 160 to 4000 MHz with a 160 MHz step. In the RT mode, an OFDM PHY implemented in the programmable logic can be used for both data communication and sensing. There is a sensing controller in the HW that schedules time slots for sensing.

3.2.3.2.1 Real-time operation

The architecture of the real-time mmWave system is shown in Figure 3-12. The **Green** color indicates blocks from the basic SDR HW platform [68], whereas **purple** blocks mark the existing OFDM baseband processor [73][74] and its infrastructure. Orange blocks show the new blocks developed for the ISAC functionality. The mmWave ISAC system operation is controlled from a PC application through a transmission control protocol (TCP) connection over Gigabit-Ethernet (GigE).

The scope of this work is meant to enhance a real-time mmWave communication system [75] by (monostatic) radar in an ISAC approach. While it is a joint communication and sensing system meaning that the radar functionality is realized just by using the components of the communication part, sensing and communication do not operate simultaneously.

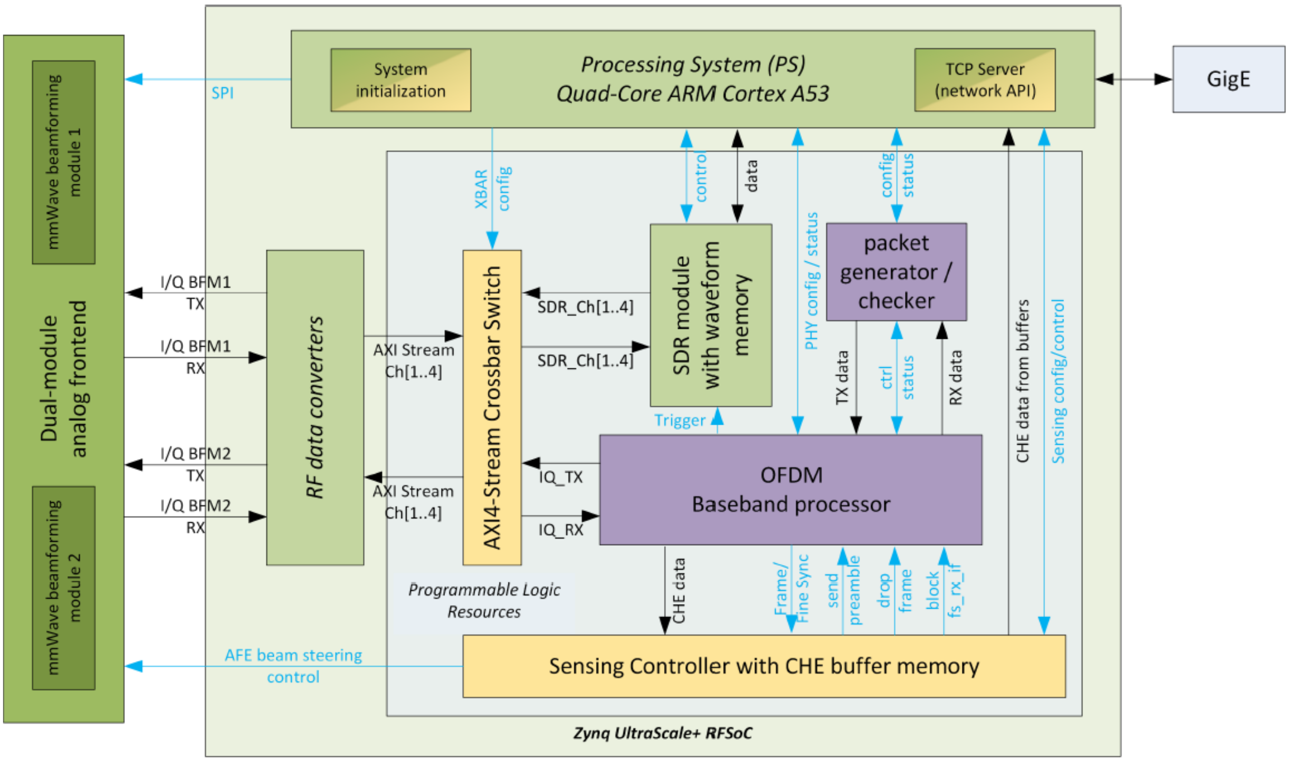

Figure 3-12 Architecture of the mmWave ISAC system (blue arrows: control signals; black arrows: data signals) [62]

Given that analogue beam-steering frontends are used, the (monostatic) radar sensing requires a beam scan over all possible beams, while for the communication, one (fixed) transmit/receive beam has to be set.

It uses the same waveform and the same HW resources. (1) OFDM preamble is sent into every beam direction; (2) Reflected frame is processed in receiver chain, channel coefficients are stored; (3) Reflections appear as spikes in the CIR; and (4) Slot-based medium access (One full angular scan: ~ 500 µs).

3.2.3.2.2 SDR operation

The SDR implementation considers an analog beamforming mmWave antenna frontend (with only one RF chain), which is designed for communication. A horizontal beam scan is used to obtain a range-angular radar map.

Separate time slots are used, i.e., in each slot, either the communication or the sensing functionality is active. In the sensing mode, a full beam scan is done by sending out a preamble in every beam direction, processing the received frame from every beam and storing the estimated channel coefficients (CHEs) provided by the baseband processor. These estimates are transferred to a PC, where the SW-based post-processing consists of an Inverse Fast Fourier Transform (IFFT) operation to transfer the frequency-domain CHEs into time-domain CIRs. The transfer of the CHE data and the post-processing do not need to be performed within a sensing time slot, it can be independently done at any time. Thus, the duration of the sensing time slot can be shortened.

3.2.3.3 HW abstractions

The firmware running on the processing system implements routines for the initial system configuration in a bare metal (standalone) application. It furthermore includes a TCP server with a network API. Through this API, firmware routines to configure the parameters of the implemented blocks, to start and stop the different operational modes and to readout the status and results can be called.

A PC API implemented in Matlab (full, with examples) and Python (only low-level routines) are provided.

3.2.3.4 Platform evaluation and preliminary results

In 6G-SENSES, a hybrid beamforming (HyBF) solution supporting both mmWave communication and sensing with sub-array topology will be implemented, utilizing multiple beamforming (BF) modules. The current status of the work only allows for monostatic sensing, as depicted in Figure 3-13 [69].

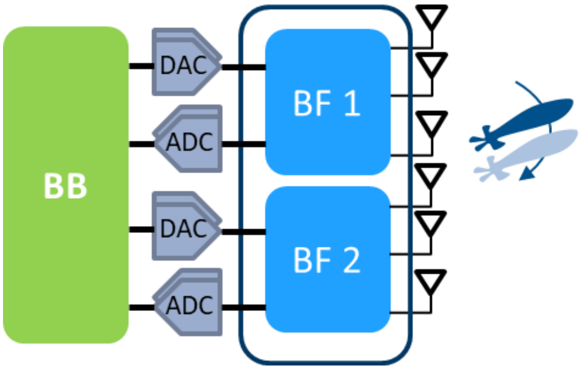

(a)

Figure 3-13 (a) Monostatic RADAR-like sensing scenario (full-duplex required)

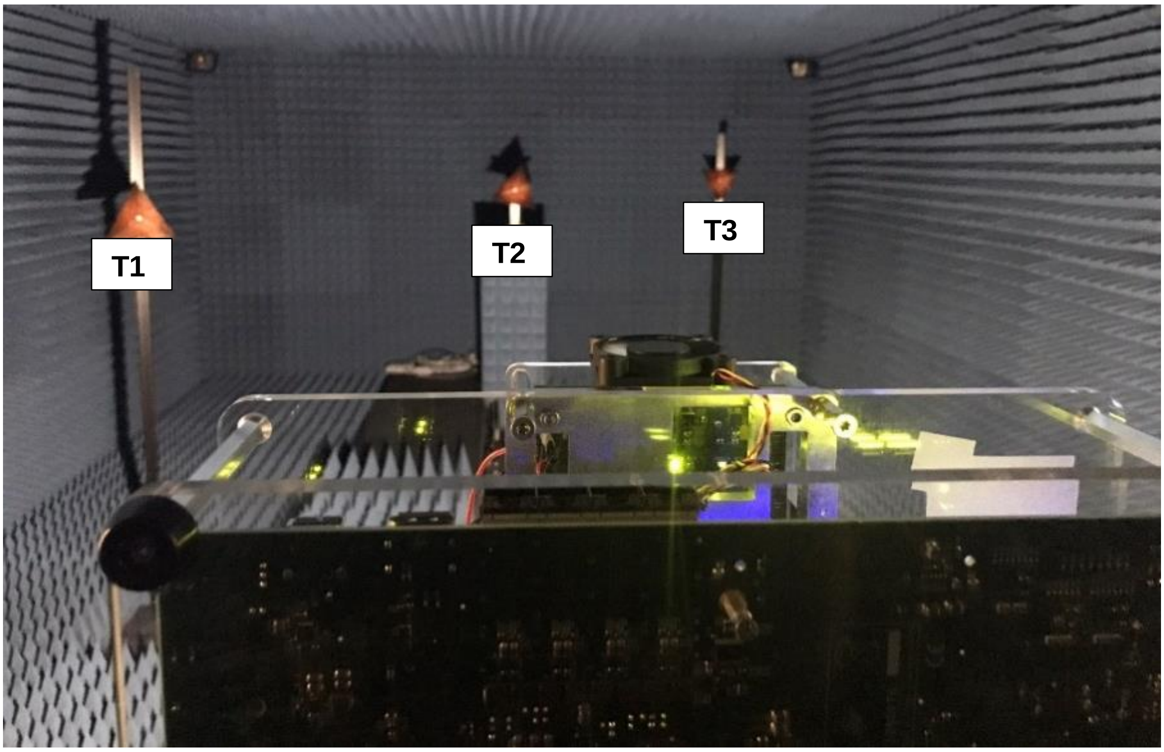

Figure 3-14 Test setup in IHP's anechoic chamber

Utilizing hybrid beamforming sub-array topology of the 60 GHz radio and multi-channel RF-DAC/ADC of the RFSoC, two-stream data communications, **monostatic** and **bistatic radar-like sensing** can be supported. Both Time Division Duplex (TDD) or frequency division duplex (FDD) are possible for data communication. When performing D2D communication in, e.g., TDD, the 60 GHz radio can be used in TX or RX mode supporting two-stream communications. Furthermore, if the two BFMs of the radio operate in TX and RX modes but at different RF channels then FDD mode can be supported. For monostatic sensing, in-band full duplex (IBFD) is preferable, i.e., simultaneous transmission and reception at the same frequency. To support this scenario, one BFM module will be set to the TX mode and the other will be programmed in the RX mode. In addition, bistatic sensing can be done using data communication between two devices, in dedicated time slots where full beam scanning is performed.

The monostatic version uses the same waveform and same HW resources and it is based on a proprietary OFDM baseband processor [75]. The OFDM preamble is sent into every beam direction (up to 63) and the reflected frame is processed in the receiver chain. Then the channel coefficients are stored, where reflections appear as spikes in the CIR. The access to the medium is slot-based, taking ~ 500 µs a full angular scan.

The sensing functionality has been initially tested in an anechoic chamber, as shown in Figure 3-14. The setup consists of the ISAC platform and a few targets (RADAR corner reflectors) placed arbitrarily in space. The positions of the targets are reported in Table 3-4. These are measured using a commercial laser from LEICA and are used as a ground truth.

A sequential beam scan of 63 beams is performed by steering TX and RX beams together from -45° to 45° with a step size of 1.45°. For each beam direction, a typical OFDM communication signal is transmitted and the reflected signal is processed by the receiver.

From the received signal, after signal post-processing, the CSI is extracted and the CIR is derived by IFFT. The range-angle heatmap is shown in Figure 3-15. Three peaks are clearly visible in the figure. These are the reflections from three objects and they appear at 3.21 m, 4.08 m and 5.15 m. Note that the estimated distances are very close to the ground truth values. The difference arises from the fact that the system has an FFT bandwidth of 2240 MHz, so that distance estimates are quantized with a resolution of approximately 6.7 cm.

Table 3-4 Position of the targets in IHP's anechoic chamber

Object	Description	R [m]	Θ [°]	Size [cm]	RCS [dBsm]
T1	Corner	3.23	-22.8	21	25.1
T2	Corner	4.17	00	21	25.1
T3	Corner	5.19	13.0	21	25.1

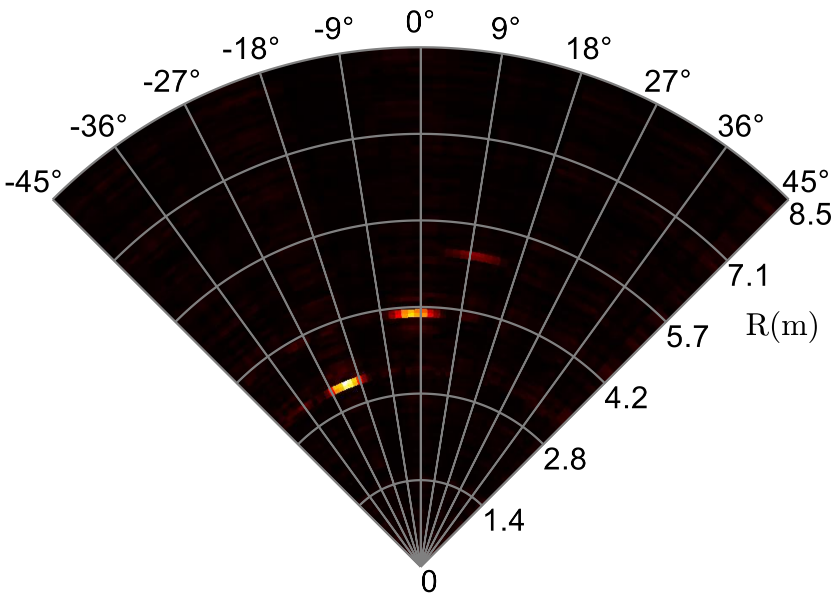

Figure 3-15 Range-angular 2D plot

3.2.4 5G NR

The availability of wide bandwidths in higher frequency bands in (FR3, FR2 and THz), and massive antenna arrays in 5G and 6G systems are expected to offer not only higher data rates but also offer high-resolution environment sensing capabilities. This convergence between radio-based sensing and communication is driving the development of ISAC systems. ISAC 6G use cases and system requirements are expected to be included in future 3GPP and ITU-R releases [76].

The purpose of incorporating sensing capabilities to 5G NR is to access IQ samples collected over the Open Fronthaul interface, which can be duplicated for parallelizing the decoding/demodulation processes and the potential ISAC process. In O-RAN, these use cases can be enabled applications that embed signal processing and waveform analysis functionalities (which can also use AI) that analyze IQ samples to perform one (or more) of the above procedures.

This section presents the different 5G platforms that will be used to implement ISAC functionalities and to carry out the demonstration activities towards the showcasing of PoC#1. The two first platforms will be used to carry out tests that can assist and complement the demonstration activities to be showcased for the final multi-WAT ISAC implementation in the third platform described in section 3.2.4.3.

3.2.4.1 BubbleRAN (BR) testbed

The BubbleRAN (**BR**) platform is located in SophiaTech Campus, French Riviera, and it is an advanced Multi-x (MX)[2] 5G network infrastructure.

3.2.4.1.1 System components

This testbed comprises the following SW and HW components:

- SW components:
  - MX-RAN: 3GPP Rel 16 eNB/gNB/CU/DU/RU, Split 2/7.2/8.
  - MX-CN: 3GPP Rel. 16 4GC/5GC.
  - MX-Operator: Enhanced O-RAN SMO (RAN and Edge and CN) in form of a K8s Operator, Observability Stack, Fault Management.
  - MX-RIC: O-RAN Near-RT and non-RT RIC with xApps and rApps, O-RAN service models (SMs): KPM v2/v3, RC v1.x, CCC v3.x, custom SMs.
- HW components:
  - 2-8x servers (minimal setup: one server playing the role of the 5GC and RAN control plane functions and another one for the real-time gNB-DU).
  - 1-2x O-RAN compliant 7.2 O-RUs (Open RAN Radio Units), 1x eCPRI split 8 Remote Radio Head (RRH), and 1x USRP in FR1.
  - a FibroLAN fronthaul switch with Precision Time Protocol (PTP) support and a PTP grandmaster responsible for synchronization of the different network components.
  - A Power Distribution Unit allowing to accurately monitor and control power consumption at the level of each compute node in the K8S Cluster.

The HW components are indicatively illustrated in Figure 3-16, where some of their features are also highlighted.

3.2.4.1.2 Functional definition

BR testbed is based on multi-x1 platform development kit (MX-PDK), and presents a diverse range of both open-source and commercial network components. The 5G RAN and CN-supported SW stacks include OpenAirInterface (OAI) and srsRAN open-source solutions, as well as Amarisoft and Lite-On commercial solutions. This not only offers various options for conducting evaluations but also advances the vendor-agnostic concept in telecommunications. For this reason, the term “MX” is used to highlight the diversity of the network components in the testbed. However, this diversity is not limited to the network components; it can also extend to various environments in terms of HW equipment, operating systems (OSs), and multiple Clouds (on-premises, public, or hybrid) where these components can be deployed.

Additionally, the testbed offers the capability of either emulated or real over-the-air environments. The only difference between the two is that, in the former option, both the channels and UEs are emulated (layers 2 and above are identical).

The physical testbed is also shown in Figure 3-17, highlighting how the SW and HW components mentioned above are combined in the **BR** testbed. Typically, the Master Node includes different Kubernetes Operators, namely O-RAN SMO/OAM as well as the user interface to operate and manage the whole infrastructure and network, while the different NFs and applications are deployed in the worker nodes. Note that the testbed

[2] Multi-x may refer to multi-vendor and multi-version, and may also refer to may also refer to multi-node, multi-distribution, multi-runtime, multi-cloud, and multi-instance

supports a range of different UE devices that could be connected, including Quectel RM500Q-GL, Google Pixel phones, and Apple iPhones.

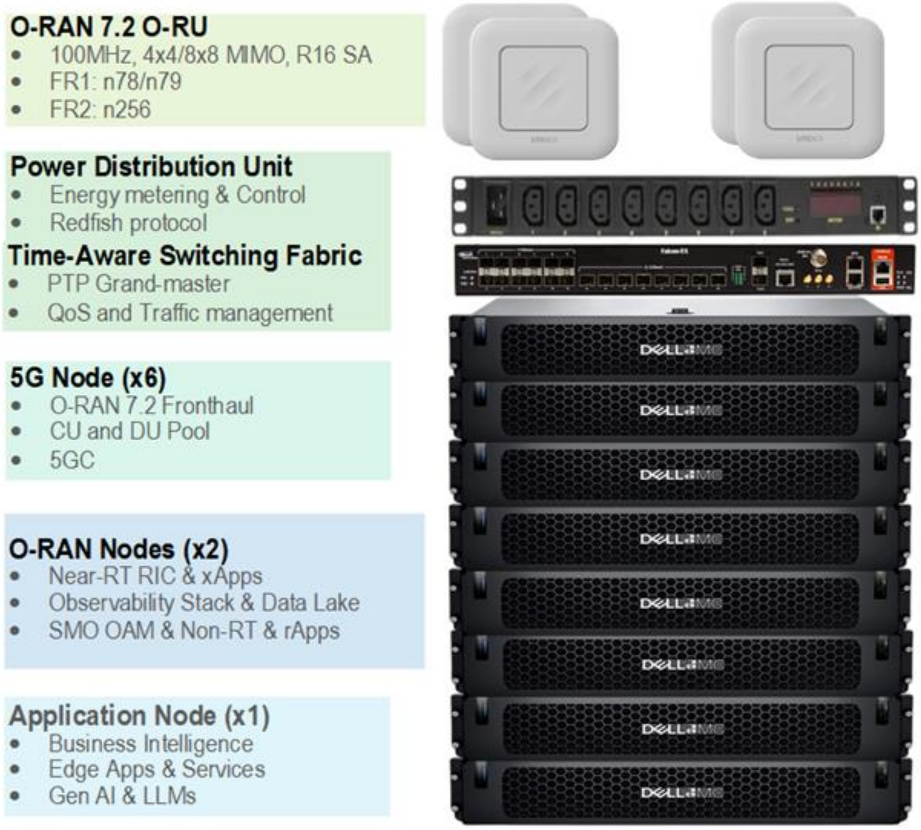

Figure 3-16 Indicative illustration of the HW components in BubbleRAN testbed

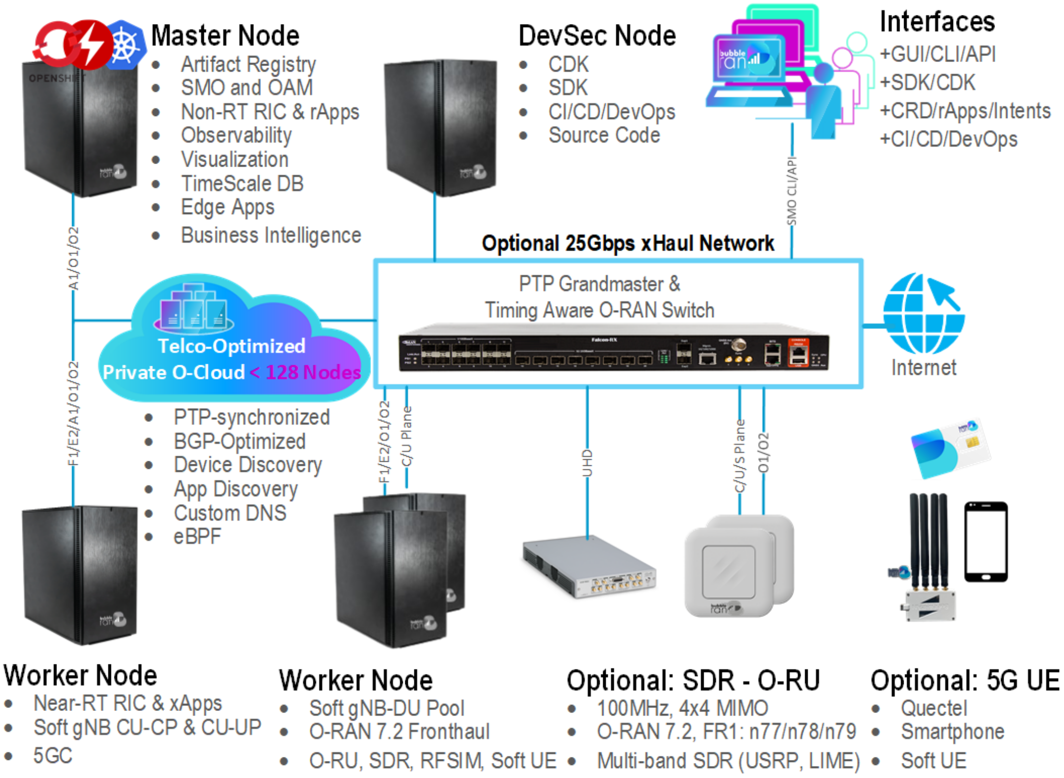

Figure 3-17 BR Testbed sample deployment diagram

3.2.4.1.3 HW abstraction

Finally, in the following list, we highlight some of the most important features of the **BR** testbed that are relevant to 6G-SENSES and can facilitate PoC demonstrations:

- 5G-optimized and distributed Kubernetes cluster (with PTP synchronization).
- BubbleRAN MX-Operator as a cloud-native SMO SW platform that allows to seamlessly design operate, and automate multiple concurrent E2E multi-vendor 5G networks.
- BubbleRAN control fabric (MX-RIC) with O-RAN and custom SMs along with a Software Development Kit (SDK) to facilitate xApp development in different programming languages (C, C++, Python, Go).
- Multi-Source Data Lake: Utilizing TimeScale DataBase (TSDB), the testbed integrates a comprehensive data lake that harmonizes various data sources, including RAN metrics sourced from Near-RT RIC, energy metrics from Kepler, and compute metrics via Prometheus.
- Data Visualization with Grafana to enable users create dynamic and insightful visual representations of data and aid in their intuitive understanding and analysis.

Using this testbed, results from the lower PHY layers, can easily be incorporated into a complete O-RAN solution.

3.2.4.2 IASA ISAC testbed

3.2.4.2.1 System components

The **IASA** system used for the evaluation of ISAC services (Figure 3-18-①) exploits an optoelectronic transport network interconnecting the RAN with the CN functions located at the multi-access edge computing (MEC). The hierarchical structure of the proposed architecture offers RAN connectivity and collects and aggregates transport network and sensing traffic streams from the BSs, while it transports these to the servers (shown in **green**). Both the RAN and the aggregation transport network segments are implemented through multi-vendor SW Defined Networking (SDN)-controlled optoelectronic switches with different capabilities (port no, capacity per port and latency). The access network is equipped with low energy consuming switching nodes with limited number of input ports and relatively small capacity (1/10GbE/port). The aggregation transport network comprises high-end optoelectronic and all-optical fast switches with higher capacity and density (10G/40G/100GbE/ports), offering much higher EE. All-optical fast switches are a key enabler that facilitates transparent routing of IQ sensing flows to the MEC servers needed to achieve acceptable transport delays.

For the RAN segment, an SDR platform (based on USRP B210 and N310) transmitting 5G NR OFDM-modulated signals is used (Figure 3-18-②) to support the functionality of Remote Units (RUs). For the compute domain, edge servers attached to the access switches and central cloud servers connected to the aggregation/core switches are adopted. These servers are used to host containerized RAN elements, i.e. Distributed Unit (DU)/Central Unit (CU), and sensing functions (storage of IQ echoes and processing). The sensing app implements a passive OFDM-based radar [77] that uses as input, signals reflected on objects in the surrounding area, when connectivity between BSs and UEs is established. The sensing app evaluates the quality of the reflected signals captured per BS and, if these are above a specific SNR threshold, they are used to estimate the position of the corresponding object. These results are then communicated to the E2E orchestrator that calculates the optimal resource allocation policy needed to accommodate both communication and sensing services. This is achieved by identifying the appropriate capacity for the paths implementing “RU-DU-CU” and “RU-Sensing” function connectivity, executed by the SDN transport network controller. Finally, for the wireless channel, at this stage of development, a dedicated virtual machine has been deployed hosting the open-source GNU Radio platform, emulating channel impairments and objects in the surrounding area using the “Noise Source” and “Static Target Simulator” blocks, respectively [78]. Sensing

Information exchange between different system building blocks is based on ZeroMQ messaging platform [79]. Further details on the developed platform are provided in [80].

3.2.4.2.2 Functional definition

The IASA platform comprises an optical transport network that interconnects Radio Access Network (RAN) and core domains, to facilitate joint support of sensing and communication services. Sensing is performed based on the principle of a distributed passive wireless radar. According to this, 6G BSs generate communication signals reflected on “objects” located in the surrounding area, creating IQ echo streams. These IQ echo streams are transmitted in the form of uplink fronthaul streams and are redirected to a MEC node for storage and processing. A sensing app is used to analyze the quality of the IQ echo streams at the MEC and decide which IQ streams can be used to support the required sensing. The IQ streams that are not carrying useful information are dropped. The sensing app output, including only useful IQ streams, is passed to the network orchestrator that decides the optimal transport network configuration to support both communication and sensing services. To perform this, the orchestrator solves the optical transport network optimization problem considering both communication (i.e., fronthaul backhaul) and sensing (IQ echo streams) services. The identified configuration is then executed by the SDN control of the optical transport network. The proposed architecture has been experimentally implemented and evaluated using a platform that comprises actual HW for the optical transport network, compute servers and wireless transceivers [81]. The wireless channel (over the air transmission) is emulated through the GNU Radio platform.

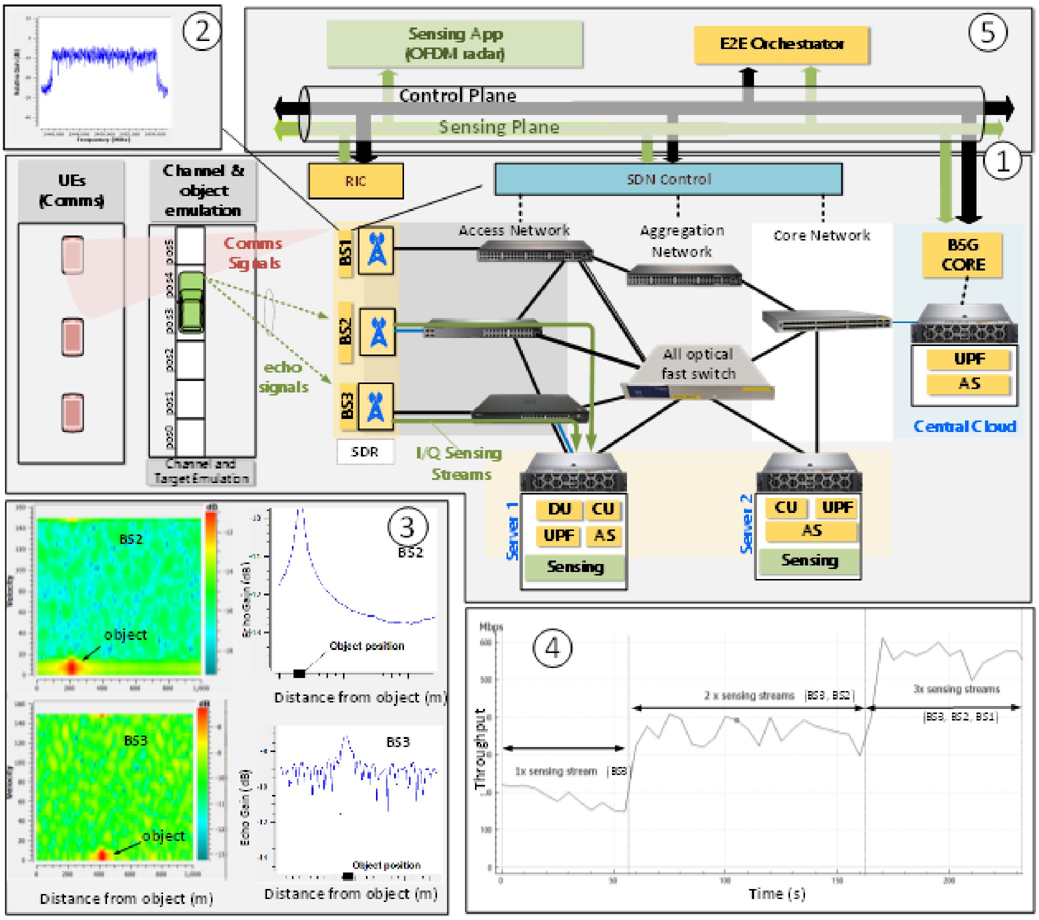

Figure 3-18 ① Optical Transport network supporting ISAC ② Transmitted 5G-NR compliant OFDM signal ③ (left) Object detection using the echoes at BS2 and BS3. (right) Echoes used for the estimation of the object from BS2 and BS3, ④ Echo streams from various BSs directed to server 1. ⑤ Sensing information exchange between the sensing app and network orchestrator.

3.2.4.2.3 HW abstraction

The platform developed by IASA relies on a heterogeneous transport network combing electronic and optical network technologies to interconnect the RAN and the CN domains supporting ISAC services. Each local domain is managed by its own controller exposing the necessary interfaces to the overlay Service Management and Network Orchestration platform (SMO/MANO). Regarding local domain controllers, the management and control of integrated transport networks mainly rely on multi-domain SDN solutions interacting with the transport network elements and the overlay SMO/MANO. The transport network controller based on the sensing and communication flow requirements can set up E2E paths interconnecting the BSs with the MEC entities. The relevant communications exploit standard OpenFlow protocols. Exposure of the sensing information to the sensing app is performed using the ZeroMQ protocol whereas control of the RUs is based on NETCONF.

3.2.4.2.4 Platform evaluation and preliminary results

To evaluate the performance of the proposed architectural approach and technical implementation, an optimization framework has been designed and deployed in the testbed of Figure 3-18. This framework aims to minimize the number of network links used by identifying the optimal routing and network capacity allocation policies under communication (fronthaul, backhaul) and sensing flow (IQ echo streams) traffic requests. This problem is solved considering the following parameters and constraints: (*1) The characteristics of* the optical transport network and compute servers including number of nodes, connectivity graph, and capacity. (*2) The characteristics of* the RAN and mobile core segments including deployment options for the mobile communication (location of RU, DU, CU, UPF elements) and its operational parameters (spectrum allocation, numerology). (3) *The received signal strength* of the echoes captured by the various BSs. This last parameter is quite important, as received signals with low SNR cannot be exploited by the sensing app in the estimation of the object location. To reduce unnecessary overheads, the model considers as input sensing streams captured by BSs with SNRs exceeding a predefined SNR threshold ($\mathrm{SNR_{th}}$). $\mathrm{SNR_{th}}$ depends on several parameters such as transmission conditions, the environment where the system is installed, the location of the RUs, etc., and can be experimentally precomputed. A typical numerical example is shown in the left column of Figure 3-18-③, illustrating the spectrograms of the received IQ streams at BS2 and BS3 when their distance from the object is 200 and 400m, respectively. From the same figure we observe (right column) that for objects closely located to a BS (case of BS2) the received SNR is high and, therefore, the object can be detected with high accuracy. However, as the object-BS distance increases, the received SNR is reduced, reducing also the track detection accuracy. The object detection accuracy can be further improved combining estimations from multiple BSs [80]. (4) *The capacity requirements* for the sensing and communication traffic flow. For the sensing flows, these requirements increase with the number of BSs involved in the sensing process collecting and transmitting IQ echo streams. A typical set of measurements for IQ streams collected for 10MHz bandwidth allocation in the wireless segment (OFDM modulated) is shown in Figure 3-18-④. This set of measurements shows the throughput of the IQ streams forwarded by “BS3”, “BS3-BS2” and “BS3-BS2-BS1” to the edge server #1. For the fronthaul and backhaul requirements (due to space limitations) the reader is referred to [82] providing a detailed discussion. (5) *Delay requirements for the sensing streams.* To handle this, sensing flows are transparently transported to the sensing servers through the all-optical transport network switch, acting as an IQ sensing switch, eliminating transmission delays introduced by optoelectronic devices. The use of the all-optical switch is a key enable that allows to maintain the overall transport delay acceptable.

The proposed scheme is evaluated for the topology of Figure 3-18-① considering an object located at different positions. We evaluate three different management policies: a) “single” echo approach, where IQ signals captured by the BS with the strongest SNR are transmitted to the sensing app, b) “optimal” dynamic approach considering echoes with SNR exceeding a specific threshold, and c) “all-active” approach using echoes from all BSs. IQ streams for communication services coexist with sensing streams. Figure 3-19 (a) and (b) compare the transport network utilization (ratio of links used vs total available links) and received echo SNR, respectively, for different object positions and ISAC optimization policies. In the "optimal" approach, the selected echoes are dynamically routed to the sensing server. Optimal routing paths are calculated by the E2E orchestrator and executed by the transport network SDN controller. The "optimal" approach has higher network requirements compared to the "single" echo (~15%) and it is 30% more efficient than the static "all-active" approach. As shown in Figure 3-19 (c) illustrating the sensing accuracy of all schemes, the "optimal" scheme receives echoes of similar SNR with the "all-active" approach, while requiring 50% less network resources.

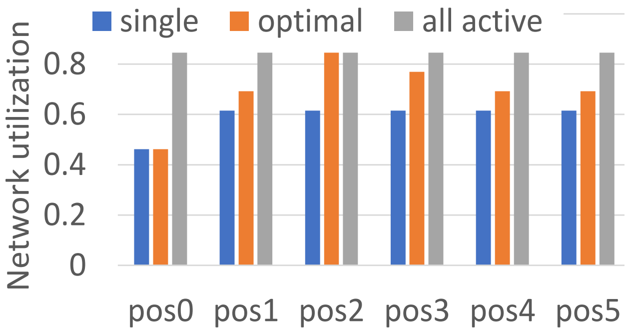

a)

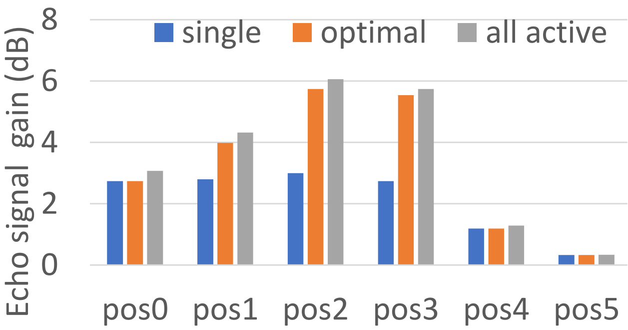

b)

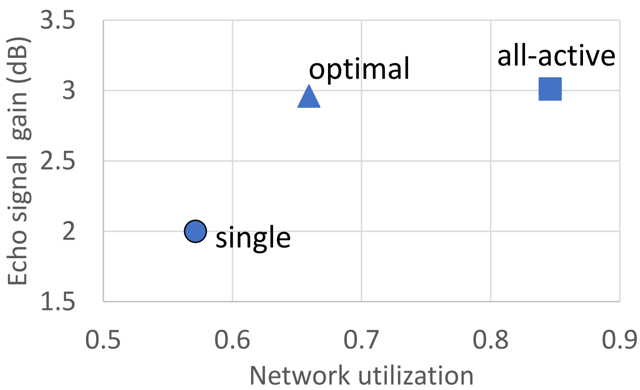

c)

Figure 3-19 a) Network utilization vs object position for different ISAC optimization policies, b) Sensing accuracy (measured through echo signal margin) vs object positions, c) Echo signals strength vs network utilization

3.2.4.3 UC/IHP ISAC testbed

3.2.4.3.1 System components

The ISAC testbed residing at the **UC** comprises the **BR** components that were described section 3.2.4.1.1, i.e., MX-RAN, MX-CN, MX-Operator, and MX-RIC. These components will be leveraged and their implementation will be tailored to integrate an ISAC service model implementation (more details in section 3.3.3), sensing Apps, implemented as xApps, and additional HW (3GPP and non-3GPP), turning the testbed into the 6G-SENSES multi-WAT ISAC testbed claimed in the Description of Work (DoW).

The **UC**/**IHP** testbed can accommodate different RUs, as depicted in Figure 3-20:

1. the N321 RUs that will act as radar-based sensing nodes. It includes the Sub-6 GHz (non-3GPP) sensing system (based on that described in section 3.2.2) and, in the near future, the mmWave nodes described in section 3.2.3,
2. commercial O-RUs (LITEON) interoperable with **BR** ecosystem to gather sensing information as described in Section 3.3.3,
3. an O-RAN O-RU SDR White Box System from Massive Beams (link). This platform will allow, with the scope of providing an increased openness and flexibility of an O-RAN-based RU, to perform additional tasks at RU level such as modifiable signal processing blocks for 5G-NR low-PHY baseband signal processing and can incorporate sensing functions at PHY layer.

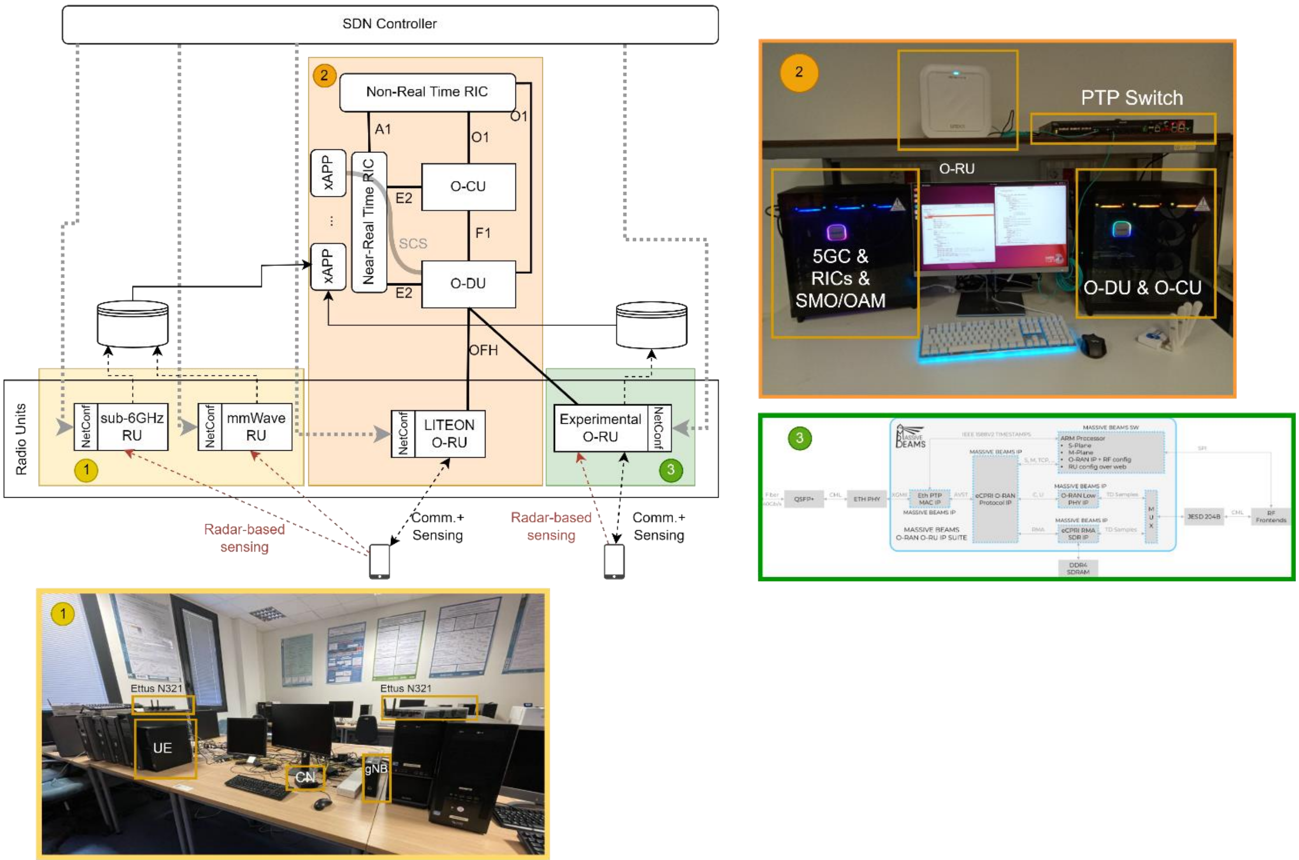

Figure 3-20 UC/IHP ISAC platform, ① Sub-6 ISAC platform and mmWave platform, ② BR platform, ③ Planned integration of an SDR-based O-RU from Massive Beams[3]

[3] https://www.massivebeams.com/

3.2.4.3.2 Functional definition

The purpose of this platform is to test ISAC the 6G-SENSES functionalities that will lead to ISAC demonstrations in the context of PoC#1. The PoC will comprise: 1) an SMO used to facilitate validation and experimentation and provide reproducibility; 2) a network of multi-WAT RUs connected to the OAI-based disaggregated RAN and CN network functions in a form of container images; 3) real-time control fabrics enriched with ISAC control logics including spectrum management, RAN sensing, RAN monitoring, RAN control, and user positioning enhanced with CN location management functions (LMF) deployed as edge applications, i.e. xApps; and 4) 5G optimized compute nodes all synchronized using IEEE 1588v2 Precision Time Protocol (PTP).

The expected results will be to experimentally measure and assess the performance and energy improvement in different deployment scenarios up to Technology Readiness Level (TRL) 4 considering different user spatio-temporal connectivity and traffic patterns.

3.2.4.3.3 HW abstraction

The most important features relevant to 6G-SENSES that will facilitate PoC demonstrations, particularly for PoC#1, have been already included in section 3.2.4.1.3.

We contemplate HW abstractions at two levels: 1) sensing control solutions, 2) sensing-assisted network management. As for the former, RUs will be equipped with SDN-based control interfaces that will be exposed to an SDN controller residing in the SMO/MANO layer. It will permit the reconfiguration of the communication and sensing capabilities of the multi-WAT RUs at a large time scale according to the scenario characteristics. Regarding the latter, sensing-assisted management will be implemented as xApps, located at the near-RT RIC, able to fine-tune the operation of the gNBs in a more time strict manner. These applications will leverage the gathered sensing information, along with legacy network data, to optimize the usage of radio resources by the O-RUs.

3.3 6G-SENSES ISAC target implementation

6G-SENSES proposes a 6G architecture that interconnects a multi-technology RAN able to offer sensing functionalities (3GPP and non-3GPP) with CN domains through an advanced transport network, to facilitate joint support of sensing and communication services. The RAN technologies of interest include Sub-6 (non-3GPP), Wi-Fi, mmWave and 5G NR, which will coexist in an ISAC framework the goal of which is to obtain an accurate representation of the surrounding environment and to perform active sensing with UEs [1].

Sensing is performed based on the principle of a distributed passive wireless radar, or as denoted in [1], considering a monostatic sensing scheme. In this case, the reception of the signal(s) should be simultaneous to transmission n to be able to measure the reflecting and scattering waves, thus functioning as an IBFD transceiver. According to this, the RUs will generate communication signals reflected on “objects” located in the surrounding area, creating IQ echo streams. These IQ echo streams are transmitted in the form of uplink fronthaul streams and are redirected to a MEC node for storage and processing. Purposely developed sensing apps (xApps) can be used to analyze the quality of the IQ echo streams at the MEC and decide which IQ streams can be used to support the required sensing. The sensing app output can be passed to the network orchestrator that decides the optimal network resource configuration to support both communication and sensing services.

Extension of the ISAC platforms to support **bistatic** sensing are considered for the remaining of the duration of the project, and they could potentially play a role in PoC#1. Extensions of 3GPP LMF / O-RAN RIC features to integrate non-3GPP technologies are currently being assessed.

More details of the integrated implementation for ISAC will be provided in deliverable D3.2. The following sections, i.e. sections 3.3.1 and 3.3.2, provide parallel assessments of technologies that are being tested in separate platforms and that can, potentially, be integrated with the ones described above.

3.3.1 6G-SENSES mmWave (60 GHz) implementation

Wi-Fi sensing can be generally classified into two main approaches: passive sensing and active sensing. In the active sensing scheme, the same device transmits and receives a “sensing” PPDU, which performs like traditional radar systems (monostatic/active radar), such as those based on a FMCW radar. In the passive sensing scheme, the sensing is performed by tracking changes on a wireless channel through the reception of multiple PPDUs over time (bi-static/passive radar). The active Wi-Fi sensing and passive Wi-Fi sensing examples are depicted in Figure 3-21 a) and b), respectively. In the sequel, passive Wi-Fi sensing is focused on in this study.

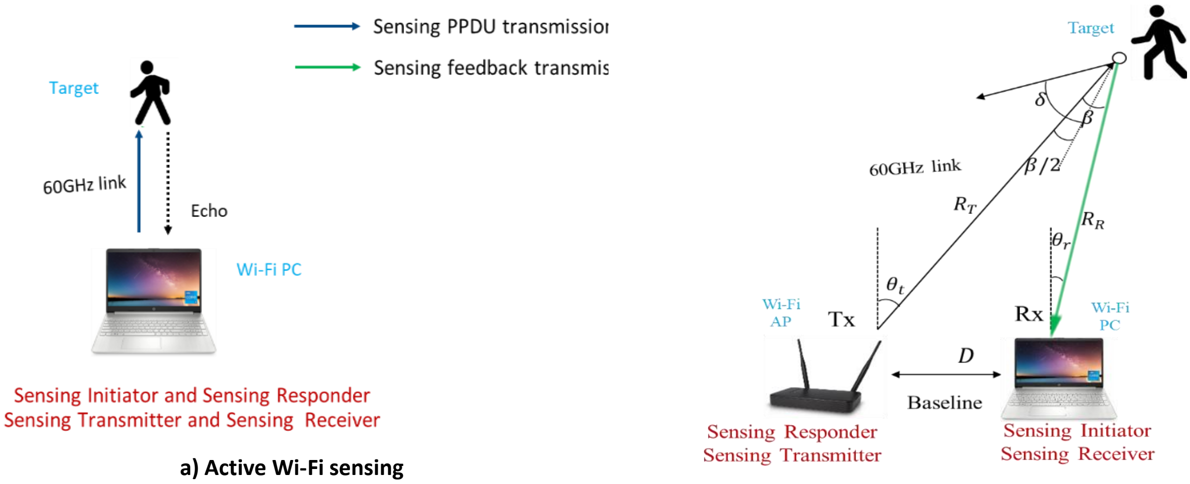

a) Active Wi-Fi sensing

b) Passive Wi-Fi sensing

Figure 3-21 Active and Passive Wi-Fi sensing

L-STF	L-CEF	L-Header	EDMG-Header-A	EDMG-STF	EDMG-CEF	EDMG-Header-B	DATA	TRN

Figure 3-22 EDMG frame structure

In the IEEE standards association, the IEEE 802.11 Integrated Millimeter Wave (IMMW) study group (SG) aims to address the problem of WLAN non-standalone operation in unlicensed bands between 42 and 71 GHz using single-user (SU) OFDM-based transmissions [83]. Specifically, IEEE 802.11 IMMW (i.e., IEEE 802.11bq) aims to integrate mmWave to support emerging use cases (e.g., immersive communications, peer-to-peer communication, cloud computing, AI/ML, and multi-player gaming), since mmWave band offers abundant spectrum [84]. Moreover, ISAC is also studied in IEEE 802.11bq as an additional sensing use case. Within the ongoing IEEE 11bq standard activities, a promising option in PHY layer is adopting the directional multi-gigabit (DMG)/ Enhanced directional multi-gigabit (EDMG) waveform to support mmWave Wi-Fi sensing. To align with this trend, new sequences designed for mmWave Wi-Fi sensing are investigated and evaluated in WP3.

We focus next on providing more details on some of the components of the EDMG frame [85].

I) ***Channel Estimation Field (CEF)*** **sequences**: CEF sequences in DMG/EDMG SC PHY, also called legacy DMG-CEF in IEEE 802.11ad and 802.11ay standards, could be used for sensing tasks. To be specific, the legacy DMG-CEF sequences are composed of 9 Golay sequences of length 128, which are characterized as follows:

- The legacy DMG-CEF uses a Golay pair of complementary sequences Ga128 and Gb128 of length 128 chips.
- The CEF field is composed of the following Gu512 and Gv512 sequences:

$$\mathrm{Gu}_{512} = [-\mathrm{Gb}_{128}, -\mathrm{Ga}_{128}, +\mathrm{Gb}_{128}, -\mathrm{Ga}_{128}] \tag{3-16}$$

$$\mathrm{Gv}_{512} = [-\mathrm{Gb}_{128}, +\mathrm{Ga}_{128}, -\mathrm{Gb}_{128}, -\mathrm{Ga}_{128}]; \tag{3-17}$$

to which a final -Gb128 sequence is added at the end.

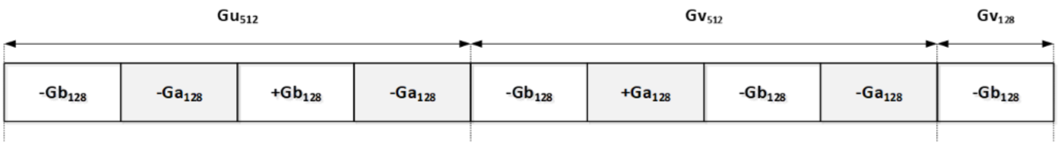

The following parameters/features are to be focused on for this waveform sequence (i.e., CEF):

- **Pulse repetition frequency (PRF)**
  - Each pulse is a received Wi-Fi packet, containing the Golay sequences in the CEF
  - PRF is adaptively configurable based on the sensing requirements; the PRF is 2 kHz by default
- **Bandwidth: $BW = 1.76\ GHz$**
  - The chip time τ is 0.57 ns, which is dictated by the bandwidth $\tau = (BW)^{-1}$
- **Potential implementation**: Zero auto-correlation zone of 128 chips for accurate and efficient channel estimate:
  - Use the default DMG/EDMG CE sequences in the DMG/EDMG subclause.
  - Allow usage of existing HW.
  - Maximum propagation delay limited to 128 samples (10.9 meters).
  - Delayed correlation with the CEF, that is, the output of the correlator (of both Ga and Gb) is summed with appropriate delay and sign change to possibly extend the range.

*II) **Training fields** sequences*: Training fields (TRN-R, TRN-T, TRN-TR) sequences in DMG/EDMG SC PHY could be used for sensing task (i.e., the waveform sequences are identical to that defined in IEEE 802.11ad and 802.11ay). Like CEF, the same parameters are proposed for the waveform sequences:

- PRF = 2 kHz
- BW = 1.76 GHz

IEEE 802.11ay specifies the Beam Refinement Protocol (BRP), which transmits a variable number of TRN units, each one using a different Beam Pattern (BP). Herein, the TRN could be thus adopted to accomplish the sensing task; that is:

- **Potential implementation 2**: Especially, for mmWave radar sensing, EDMG TRN can be transmitted in different directions and can be used for radar scan within a single PPDU or BRP packets.

More specifically, considering that the common speed of human motion is in the range [2 - 3 m/s] conducting the beaconing/BRP every, e.g., 100 ms allows precisely estimating human location in the FoV of the APs. The high bandwidth (1.76 GHz) can bring in a range resolution of about 8.5 cm based on the estimated CSI. Furthermore, to evaluate the achievable sensing performance, a TRN design with various length of subfield sequence (Golay) could be investigated by defining the number of samples of the subfield as 64, 128, and 256.

Two main technologies are used for a mmWave radar at 60 GHz: FMCW signal and Golay sequences. For comparison, their key features are listed in Table 3-5.

Table 3-5 Waveforms and features for mmWave/60GHz Radar

Waveform Type	Features
FMCW signal	• Sweeping CW signal covering a large spectrum. • Simple HW implementation.
Golay sequences	• Type of full-duplex Radar where a wide-band waveform with very good autocorrelation is used. • Golay sequences same/similar to those used in DMG.

In 6G-SENSES, **INT** focuses on Golay sequences-based mmWave Wi-Fi sensing and the proposed sensing waveform is compared to FMCW radar, which is taken as baseline. The idea is to understand how the proposed waveform in the same configuration (frequency, bandwidth, etc.) would compare with the FMCW radar, regarding the various sensing KPIs such as Range/Doppler resolution. In this way, we can estimate the performance delta for the FMCW radar vs. the proposed system. It could be a valuable comparison since the FMCW radar would be utilized as an alternative to developing sensing algorithms, as a commercial mmWave Wi-Fi sensing platform is currently unavailable.

In particular, the PRF is changeable and should be consistent with the sampling frequency of the channel model. Different BW could be tested to evaluate the performance of the designed sequence. Moreover, a single carrier is a suitable waveform for a less discrepancy LoS channel, while an OFDM waveform can cope with highly dispersive channels. The parameters proposed for the waveform sequences are PRF = 2 kHz and BW = 1.76 GHz. Based on these parameters, the most important KPI is presented in the sequel.

3.3.1.1 ISAC Implementation

Based on the IEEE 11ay/ad specifications [85], the ISAC system is being devised with additional waveform candidates and the corresponding mmWave Wi-Fi sensing model, which are currently being investigated in IEEE 11bq. As shown in the framework depicted in Figure 3-23, an ISAC implementation mainly consists of a mmWave waveform generated and transmitted at the transmitter side and the signal preprocessing within the sensing model at the receiver side. The crucial components of a possible deployment are presented in the following.

I) ISAC mmWave sequence waveform generator

Following a SotA analysis, the main goal of our research is to investigate new ISAC waveform sequences, which can be specifically categorized as follows:

- **Frequency domain sequences** [64], [85]
  - OFDM PHY.
  - CEF at 60 GHz (OFDM PHY in 802.11ay).
- **Time domain sequences** [85]
  - Single carrier PHY in 11ad and 11ay.CEF and TRN field at 60 GHz (802.11ad and SC PHY in 802.11ay).

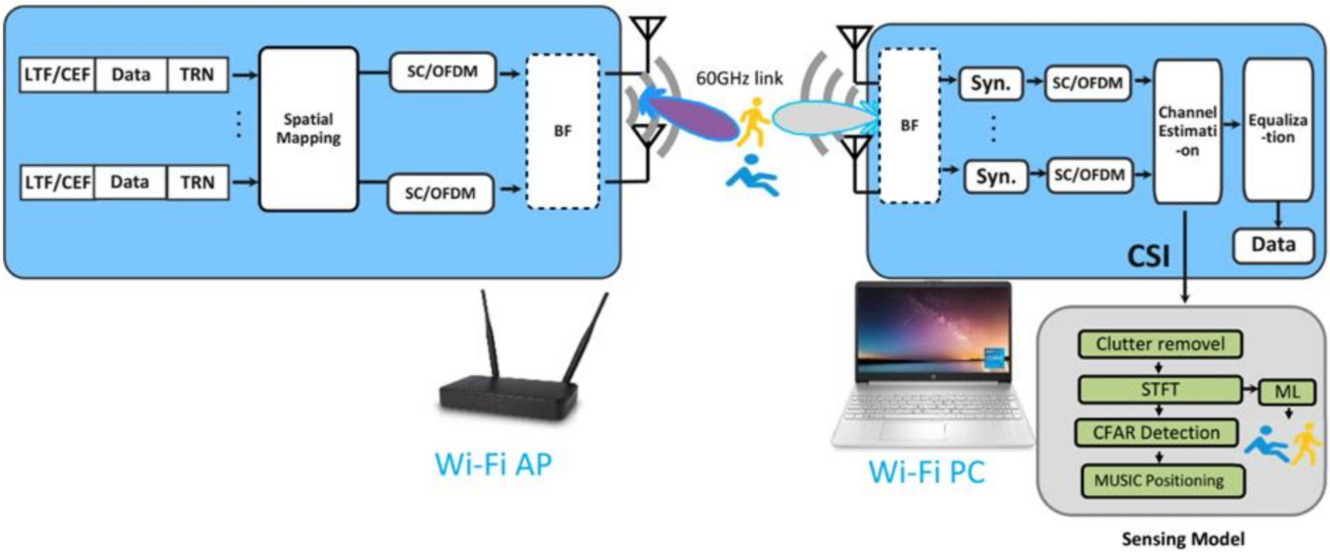

Figure 3-23 The mmWave Wi-Fi ISAC processing framework

Currently, these legacy sequences are used for synchronization, channel estimation, and beam training in IEEE 802.11 ay/ad communication systems. Within 6G-SENSES these legacy sequences are being investigated and optimized to support high-resolution mmWave Wi-Fi sensing.

II) ISAC Signal preprocess for human sensing

To accomplish ISAC sequence designs, the below ISAC signal preprocess is correspondingly conducted at the receiver side, with an exemplary user case focused on human sensing.

1) Synchronization: After capturing the received data with beamforming (BF), coarse synchronization needs to be first conducted by performing the cross-correlation operation among the locally generated pilot and the received signals. Consequently, the direct LoS propagation delay can be estimated and eliminated for the radio link between transmitter and receiver.

2) CSI estimation and acquisition: then, the CSI estimation is performed. For instance, according to the specification of the CEF-based time domain channel estimation method, the pilot sequence $\{s[n]\}$ within CEF consists of two sets of 512-sample Golay complementary sequence pair, and the Gu512 and Gv512 sequences are exploited for the CSI estimation. Particularly, up to the selected single carrier or OFDM waveform, a specific pilot sequence could be conveyed to estimate the time-domain CSI or frequency-domain CSI, using a corresponding channel estimation procedure. After the CSI acquisition needed for the communication link, the equalization is sequentially executed for data detection. In parallel to the communication link, the sensing model within the ISAC processing framework is invoked by the input of estimated CSI, as summarized below.

(3) Doppler Computation via STFT: by exploiting the estimated CSI at the receiver, sensing pre-processing is implemented. Since CSI always changes over time, the STFT is applied to the acquired CSI. Thus, the magnitude squared of the STFT of the CSI can be abstracted as the spectrogram time-frequency representation of the CSI (i.e., the micro-doppler signature induced by the target). In addition, there are other complementary sensing signal processing components contained in the sensing pipeline, such as clutter removal, two-dimensional constant false alarm rate (2D-CFAR), human detection with ML, and positioning.

3.3.1.2 Expected mmWave Wi-Fi sensing accuracy

I) Range/Doppler resolution of Wi-Fi sensing: To further define the KPI of new sequences designed for Wi-Fi sensing, some assumptions are made: (i) the pulse repetition frequency/interval (PRF/PRI) is changeable and should be consistent with the channel sampling frequency; (ii) different bandwidth could be tested to evaluate the performance of the designed sequence.

In the passive/bistatic Wi-Fi sensing scheme (shown in Figure 3-21), the range resolution can be expressed as [22][64]:

$$\Delta r = \frac{c}{2\cos\left(\beta/2\right)B} \tag{3-18}$$

where the parameter c is the speed of light, β is defined as the bistatic angle and B is the bandwidth of the signal.

Furthermore, the relationship between the speed and Doppler velocity, $\mathrm{f_d}$, and the Doppler resolution, Δf, of the target can be formulated as [64], [86]:

$$\begin{gathered} f_d = \frac{2v}{\lambda}\cos\delta\cos\left(\beta/2\right) \\ \Delta f = \frac{1}{T_{CPI}} \end{gathered} \tag{3-19}$$

where v is the target velocity, λ, is the wavelength corresponding to the carrier frequency, δ is the angle between the velocity of the target and the angular bisector of bistatic angle, β, and T_{CPI} is the coherent processing interval.

3.3.2 6G-SENSES OTFS-ISAC implementation

3.3.2.1 Introduction to OTFS

Each generation of wireless communications introduces new application scenarios, bringing additional challenges and improved solutions. The 5G wireless mobile networks introduced different use cases in which high mobility was one of the targets [1]. In 6G, high-speed trains, satellites, and unmanned aerial vehicles are a few of the planned targeted applications [87]. The major challenge faced by high mobility is reliability, which is deteriorated due to the presence of high Doppler effects.

In the presence of high Doppler effects, key enabling technologies, such as OFDM, have limited performance [88]. The main difficulty is the reciprocal relation of channel coherence time with the Doppler shift, as the estimated Time-Frequency (TF) channel can change within a symbol/frame period. With the enormous increase in device numbers and data rate, several high-frequency bands sensitive to Doppler will be accessible in the future. In the THz-band, even small mobility can cause considerable Doppler effects. All these challenges altogether call for a solution that can address these problems efficiently and simply.

The Doppler effects in a multipath environment change the single-dimensional time-invariant channel into a 2D time-variant channel. For such 2D cases, there is an inherent need for a 2D channel model. Delay-Doppler (DD) processing is an efficient tool that can be utilized for such fast-fading channel scenarios, and it is the baseline for the proposed 2D waveform known as Orthogonal Time Frequency Space (OTFS) [90][91]. OTFS waveform is specifically developed for such challenges as it represents the information corresponding to the actual geometry in a physical radio environment. Due to the geometric representation of the radio environment, the DD channel changes much slower than the TF channel [90]. Channel estimation in the DD domain is also more straightforward and can be easily estimated via embedded pilots [92]. The channel effect on the whole DD plane can be calculated via interpolation [93]. The estimated channel is valid for the whole frame, as all of the symbols experience approximately the same channel effects [94]. Figure 3-24 illustrates the resulting estimated channel for an Extended Vehicular A model (EVA) [96]. It is evident from the estimation that the DD plane provides a sparser channel estimation [95].

The core of the OTFS waveform lies in the DD plane. Both the TF plane and DD plane are 2-D, so a matrix representation is used to define them. DD plane has a close relation with the TF plane by a pair of forward and reverse Fast Fourier Transforms (FFTs). This pair is known as Symplectic Fast Fourier Transform (SFFT) and is performed on the rows and columns of the frame. Figure 3-25 visualizes the interchangeability between TF and DD domains via ISFFT/SFFT.

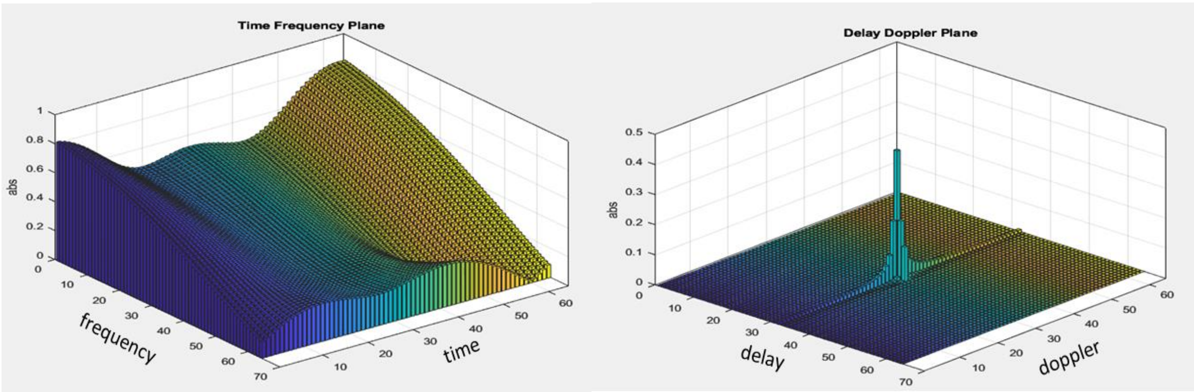

Figure 3-24 Channel Estimation in TF and DD domain

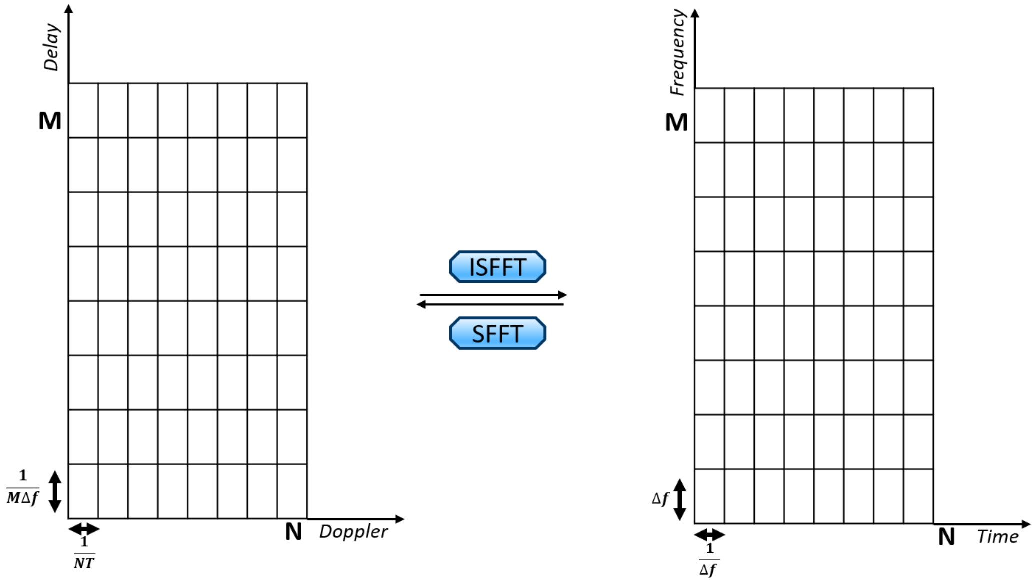

Figure 3-25 Time-Frequency and Delay-Doppler Relation

The Range-Speed map from radar processing is similar to the DD plane, as it is also obtained via a pair of reverse and forward Fourier Transforms.

In OTFS, data symbols are mapped onto a DD matrix or a TF matrix, depending on the modulation scheme. An OTFS frame, existing in the DD domain, is specifically created in a way to combat doubly-dispersive channels, and the data symbols are mapped to it. For OFDM systems, data symbols are mapped in the TF domain – total frame containing multiple Resource Blocks (RBs). Intrinsically, OTFS performs better in high-mobility systems as the advantages of OFDM are more evident in static and low-mobility systems.

Each data symbol in OFDM is mapped onto a specific subcarrier. However, in the case of OTFS, each data symbol occupies the whole TF plane. This provides frequency and time diversity for OTFS systems and improves performance. This is also the reason for longer channel estimation in OTFS systems. Figure 3-26 depicts how a single OTFS data symbol in the DD domain covers the whole TF domain.

When comparing OFDM-based systems with Discrete Zak Transform (DZT) based OTFS systems, for the former the transmitter takes an IFFT column-wise, while for the latter the IFFT is taken row-wise.

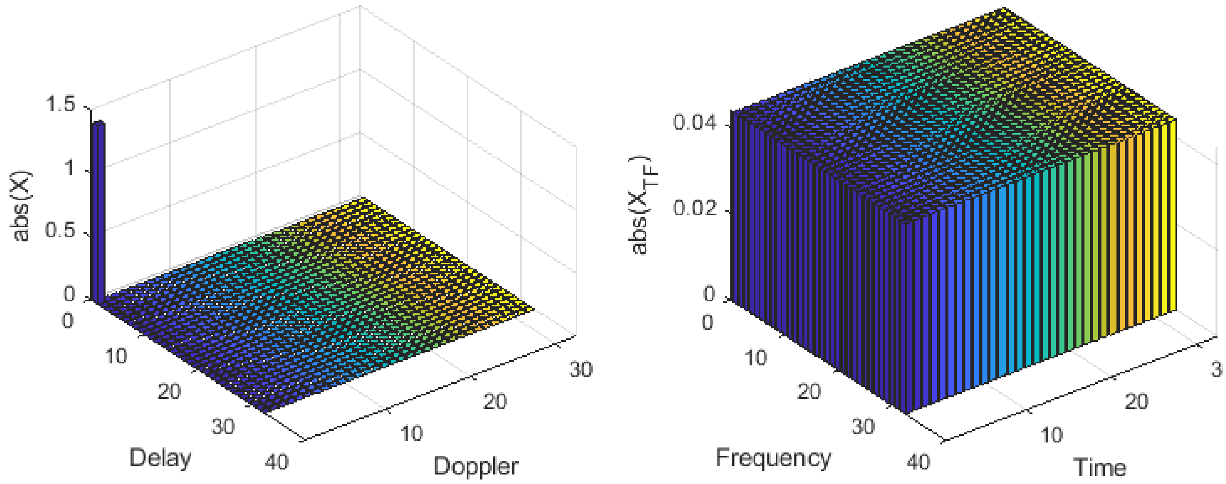

Figure 3-26 OTFS data symbol: left) in DD plane, right) in TF plane

3.3.2.2 OTFS Transmitter

There exist two types of OTFS implementation schemes:

- SFFT based.
- ZT based.

The first type allows the utilization of OTFS as a precoder to OFDM with increased computational complexity. The same HW elements of OFDM can be utilized, and all the processing can remain the same. The second type allows direct conversion from the DD domain to the Delay-Time domain for a similar computational complexity.

3.3.2.2.1 Zak Transform-based transmitter

For the Zak Transform-based systems, OTFS frame **X** of size M×N directly transforms to the DT domain via an IFFT across the Doppler axis. The bandwidth of the system is given by *B=M Δf*, where Δf is the frequency separation, and *NT* is the frame duration (*T = 1/Δf*) [93]. Delay and Doppler resolutions are also calculated by these system constraints. Bits are converted into symbols $c_{m,n}$, depending upon the chosen modulation scheme (e.g., M-PSK, M-QAM). The modulated symbols are then placed in the **X** matrix [93].

After mapping the data symbols, a pilot is also placed with a zero region around it to prevent interference between data symbols and the pilot [6]. The pilot is placed at zero Doppler, such that **X** becomes:

$$X[m,n] = \begin{cases} x_{pilot}, m = m_{pilot}, n = 0 \\ 0, m \in [m_{pilot} \pm l_p], 0 \leq n \leq N-1 \\ c_{m,n}, otherwise \end{cases} \tag{3-20}$$

x_{pilot} is the pilot symbol, m_{pilot} is the location of pilot on Delay axis and l_p is the considered largest delay tap. A typical OTFS frame is shown in Figure 3-27. A simple IFFT over the Doppler axis can yield [156][93]:

$$X_{DT}[m,k] = \frac{1}{\sqrt{N}} \sum_{n=0}^{N-1} X[m,n] e^{j2\pi\left(\frac{nk}{N}\right)} \tag{3-21}$$

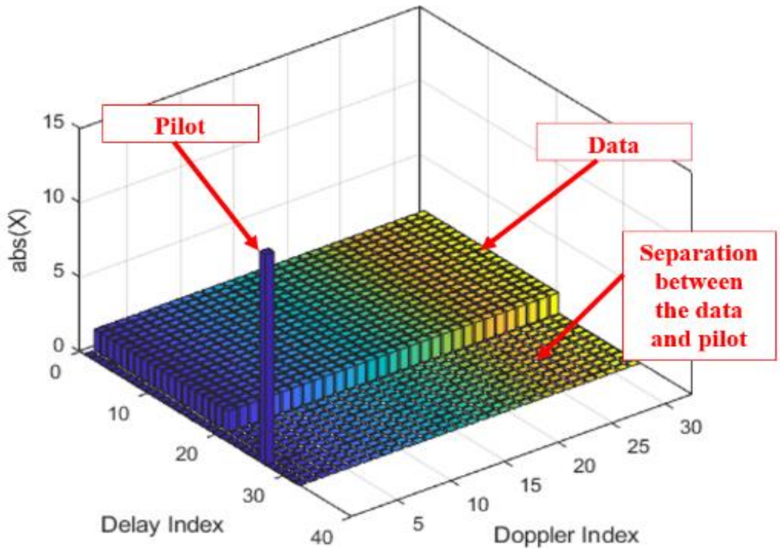

Figure 3-27 OTFS frame X

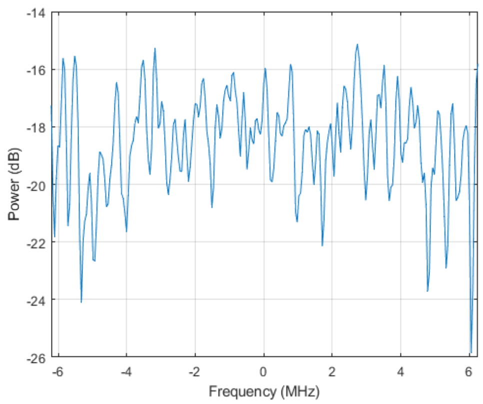

a)

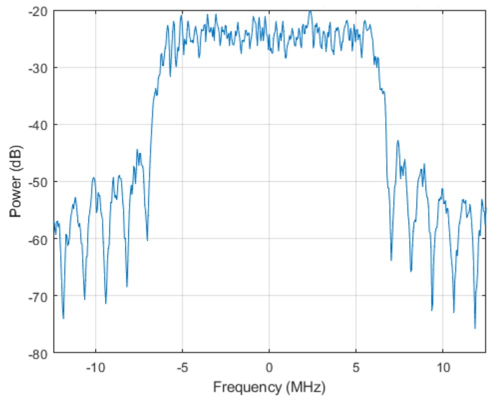

b)

Figure 3-28 Power spectrum of OTFS frame, a) without rate-change, b) applied rate-change

After this, X_{DT} is serialized and pulse-shaped for transmission. Rate change and pulse shaping are necessary as the OTFS frame occupies the whole TF plane. Figure 3-28 illustrates a resulting pulse-shaped frame of a Zak Transform-based OTFS system. For the SFFT-based OTFS systems, OTFS frame X, the size of the matrix is $M'\times N'$. Similar to the ZT approach, pilot, zeros, and data symbols are placed, and an Inverse Symplectic Fourier Transform (ISFT) is applied to get TF matrix X_{TF}.

$$X_{TF}[k,l] = \frac{1}{\sqrt{N'}} \sum_{n=0}^{N'-1} \sum_{m=0}^{M'-1} X[m,n] e^{j2\pi\left(\frac{nl}{N'} - \frac{mk}{M'}\right)} \tag{3-22}$$

For utilizing a single processing rate, rate change can be applied in the TF plane. After rate changing, an identical OFDM modulator can be also utilized. For using an identical OFDM modulator, the value of M' is set as equal to the number of data subcarriers, and after ISFT, zero tones are appended at **f$_{corner}$** to the matrix X_{TF}, increasing the total number of elements in TF plane. X_{TF2} is given by:

$$X_{TF2}[m,n] = \begin{cases} 0, 0 \leq n \leq N' - 1, m \in \pm f_{corner} \\ X_{TF}, otherwise \end{cases} \quad (3\text{-}23)$$

After that, an M-point IFFT is applied to get the final DT frame, this operation could be performed via an OFDM modulator. The process is visually illustrated in Figure 3-29 for M' = 56, N' = 16, M = 64. X_{DT} is finally serialized and a cyclic prefix is added.

$$X_{DT}[l,k] = \frac{1}{\sqrt{M}} \sum_{m=0}^{M-1} X[m,n] e^{j2\pi\left(\frac{ml}{M}\right)} \quad (3\text{-}24)$$

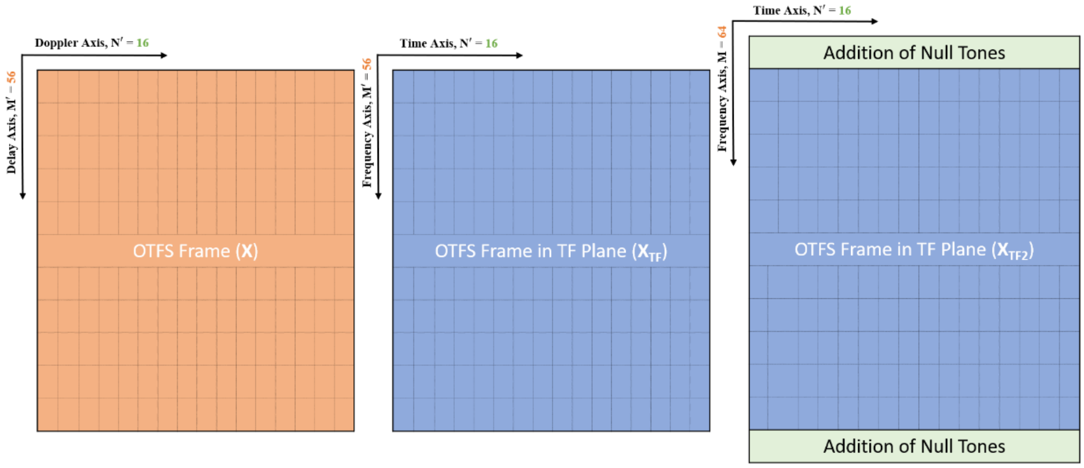

Figure 3-29 Original frame X, frame X$_{TF}$ resulted from ISFT and frame X$_{TF2}$ after appending null tones

3.3.2.2.2 SFFT-based transmitter

For the SFFT-based OTFS systems, OTFS frame, **X**, the size of the matrix is $M' \times N'$. Similar to the ZT approach, pilot, zeros, and data symbols are placed, and the ISFT is applied to get TF matrix X_{TF}.

$$X_{TF}[k,l] = \frac{1}{\sqrt{N'}} \sum_{n=0}^{N'-1} \sum_{m=0}^{M'-1} X[m,n] e^{j2\pi\left(\frac{nl}{N'} - \frac{mk}{M'}\right)} \quad (3\text{-}25)$$

For utilizing a single processing rate, rate change can be applied in the TF plane. After rate changing, an identical OFDM modulator can be also utilized. For using an identical OFDM modulator, the value of M' is set as equal to the number of data subcarriers, and after ISFT, zero tones are appended at $\mathbf{f}_{\mathbf{corner}}$ to the matrix X_{TF}, increasing the total number of elements in TF plane. X_{TF2} is given by:

$$X_{TF2}[m,n] = \begin{cases} 0, 0 \leq n \leq N' - 1, m \in \pm f_{corner} \\ X_{TF}, otherwise \end{cases} \quad (3\text{-}26)$$

After that an M-point IFFT is applied to get the final DT frame, this operation could be performed via an OFDM modulator. The process is visually illustrated in Figure 3-30 for M' = 56, N' = 16, M = 64. X_{DT} is finally serialized and a cyclic prefix is added.

$$X_{DT}[l,k] = \frac{1}{\sqrt{M}} \sum_{m=0}^{M-1} X[m,n] e^{j2\pi\left(\frac{ml}{M}\right)} \quad (3\text{-}27)$$

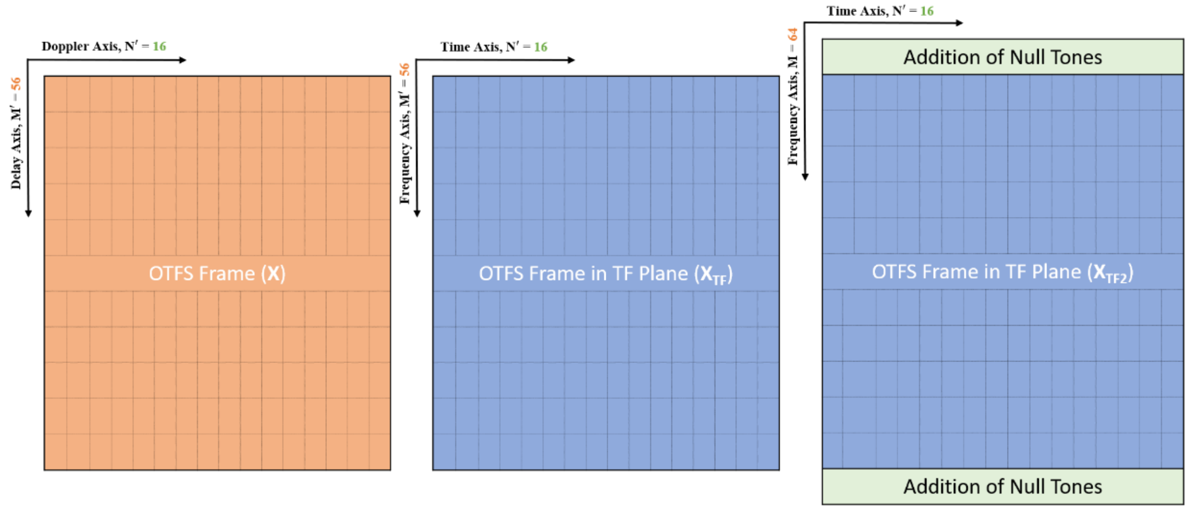

Figure 3-30 Original frame X, frame X_{TF} resulted from ISFT and frame X_{TF2} after appending null tones

3.3.2.3 OTFS Receiver

At the receiver, the reverse operation is applied based on the chosen Zak Transform or SFFT-based implementation. Before the main OTFS processing, it is necessary to perform frame synchronization to find the correct Start of Frame (SOF). This task is achieved by employing an M-Sequence. Synchronization challenges such as CFO and STO and their impact will be further discussed in the next section.

3.3.2.3.1 Synchronization

As OTFS is closely related to OFDM, it also inherits its synchronization challenges. Finding the correct SOF is necessary. A simple preamble can find SOF, which can be based on either cross-correlation or autocorrelation. After sample level synchronization, residual/fractional STO remains. This STO fluctuates between ±0.5Ts (Ts is the sampling time) and can cause 1 sample drift after some time. Figure 3-31 elucidates the detrimental effects of residual STO for a 20-ppm sample rate offset.

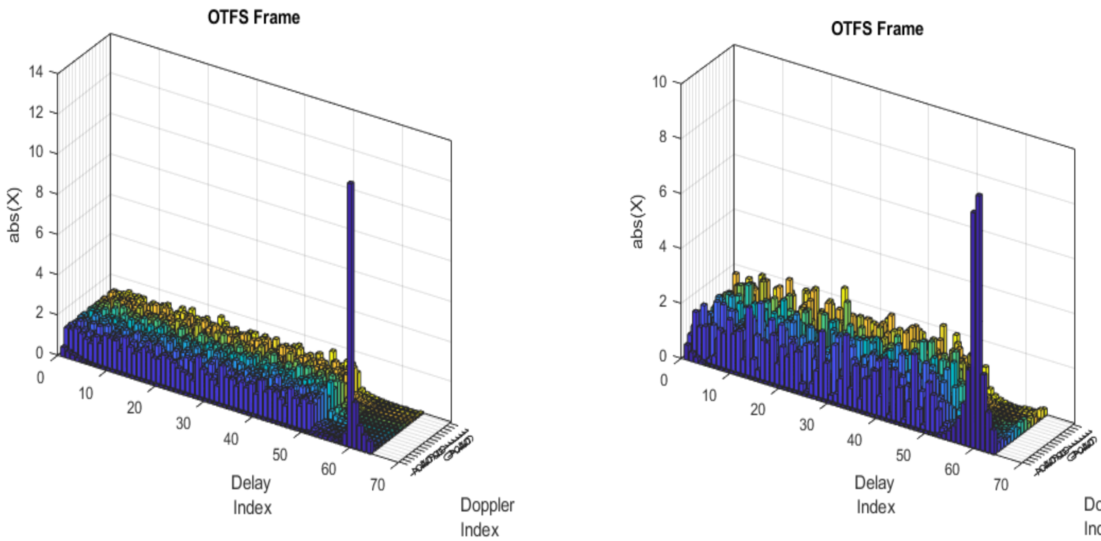

a) **b)**

Figure 3-31 OTFS Frame in the presence of STO, a) STO gradually increases the leakage of a single symbol into multiple symbols in the Delay-Doppler domain, b) STO causes the worst spillage of a single symbol into multiple symbols. A LoS channel can be mistaken for a multipath channel in STO presence.

The fractional STO causes increased computational complexity at the equalizer end, as now it needs to equalize a higher number of (false) multipath effects. A simple interpolation of a factor L can alleviate this problem, and the same preamble utilized for SOF can assist with it. The interpolated signal is down-sampled and has different starting points (called branches). One of the branches matches closest to the ideal sampling point, and with this, fractional STO can be minimized. The effect, interpolation, and a few suitable branches are shown in Figure 3-32, with L = 8. The increased size of L also makes it closer to the ideal sampling point.

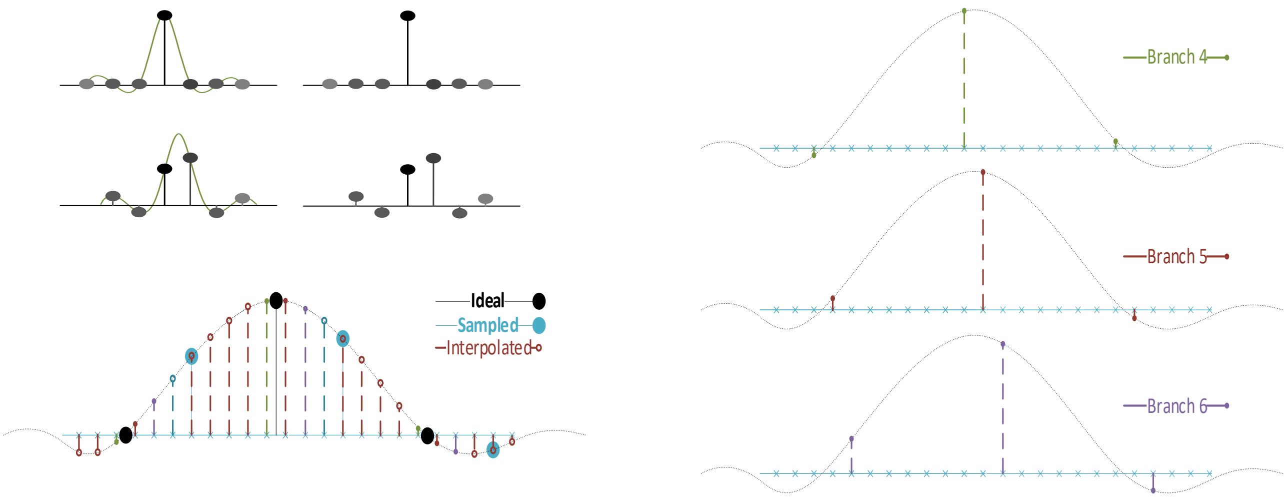

Figure 3-32 Result of a fractional STO. Interpolation improves the fractional STO-affected signal.

CFO is a frequency shift, which is similar to a Doppler shift in this way. CFO becomes a part of channel response and can be equalized by the same OTFS equalizer. This can alleviate the need for a separate CFO correction module. Figure 3-33 shows how the CFO causes spillage on the Doppler axis.

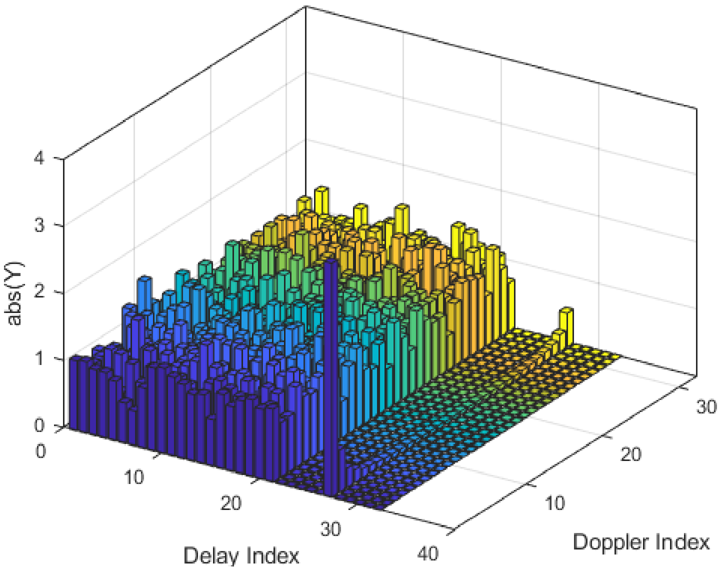

Figure 3-33 Impact of CFO on OTFS Frame

3.3.2.3.2 Equalization

For static and low mobility channels single- tap (Zero-forcing or Minimum Mean Square Error) equalizer can be used in TF domain. However, for the scenarios, in which subcarriers lose their orthogonality, alternative solutions are required. Few of these alternatives are:

- Linear Minimum Mean-Square Error (LMMSE) [93].
- Message Passing (MP) detection [93].
- Maximum-Ratio Combining (MRC) Detection [93], [94].

Each of these equalizers provide similar performance, with MRC providing it at the lowest complexity [93].

3.3.2.3.3 Demodulation

After achieving frame synchronization, CP is removed and the received signal is converted again into a matrix Y_{DT}. Similar to the selected Zak Transform-based OTFS modulator, the OTFS demodulator performs Zak Transform on Y_{DT} to get the DD matrix Y.

For the other scheme i.e. ISFFT, Y_{TF2} is found by taking an M-point IFFT:

$$Y_{TF2}[k,l] = \sum_{m=0}^{M-1} Y_{DT}[m,n] e^{-j2\pi\left(\frac{mk}{M}\right)} \tag{3-28}$$

where n is equal to l. The additional M/M' tones are removed to get the matrix Y_{TF}, which is equivalent to X_{TF} in ideal conditions. Forward SFT is applied finally to get the resulting matrix Y [93]:

$$Y[m,n] = \frac{1}{\sqrt{M'}} \sum_{k=0}^{N'-1} \sum_{l=0}^{M'-1} Y_{TF}[k,l] e^{-j2\pi\left(\frac{nk}{N'} - \frac{ml}{M'}\right)} \tag{3-29}$$

3.3.2.4 Simulation Results

For the simulation, MATLAB has been used. The following toolboxes were used to carry out the simulation:

- Signal Processing Toolbox.
- Communications Toolbox.
- WLAN Toolbox.

WLAN Toolbox was used to compare an existing OFDM standard, i.e., IEEE 802.11n, and OFDM precoding is employed.

Table 3-6 illustrates the OTFS simulation parameters. The OFDM model uses the FFT size 64, with 56 active subcarriers [90]. The total bandwidth of the system is 20 MHz, and to keep the same occupied bandwidth, the value of the OTFS delay bins M' is set to 56. For Doppler bins N', the value is set to 16. This corresponds to a Doppler resolution of 19531.25 Hz and a Delay resolution of 57.1 ns. The carrier frequency is set at 5.85 GHz.

Table 3-6 OTFS Simulation Parameters

Constraint	Value
Carrier Frequency f_c	5.85 GHz
Bandwidth B_T	20 MHz
Occupied Bandwidth B_O	17.5 MHz
Δf Subcarrier Spacing	312.5 kHz
M×N	64×16
M′×N′	56×16
$\frac{1}{B_O}$ Delay Resolution	57.1 ns

$\frac{B_O}{M' \times N'}$ Doppler Resolution	19.531 kHz
Modulation Scheme	4-QAM
Tx Power	≈0 dB
Simulated Vehicular Speeds	150, 200, 250, 300 km/h
Maximum Doppler Shift	813, 1084, 1355, 1626 Hz

The performance of both systems is evaluated against different mobility scenarios [89]. The channel delay profile uses seven paths. The path coefficients are taken from the 3GPP specification for an extended pedestrian A channel model [96], with tap delays and power defined as follows {0, 30, 70, 90, 110, 190, 410} [ns], {0, -1, -2, 3, -8, 17, -21} [dB]. We simulated this channel with additional mobility effects at 150, 200, 250, and 300 km/h. The power spectral density (PSD) of the Doppler spectrum is Jakes classical shaped, and Rayleigh fading variates are generated with the sum of sinusoids method. A sampling rate offset of 25 ppm is also applied to consider a high sampling rate mismatch between ADC and DAC clocks.

No prior information about the channel is available at the receiver, and it is performed via pilots in both OFDM and OTFS frames. In practical cases, the channel information is either estimated at the receiver or transmitted to it; our simulation is more suitable for practical scenarios. OFDM system utilizes the HT-mixed preamble and four pilots per symbol, and the OTFS system uses a single pilot in the DD domain (surrounded by zeros to avoid interference).

The MRC algorithm is used to equalize the OTFS system [94]. Due to its reduced complexity, the MRC is operated in the delay-time domain [94]. A maximum of ten total paths are used for channel estimation (CE) and equalization. Ten paths account for around 450 nanoseconds of delay spread tolerance (considering fractional delays and residual fractional STO). At higher frequencies, the multipath component becomes weaker, and a smaller number of total paths can be utilized for channel estimation and equalization, thus reducing the complexity even further.

Error Vector Magnitude (EVM) comparisons are carried out to compare OFDM and OTFS systems at different mobilities. A system performance metric is utilized, which is given by:

$$P_{SNR}[\%] = \left(1 - \overline{EVM}_{SNR}\right) \times 100\% \tag{3-30}$$

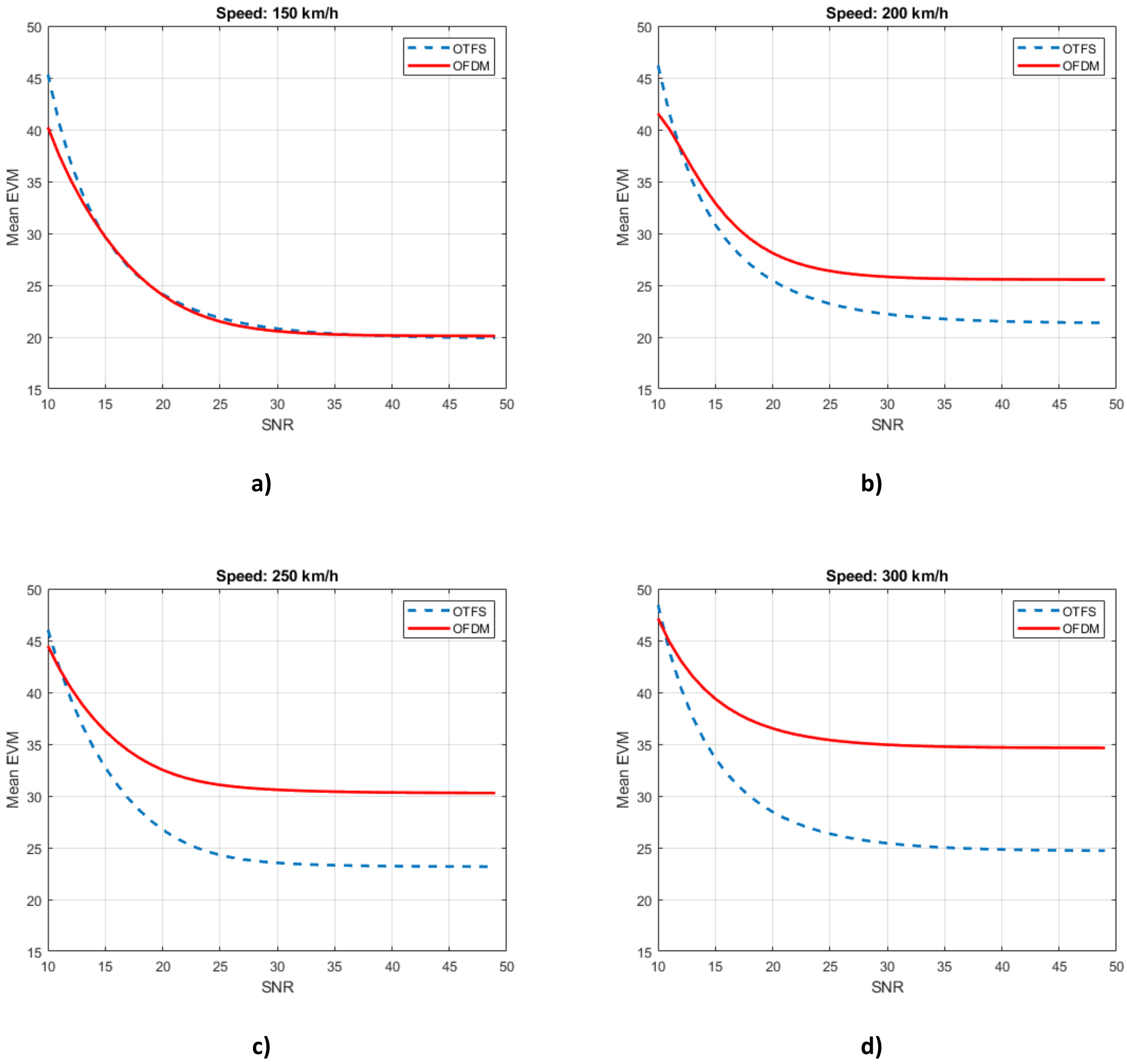

Figure 3-34 Resulting EVM vs. SNR comparisons for different vehicular speeds (a) 150 km/h, (b) 200 km/h, (c) 250 km/h, (d) 300 km/h.

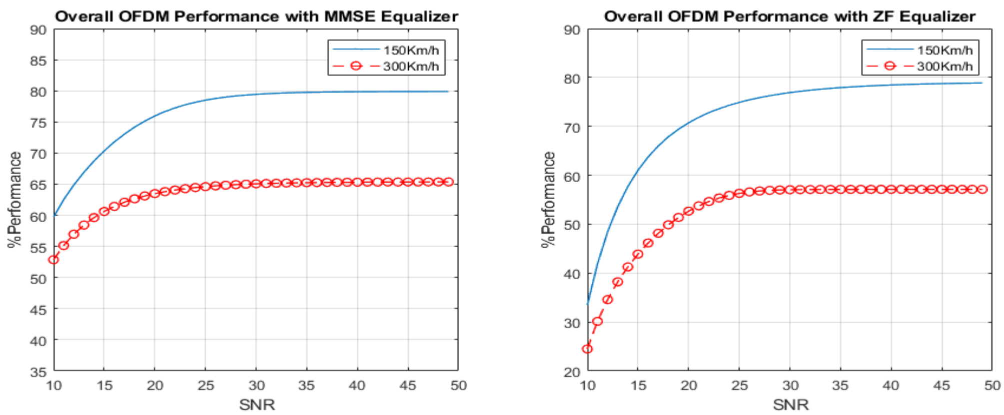

a)

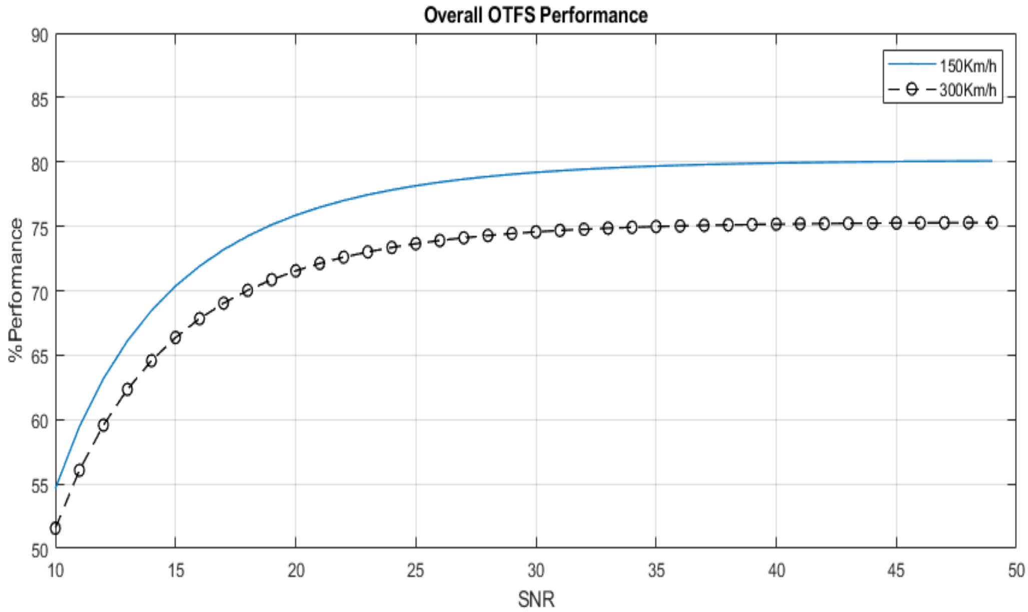

b)

Figure 3-35 Resulting Percentage Performance vs. SNR comparisons (a) OFDM performance with MMSE and (b) ZF Equalization OTFS performance.

A proper and complete OFDM system was chosen specifically for a fair comparison with the OTFS waveform, which is built for high-mobility scenarios. Figure 3-34 a) illustrates the EVM results between OFDM (with MMSE equalizer) and OTFS waveform at 150 km/h mobile speed. It can be seen that both OFDM and OTFS achieve similar results with the improved SNR. This indicates that OFDM can also work fine in typical high-mobility scenarios, with longer channel estimation validity and good equalizer performance. Figure 3-34 b) demonstrates the results at 200 km/h. The OFDM system's performance has now started degrading, and the performance of the OTFS has not changed much. Figure 3-34 c) and Figure 3-34 d) indicate further degradation of the OFDM system, whereas the OTFS system has slight degradation compared to the OFDM. This shows how the complete OFDM system with efficient equalization can also not accurately manage high-mobility scenarios.

Figure 3-35 a) indicates the total performance degradation of the OFDM system with increased speed. It is evident that with increased speed, the OFDM system loses significant performance. Figure 3-35 a) also illustrates the poor performance of the ZF equalizer. Figure 3-35 b) indicates slight degradation of the OTFS system as compared to OFDM. The results in clearly indicate that the OTFS system will outperform the OFDM system in high-mobility scenarios.

Various factors influence the performance of OTFS systems. Although it provides robustness against Doppler, for static and low-mobility channels, OFDM provides similar performance at lower complexity. Also, the OTFS benefits are dependent upon efficient channel estimation, which can be corrupted by noise. Figure 3-36 shows how difficult can CE become in the presence of noise. A thresholding is necessary for that.

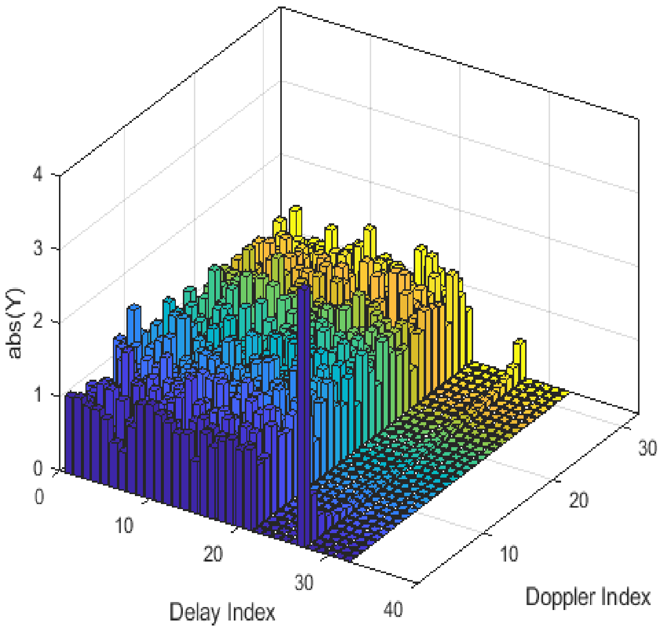

a)

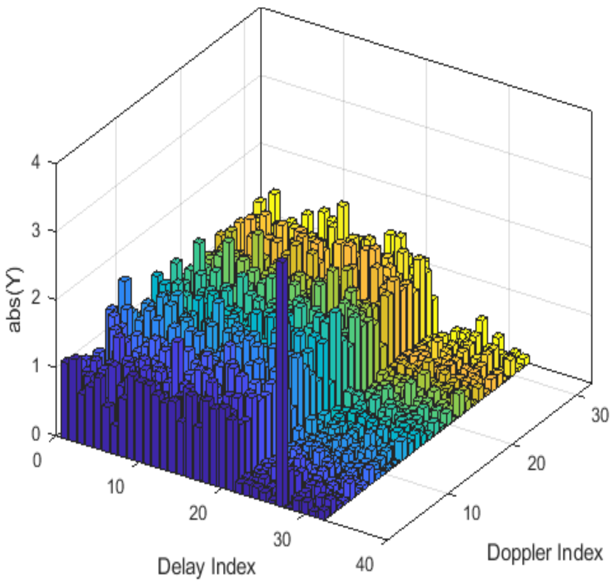

b)

Figure 3-36 OTFS frame with CFO in the presence of a) less noise, b) high noise.

Single-tap (MMSE or ZF) equalizers can provide low complexity equalization, but with high-mobility cases, performance can significantly degrade. Also, single-tap equalization makes sense for ISFT-based OTFS systems, where the TF plane arises naturally from the processing. With MRC equalization, for longer frames ($M \geq 256$) with substantial multipath, processing can slow down due to the iterative nature of MRC.

Additionally, a DFT is utilized for ISFT-based implementation to match the existing OFDM frame requirements, which hinders the use of fast FFT. This can also slow down the speed of the transmitter and receiver processing chain.

The current channel estimation scheme requires high SNR and an efficient estimation of channel noise, to properly estimate the channel. Furthermore, a DD domain high power pilot with a zero region also causes a significant Peak Average Power Ratio (PAPR) in the time domain. PAPR creates various issues with power amplifiers. Pilot power needs to be carefully designed in order to prevent PAPR-related problems. The impact of pilot power is illustrated in Figure 3-37.

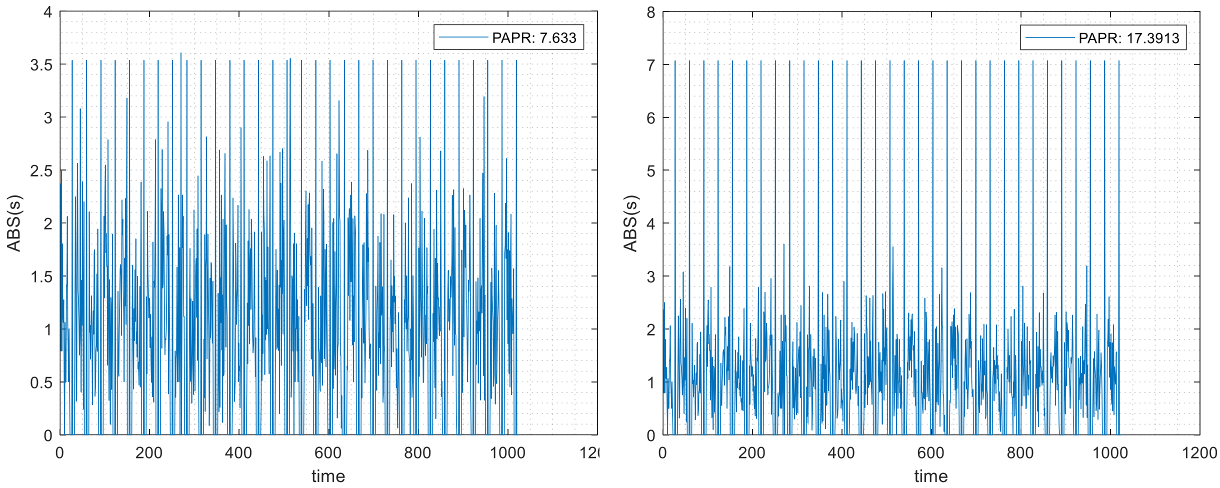

a) **b)**

Figure 3-37 Final frame in TD with, a) low-power pilot, b) high-power pilot.

3.3.3 ISAC Service Model implementation

ISAC will play a pivotal role in beyond 5G (B5G) and 6G future cellular networks in a myriad of emerging applications. However, due to its early stage, a process of discovering the needed requirements is being conducted. The OFDM frame structure of cellular networks permits the ability to infer the information transported by each subcarrier during each symbol duration assuming a high SNR. Nevertheless, following the finite-state-machine (FSM) where the 5G protocol stands at each slot, leads to practically reimplementing the full 5G stack. Additionally, many ISAC applications are interested to measure the channel and, therefore, they are only interested in a relatively small amount of UL IQ pilot samples. The way 5G measures the UL channel is primarily using the SRS, which can be transmitted periodically or aperiodically, depending on the configuration. A pilot RS is generated in the UE and transmitted in UL, permitting noise inference and channel estimation and equalization in the gNB.

Therefore, a natural choice for an application in this regard (an xApp) is to retrieve the received SRS signal, as well as the noise, to infer the channel and act accordingly. On account on that, **BR** will develop a new ISAC Service Model (SM) PoC, based on O-RAN on top of OAI. Due to the extending capability of E2AP, *à la carte* SMs can be conceived as demonstrated in FlexRIC's[4] sublayer-based SMs (e.g., MAC, RLC or PDCP). Moreover, even though the nearRT-RIC latencies range from 10 ms to 1 second according to O-RAN, experimental results show the possibility of achieving sub-millisecond E2AP Indication messages transfer, permitting real-time communication even at the xApp level, and pioneering using xApps with ISAC purposes.

[4] R. Schmidt, M. Irazabal, and N. Nikaein, "FlexRIC: an SDK for next-generation SD-RANs", in Proceedings of the 17th International Conference on emerging Networking EXperiments and Technologies (CoNEXT'21).

4 Cell-Free massive MIMO activities

CF-mMIMO involves distributing antennas over a large area, increasing coverage and improving radio wave usage efficiency. As we advance towards 6G networks, CF-mMIMO is becoming increasingly relevant due to its potential to support ISAC [97].

6G-SENSES promotes the development of signal processing and algorithmic blocks of the CF-mMIMO architecture – i.e., multiple distributed multi-antenna systems (APs or RUs) connected to CPUs[5]. The project will develop distributed signal processing and optimization algorithms for APs including channel estimation, beamforming, and AP clustering given HW and fronthaul constraints that scale for large terminal and AP numbers. Moreover, we will provide characterizations of achievable performance in terms of data rates, sensing accuracy, EE, uniform coverage, reliability and availability. A thorough analysis of reciprocity in CF-mMIMO systems will be provided, to ensure coherent processing, i.e., phase synchronization between the communication nodes, including intra-AP and inter-AP synchronization. Initial details are included in section 4.3.3. Additionally, the project will explore the potential of the unsourced random access (URA) paradigm (see section 4.3.4), which enables a large number of devices to communicate concurrently on the uplink.

Once the algorithm development is completed, the algorithms with the most desirable performance/complexity trade-offs will be integrated into the 6G-SENSES CF-mMIMO PHY prototype. The algorithms related to this implementation will be deployed on top of representative real-time (RT) / SDR HW components to demonstrate the feasibility of the concept (as per PoC#2 description in the DoW) as well as achieving high network performance. All relevant aspects of an operational CF-mMIMO network will be demonstrated, including tight timing synchronization, distributed signal processing for channel estimation beamforming and fronthaul/backhaul data plane traffic exchange.

4.1 State-of-the-Art in CF-mMIMO activities

4.1.1 Use Cases and applications

CF-mMIMO technology holds great promise for achieving dual functions: transmitting data while simultaneously sensing the environment. This capability enables networks to provide high-speed internet access to users while also collecting essential information about their surroundings. Such functionality is particularly beneficial for emerging technologies like autonomous vehicles, smart cities, and Internet of Things (IoT) devices, all of which require rapid data gathering and sharing to operate effectively and safely [98]-[100]. The limitations of the technology due to the limited transmission power of APs and expensive wired fronthaul [101], make the coverage range provided by CF-mMIMO limited. Authors in [102] consider wireless fronthaul connections and propose a joint antenna activation and power allocation algorithm to minimize the e2e – from radio to cloud – power while satisfying the quality-of-service requirements of the UEs under wireless fronthaul capacity limitations.

The CF-mMIMO deployment improves significantly the reliability and delay performance of communication links [103] by minimizing the average distance between users and APs due to the spatial distribution of multiple antennas [105]. Moreover, this architecture allows serving multiple users simultaneously through spatial multiplexing using the same frequency resources [106]. Another important benefit of such architectures is the potential use of transmit beamforming over multiple spatially distributed antennas, being able to steer the signals in a particular direction thus reducing the interference to other potential users [107], [108].

[5] In the O-RAN nomenclature, the RU corresponds to the AP and the CPU is disaggregated into DU/CU units. In this section, we will use interchangeably the usual CF-mMIMO nomenclature (AP/CPU) or the O-RAN nomenclature (RU/DU/CU).

4.1.2 CF-mMIMO practical implementation in testbeds

CF networking has gained a lot of attention given its outstanding performance in theoretical studies under ideal conditions [110]. Recent research focuses on a more practical analysis of its benefits, assuming non-ideal HW, thus providing insights into facilitating a potential practical implementation. Given this, the ongoing studies contemplate two options: 1) analytical and simulation studies that employ more realistic assumptions; and 2) development of testbeds using (SDR) HW whose aim is to test the feasibility of CF networking in real scenarios.

In [111], the authors have implemented a fully distributed CF-mMIMO testbed with an ultra-dense network (UDN) scenario. The main advantage of the proposed testbed is its distributed architecture without any CPU. The experiment results show that multiple UEs can simultaneously be served without interference in a fully distributed manner.

The authors in [112] propose a new fully distributed CF-mMIMO architecture that enables independent deployment of APs that carry out baseband processing functions in a distributed manner without any CPU, thanks to the fully distributed functional split structure.

The authors in [113] implement in a testbed a centralized cloud-based CF-mMIMO network, where a CPU serves 16 8-antenna UEs with 16 8-antenna APs. In [6], the KU Leuven CF-MIMO testbed is used to obtain the CSI in a dense CF deployment consisting of 8 APs with 8 antennas each (64 antennas in total). In both works, most of the HW Impairments (HWI) effects are implicitly assessed since real equipment is used. Unfortunately, both works used a common clock and the effect of Phase Noise (PN) is not estimated.

In [114] authors concentrate on a HW implementation of CF-mMIMO and dynamic TDD using the OAI 5G new radio (NR) SW stack, with the aim to experimentally understand the role of CF-mMIMO and dynamic TDD in providing better connectivity at the cell-edge and improving network throughput.

In [115], a design of a RS for over-the-air (OTA) reciprocity calibration is proposed. The frequency domain generated RSs can make full use of the flexible frame structure of the 5G NR, which can be completely transparent to commercial off-the-shelf (COTS) RRUs and commercial UEs. A CF-mMIMO prototype system with COTS RRUs is used to demonstrate the statistical characteristics of the calibration error and the effectiveness of the calibration algorithm, and to evaluate the impact of the calibration delay on the different cooperative transmission schemes.

4.2 Description of selected CF-mMIMO platforms

The work on CF-mMIMO in 6G-SENSES will be tackled by different partners and several testbeds will be used for testing the development work. Two of the testbeds, which are hosted by the Technical University of Braunschweig (**TUBS**), will be the main playground for incorporating the methods and algorithms being assessed overall. The first testbed is presented in section 4.2.1 and tackles the PHY layer perspective of CF-mMIMO, while the second one (section 4.2.2) is being built focusing on the extension of the PHY-layer testbed with the integration of networking aspects.

4.2.1 PHY layer testbed

An experimental platform for a CF-mMIMO system has been implemented in the context of 6G-SENSES. This platform is mostly dedicated to PHY layer research and is depicted in Figure 4-1. Its overall architecture leverages Ettus Research's product USRP Hardware Driver (UHD) and compatible SW, such as GNU Radio for visualization and signal processing tasks. The DU is connected to two different RUs via a fronthaul network. The system supports the following two communication modes: 1) each RU uses a different beamforming technique to communicate independently with each UE; 2) both RUs use the same beamforming strategy to serve both UEs jointly. Our research objective is to verify the feasibility of finding suitable beamforming methods for these two communication modes.

The physical setup would comprise 24 USRPs with 48 antennas in total, which are used to form 2 RUs with 12 USRPs each, and 24 antennas each to facilitate communication with 2 UEs. Each UE is connected to a corresponding laptop for signal processing and data exchange.

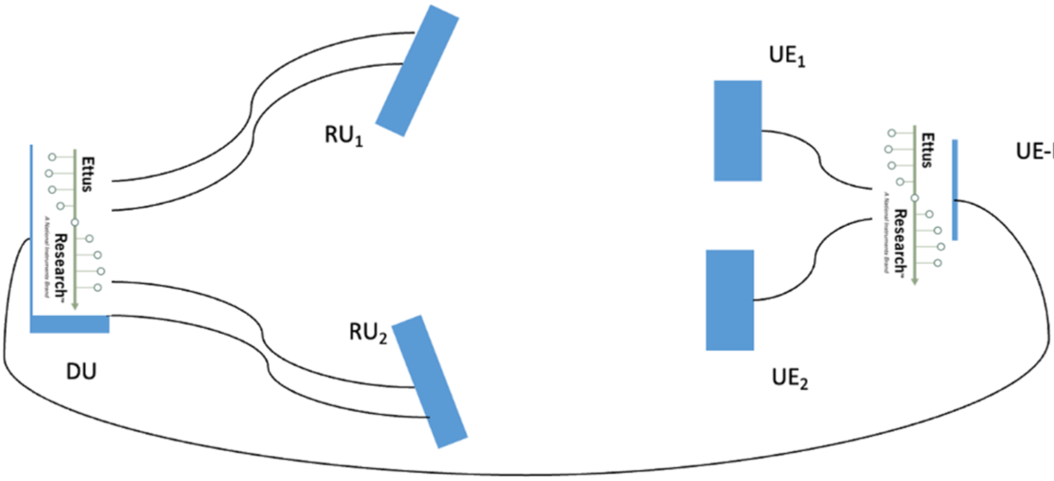

Figure 4-1 Massive MIMO System for CF-mMIMO – Setup

4.2.1.1 System Components

The USRP RIO 294XR / 295XR HW in Figure 4-2 is a high-performance wireless communication platform, with each device equipped with 2 RF frontends and a Kintex-7 FPGA, enabling real-time signal processing. It supports multiple frequency bands, making it suitable for a wide range of wireless communication applications. Specifically, the USRP RIO 2943R / 2953R supports a frequency range from 1.2 GHz to 6 GHz, while the USRP RIO 2942R / 2952R covers 0.4 GHz to 4.4 GHz, and the USRP RIO 2940R / 2950R supports 0.05 GHz to 2.2 GHz. The GPS Disciplined Oscillator (GPSDO) inside provides high-precision clock synchronization, ensuring timing consistency across different devices in a distributed system, which is crucial for applications requiring precise timing. For data transmission, the HW uses 4 MXI cables, each supporting 830 MB/s throughput in both directions, enabling high-speed data exchange between devices. This high-throughput interconnect allows the system to efficiently handle large data streams and supports peer-to-peer data streaming between devices, ensuring low latency and high reliability, especially for high-performance MIMO communication systems.

Figure 4-2 USRP RIO 294XR / 295XR hardware

Figure 4-3 Universal Ethernet Switchbox

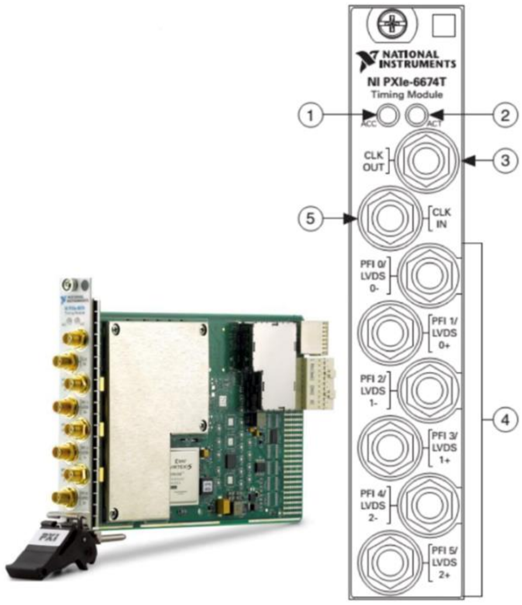

Figure 4-4 NI PXIe-6674T

The Universal Ethernet Switchbox in Figure 4-3 is a high-performance data aggregation device that combines 8 PCIe connections into a single data stream, supporting a 3.2 GB/s data rate via a PCIe x8 Gen 2 connection. It enables peer-to-peer streaming between multiple USRP RIO devices, allowing direct, low-latency data transfer without CPU intervention. This capability simplifies system architecture and ensures efficient, high-speed communication, making it ideal for applications like massive MIMO, high-throughput wireless systems, and real-time signal processing.

The NI PXIe-6674T Timing and Synchronization Module in Figure 4-4 provides precise clocking and synchronization for MIMO systems, with a 10 MHz Oven Controlled Crystal Oscillator (OCXO) clock offering accuracy better than 5 ppb. It supports high-resolution Direct Digital Synthesis (DDS) clock generation from 0.3 Hz to 1 GHz with microhertz precision. The module allows flexible routing of internal and external clock and trigger signals and offers configurable Input/Output (I/O) options, including 6 single-ended PFI lines or 3 LVDS pairs. This ensures accurate timing and synchronization, critical for high-performance MIMO system operation.

4.2.1.2 Functional definition

In this CF-mMIMO system, three configurations for communication between two RUs and two UEs are explored, each with distinct technical feasibility and channel requirements. The first configuration (baseline configuration) involves each RU independently serving a different UE using separate beamforming, where RU1 exclusively serves UE1 and RU2 exclusively serves UE2. The second configuration has both RUs serving both UEs on the same RB, requiring synchronized transmission to prevent interference. The third configuration, where both RUs serve both UEs using different beams with consideration of phase offsets, requires careful phase alignment and channel knowledge for effective transmission.

Each of these configurations presents unique challenges and advantages. We analyze them individually below, focusing on their technical feasibility and requirements.

4.2.1.2.1 Configurations of the CF-mMIMO platform

The Baseline configuration (Figure 4-5) involves each RU independently serving a different UE through separate beamforming. Here, RU1 exclusively serves UE1, while RU2 exclusively serves UE2, each using its own beam. This setup is technically straightforward, as it requires no coordination or synchronization between the RUs. Each RU simply performs beamforming based on the CSI of its assigned UE, making implementation relatively simple. Additionally, this configuration imposes no specific similarity requirements between the channels from each RU to each UE, making it robust to varying channel conditions and suitable for fast-changing or heterogeneous environments.

In the second configuration (Figure 4-6), both RUs serve both UEs on the same RB. In this mode, RU1 and RU2 simultaneously serve UE1 and UE2 using the same RB. This approach demands a high level of coordination to avoid destructive interference, as both RUs are transmitting over the same frequency and time resources. To maximize signal strength and ensure coherent reception at the UEs, the RUs must synchronize their transmission timing and possibly adjust their beamforming strategies. This configuration requires channels between each RU and UE to be sufficiently similar or compensated for in real-time, and it places stringent demands on synchronization and CSI sharing, particularly in dynamic channel conditions.

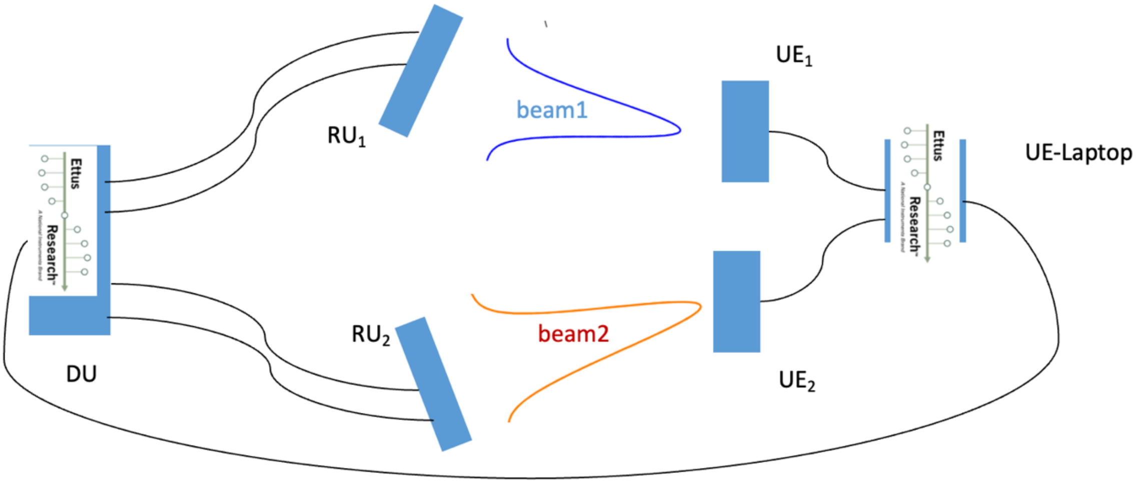

Figure 4-5 Baseline: Two RUs serve two different UEs separately through beamforming

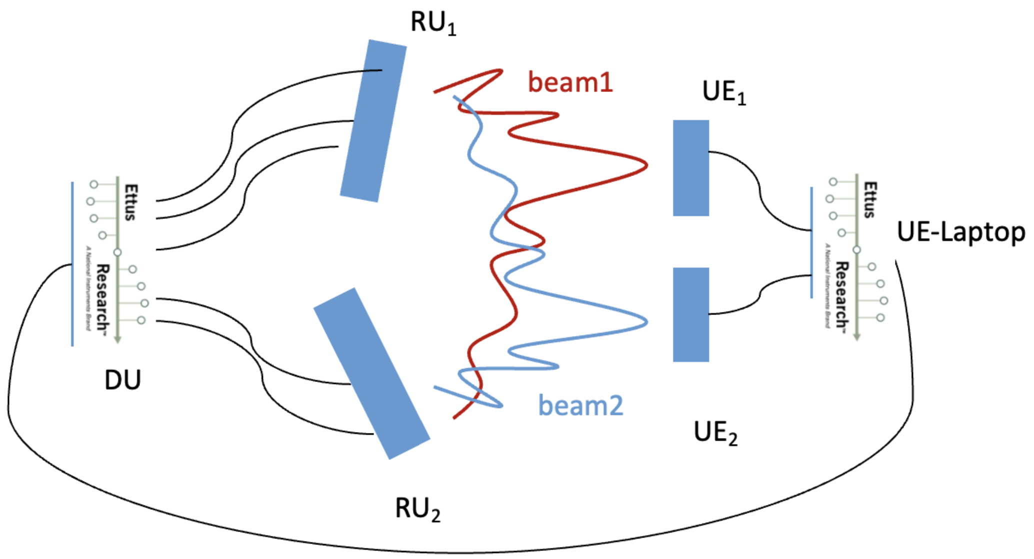

Figure 4-6 Second configuration: both RU1 and RU2 are serving UE1 and UE2 on the same RB

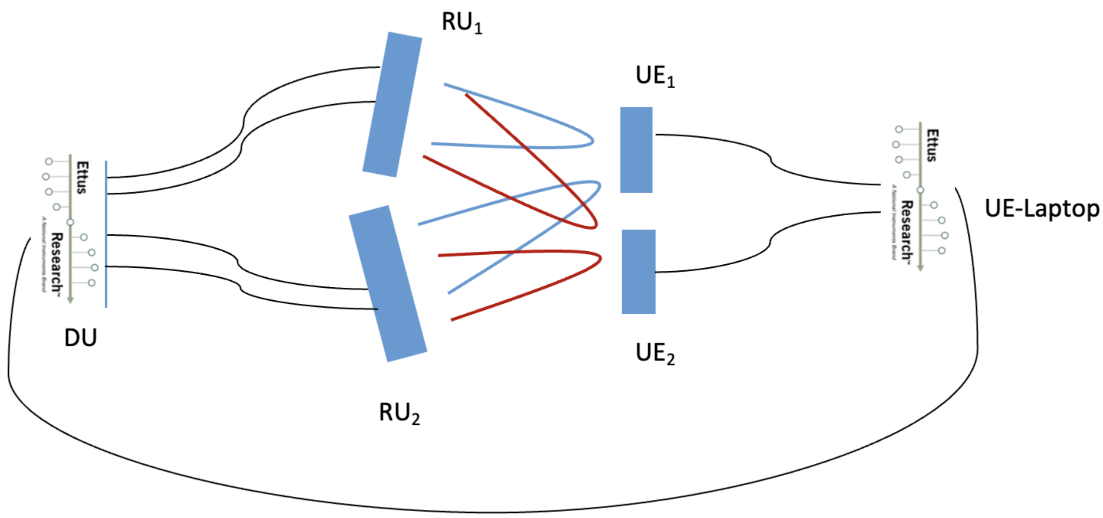

Figure 4-7 Third configuration: both RUs serve both UEs with different beams, accounting for synchronization and phase offsets

The third configuration (Figure 4-7) involves both RUs serving both UEs with different beams, accounting for synchronization and phase offsets. In this setup, each RU uses distinct beams to communicate with both UEs, taking into consideration any phase offsets between the RUs. This setup is technically challenging, as it requires sophisticated signal processing and synchronization mechanisms to adapt the beamforming for each RU-UE link while compensating for phase mismatches. It demands a detailed understanding of the channel characteristics and precise adjustments for phase alignment, which may require stable, low-latency fronthaul links to support real-time synchronization and CSI updates. This configuration is highly sensitive to variations in channel phase and amplitude, making it technically complex but potentially valuable for achieving flexible and adaptive communication.

4.2.1.2.2 CF-mMIMO system parameters

This system, whose parameters are included in Table 4-1, is a high-speed MIMO wireless communication system designed to support flexible configurations for both the RUs and UEs. It uses OFDM for efficient transmission, with a bandwidth of 20 MHz and a center frequency ranging from 0.05 to 6 GHz. The system supports multiple modulation formats (4-QAM, 16-QAM, 64-QAM, 256-QAM) for varying data rates and has a peak uncoded rate of 1612.8 Mbps. With scalable antenna configurations (from 2 to 48 RU antennas and 1 to 8 UE antennas), it ensures high capacity and performance in modern wireless networks like 6G.

Table 4-1 System Design Parameters

Parameter	Unit	Value
Center frequency	GHz	0.05 – 6
Channel bandwidth	MHz	20
Sampling rate	MHz	30.72
Subcarrier spacing	kHz	15
FFT Size	-	2048
Number of used subcarriers	-	1200
Number of RBs	-	100
OFDM symbol duration	µs	66.67
CP duration (Normal CP mode)	µs	5.21 (1st OFDM symbol in a slot) 4.69 (remaining OFDM symbols in a slot)
CP length (Normal CP mode)	Number of samples	160 (first OFDM symbol in a slot) 144 (remaining OFDM symbols in a slot)
OFDM symbols per slot	-	7
Slot duration	-	0.5
Modulation format	-	4-QAM, 16-QAM, 64-QAM, 128-QAM
PHY layer uncoded peak rate	Mbit/s	1612.8 (12 layers, 256-QAM)
Number of RU antennas (M)	-	2, 4, 6, 8, 10, …, 48
Number of UE antennas (K)	-	1, 2, 4, 6, 8
Number of spatial layers	-	1, 2, 3, 4, …, 12

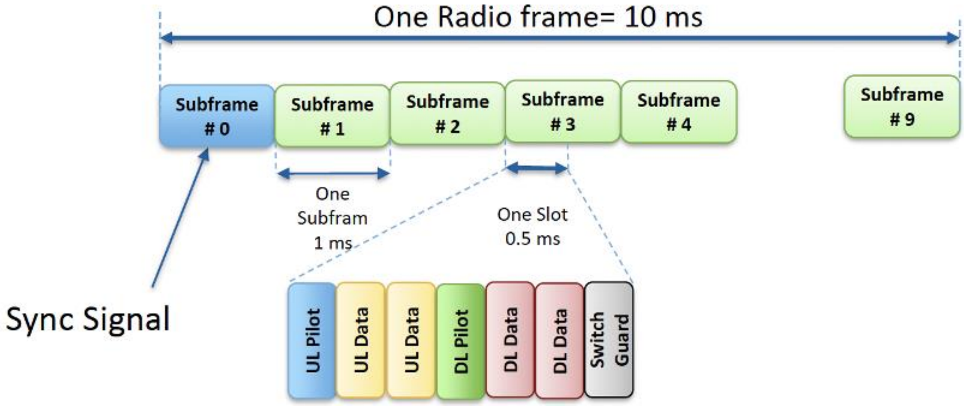

Figure 4-8 Radio Frame Structure: TDD

In this system, the TDD radio frame structure in Figure 4-8 is used to efficiently support uplink (UL) and downlink (DL) signal transmission. The frame structure includes various types of signals to ensure proper synchronization, data transmission, and channel estimation.

First, the Primary Synchronization Signal (PSS) serves as a synchronization signal, helping the UEs synchronize with the network, which is crucial for establishing the communication link. Next, the UE-specific Reference Signals include both DL Pilot and UL Pilot signals, which are essential for channel estimation. The DL Pilot is used for DL channel estimation, while the UL Pilot is used for UL channel estimation, ensuring that the UE can optimize its transmission based on the current channel conditions.

For data transmission, the Physical Downlink Shared Channel (PDSCH) carries actual downlink data to the mobile station, while the PUSCH handles UL data from the UEs to the RU. To prevent interference between different signals, the system includes guard periods to ensure there is no overlap between signals, avoiding signal distortion and maintaining data integrity and transmission quality.

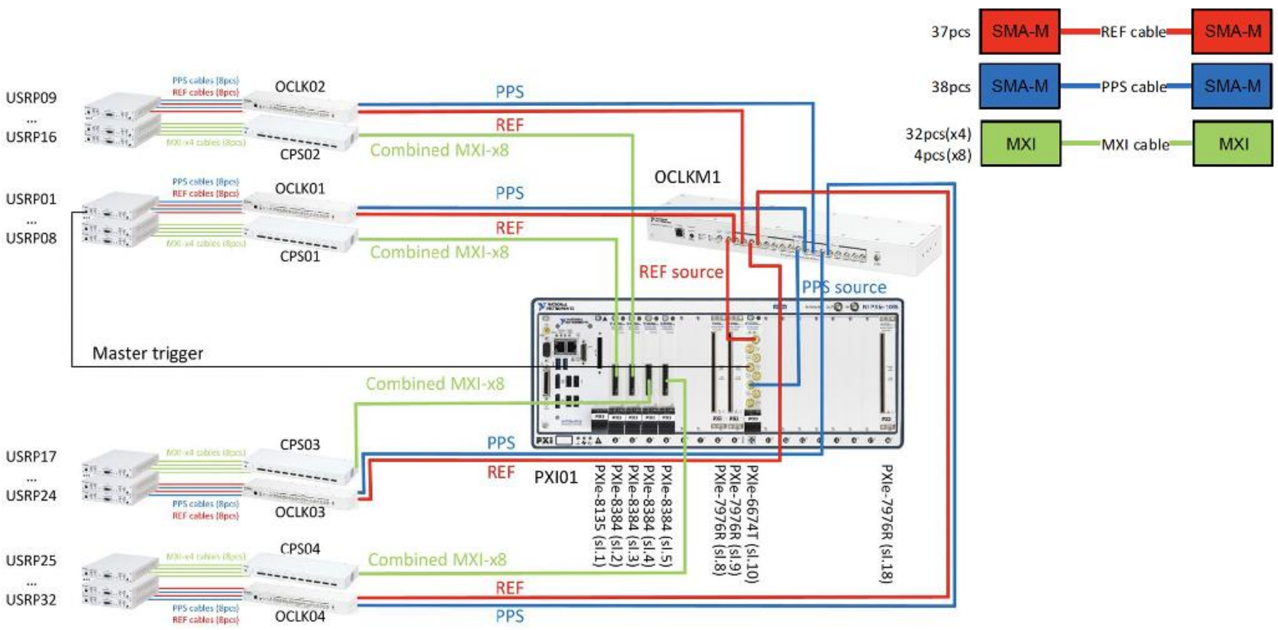

Figure 4-9 RU Hardware Architecture: 48 Antennas

Based on the previous system design, we have developed the RU HW Architecture featuring 48 antennas in Figure 4-9. This architecture is designed to leverage the full potential of MIMO technology, allowing the RU to handle multiple data streams simultaneously, thereby significantly increasing the system capacity and performance. With 64 antennas, the RU can support a large number of simultaneous users, improve spatial diversity, and enhance signal quality, even in challenging environments with high interference or long-distance communication.

The use of 48 antennas enables a higher degree of spatial multiplexing, allowing the RU to send and receive multiple data streams on the same frequency band, making the most efficient use of available spectrum. Additionally, this architecture provides enhanced beamforming capabilities, which improves signal strength and coverage by directing the transmission towards specific users or areas, further increasing the overall network throughput and reliability.

To implement the three above mentioned communication configurations between two RUs and two UEs in our CF-mMIMO system, a specific set of **HW requirements** must be met. The system utilizes the UHD as the interface with USRP RIO 294XR/295XR devices serving as the RUs and UEs. For SW development and HW interaction, GNU Radio is used as the interface or, alternatively, code can be directly compiled to enable communication between the SW and HW.

Each UE is connected to a laptop, which is linked to the DU via a backhaul network. The DU requires essential components to manage synchronization and real-time signal processing. These components include high-performance processing units or FPGA modules, which are crucial for handling signal processing and coordinating communication between the RUs and UEs, particularly for configurations requiring coherent beamforming. A stable, low-latency backhaul network interface is also essential to connect the laptops at each UE to the DU. This network must support high data rates and enable rapid updates of CSI, which is critical for configurations that require synchronization and precise coordination.

At the UE setup, an USRP RIO 294XR/295XR device is used to receive signals from the RUs. These reconfigurable devices support adaptive reception, enabling the UEs to receive complex multi-RU transmissions across different beamforming configurations. Each UE is connected to a laptop that handles signal processing on the UE side and communicates CSI and feedback to the DU via the backhaul network.

The backhaul connection needs to be stable and have low-latency, ensuring high data rates and fast CSI updates for seamless coordination with the DU.

Finally, additional network infrastructure is necessary to maintain low latency in the fronthaul and backhaul connections. High-performance switches and low-latency cables are required to support real-time data exchange and synchronization among the DU, RUs, and UEs, particularly for configurations demanding precise coordination.

The backhaul network plays a critical role in achieving synchronization and calibration across the system. It transfers timing signals and synchronization information, ensuring that signals are transmitted and received at the correct times, enabling coordinated operations across the different network elements (UEs, RUs, DU). For calibration, backhaul communication facilitates the transmission of system parameter adjustments (e.g., power levels, frequency, or beamforming vectors) between the DU and other system components. This allows for real-time calibration and ensures that the system operates optimally by adjusting for changing channel conditions, power levels, and frequency drift. The backhaul network, therefore, enables low-latency communication that supports synchronization and calibration, ensuring precise updates of CSI and feedback across the system.

4.2.1.2.3 System Structure and Synchronization Mechanism

The clock generator serves as the global RS source, outputting a 10 MHz RS and a Pulse Per Second (PPS) signal as the foundation for frequency and time synchronization. These signals are provided to the Master OctoClock via SMA connections. The Master OctoClock distributes the signals to three OctoClock distributors, each of which connects to eight USRP devices, ensuring uniform signal distribution.

Each USRP device receives PPS and 10 MHz reference signals via SMA connectors from the OctoClock Distribution module. To synchronize with the global reference signals, all USRP devices are configured in software to use external sources for both clock and time.

For data transmission, the Universal Ethernet Switchbox shown in Figure 4-3 is used to connect transmitters and servers. This setup ensures efficient and reliable data flow between the devices and the server.

4.2.1.2.4 Device Synchronization

The core of the synchronization mechanism lies in ensuring consistent timing and frequency. Specifically:

1. **Frequency Synchronization**: All USRP devices maintain a consistent frequency using the 10 MHz reference signal. This signal, distributed via the Master OctoClock and OctoClock Verteilers, ensures that the LOs of all devices operate on the same frequency standard.
2. **Time Synchronization**: The PPS signal, as the critical reference for time synchronization, periodically aligns the time registers of the USRP devices to a unified time point. This ensures that all devices share a common timing reference, enabling synchronized transmission and reception of signals.
3. **Signal Stream Alignment**: Building on synchronized timing and frequency, specific time parameters can be set to ensure that multiple USRP devices begin transmitting or receiving signals simultaneously. This synchronized triggering mechanism further enhances the temporal precision of experimental data.

4.2.1.2.5 Calibration Capabilities

Following synchronization, calibration is necessary to eliminate residual inconsistencies and address runtime deviations. This includes:

1. **LO Phase Alignment**: The LOs of USRP devices may exhibit random phase offsets after initial or subsequent tuning. While these offsets remain constant during operation, they can impact experimental outcomes. To mitigate this, the system synchronizes LO tuning across multiple devices to

minimize relative phase offsets. Additionally, training sequences are used during signal processing to estimate and compensate for these offsets, achieving phase coherence.

2. **Long-Term Frequency and Time Maintenance**: Over extended operation periods, slight discrepancies in frequency and time may arise due to environmental factors such as temperature variations. Re-locking the 10 MHz reference and PPS signals periodically corrects these drifts, maintaining consistent device performance.
3. **Periodic Calibration**: As the LO phase and frequency may drift over time, periodic calibration is essential. This involves re-tuning the RF front-ends of the devices and analyzing training sequences in signals to adjust for phase or frequency errors.

4.2.1.3 Target implementation

The PHY-layer demonstrator in Figure 4-10 focuses on the development and testing of beamforming algorithms, using a massive MIMO prototyping system to enhance wireless PHY-layer functions.

The CF-mMIMO Prototyping System is designed to support advanced wireless communication experiments and trials with a highly flexible configuration. It features 48 transmit (Tx) antennas and 6 receive (Rx) antennas, providing a robust platform for testing large-scale MIMO systems. The system operates within a bandwidth of 160 MHz and supports frequency ranges up to 6 GHz, making it adaptable to various communication scenarios.

The system includes source code for both the PHY and MAC layers, offering customization options for researchers and developers. Key features of the system include the adaptation of Modulation and Coding Schemes (MCSs), precoding techniques, and Successive Interference Cancellation (SIC), which are essential for optimizing performance in complex environments. The system supports real-time operation, ensuring that experiments reflect actual network conditions, and also supports symbol-synchronous transmission, allowing for precise signal synchronization during transmission.

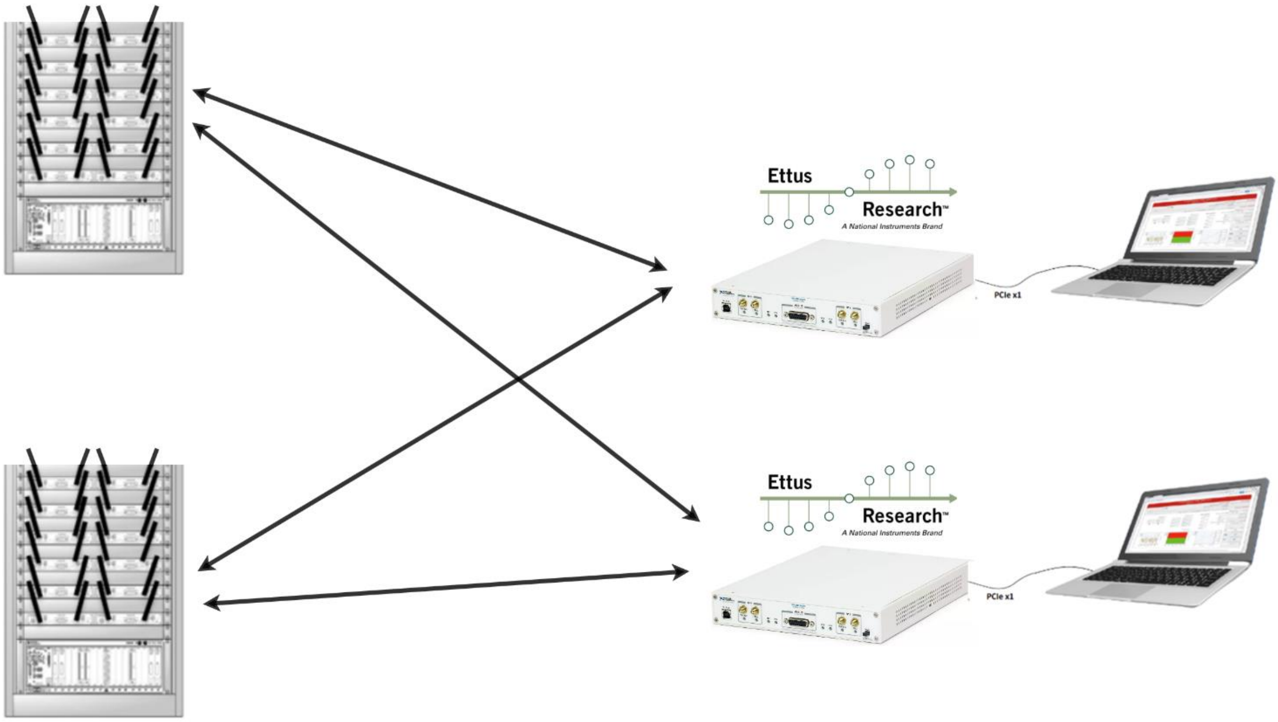

Figure 4-10 PHY-layer small-scale demonstrator

4.2.2 IAF-based CF-mMIMO Testbed

In addition to the Ettus-based CF-mMIMO testbed described in section 4.2.1, 6G-SENSES plans to implement a complementary CF-mMIMO testbed based on the IAF[6] Prototyping System (SDR 6004), which is shown in Figure 4-11. The way this system is architected (see the SW architecture in Figure 4-12) makes it flexible and powerful enough to support advanced research and deployment scenarios for 5G and 6G networks, including sensing applications, allowing for scalable and flexible network performance.

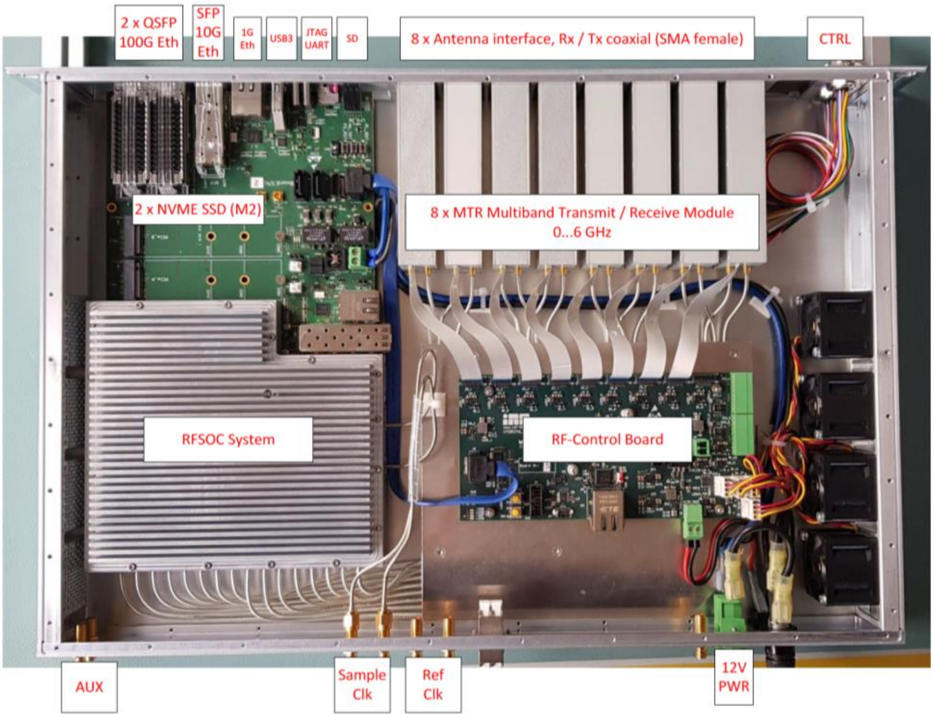

Figure 4-11 IAF Prototyping System (SDR 6004)

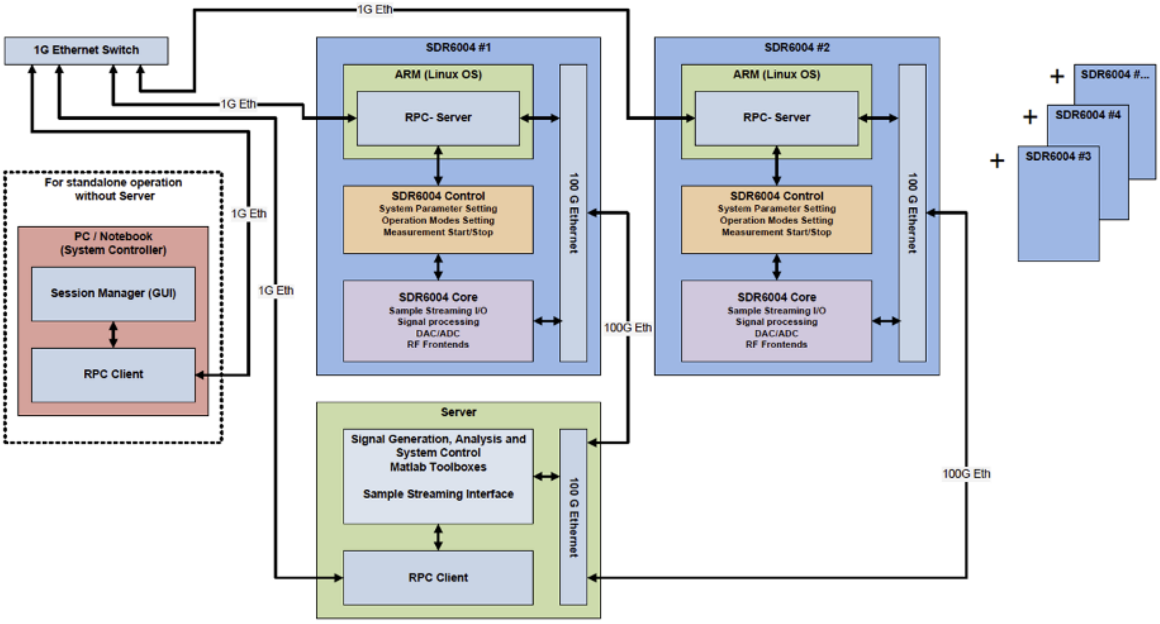

Figure 4-12 SDR 6004 Software Architecture Overview

[6] iAF Future Radio Technology (subcontract of TUBS), https://www.iaf-bs.de/en/

4.2.2.1 System Components

This system features an 8-channel SDR transceiver with an integrated Multiband Transmit/Receive (MTR) front-end module operating in the 0 to 6 GHz range. It is equipped with a Xilinx RFSoC XCZU47DR HW module and a mainboard that serves as a carrier for the RFSoC module. The mainboard also includes analog signal adaptation (differential/single-ended), digital interfaces such as 2 x 100 G Ethernet, 1 G Ethernet, and USB 3, as well as clock generation and a DC/DC power supply. Additionally, there is an RF control board for managing the MTR RF frontend modules, GPIO, and fan control. The SDR 6004-based system supports sample streaming over 100G Ethernet, with potential Xilinx IP cores available for eCPRI and O-RAN integration.

The SDR 6004-based CF-mMIMO system has various essential HW requirements to ensure it can perform at a high level in real-time, low-latency communication environments. Among these, the CPU is critical for handling joint processing tasks such as channel estimation, signal processing, and network resource management, all of which require significant computational power and low latency to ensure high throughput. The CPU must be able to process multiple complex tasks simultaneously to support the operation of the system, especially given the multiple UEs and RUs in use.

Another key component are the RUs, which need to support high-speed data transmission via high-bandwidth Ethernet links, ensuring that the system can handle high data throughput between the central CPU and the connected user equipment. The RUs must also operate across a wide frequency range (0 to sub-6 GHz) and support multi-channel communication to allow for effective mMIMO operation, where large numbers of UEs are served simultaneously.

For synchronization, a high-precision clock generator is needed to provide a global time reference, ensuring that the system components remain synchronized in both time and frequency. The clock signal must be distributed accurately across the entire system, including the central CPU, RUs, and UEs, to avoid timing mismatches that could degrade system performance. RF control boards and analog signal adaptation capabilities are also required to maintain signal integrity, minimizing distortion and noise during transmission and reception.

Additionally, the system requires 100G Ethernet interfaces for fast data transmission between components, ensuring that the system can handle the high bandwidth required for real-time processing in mMIMO configurations. The system should also support multiple network interfaces, such as 1G Ethernet and USB 3, for flexibility in connecting to other devices and systems.

Power management is another crucial aspect, with a DC/DC power supply needed to ensure stable and efficient power delivery to all system components, including the CPU, RUs, and clock generator. Effective thermal management through cooling mechanisms, such as fans and heat sinks, is also essential to prevent overheating and ensure the system operates under optimal conditions during high computational loads.

Lastly, the system should have a modular design to allow for expansion as needed. This flexibility enables the addition of more RUs or CPUs to scale up the system for larger deployment scenarios. Moreover, the integration of Xilinx IP cores for supporting future communication standards like eCPRI and O-RAN ensures that the system is future-proof and capable of supporting emerging wireless technologies such as 5G and 6G.

4.2.2.2 Functional definition

Synchronization and calibration are critical to ensuring the accuracy and efficiency of the resulting CF-mMIMO system. For synchronization, the system uses a global time reference to synchronize all components, with GPS or PTP, ensuring time alignment between the central CPU, RUs, and UEs. Additionally, a high-precision clock generator and RF control board are used to distribute clock signals, ensuring frequency synchronization and preventing frequency drift that could impact system performance. In terms of calibration, the system utilizes RF calibration, channel estimation, and digital calibration to ensure the accuracy of the radio units and analog-to-digital converters (ADC/DAC), reducing signal distortion and quantization errors, thus improving reliability and precision.

Furthermore, the system has robust cross-link synchronization capabilities to ensure the coordinated operation of multiple RUs. Synchronization between the central CPU and remote RUs is achieved through a distributed architecture, with synchronization signals exchanged between RUs to ensure alignment. Through the feedback mechanism of the backhaul, the system can continuously monitor and adjust synchronization parameters, detecting and correcting timing or frequency drift issues in real time. In dynamic mobile scenarios, the system can adapt beamforming and power allocation based on UE position changes and environmental interference, ensuring optimal signal strength even as devices move.

Synchronization and calibration are essential for the accuracy and efficiency of the system, ensuring reliable performance across all components. The SDR 6004-based CF-mMIMO system will integrate backhaul and UHD interfaces for achieving system-wide synchronization and leverages advanced calibration techniques to maintain precision.

4.2.2.2.1 Synchronization

1. Frequency Synchronization: The system employs a 10 MHz reference signal, generated by a high-precision clock source, to ensure frequency stability across all devices. This reference signal prevents frequency drift, critical for maintaining synchronization between the central CPU, RUs, and UEs. The UHD interface ensures that all RF components operate on a consistent frequency standard.

2. Time Synchronization: A PPS signal ensures precise timing alignment across components. The system uses the backhaul network to distribute SSs, maintaining unified timing across the CPU, RUs, and UEs. The UHD interface manages time synchronization, periodically re-aligning time references to eliminate timing discrepancies.

3. Cross-Link Synchronization: Synchronization between the central CPU and remote RUs is achieved through a distributed architecture, where SSs are exchanged between RUs. The backhaul feedback mechanism allows for real-time monitoring and dynamic adjustment of synchronization parameters, correcting timing or frequency drifts as they arise.

4. Signal Stream Alignment: The system ensures that multiple USRP devices transmit and receive signals simultaneously. This is accomplished through synchronized triggering mechanisms that enhance the temporal precision of signal transmission and reception, enabling seamless multi-device operations in joint channel estimation and beamforming.

4.2.2.2.2 Calibration

1. RF and Digital Calibration: To minimize distortions and quantization errors, the system employs RF calibration to align the RF chains and digital calibration for ADC/DAC components. These processes improve the reliability and precision of signal transmission and reception.

2. LO Phase Alignment: The LOs in USRPs may have random phase offsets, which can impact experimental results. Calibration ensures that LOs are aligned to minimize relative phase offsets. During signal processing, training sequences are used to estimate and compensate for these offsets, achieving phase coherence across devices.

3. Long-Term Frequency and Time Maintenance: Over time, environmental factors such as temperature changes can lead to slight deviations in frequency and timing. The system addresses these issues by periodically re-locking the 10 MHz and PPS signals, ensuring long-term stability.

4. Dynamic Calibration in Mobile Scenarios: In dynamic scenarios with moving UEs, the system recalibrates beamforming and power allocation in real time, adjusting to changes in UE positions and environmental interference. This ensures optimal signal strength and communication quality.

The system extensively utilizes the backhaul network for synchronization and calibration. SSs, including the 10 MHz reference and PPS, are distributed to all components via the backhaul. Calibration parameters are continuously monitored and adjusted through the backhaul, enabling real-time corrections based on system feedback. This robust mechanism allows the system to detect and correct timing or frequency issues dynamically, ensuring consistent performance in both static and mobile environments.

By leveraging backhaul capabilities, the SDR 6004-based system achieves enhanced synchronization and calibration, enabling scalable and efficient operations for advanced wireless communication research.

4.2.2.3 Target implementation

Using the IAF Prototyping System in Figure 4-11, we have illustrated in Figure 4-13 the envisioned CF-mMIMO testbed that will be built in the context of 6G-SENSES. The system incorporates a single **central CPU** for joint processing and **two RUs** connected via high-speed fronthaul/Ethernet links to the central CPU. These two RUs enable communication with two UEs, facilitating flexible and dynamic connections across the system. The CPU handles joint processing tasks such as channel estimation, signal processing, and network resource management, ensuring high throughput and low latency. Each UE is connected to a separate CPU, allowing for efficient management and synchronization across the network, optimizing resource allocation and performance.

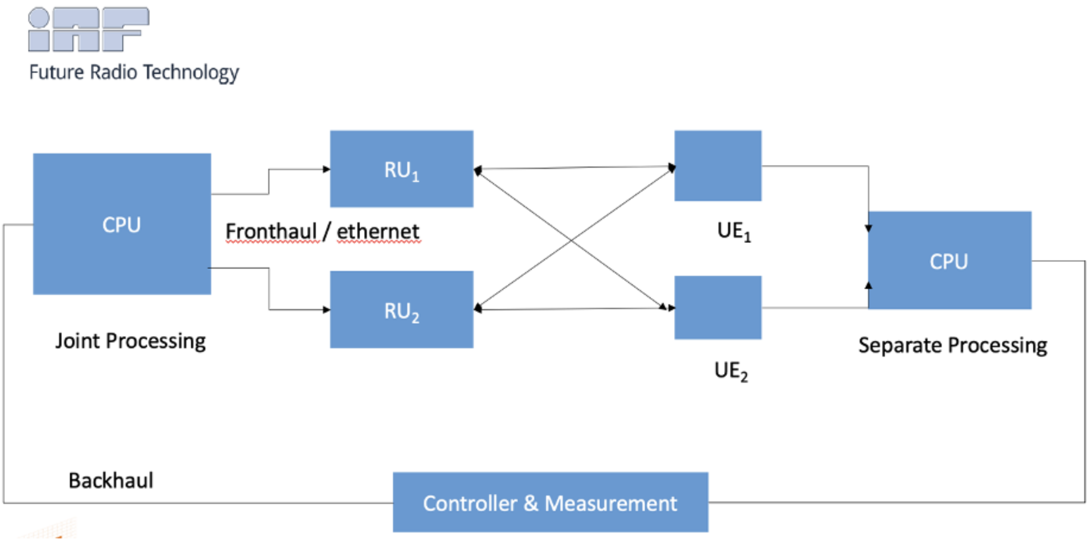

Figure 4-13 SDR 6004-based CF-mMIMO Setup

The network-layer demonstrator in Figure 4-14 features an IAF-based 2x2 system, aiming to improve rate splitting for efficient fronthaul balancing. This system will support beamforming techniques selected from the options tested with the NI-based system and will integrate them within a 5G stack, to streamline communication and optimize network performance. The demonstrator showcases the impact of constraints on the fronthaul links on the achievable performance for internet traffic.

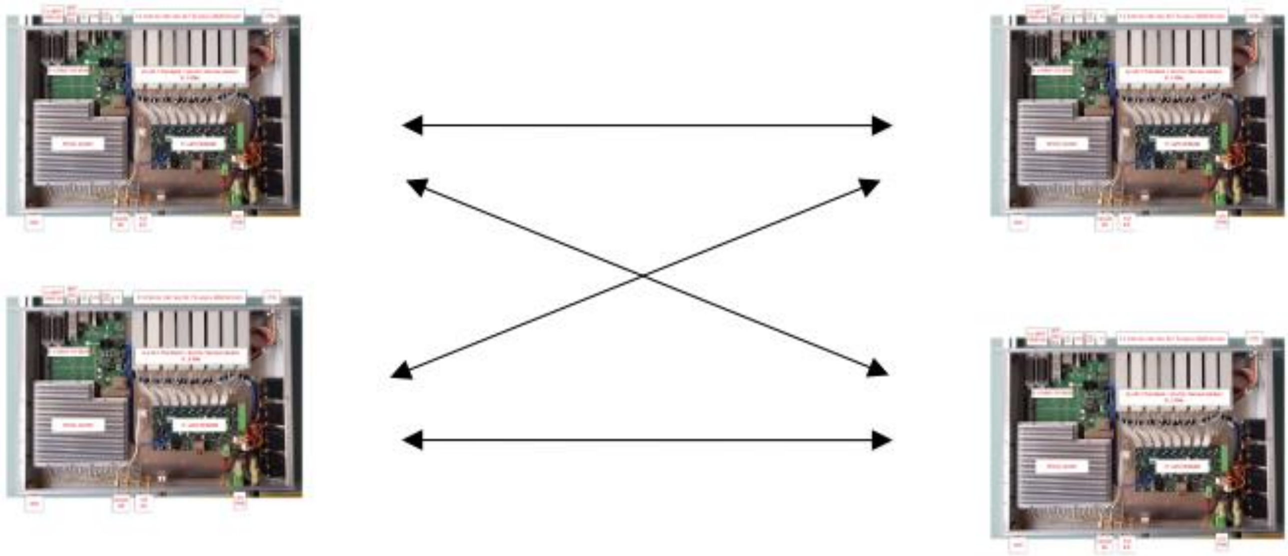

Figure 4-14 Network-layer small-scale demonstrator

4.3 6G-SENSES CF-mMIMO target implementations

This section presents different techniques and implementations that have the potential to be running onto the CF-mMIMO testbeds. The following ones have been identified so far, each of them targeting different TRLs, given the implications and applicability to small-scale CF-mMIMO networks.

The provision of these functionalities on top of any of the CF-mMIMO testbeds will be fully described in deliverable D3.2 that, ultimately, will lead to the delivery of a 6G CF-mMIMO PHY prototype that will be extended to support real-time control loop assessment in the context of PoC#2. The plan towards this objective will be delineated in deliverable D5.1.

This section begins by outlining the O-RAN architecture and its influence on next-generation multiple-access strategies. It then explores three emerging architectural paradigms that have garnered significant attention in the research community: CF or distributed antenna systems, unsourced massive random access, and their potential integration. The choice of multiple access technique on the PHY and MAC layers has a tremendous impact on the overall network architecture. This impact is illustrated by a simple anecdotal example which is also one target for the implementation in the two NI-based and IAF-based prototypes outlined in the last sections.

4.3.1 Design and optimization of multiple access techniques in modern architectures

With the ongoing shift toward a disaggregated RAN enabled by open interfaces (O-RAN), the MAC layer is now decoupled from lower PHY layer functions. This evolution necessitates a fresh examination of the interfaces in this modular architecture to effectively design and optimize multiple access techniques.

4.3.1.1 O-RAN

The O-RAN architecture simplifies and democratises the development and operation of mobile networks. The open, standardised interfaces between devices and units, and the flexibility offered, allow different vendors and suppliers to participate and provide solutions. This leads to more competition, faster development cycles, greater diversity and avoids monopolies or oligopolies.

O-RAN deployments are based on disaggregated, virtualised and SW-based components that are connected through open and standardised interfaces and are interoperable across different vendors [116]. SDN and NFV on the one hand, ML and AI on the mobile edge cloud on the other hand, via cloud RAN architectures, led to the idea of disaggregating BS into RU, DU and one or more CUs. Figure 4-15 shows an overview of the basic building blocks of the O-RAN architecture, where the CU provides RRC, PDCP, and SDAP; the DU supports

RLC, MAC, and the higher part of the PHY layer; and the RU implements lower PHY layer functions, such as frequency-domain functions, including scrambling, modulation, mapping, part of the precoding, and time-domain functions, including precoding, FFT with CP handling, spatial processing, and the RF chain (adapted from [116], Fig. 2).

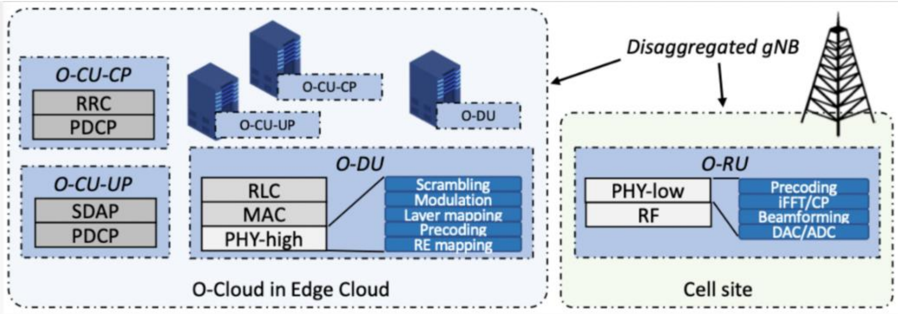

Figure 4-15 Open RAN building blocks according to functional split 7.2

Another innovation in the O-RAN standard is the two so-called RICs, which manage network parameters and configurations in near-RT (10 ms – 1 s) and non-RT (more than 1 s) time scales. The O-RAN architecture defines interfaces between the different units and between the two RICs, which complement the 3GPP interfaces. For a complete overview of O-RAN, the interested reader is referred to [117].

The O-RAN architecture has important implications, as the multiple access scheme affects all three disaggregated units: 1) the RU, where the interference is generated and handled, e.g., via beamforming; 2) the DU, where access control, resource allocation, and scheduling are performed; and 3) the CU, where decisions on the configuration of the MAC protocol are made.

Furthermore, the O-RAN architecture impacts also the communication theoretic modeling of the multiple access network. This is shown in Figure 4-16, where the wireless access MAC, BC, and IC are supplemented with the fronthaul links between DU and RUs. In Figure 4-16, the midhaul links between DU and CU are shown (the backhaul links from the CU to the core network are not shown).

We denote the wireless channel RUi to UEj by hij. We collect all wireless channel gains in the matrix H. The midhaul rate constraints are denoted by c1 and c2. The fronthaul rates from DUk to RUi are denoted by dki.

Based on the example O-RAN architecture is shown in Figure 4-16, the entire network configuration, including midhaul, fronthaul, and wireless multiple access, is considered. While the links may have different characteristics in terms of data rate, reliability, latency, and EE depending on their link technologies, e.g., fiber, copper, and wireless, the overall network throughput between source (CU) and DL destinations (users) can be computed by the cutset bound for graphical unicast networks ([118], Sec. 15.2).

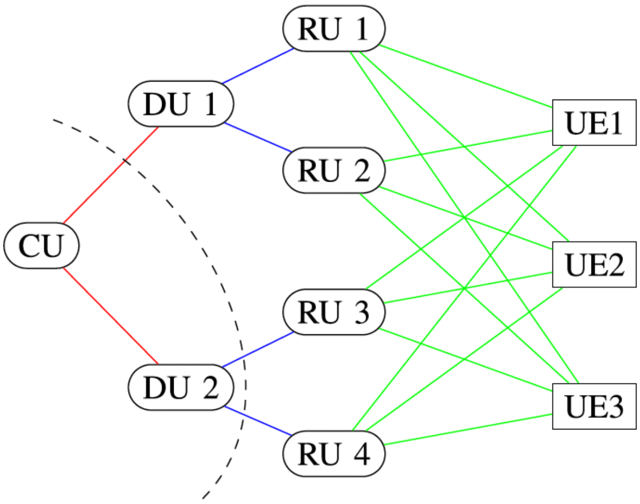

Figure 4-16 O-RAN architecture with midhaul (red), fronthaul (blue), and wireless access (green) links

Variable	Link	Rate
c_1	midhaul $CU - DU_1$	1.3 Gbit/s
c_2	midhaul $CU - DU_2$	1.5 Gbit/s
d_{11}	fronthaul $DU_1 - RU_1$	700 MBit/s
d_{12}	fronthaul $DU_1 - RU_2$	800 MBit/s
d_{23}	fronthaul $DU_2 - RU_3$	600 Mbit/s
d_{24}	fronthaul $DU_2 - RU_4$	500 Mbit/s

Figure 4-17 Example Parameters for Link Capacities in the Open RAN Architecture from Figure 4-16

To illustrate the different schemes, let us assume the following configuration as shown in Figure 4-17, where we focus on data rates and rate constraints.

1. **Cutset Bound for Graphical Unicast Networks**:

   To apply the cutset bound, the open RAN graph shown in Figure 4-16, with nodes (CU, DUs, and RUs) and corresponding edges will be assigned a link capacity for each edge, e.g., the midhaul link from CU to DU1 has capacity $C_{c,d1} = 100$ GBit/s. Then, the cutset bound ([118], Th. 15.2), has the capacity to the destination node UE1 is given by[7]

$$C_1 = \min_{\substack{\mathcal{S} \subset \mathcal{N} \\ CU \in \mathcal{S}, \mathrm{UE1} \in \mathcal{S}^c}} C(\mathcal{S}) \tag{4-1}$$

   where $\mathcal{N}$ is the set of nodes, and the capacity of the cut $\mathcal{S}$ is given as

$$C(\mathcal{S}) = \sum_{\substack{(k,l) \in \mathcal{E} \\ k \in \mathcal{S}, l \in \mathcal{S}^c}} C_{kl} \tag{4-2}$$

   where $\mathcal{E}$ is the set of all edges. The result is also called min-cut max-flow theorem. The capacity can be computed for different network architectures and it can also be combined with the capacity and

[7] The function C(S) is the Shannon capacity formula C(S) = log(1 + S).

achievable rate regions explained in ([122], Section II) and the MAC schemes in ([122], Section IV). For the example values in Figure 4-17, the maximum sum rate for the midhaul and fronthaul is upper bounded by the cut illustrated in Figure 4-15 as the dashed line. The maximum flow value for the cut is given by 1300 + 600 + 500 =2400 Mbit/s.

2. **Classical Orthogonal Multiple Access (OMA)**:

   Suppose that we use the classic orthogonal MAC schemes, where a user is served by only one RU on orthogonal resources only. Then, we need an assignment of users to RUs. In the simple example in Figure 4-16, we consider the canonical assignment of $RU_i \leftrightarrow UE_i$, i = 1, 2, 3.

   Then, the resulting graph degenerates to a tree with the source CU and the three leaves UE_1–UE_3 and the unassigned RU. For the anecdotal example, we assume that the channel matrix, $\boldsymbol{H}$, which describes the channel from RUs to the users, is given as follows:

$$H = \begin{bmatrix} 10 & 8 & 2 \\ 9 & 10 & 4 \\ 3 & 9 & 9 \\ 1 & 7 & 10 \end{bmatrix} \tag{4-3}$$

   Note that these channel gains can include the contributions of multiple antennas at the RUs. Then, the channel gain is computed as in the SINR expression in ([122], Eq. (38)) as $h_{ij} = \left|h_j^{\boldsymbol{H}} v_i\right|^2$.

   For the wireless links, we further assume for simplicity that the transmit SNR is 10 dB and the total bandwidth is B = 300 MHz. For OFDMA, this given W = 100 MHz for each user. For the orthogonal wireless link from RU1 to UE1, this gives the P2P capacity in ([122], Eq. (1)) calculated as

$$\mathrm{C}_{11} = \mathrm{W}\log_2(1 + 10 \cdot 10) = 692 \;\; \mathrm{Mbit/s}.$$

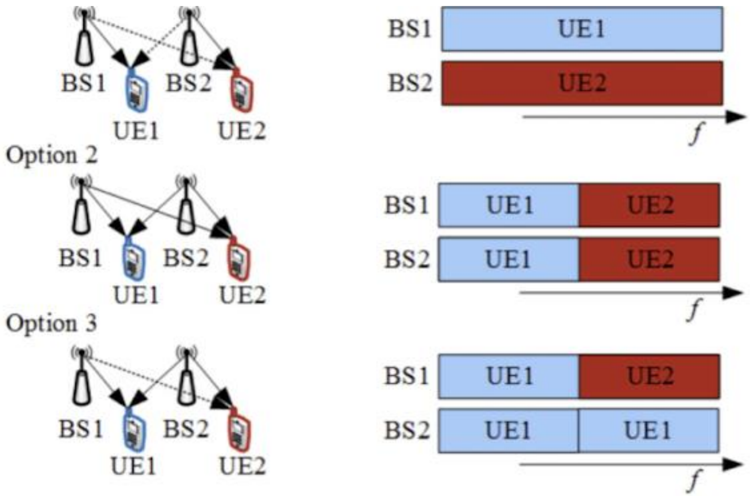

Figure 4-18 Connectivity options in a two BSs and two user's scenario. Solid lines are desired links and dashed lines represent the non-desired, interfering links (adapted from [124]).

Similarly, we compute the other two rates C_{22} =692 Mbit/s and C_{33} = 651 Mbit/s. The rate limits $\mathrm{r}_1, \mathrm{r}_2, \mathrm{r}_3$ for the three users are computed as follows:

$$\begin{gathered} \mathrm{r}_1 \leq \mathrm{C}_{11},\ \mathrm{r}_2 \leq \mathrm{C}_{22},\ \mathrm{r}_3 \leq \mathrm{C}_{33} \\ \mathrm{r}_1 \leq \mathrm{d}_{11},\ \mathrm{r}_2 \leq \mathrm{d}_{12}, \mathrm{r}_3 \leq \mathrm{d}_{23} \\ \mathrm{d}_{11} + \mathrm{d}_{12} \leq \mathrm{c}_1,\ \mathrm{d}_{23} \leq \mathrm{c}_2 \end{gathered} \tag{4-4}$$

The inequalities in (4-4) are linear in the rates and can be easily checked via linear programming. In the anecdotal example, the three users are limited by $r_1 + r_2 \leq 1300$ Mbit/s and $r_3 \leq d_{23} = 600$ Mbit/s. In total, a sum rate of 1900 Mbit/s is achievable. Compared to the upper bound from ([122], Section V-A1) there are 500 MBit/s left for improvements.

Note that in this example, we are only interested in the achievable rate and neglect both latencies and energy consumption. Furthermore, we assume homogeneous services for the three users. In a complete system design, the E2E performance for heterogeneous users can be optimized using network slicing [123]. The ML-based resource allocation under uncertainty is able to solve the corresponding nonconvex mixed-integer nonlinear programming problem.

To improve the data rates of users 1 and 2, the orthogonal resource allocation should be improved and NOMA schemes should be applied as it is discussed in ([122], Section IV).

One approach to remove the limitation of user 3 from the fronthaul constraint d_{23} would be to let the user connect to multiple RUs, in this case, RU3 and RU4. The same approach can be useful for users 1 and 2 who share the spectrum in an orthogonal way. In the case of two connections, this scheme is called dual connectivity, while for more connections, it is called multi-connectivity.

4.3.1.2 Cloud-RAN

Another special case of the O-RAN architecture in Figure 4-16 is the C-RAN, where all RUs are directly connected to a CU that centrally operates and controls all parameters [125], resource allocation and PHY optimization. The main idea behind C-RAN is to combine the BBUs of several BSs into a centralized BBU pool for statistical multiplexing gain while shifting the burden to high-speed wired transmission of IQ data [158]. The idea of moving the necessary transmission and processing resources for a wireless access network to the cloud has already been formulated in [127].

In this case, the midhaul link capacities in Figure 4-16 would be set to infinity. This makes the entire network act as a massive distributed antenna system covering the entire network coverage area. This case was illustrated in Figure 4-19, where all BSs transmit together to serve the users. From an information-theoretic point of view, the downlink would correspond to a two-hop or BC, while the uplink is the two- hop MAC. The two-hop comes from the transmission from the CU to the RUs.

The achievable rates can be calculated based on the fundamental limits from ([122], Section II) and constrained by the fronthaul rate limits. Since all RUs serve all users, they require the data for all users sent over the fronthaul links. The total sum data rate is limited by min(d_{ij}) overall i, j. This shows that this network architecture requires significant computing and processing power from the CU, including very high data links for the fronthaul, especially with the massive increase in the number of UEs per unit area in beyond 5G/6G networks.

In the heterogeneous C-RAN, a combination of distributed RUs controlled by the CU and macro BC is used. The offloading of macrocell users to the C-RAN and efficient resource allocation is discussed in [129]. The coexistence between macro-BS and C-RAN can be modelled by cognitive radio approaches where LSA is negotiated between primary and secondary users [130].

The combination of RS and C-RAN is studied in [131] and [132]. Statistical CSI at the transmitter is considered and the problem of stochastic coordinated beamforming for ergodic sum-rate maximization is proposed and solved. A gain of up to 27% of RS over TIN and NOMA is reported.

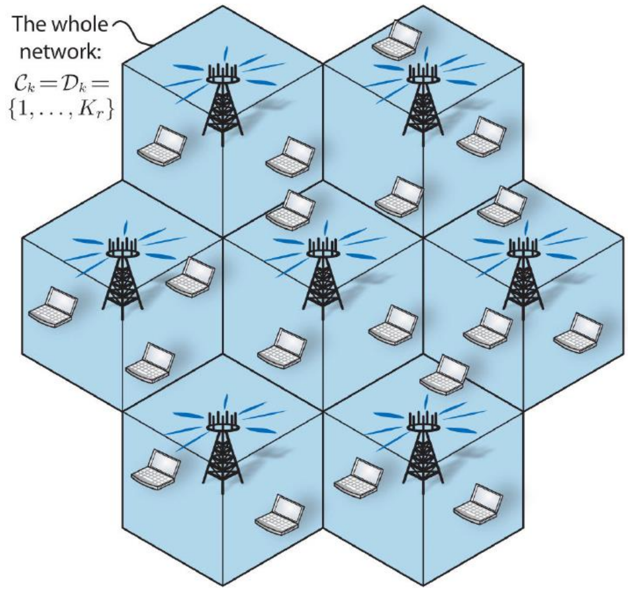

Figure 4-19 Illustration of the JT scenario, where all cells and cell sectors are connected and perform JT to all users in the whole network (adapted from [157]).

4.3.1.3 Cell-Free Multiple Access (CFMA)

The CFMA network architecture is a user-centric design. Each user connects to a number of RUs required to obtain the service. This is a departure from the network-centric design of all the schemes discussed above. The RUs serving a user form a cooperation cluster for that particular user. One of the first references to CFMA with massive numbers of RUs is [136].

The three clusters in Figure 4-20 can be interpreted as three distributed antenna systems or three multiple-antenna cells serving the three users. Depending on the functional split chosen, part of the signal processing is performed at the RUs, and part is performed at the DUs or the CU [134].

The main challenge is to achieve the benefits of cell-free operation practically, with computational complexity and fronthaul requirements that are scalable to enable massively large networks with many mobile devices [135]. The monograph [135] describes the SotA signal processing algorithms for channel estimation, uplink data reception, and downlink data transmission with either centralized or distributed implementation.

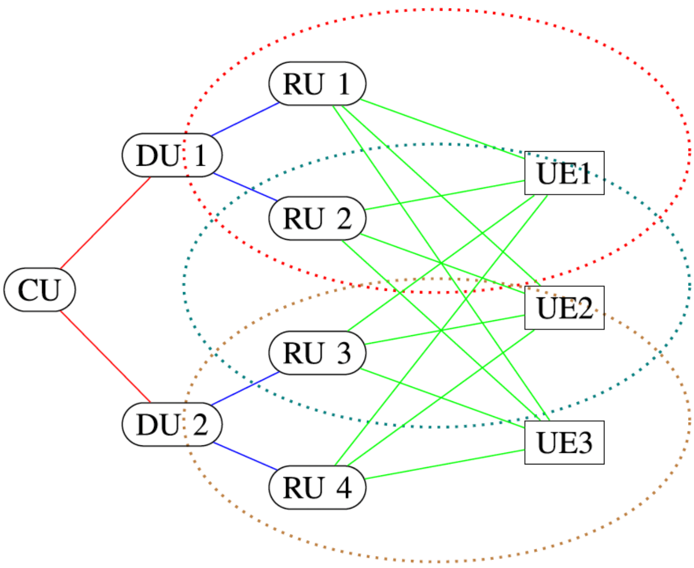

Figure 4-20 Open RAN architecture with CF configuration and user clusters

Let us first concentrate on one user, e.g., user 1, and its corresponding cluster, i.e., RU_1 and RU_2 (red dashed ellipsoid in Figure 4-20). Let us denote the channel coefficients as h_{11} and h_{21}, which are complex numbers with attenuation(amplitudes) and delay (phases). This looks like a MISO channel with two transmit antennas and one receive antenna. With perfect CSI at the transmitter and with a sum power constraint P = 2, the optimal beamforming strategy is MRT and the resulting effective channel is $h_{12}^{mrt} = |h_{11}|^2 + |h_{21}|^2$. Usually, each RU has its own power constraint P = 1. Then, the optimal beamforming strategy is to adjust the phase of the two signals arriving at the user (similar to equal gain transmission) and obtain the effective channel $h_{12}^{egt} = 1/2 \cdot (|h_{11}| + |h_{21}|)^2$. In the literature, this is also called coherent beamforming or joint beamforming. Without accurate phase information at the two RUs, noncoherent beamforming can be applied, which achieves an effective channel $h_{12}^{nch} = 1/2 \cdot (|h_{11}|^2 + |h_{21}|^2)$. Clearly, $h_{12}^{mrt} \geq h_{12}^{egt} \geq h_{12}^{nch}$, where equality is achieved for the first inequality with $|h_1| = |h_2|$ and for the second inequality if at least one channel is zero. For our example channel matrix H, we have the following inequalities for the three transmission schemes: 19 ≥ 18.99 ≥ 8.5. This shows clearly that coherent beamforming achieves a significant gain in terms of received signal power because the channels to user 1 have similar gains.

The DL SINR in [64, Eq. (38)] can be specialized to the example. The SINR expression for user 1, including power control and interference (teal and brown dashed clusters in Figure 4-20) from the other users' codewords, is given by $\mathrm{SINR}_1 = \frac{(|h_1|\sqrt{p_{11}}+|h_2|\sqrt{p_{21}})^2}{\sigma^2+|h_{21}|^2 p_{22}+|h_{31}|^2(p_{32}+p_{33})+|h_{41}|^2 p_{43}}$.

Similar expressions for the SINRs of the other users can be derived from the power allocation. Next, various power control problems can be formulated, including min–max power control [133], [136], sum-rate maximization [137], EE maximization [128], and power minimization under rate constraints [139]. There are also results on power control under fronthaul and midhaul constraints. There are also differentiated results for uplink and downlink operation and for the pilot signal phase.

The combination of RS at the RUs to improve the achievable data rates of the wireless network is performed in [140] for specific beamformers and in terms of sum rate. In [141], max–min power control for RS in cell-free MIMO is performed. Robustness against pilot contamination is reported. Finally, Zheng et al. [142] report on asynchronous cell-free massive MIMO with RS and its robustness to HWIs.

In the case of multiple-antenna RUs, there are several proposals for beamforming optimization. Let us denote the local channels at the multiple-antenna RU by $h_1, \ldots, h_L$ for L users. The conjugate beamformer is then given $w_k = h_k^*$ [136]. Variants include extended normalized conjugate beamforming $w_k = h_k^* ||h_k^*||$ [143], modified conjugate beamforming [144], local partial ZF precoding [145], and team MMSE precoding [146].

Note that we have not discussed the challenges associated to obtaining the CSI at the transmitter. This is usually achieved by TDD operation and exploitation of channel reciprocity. The interested reader is referred to the monograph [135].

As we have seen in our anecdotal example in ([122], Section V-A2), an optimal design must consider the constraints and limitations of both midhaul, fronthaul, and wireless access. In [147], joint fronthaul load balancing and compute resource allocation are performed. We follow a slightly different approach for simplicity. For a holistic design, fronthaul constraints could be modeled by simple rate constraints, as explained in ([122], Section V-A2). Let us conclude the anecdotal example with a combination of OFDMA, CFMA, and RS. We allocate 100 MHz to each user (OFDMA), assign users according to the clusters shown in Figure 4-20, and perform RS for all three users. (Note that we could also optimize powers and rates. Initial results are reported in [148].)

1) Cluster user 1 (decoding order):

First, codewords received from RU2 are decoded and then subtracted, then, codewords received from RU1[8] are decoded, i.e.,

$$R_{21} = W \cdot C\left(\frac{10 \cdot 9}{1 + 10 \cdot 10}\right) = 92 \text{ Mbit/s}$$

$$R_{11} = W \cdot C(100) = 666\text{Mbit/s}$$

$$\underline{R_1 = 666 + 92 = 758\text{Mbit/s}}$$

2) Cluster user 2: The sum rate is directly computed as

$$R_2 = R_{22} + R_{32} = W \cdot C(100 + 90) = 758 \text{ Mbit/s},$$

and by using time-sharing (TS), the rate can be split between the two decoding orders, as shown in Figure 4-21. The total rate for both RUs is divided equally into 379 Mb/s each.

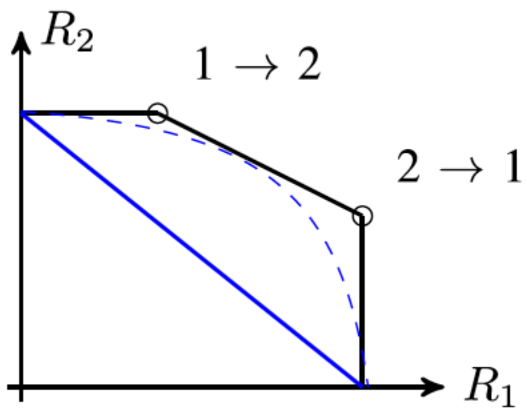

Figure 4-21 Achievable rate region for the two-user MAC with AWGN. The two circles indicate the achievable rate pairs with the two decoding orders. The line between the two circles is achieved by time sharing (TS) [64]

3) Cluster user 3 (decoding order):

First, codewords received from RU3 followed by codewords from RU4. Note also that the fronthaul between DU2 and RU4 is limited to 500 Mbit/s. Therefore, the power required for RU4 can be reduced to achieve exactly the maximum of 500 Mb/s, which is $SNR_4 = 3.1$.

4) Fronthaul constraints:

$R_{11} = 666 \leq 700 = d_{11}$, $R_{21} + R_{22} = 92 + 379 = 471 < 800 = d12$, $R_{32} + R_{33} = 379 + 193 = 572 < d_{23}$, R43 = 500 = d_{34}, and the midhaul constraints: 666 + 471 = 1137 < c_1 and 572 + 500 = 1072 < 1500.

The total sum rate achieved is 2209 Mbit/s, which is much closer to the upper limit of 2400 Mbit/s than the baseline scheme with single-user allocations and OFDMA, which achieved 1900 Mbit/s. This is an improvement of over 300 Mbit/s.

The data rate computations for the example network show that a joint design of midhaul, fronthaul, and wireless access can improve the data rates in the system significantly. The theoretical rate gains will be demonstrated for corresponding network scenarios on the NI-based and/or IAF-based systems.

[8] We use C(x) = log2(1 + x) to denote the capacity function.

While we have focused on the achievable data rate region, another critical and relevant KPI is the EE and energy consumption of the network. The next section describes the system available for energy consumption measurement in the distributed MIMO setup.

4.3.2 Energy consumption evaluation in a MIMO system

In this study, a a 2x2 MIMO communication system was implemented using NI USRPs to assess the energy consumption under different modulation schemes and transmission frequencies. These tunable transceivers support the development and deployment of communication systems, with antennas capable of operating up to 6 GHz. The real-time MIMO setup is managed through NI's LabVIEW SW toolkits, which provide a user-friendly graphical user interface (GUI) for designing, implementing, and evaluating real-world scenarios. This flexible and scalable setup enables rapid prototyping and testing of advanced communication algorithms, bridging the gap between theoretical designs and practical deployment.

To simulate these scenarios, the setup utilizes four USRPs, an OctoClock-G CDA-2990 clock distribution device, and two types of omni-directional vertical antennas. Specifically, the USRPs selected are Ettus Research B210s, configured as transceivers. As each device cannot simultaneously transmit and receive, two USRPs are configured as transmitters and two as receivers. This separation of functionality ensures reliable and efficient transmission and reception without interference. The antennas used are selected based on the operating frequency of the MIMO system: four VERT900 antennas, operating in the 824-960 MHz and 1710-1990 MHz ranges, and four omni-directional antennas operating between 3.3-3.8 GHz.

The antennas are connected to the transmit (Tx) or receive (Rx) ports of the USRP B210s, depending on their role as transmitters or receivers. For ease of operation, all USRPs are configured with VERT900 antennas on channel 2 Tx/Rx and the higher frequency antennas on channel 1 RF Tx/Rx. This standardized configuration simplifies switching between frequencies and enhances the flexibility and adaptability of the system, making it particularly well-suited for multi-frequency experimental setups.

To ensure precise multi-device synchronization across the four USRPs, we utilize an OctoClock-G CDA-2990 device, that accepts both an external 10 MHz reference clock and a PPS input signal and then amplifies and distributes each to eight output ports. This setup ensures that all modules are synchronized to a common timing source, enabling seamless coordination between the devices.

4.3.2.1 System setup

Figure 4-22 and Figure 4-23 illustrate the complete experimental setup for the 2x2 MIMO system. In this configuration, the two transceivers positioned at the top are designated as transmitters, while the two at the bottom serve as receivers. All four USRP B210 devices are connected to a host PC running LabVIEW via USB 3.0. From the rear view of the HW configuration, the synchronization connections are clearly visible: the 10 MHz reference clock (on the left side of the image) and the PPS input signal (on the right side) are being fed directly from the OctoClock-G to the USRPs via coaxial cables. This arrangement ensures the required synchronization for high-performance MIMO experimentation.

The described HW setup is fully supported and managed by the NI LabVIEW SW platform, which provides a comprehensive suite of toolkits tailored for advanced communication system development. Among these, the LabVIEW Modulation Toolkit enables implementation of various modulation schemes, such as QAM, AM, FM, PM, ASK, FSK, and PSK, for both signal modulation and demodulation. In addition to modulation capabilities, the toolkit offers robust functions for analyzing and processing analog and digital signals, validating signal quality through metrics like frequency error and Bit Error Rate (BER), and visualizing signal behavior through tools such as constellation plots and eye diagrams. These features ensure comprehensive evaluation and fine-tuning of the communication system, making it suitable for high-precision applications.

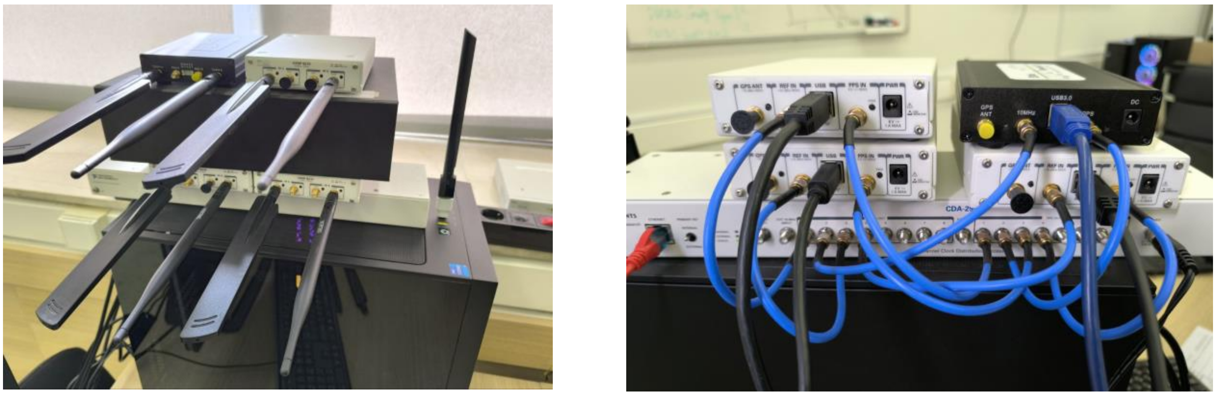

Figure 4-22 USRP-based 2x2 MIMO testbed (Front view), USRP-based 2x2 MIMO testbed (Rear view)

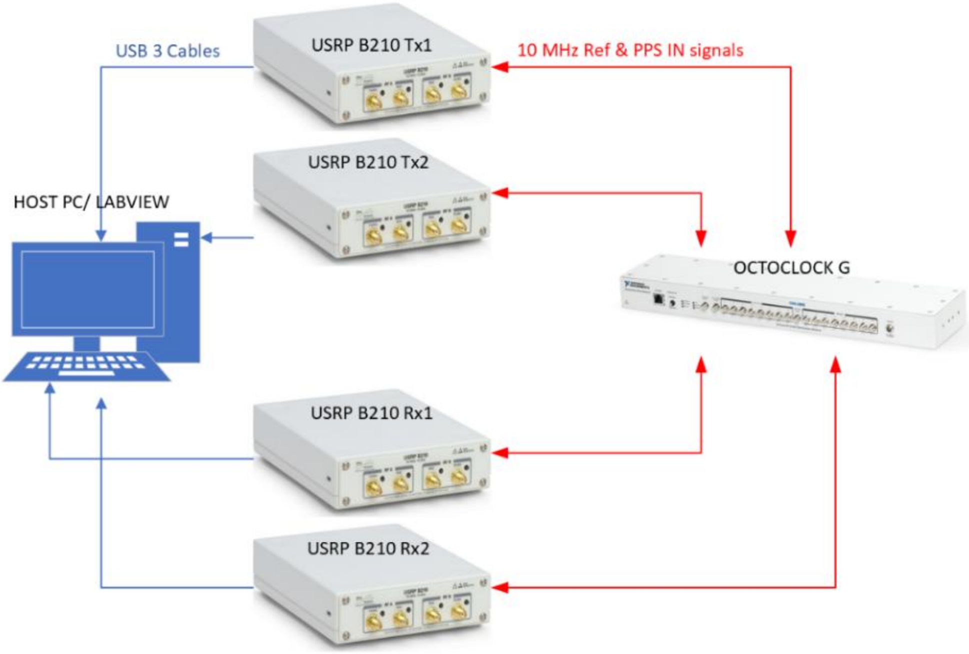

Figure 4-23 Ettus USRP-based 2x2 MIMO setup

LabVIEW provides a graphical programming environment based on Virtual Instruments (VIs), which represent modular HW or SW components. These VIs are interconnected to create intuitive data flow diagrams, enabling efficient signal processing, modulation, and other tasks. LabVIEW uses dataflow programming, allowing parallel execution and real-time monitoring through visual tools like graphs and charts. Its seamless integration with HW supports real-time testing and debugging, making it ideal for rapid prototyping in fields such as communication systems and industrial applications. This flexibility significantly reduces development time by enabling quick adjustments and iterative testing.

4.3.2.2 Test Results

To construct a reliable and accurate dataset, it is crucial to prevent system underflows or overflows. To achieve this, we strictly adhere to defined boundaries, such as selecting appropriate symbol rates and determining the correct number of symbols per packet. This ensures that the system operates within optimal limits and generates consistent data. The performance of our MIMO system is evaluated using several metrics, including BER, constellation diagrams, and the data extracted from the receivers across a wide range of frequencies. These parameters provide a comprehensive assessment of the performance of the system under various conditions. For this experiment, the following key parameters are utilized to acquire real-time results and assess system performance.

Table 4-2 System Parameters

Parameters	Transmitter	Receiver
Carrier frequency (Hz)	900 MHz 1850 MHz 3.5 GHz	
Active Antenna	Tx/Rx (RF Ch A)	Tx/Rx (RF Ch B)
Symbol Rate	1-2 MSPS	
Modulation Scheme	4QAM, 16QAM	
Ref Freq source	10 MHz	
Timebase clock source	1 PPS	
Symbols per packet	3000	

The first two images presented in Figure 4-24 illustrate the waveforms that confirm the successful reconstruction of transmitted signals. Specifically, the upper plot displays the received time-domain signal samples for the IQ components of the signals received by both antennas. The constellation plots in the bottom left illustrate the signals received by the two receive (Rx) NI USRP transceivers. Finally, the last plot demonstrates the reconstructed constellation plot after applying Alamouti decoding, MRC, and channel equalization, which ensure that the signals are accurately recovered, even in the presence of noise or fading.

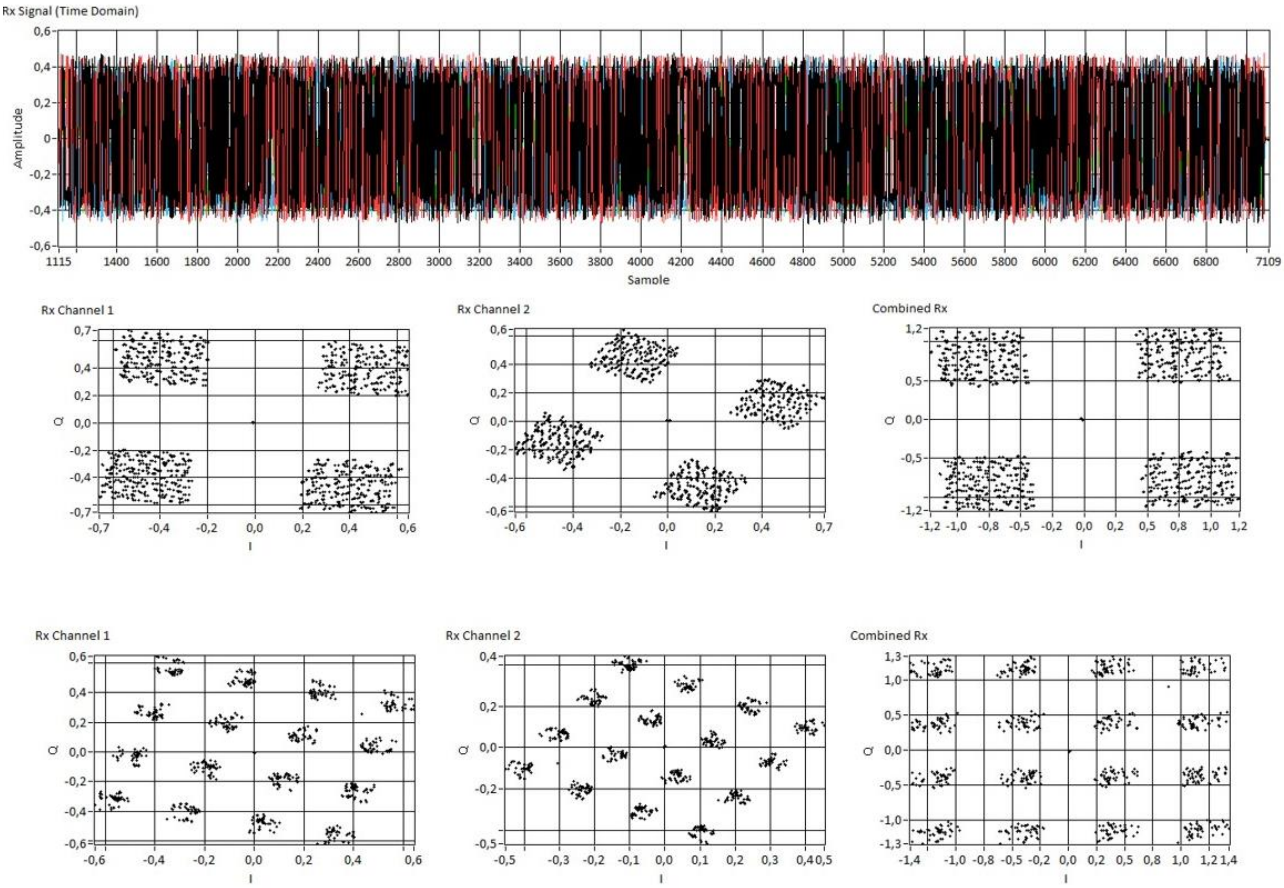

Figure 4-24 Signal received from both antennas and the corresponding constellation diagrams – 4QAM & 16QAM

Our study examines the energy consumption characteristics of a MIMO system tested under varying modulation schemes and transmission frequencies, offering critical insights that can influence the design of future 6G communication systems. The primary focus of the study was to quantify the minimum energy required to ensure **error-free transmission** of packets containing 3000 symbols. The findings reveal how these measurements could guide the development of energy-efficient configurations for next-generation wireless networks, where the balance between energy consumption and system performance will play a pivotal role in achieving sustainability goals.

The experiments were conducted using a range of modulation schemes, including 4-QAM and 16-QAM across various transmission frequencies. For each configuration, energy consumption was systematically measured while ensuring error-free transmission. System parameters (such as gain) were adjusted to optimize performance and reduce energy usage. This methodology enabled a detailed evaluation of how both modulation complexity and operating frequency affect the energy profile of the system.

Figure 4-25 illustrates the energy consumption per bit (in picojoules) as a function of transmission frequency (GHz) for two modulation schemes: 4-QAM and 16-QAM. The results indicate that as the frequency increases, the energy consumption per bit grows significantly for both modulation schemes. 4-QAM exhibits lower energy consumption compared to 16-QAM. For example, at 900 MHz, 16-QAM requires 9.559 pJ/bit, while 4-QAM consumes slightly less energy. As the frequency increases, this trend continues, with 16-QAM showing a steeper energy consumption curve. For example, at 3.5 GHz, 16-QAM reaches an energy consumption of 3668.262 pJ/bit, compared to 1904.526 pJ/bit for 4-QAM.

This behavior can be attributed to the higher complexity of 16-QAM, which requires more precise signal processing and is more sensitive to noise, especially at higher frequencies. Consequently, 16-QAM demands significantly more energy to maintain error-free transmission at these higher frequencies. In contrast, 4-QAM, being a simpler scheme, remains relatively more energy-efficient across the frequency range. Transmission frequency also played a crucial role, with lower frequencies requiring less energy for error-free communication due to superior propagation characteristics. In contrast, higher frequencies demanded significantly more power, attributed to increased path loss and HW limitations, even though they provide access to larger bandwidths.

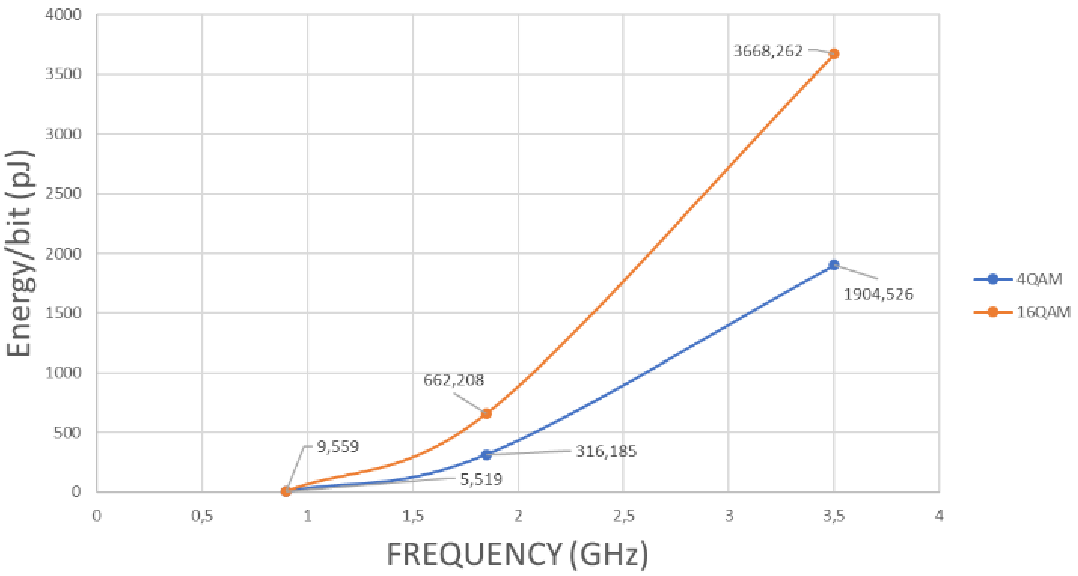

Figure 4-25 Energy per bit for each frequency and modulation scheme

These results have profound implications for the design of 6G networks, particularly in addressing the trade-offs between performance, EE, and system adaptability. One of the most promising applications is the dynamic configuration of modulation schemes and transmission frequencies. For instance, a system could employ adaptive resource management techniques, selectively utilizing higher frequencies and complex modulation schemes in scenarios demanding high data rates, such as autonomous vehicle networks, while reserving energy-efficient settings for low-data-rate applications like environmental monitoring. This flexibility becomes even more critical when scaling to massive MIMO systems, where the simultaneous management of numerous transmission paths further amplifies the importance of energy-efficient design. This approach ensures optimal resource utilization tailored to diverse operational needs, while maintaining system sustainability and reliability.

Additionally, these insights could support the development of AI-driven energy optimization frameworks for 6G systems. By leveraging ML algorithms, future networks could predict and implement the most energy-efficient transmission settings based on current conditions, traffic demands, and application requirements. This capability would not only enhance the sustainability of communication systems but also enable seamless operation in environments where energy availability is limited or highly variable.

Another key area of application lies in the design of hybrid systems that combine multiple modulation schemes and frequency bands, optimizing energy use across diverse communication scenarios. For instance, a hybrid strategy could use high-order modulation and higher frequencies for high-throughput applications in urban areas, while defaulting to simpler schemes and lower frequencies for rural or energy-sensitive deployments. Such flexibility would make 6G networks highly adaptable, supporting a wide array of use cases with tailored energy-performance trade-offs.

While this study primarily focused on energy measurements under controlled conditions, its findings establish a foundation for integrating EE into the core design principles of 6G systems. The inclusion of massive MIMO systems in these considerations introduces new dimensions of scalability, as optimizing energy use across numerous antennas and transmission paths will be a key enabler for meeting the demands of ultra-dense networks in 6G. By leveraging these results, future networks can dynamically adapt to environmental and operational changes, enabling sustainable, high-performance communication that aligns with modern application demands.

The presented environment for energy consumption evaluation and results thereof can then be used to feed the energy model for the CF-mMIMO setups described in previous sections.

4.3.3 Reciprocity calibration

Reciprocity calibration is essential for maximizing the performance of TDD MIMO networks, particularly in distributed systems such as CF-mMIMO networks, where it is essential that the signals transmitted by the different RUs are coherently combined at the UEs they serve. While physical channels are reciprocal, discrepancies arise due to the differences in transmit and receive RF front-end circuits and the mutual coupling effect of antenna arrays, causing mismatches between forward and backward channels. To address this, modeling and calibration methods have been proposed to compensate these transceiver mismatches, enabling more accurate exploitation of cooperative and distributed transmission schemes. For massive MIMO systems, mutual coupling-based calibration procedures carried out at the BS side have proven effective. Experimental validations underscore the importance of reciprocity calibration for achieving the full potential of TDD-based systems and precoding in distributed and co-located MIMO systems [115][119][120][121].

This section describes the work done in 6G-SENSES to develop a distributed reciprocity calibration scheme that can be eventually integrated into the USRP-based CF-mMIMO platform described in section 4.2.1. The objective of the procedure is to achieve the phase synchronization between the antennas of the same AP or RU and between APs or RUs[9]. Two calibration processes are therefore necessary, which we call in this deliverable **intra-RU calibration**, to synchronize in phase the antennas of the same RU, and **inter-RU**

[9] In this section we use RU and AP interchangeably.

calibration, to synchronize in phase the antennas of RUs distributed across the coverage area (cf. Figure 4-26).

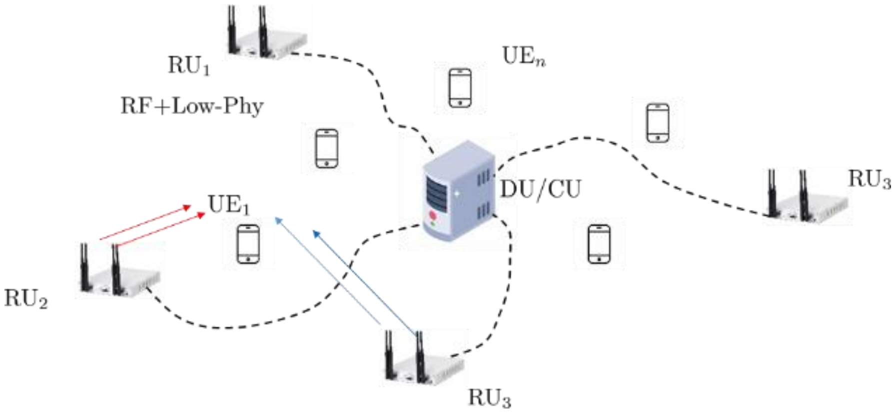

Figure 4-26 Sketch of a CF-mMIMO system

CF-mMIMO systems in 6G-SENSES consider a TDD protocol based on channel reciprocity, thanks to which the RUs use in the DL the CSI obtained in the UL phase. Channel reciprocity in TDD means that the physical channels for UL and DL are the same within the channel coherence time [196]. However, the E2E channel seen by the baseband processor contains not only the physical electromagnetic channel, but also the RF chain, from the Rx antenna to the ADC in the receiving chain, and from the DAC to the Tx antenna in the transmitting chain. Due to the differences between the amplifiers, dividers, and PLLs of the different chains, the variability in the length of the cables, etc., the baseband channels in DL and UL are not the same. To be more specific, let us consider two antennas on the same RU that wish to transmit a signal coherently to a UE equipped with a single antenna. The OTA physical channels between the antennas and the UE are denoted g_1 and g_2, respectively. Let t_1 and t_2 be the frequency response of the RF transmit HW at antennas 1 and 2, and let r_1 and r_2 be the frequency response of the RF receive HW at antennas 1 and 2, respectively. In a noiseless situation, the channel estimated with pilots during UL is

$$\begin{aligned} h_1^{UL} &= t_u g_1 r_1 \\ h_2^{UL} &= t_u g_2 r_2 \end{aligned} \tag{4-5}$$

Similarly, the actual DL channels are

$$\begin{aligned} h_1^{DL} &= t_1 g_1 r_u \\ h_2^{DL} &= t_2 g_2 r_u \end{aligned} \tag{4-6}$$

On the DL stage, the two antennas apply conjugate beamforming and therefore the channel gains as seen by the UE are

$$\begin{aligned} h_1 &= (h_1^{UL})^* h_1^{DL} = t_u^* r_1^* |g_1|^2 t_1 r_u \\ h_2 &= (h_2^{UL})^* h_2^{DL} = t_u^* r_2^* |g_2|^2 t_2 r_u. \end{aligned} \tag{4-7}$$

We observe that, for the signals from the two antennas to add up coherently at the UE, it is therefore necessary to calibrate antenna 2 by precompensating it with the phase $(t_1 - r_1) - (t_2 - r_2)$. To estimate this calibration coefficient, Argos [194] proposes to perform a bidirectional measurement by exchanging pilots between the two antennas as depicted in Figure 4-27.

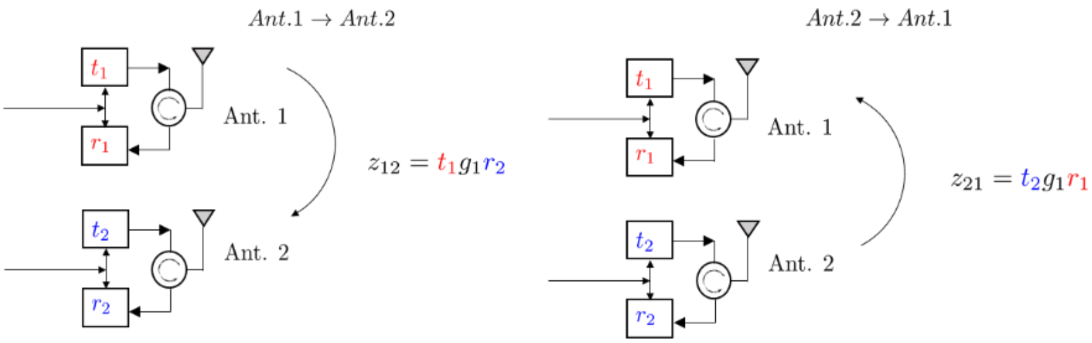

Figure 4-27 Intra-RU calibration through Argos. The calibration coefficient is $\frac{z_{12}}{z_{21}}$.

When the RU has multiple antennas, antenna 1 is taken as reference and bidirectional measurements are performed between antennas 2, 3, ... and antenna 1. All the antennas of the same RU share the LOr. Therefore, the intra-RU calibration process should be performed infrequently, thus introducing a negligible overhead to the CF-mMIMO system.

Once the intra-RU reciprocity calibration process has been performed, it is necessary to find the phase shift or calibration coefficient between the first antennas of each RU. To do this, it is first necessary to define a master RU to which the rest of RUs have to be calibrated. For the inter-RU reciprocity calibration process, we have selected the recently proposed BeamSync method [195], which does not require the transmission of signals between UEs and RUs and can be implemented in a distributed fashion without sending any measurement to the CU through midhaul. Figure 4-28 shows a summary of the stages of the inter-RU calibration procedure.

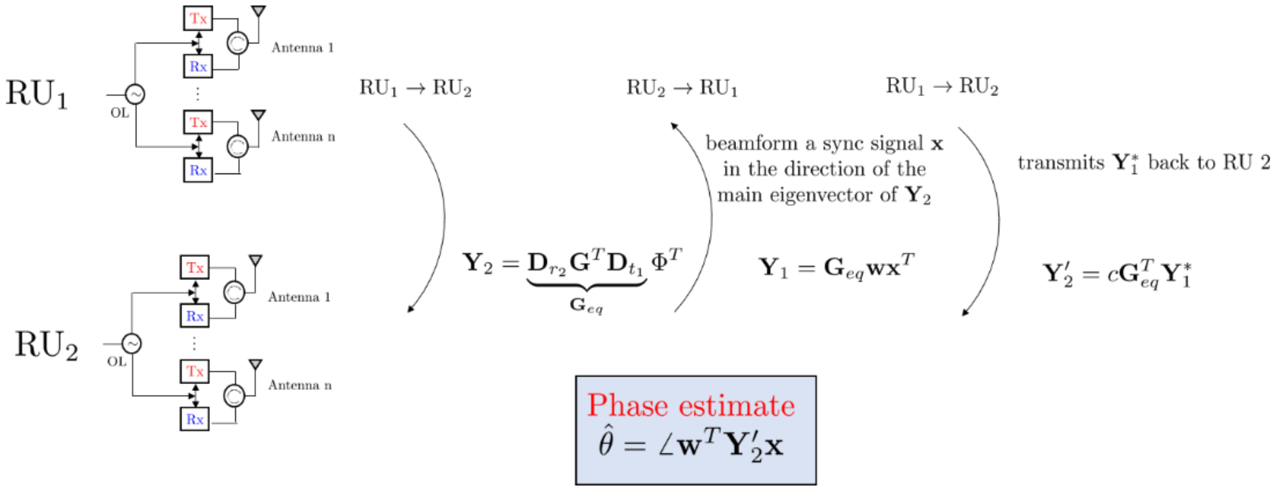

Figure 4-28 Inter-RU reciprocity calibration based on BeamSync [195].

4.3.3.1 Algorithmic implementation and preliminary results

As mentioned above, the Argos algorithm for intra-RU calibration and the BeamSync algorithm for inter-RU calibration have been selected for implementation. A first line of work during this period aimed at evaluating the performance of these two algorithms using a Matlab-based simulation environment. As an example, Figure 4-29 compares the results obtained by the proposed calibration procedure in a simple CF-mMIMO scenario, whose parameters are shown in Table 4-3. The figure compares the CDF of the SNR achieved by the following DL schemes:

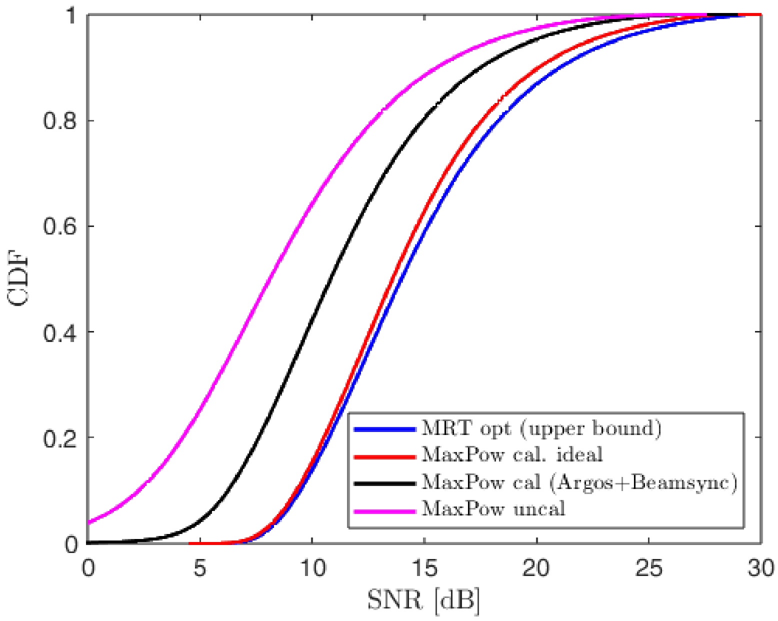

Figure 4-29 CDF of the SNR with and without reciprocity calibration

- **MRT opt**: all AP antennas (10 in our scenario) are considered as a virtual distributed array and MRT is employed over the actual DL channel. Note that if each AP has a maximum power of 20 dBm, as shown in Table 4-3, the virtual MRT beamformer has a power of 23 dBm. That is, the power of all APs is aggregated in the virtual array. This is an ideal situation, used only as a benchmark or upper bound on the best performance that can be achieved by any scheme.
- **MaxPow cal. ideal**: each PA applies a calibration stage with the ideal (non-estimated) coefficients and transmits on the DL applying MRT with the estimated channel in the UL. The APs transmit at maximum power, i.e., there is no power control.
- **MaxPow cal. (Argos+BeamSync)**: the calibration coefficients are estimated using Argos for intra-RU and Beamsync for inter-RU. The APs transmit at full power over the DL applying MRT with the estimated channel in the UL.
- **MaxPow uncal.**: No reciprocity calibration is applied. The APs transmit at full power over the DL applying MRT with the estimated channel in the UL.

Table 4-3 Parameters for Intra-RU and Inter-RU reciprocity calibration

Parameter	Value
Number of APs	2
Antennas per AP (ULAs)	5
AP Power budget	20 dBm
Number of UE	1
Number of pilots for uplink channel estimation	10
Number of pilots for intra-RU cal.	10
Number of pilots for inter-RU cal.	10
Length of the synchronism sequence (inter-RU)	10

Figure 4-29 shows that reciprocity calibration is necessary for coherent transmission in CF-mMIMO. The red curve that applies the ideal calibration coefficients approaches the upper bound provided by the MRT solution. The solution using Argos for intra-RU and BeamSync for inter-RU calibration with sequences of pilots of length 10 loses almost 3 dB with respect to the ideal calibration. This gap can be closed by increasing the length of the pilot sequences. The solution without calibration (magenta curve) loses about 6 dB with respect to the ideal calibration.

4.3.3.2 OTA evaluation

This subsection describes the preliminary experiments conducted to assess the technical requirements, implementation aspects, and performance of reciprocity calibration techniques in TDD-based CF-mMIMO systems. Figure 4-30 shows the initial setup, which is composed of three Ettus USRP B210 boards and one Ettus Octoclock-G CDA-2990 for synchronization purposes. Each USRP board is equipped with a single antenna. Two USRP boards emulate an AP/RU with two antennas while the other emulates the UE. The testbed implements a TDD protocol with uplink channel estimation, reciprocity calibration, and downlink beamforming. The *Grupo de Tecnología Electrónica y Comunicaciones* (GTEC) Testbed Interface Software (GTIS) middleware shown in Figure 4-30 is a proprietary software developed by the University of Cantabria and the University of *A Coruña* (Spain) for the remote control of multiple USRP devices using Matlab. All USRPs share the same 10 MHz reference clock provided by the OctoClock to synthesize both carrier frequency and baseband sampling clock.

As a preliminary experiment during this first phase of Task 3.2, we have implemented the intra-RU reciprocity calibration procedure using Argos [194] to calibrate the phase shift between the two transmit antennas that compose an AP. We have used a carrier frequency of 2.41 GHz, a sampling rate of 2 Msamples/s, and a sinusoidal baseband signal of 50 KHz. For this scenario, the estimated phase difference for the two antennas of RU1 is 45°. More interestingly, the time drift of this parameter is negligible at least over 43 minutes, as Figure 4-31 shows. This OTA experiment shows the effectiveness of the intra-RU calibration procedure in a TDD implementation. During DL the calibration coefficient estimated with the proposed intra-RU procedure successfully compensates the Tx-Rx chain variations.

In the next reporting period, the setup will be extended to 2 APs with two antennas each and one UE, on which both intra-RU and inter-RU calibration algorithms can be evaluated with OTA experiments. It is also necessary to extend the calibration procedure to 5G NR OFDM signals, analyzing in detail the performance of the different calibration algorithms, optimizing their parameters (length of the pilot sequences, for example), and designing a suitable protocol to update both intra- and inter-RU calibration coefficients with the appropriate frequency.

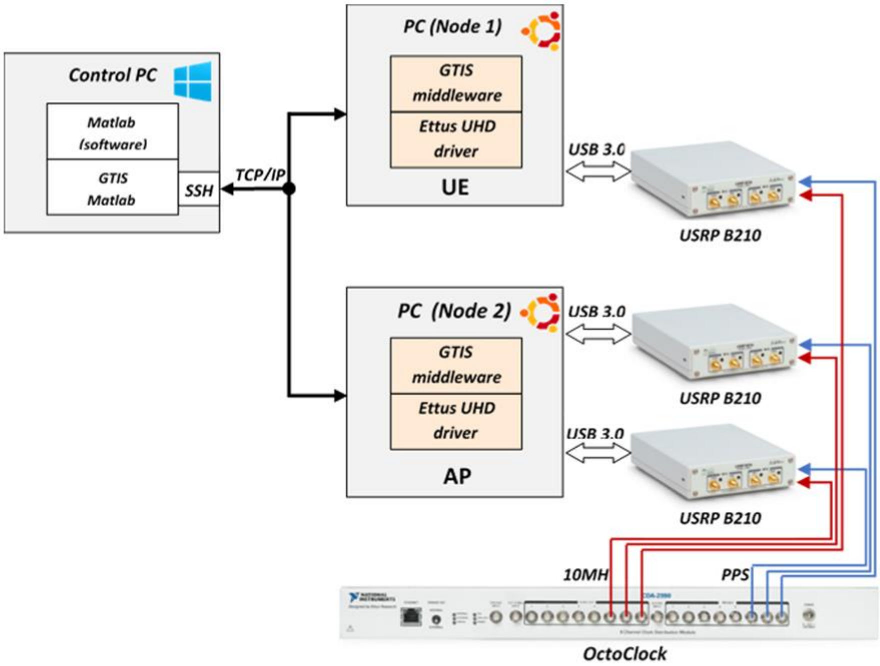

Figure 4-30 Preliminary USRP-based setup for reciprocity calibration

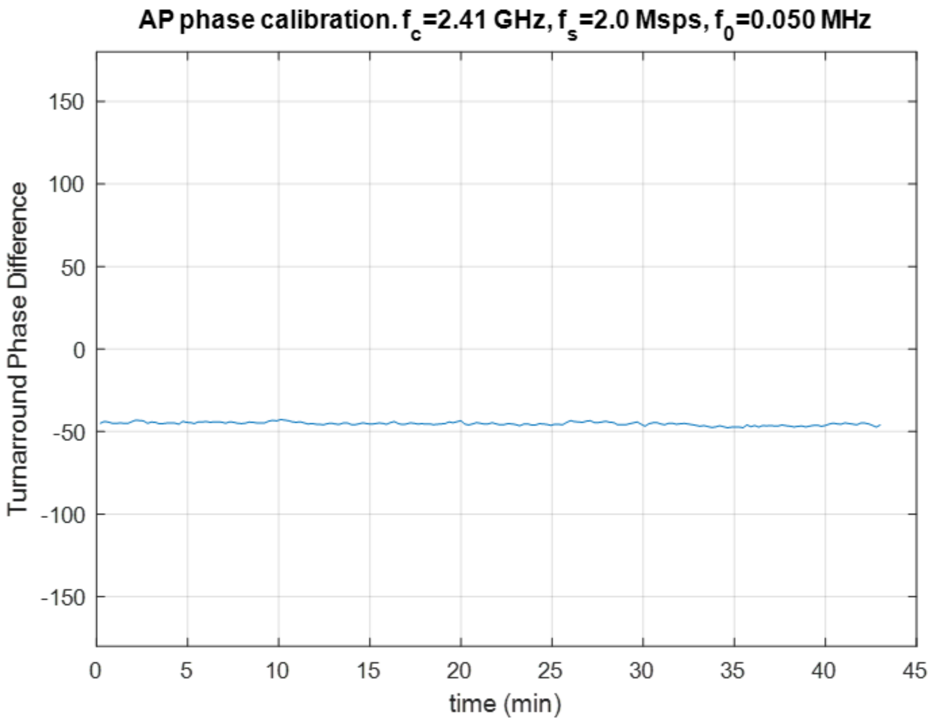

Figure 4-31 Evolution of phase calibration

4.3.4 Unsourced Random Access in Cell-Free Massive MIMO

URA [197] is an emerging paradigm addressing UL communication of a massive number of users with small payloads. The communication is sporadic, i.e., only a small subset of the users is active at any given time and uncoordinated. In URA, all devices share the same codebook; hence, there is no user identity and the purpose of the receiver becomes to extract only a list of transmitted messages. Also, per-user probability of error (PUPE) is adopted as a performance criterion.

In [197], a random coding achievability bound is derived for URA over Gaussian multiple access channel, and low-complexity coding solutions are developed in the subsequent literature [198], [199]. Moreover, the more practical fading multiple access channel is studied in [200], and MIMO receivers are considered in [201]. In CF-mMIMO, many APs with a small number of antennas distributed to the same geographic area simultaneously serve the users. In this way, cell boundaries are removed and the SE can be improved. Due to its scalability property, it is a suitable candidate to support systems with many users.

In this section, we study URA in CF environments. We employ a transmission scheme where the transmission frame is divided into two parts. The active users transmit a pilot in the pilot part followed by their modulated polar codeword that is sparsely distributed to the data part to each AP, where the APs are connected to a CPU via a fronthaul. We recover a small subset of the users at each AP to keep the system scalable. We perform joint active pilot detection and symbol estimation at APs, and pass the symbol estimates to CPU for combining and recovery of the message bits by list decoding. Numerical examples verify the high performance of the scheme and superiority of the CF structure.

4.3.4.1 System model

We consider a CF-mMIMO system with K_a active users out of an unbounded number of users transmit B bits to M APs without any coordination. The APs are equipped with M_r antennas and randomly located in a $D \times D\ m^2$ area. The received signal at the m-th AP can be written as

$$Y_m = \sum_{i=1}^{K_a} x_i g_{i,m} + Z_m, \tag{4-8}$$

where $x_i \in C^{n\times 1}$ is the transmitted signal of the i-th user, $g_{i,m} \in C^{1\times M_r}$ is the vector of channel coefficients of the i-th user at the m -th AP, and $Z_m \in C^{n\times M}$ is the circularly symmetric complex additive white Gaussian noise (AWGN) with i.i.d. elements, with zero-mean and variance σ^2. The channel vector $g_{i,m}$is defined as

$$g_{i,m} = \sqrt{\beta_{i,m}} h_{i.m} \tag{4-9}$$

where $h_{i.m}$ is the small-scale fading channel vector of the i-th user at the m-th AP, and $\beta_{I,m}$ is the large-scale fading coefficient. We consider a quasi-static fading model, i.e., the fading coefficients remain constant throughout the transmission frame. The APs are connected to a CPU via a fronthaul, where the aim is to produce a list of the transmitted messages using the symbol estimates from the APs. The system performance is measured in terms of the PUPE P_e that can be calculated as $P_e = P_{\text{md}} + P_{\text{fa}}$, where P_{md} and P_{fa} are the misdetection and false alarm probabilities.

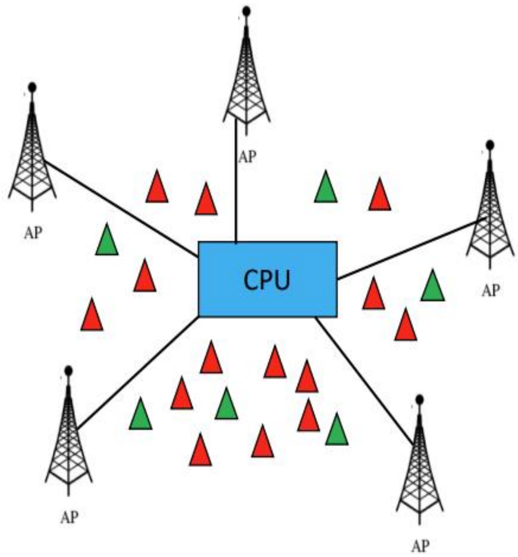

Figure 4-32 CF system illustration with 5 APs and 1 CPU. Active and inactive users are shown by green and red triangles, respectively

Transmission scheme

We assume that each user picks a pilot sequence of length n_p from a common non-orthogonal codebook $A \in C^{n_p \times N}$ with $N = 2^{B_p}$ elements where B_p is the number of pilot bits, and transmits it in the n_p time instances of the frame. The received signal in the pilot at the m-th AP is written as

$$Y_{p,m} = \sum_{i=1}^{K_a} a_i g_{i,m} + Z_{p,m} \tag{4-10}$$

where $Y_{p,m} \in C^{n_p \times M_r}$, $a_i \in C^{n_p \times 1}$ is the pilot sequence of the i-th user $Z_{p,m}$ is the AWGN. The rest of the bits are appended by r cyclic redundancy check (CRC) bits, encoded by a $(n_c, B - B_p + r)$ polar code, and modulated by quadrature phase shift keying (QPSK), where n_c is the code length. The encoded and modulated sequence is then distributed to the data part of the frame by an on-off transmission pattern determined by the first B_p message bits. Namely, the QPSK symbols are located to n_d out of $n - n_p$ time instances of the data part while rest of them being zero. The received signal in the data part at the m-th AP can be written as

$$Y_{d,m} = \sum_{i=1}^{K_a} s_d(c_i) g_{i,m} + Z_{d,m}, \tag{4-11}$$

where $Y_{d,m} \in C^{(n-n_p) \times M_r}$, $s_d(.)$ is a mapper that distributes the modulated polar codeword, c_i, to the data part, and $Z_{d,m}$ is AWGN.

Decoding

At each AP, the received signal is processed to jointly estimate the selected pilots and channel vectors followed by symbol estimation. The symbol estimates are then passed to the CPU via fronthaul, where the final decisions are made. To keep the system scalable, at each AP, only K_m users are recovered.

At each AP, we first jointly estimate the active pilot sequences and the corresponding channel coefficients. Since $K_a \ll N$, the orthogonal matching pursuit (OMP) algorithm can be applied with A being the measurement matrix. OMP is a greedy iterative algorithm that solves sparse recovery problems by finding the element of the measurement matrix that has the highest correlation with the received signal and subtracting its effect by using its projection onto the signal space at each iteration. After K_m iterations are performed, the channel vector estimates become

$$\hat{G}_m = \left(\hat{A}_m^H \hat{A}_m + N_0 I_{K_m}\right)^{-1} \hat{A}_m^H Y_{p,m}, \quad (4\text{-}12)$$

where $\hat{A}_m \in C^{n_p \times K_m}$ is the detected pilot set at the m--th AP. Given the channel vector estimates, an LMMSE solution is employed to estimate the transmitted symbols in the data part as

$$W_m = \left(\hat{G}_m^H \hat{G}_m + \frac{\sigma^2}{P_d} I_{M_r}\right)^{-1} \hat{G}_m^H$$
$$\hat{C_m} = Y_{d,m} W_m, \quad (4\text{-}13)$$

where W_m is the LMMSE matrix and $\hat{C_m}$ is the matrix of the symbol estimates. The estimated symbols are passed to the CPU without estimated large-scale fading channel coefficients; namely, we consider Level 2 cooperation between the APs. The active pilot indices are also passed since they are required to combine the symbol estimates belonging to the same user coming from different APs.

At the CPU, the symbol estimates belonging to the same user from different APs are combined, and the log-likelihood ratios (LLRs) of the corresponding message bits are extracted. The extracted LLR values are fed to a single-user polar decoder employing successive cancellation list decoding (SCLD) for message recovery. Note that we match each pilot index to a user since B_p is taken to make the pilot collision probability negligible.

4.3.4.2 Numerical Results

We evaluate the performance of the proposed scheme through Monte Carlo simulations. We take $n = 3200$ and $B = 100$. We employ Gaussian sequences as pilots where each element of a pilot is a zero-mean standard normal random variable. We utilize 5G polar codes with a code length of 1024, a CRC length of 16, and the SCLD list size of 8. We assume that the APs are distributed to a $D \times D$ area according to a Binomial point process where $D = 550\ m$.

For large-scale fading, we utilize the urban micro-cell propagation model in [202] with a center frequency of 2 GHz for the path loss, hence, $\beta_{i,m}$ can be written as

$$\beta_{\{i,m\}[dB]} = -30.5 - 36.7 log_{10} d_{\Im} + F_{i,m} \quad (4\text{-}14)$$

where $d_{\Im}$ is the distance between the i-th user and the m-th AP, and $F_{i,m} \sim CN(0,16)$ is the shadow fading. The small-scale fading coefficients are generated assuming an ULA at the APs with half-wavelength antenna spacing.

We assess the effect of distributing the receive antennas in Figure 4-33 by taking $K_m = 7$, evaluate the error probability of the proposed scheme for $M = 1$ and $M_r = 100$, i.e., the centralized scenario and compare it with that of the two distributed scenarios where $M = 49$ and $M_r = 2$ and $M = 100$ and $M_r = 1$. We set the average symbol power to 10 mW and $\sigma^2 = -84$ dBm. The results in Figure 4-33 show that distributing the antennas to the area by the APs improves the performance significantly, namely, the PUPE decreases more than an order of magnitude as the system becomes more robust to the large-scale fading with the distribution of the APs to the geographic area. As a next step, the EE of the considered scheme can be investigated and compared to that of the other schemes in the literature. In addition, the performance of different cooperation levels between APs can be studied.

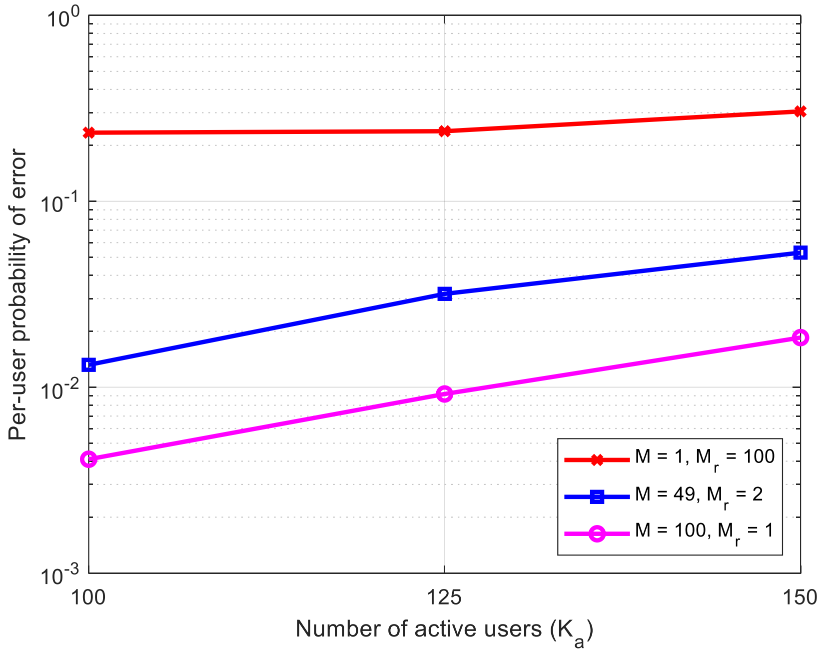

Figure 4-33 System PUPE versus number of active users for different configurations

5 Human-friendly radio systems and RIS support

This chapter introduces the work to be carried out in 6G-SENSES related to the design, development and implementation of the building blocks that are related to the analogue (RF) domain. On the one hand, 6G-SENSES proposes multi-mode ultra-low power mmWave front ends (@ 60GHz ISM band) for indoor scanning of potential high-speed communication users (FMCW sensing) and high-resolution tracking of active users' locations (CW sensing). The human-friendly adjective is coined due to the targeted objective of a lower EMF human exposure, taking recent 5G programme documents into consideration [206][207] by directing the high-data rate beam to the active user while tracking low speed movements with very high resolution. The proposed MIMO mmWave chipset and system enable scanning and low speed user tracking in parallel with a medium data communication link. Additionally, antenna requirements for ISAC, both as off-chip and on-chip antenna solutions are analyzed. For off-chip solutions, antenna in package (AiP) will be developed for monostatic radar applications at 60 GHz. Patch antenna system will be designed and optimized with the perspective of ISAC. On the other hand, this chapter analyses RIS technologies and deeps dive into modelling and optimization of signal processing for RIS to maximize different KPIs for ISAC.

5.1 60 GHz front-end module design

Under the framework of 6G-SENSES, a mmWave modular front-end design is planned for showcasing ISAC demo at mmWave band. The 60 GHz ISM band has gained popularity due to large license free bandwidth and higher propagation loss making it relevant for indoor links. Moreover, the wavelength size is also a good compromise between chip/antenna size and manufacturing difficulty trade-off. The frequency is still handleable by a Printed Circuit Board (PCB); however, manufacturing inaccuracies impacts the performance significantly and typical PCB layout resolutions may put a performance cap.

In 6G-SENSES the module design is divided into two parts depending on the technology used in each of them, i.e., the front-end chipset design using IHP SiGe technology and the AiP design based on printed circuit technology (PCT). The results for each part, obtained in the first 12 months of 6G-SENSES are summarized in the following subsections.

5.1.1 Analog front-end chipset

The design and development of a SiGe-based front-end transceiver at 60 GHz and an LO signal generation unit at 30 GHz are targeted within this task. The main design goals for both chips are achieving operation with low voltage supply and low dc power dissipation for higher energy-efficiency. In addition, a transceiver architecture that supports scalability shall be adopted for MIMO operation. To this end, the LO-scalable architecture is selected where multiple transceiver ICs can be cascaded in a daisy chain along the LO signal propagation path following the PLL chip [208].

IHP uses an already existing transceiver chip as a starting point for this task which achieves operation with a single supply voltage of only 1.5 V and dc power consumption of 72 mW [210]. Although the frequency doubler and the receiver network of this chip are optimized and suitable for highly energy-efficient operation, the 30-GHz DA and 60-GHz PA dominate the dissipation and are open for improvement. Therefore, IHP started this task with the design of high-efficiency DA and PA blocks.

A differential common-emitter topology was selected for the 30-GHz DA, the simplified schematic is depicted in Figure 5-1 (a). Here, a special attention has been given to design the output matching network together with the following power splitting stage for lower RF losses. The simulated S-parameters are given in Figure 5-1 (b)-(c), which shows a gain of 14.1 dB at the center frequency. The large-signal simulations reported in Figure 5-1 (d) show an OP1dB of 5 dBm attained with 30% PAE, which is enough to drive both the on-chip frequency doubler and the subsequent chip after the power splitting stage.

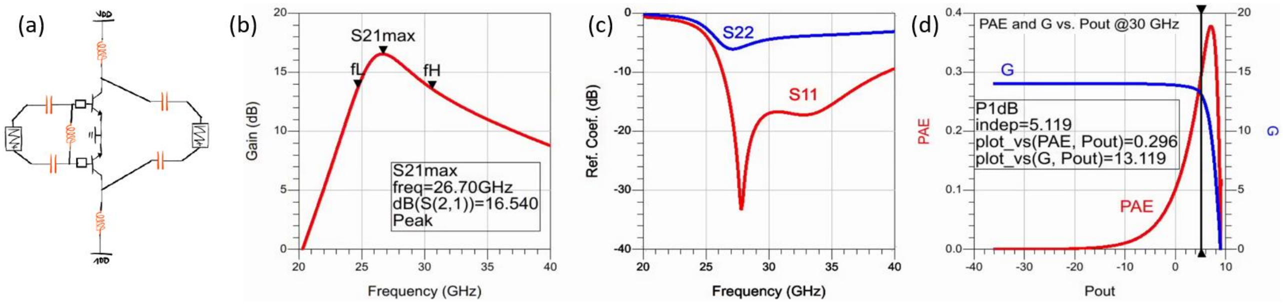

Figure 5-1 Simplified schematic and simulated performance of the 30-GHz DA

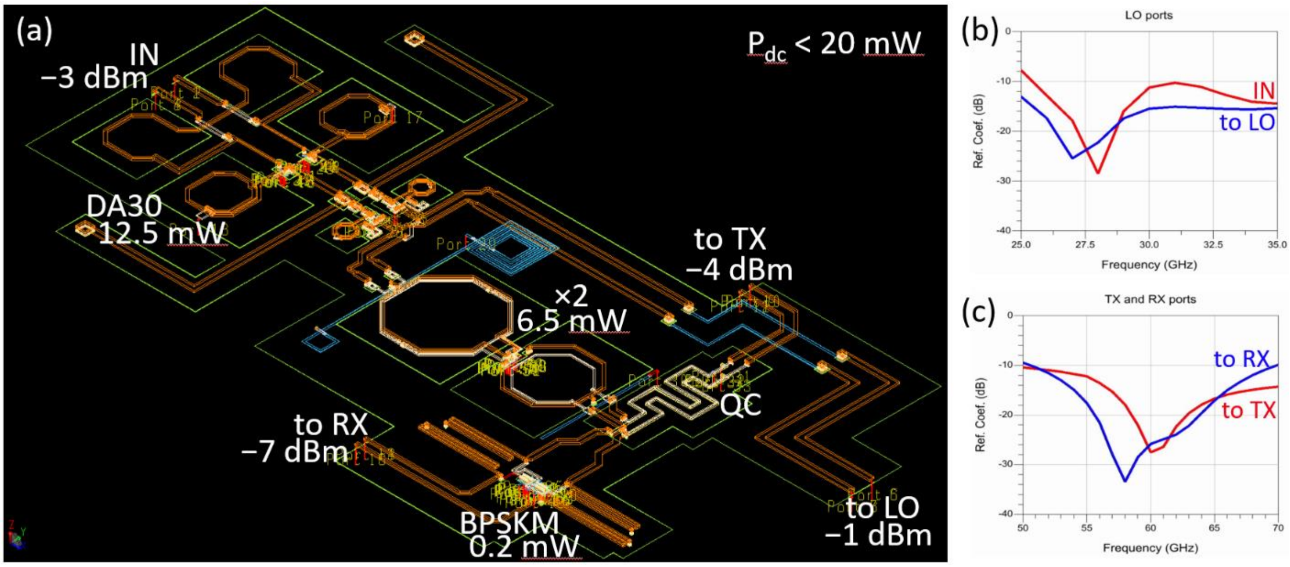

Figure 5-2 Layout of the transceiver frontend chip LO-distribution network and simulated reflection coefficients

The DA has been integrated into the LO-distribution network of the transceiver frontend IC as shown in Figure 5-2 (a). Here, the simulated dc power consumption is reduced to less than 20 mW and the power/link budgets of the sub-system are indicated. The IC requires an LO input of −3 dBm while it provides −1 dBm for the following IC which is feasible for cascading with the low-loss interconnects being developed by BI. The simulated reflection coefficients at the differential LO, RX, and TX ports are all better than −10 dB in a wide bandwidth around 30 GHz and 60 GHz as shown in Figure 5-2 (b)-(c).

A two-stage differential common-emitter topology was chosen for the 60-GHz PA as in Figure 5-3 (a), since a higher gain is required to compensate for the quasi-passive VSPS losses in the TX network. The simulated S-parameters show a gain about 20 dB at 60 GHz as reported in Figure 5-3 (b)-(c). The large-signal simulation results given in Figure 5-3 (d) show an OP1dB above 10 dBm attained with 25% PAE, while in saturation the output power increases to 12 dBm with 30% PAE. The expected drive after integrating into the transceiver IC is around −7 dBm at the output of the BPSK modulator, thus the output power will be around 11.5 dBm.

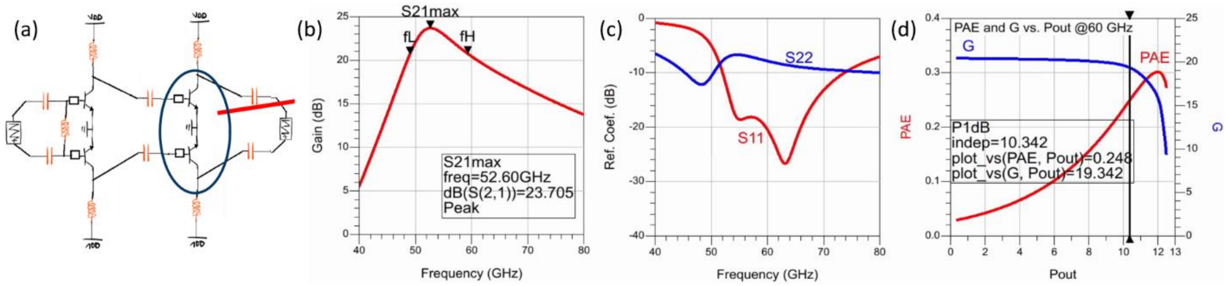

Figure 5-3 Simplified schematic and simulated performance of the 60-GHz PA

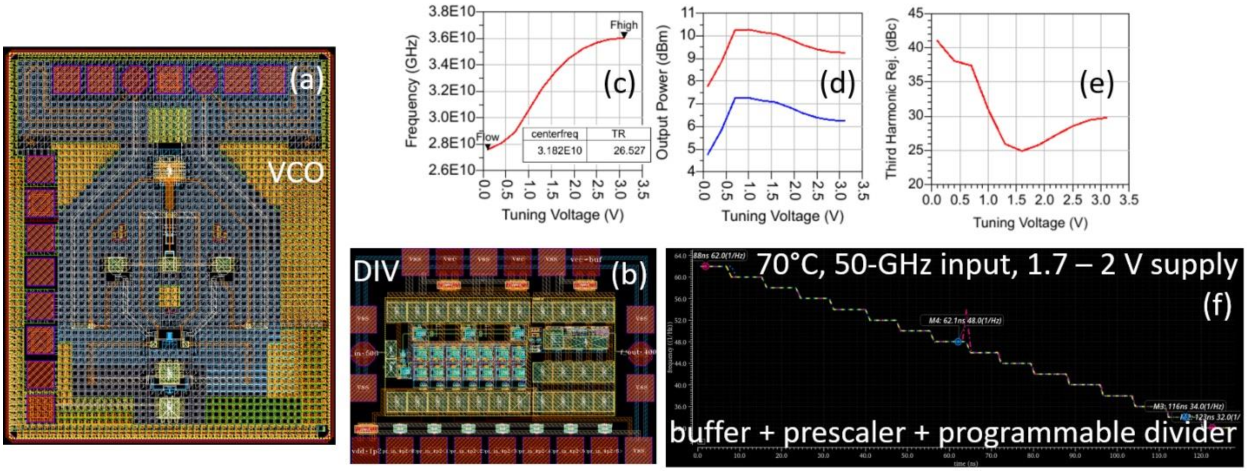

Figure 5-4 Layout of the PLL sub-blocks and their simulated performance

In the meantime, the sub-blocks of the highly-efficient 30-GHz PLL chip are developed, namely the VCO and frequency divider, whose layouts are provided in Figure 5-4 (a)-(b). For all blocks, a supply voltage of 1.8 V is selected, except the tuning voltage and PFD for achieving a wide tuning range. The simulation results of the VCO, given in Figure 5-4 (c)-(e), show operation from 28 GHz until 36 GHz with more than 8-dBm output power and 25-dB third harmonic rejection. On the other hand, as reported in Figure 5-4 (f), the programmable divider (division ratio in 32–63) has a robust operation at 70°C with an input frequency up to 50 GHz.

The transceiver design along with various test circuits, e.g. the standalone DA and PA, VCO and dividers, have been submitted for fabrication in the May SG13G2 MPW run of IHP. The chips have been delivered in November 2024. The next steps will be on-wafer characterization of all fabricated circuits. In addition, IHP will complete the design and submit the fully integrated 30-GHz LO signal generation chip in the December SG13G3 MPW run (chips are expected back in July 2025).

5.1.2 Antenna-in-package

Patch antenna designs with bondwire interconnection to the front-end chipset (being developed by IHP) is considered for this work. Patch antenna has the widest acceptability for PCB based circuits and bondwire interconnect is the mostly preferred solution for chip to antenna interconnections.

BI conducted a comprehensive literature study on various mmWave antennas and high-frequency antenna connectors. For the connectors, 1.85 mm connectors were chosen because they are cost-effective, easy to integrate, and show a working frequency range of up to 67 GHz, which meets the requirements of this project. To obtain close measured and simulated results, BI deeply investigated the 1.85 mm connectors and created EM models that align with the cutoff frequency of the connector. The developed EM model with its reflection and transmission coefficient response with the coplanar waveguide is shown in Figure 5-5.

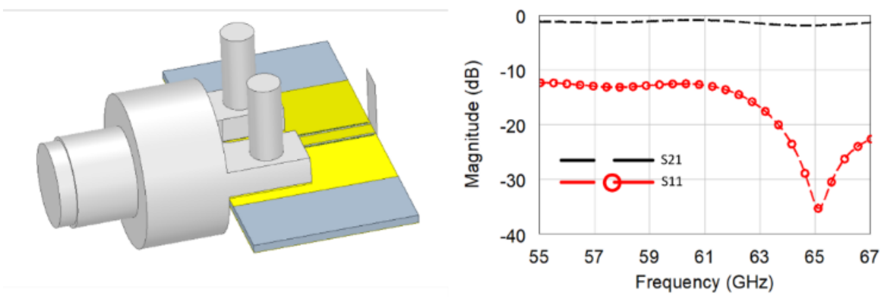

Figure 5-5 The reflection and transmission coefficient response of the 1.85 mm connector with the CPW lines

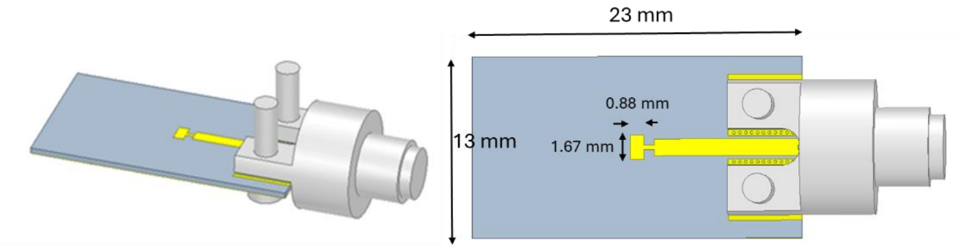

Figure 5-6 60 GHz microstrip patch antenna integrated with 1.85 mm connector

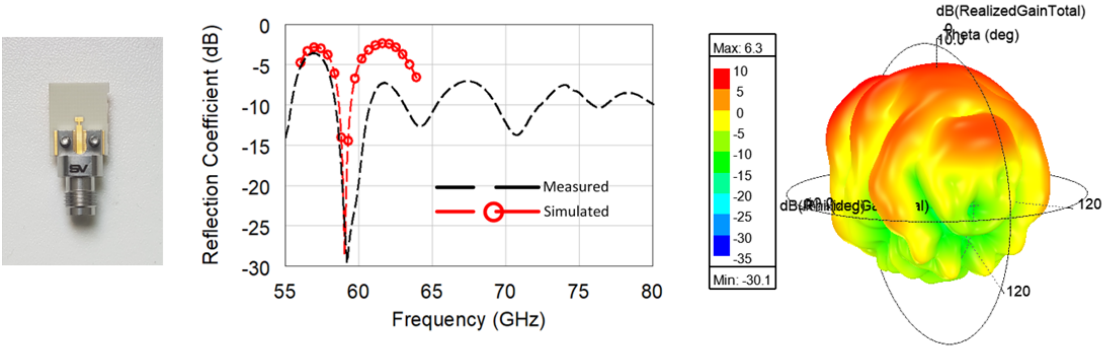

Figure 5-7 Simulated and measured the reflection coefficient of the 60 GHz antenna with it realized gain

After the analysis of the connectors, BI integrated these connectors with a designed 60 GHz microstrip patch antenna on the Rogers 4003 substrate with a thickness of 0.508 mm (Figure 5-6). The substrate offers a permittivity of 3.55 and a low loss tangent of 0.0027. The developed antenna in the EM simulation environment is shown in Figure 5-7. The patch dimensions are chosen such that it resonates at 60 GHz and a quarter wave transformer is utilized to transform antenna impedance to 50 ohms to feed it with the desired connector.

The fabricated 60 GHz antenna with a 1.85 mm connector and the simulated and measured reflection coefficients of the antenna are illustrated in Figure 5-8, showing a close agreement except for some discrepancies that are due to fabrication tolerance. The single antenna also shows a maximum realized gain value of 6.3 dBi.

Currently, BI is analyzing different transmission line transition losses to minimize the coupling of the connector and maximize the gain of the antenna at 60 GHz. Moreover, antenna elements will be increased and mutual coupling between the antennas will be analyzed, and various solutions will be proposed to mitigate this issue.

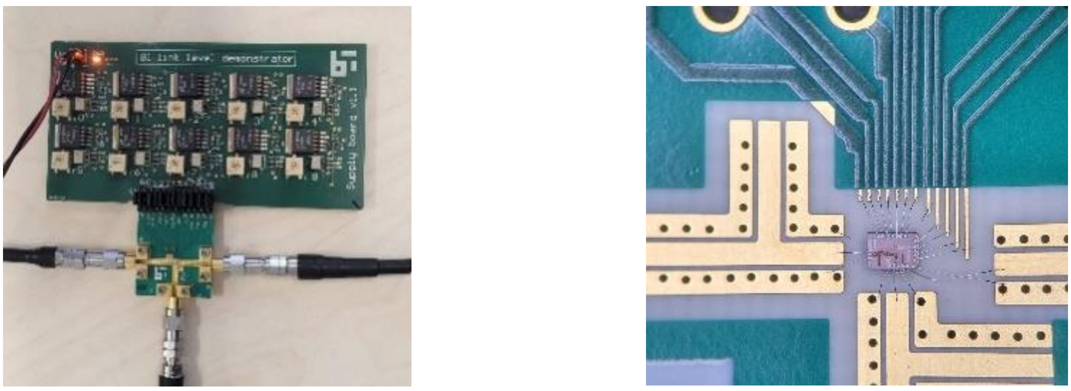

Figure 5-8 (a) LNA-Mixer package with RF, LO and baseband (BB) ports connected to the power supply module (b) Chip to PCB connection with bondwires

The analog front-end chipset is currently under design by **IHP** and the chip-to-antenna interconnection effectiveness has been verified using **BI**'s own designed receiver chipset. An intermediate frequency of 5G NR band, 25 GHz, is considered to ease the manufacturing and measurement process. The chip, fabricated using GlobalFoundries 22nm Fully Depleted Silicon on Insulator (FDSOI) technology, covers a total area of 0.74mm², including the pads. The package is built on an RO4003 substrate with a thickness of 0.508mm, a commonly available material suitable for standard PCB processes. The bottom side of the substrate serves as the ground plane, while the chip is mounted on a copper pad on the top side, with through-hole vias connecting to the ground plane below. To facilitate movement of the bonding tool, the distance between the chip and the bonding pad on the PCB is maintained at 0.54mm. Aluminum wires, 17 µm thick, are used for chip-to-PCB connections via wedge-wedge bonding. The manufactured PCB of the receiver [209] along with the supply board is shown in Figure 5-8 (a) and a zoom-in is depicted in Figure 5-8 (b).

The bondwires in the design affect the 50 Ω impedance matching between the RX chip and PCB, necessitating compensation through a matching network. An open-stub-based parasitic compensation network is implemented on the RF and LO ports of the package using grounded coplanar waveguides (GCPW). This approach offers a simpler ground-signal-ground (GSG) interface to the chip pads compared to a microstrip configuration. The structure is simulated using AWR Analyst's EM-Simulator with a finite element method (FEM) solver, and optimized for input matching and minimizing insertion loss at the RF and LO ports.

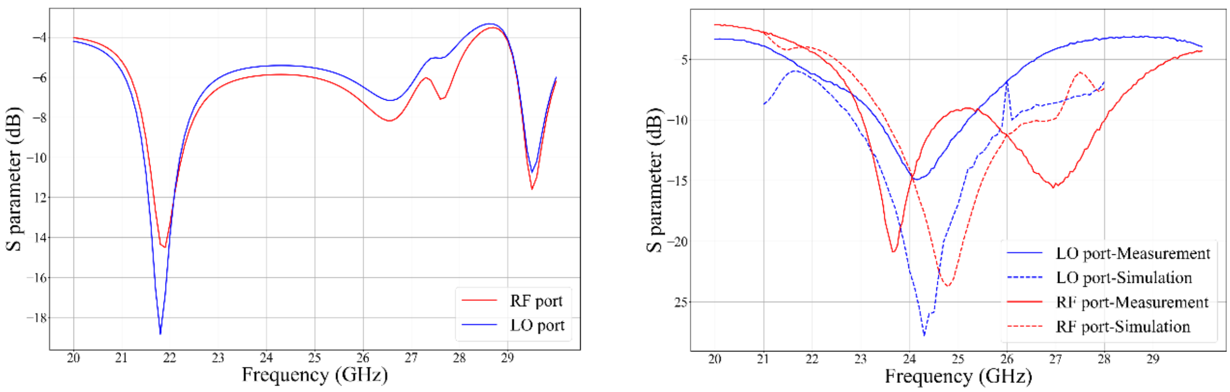

a) **b)**

Figure 5-9 (a) Unmatched S-parameter of RF and LO ports (b) Matched S-parameter response of RF and LO ports

The unmatched and matched responses of the package are shown in Figure 5-9 (a) and Figure 5-9 (b) respectively. The minor discrepancies between simulation and measurement can be attributed to variations in the bondwire loop profile between the simulated model and actual manufacturing, standard PCB manufacturing tolerances, and the use of RPC-2.92 precision connectors (Rosenberger 02K243-40ME3), which provide RF connectivity to the package.

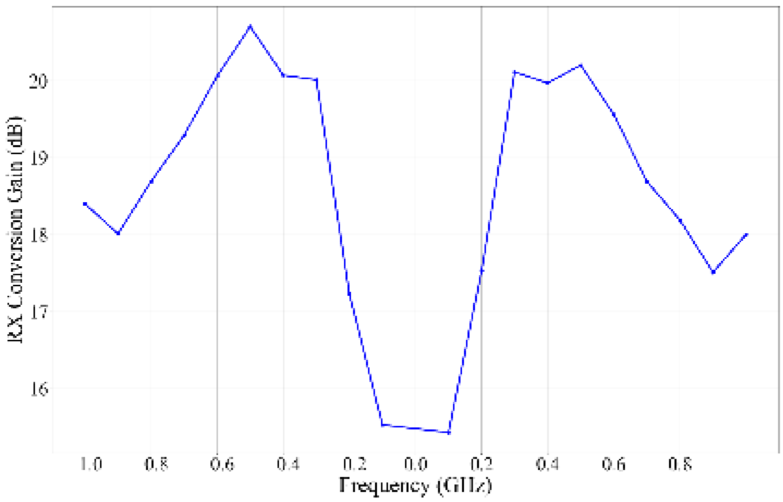

Figure 5-10 Measured IF frequency Vs Conversion gain of RX package

Figure 5-10 shows the measured IF frequency Vs Conversion gain of the RX package. The package achieves a conversion gain of 20dB at 500 MHz IF frequency.

5.2 RIS support

The potential of RISs as a PHY-layer 6G enabling technology that can improve coverage, transmission rates, EE, or network latency, is being recognized and assessed by academia and industry alike [160], [161]. RISs are expected to be crucial in achieving the KPIs for future 6G networks. The RIS elements or cells can be reconfigured through a programmable controller, thus modifying the propagation environment to optimize the transmission rate, the received signal power, the EE, or the transmitted power, among other criteria studied in numerous existing publications.

The potential of deploying RIS to improve sensing performance and to enhance the trade-off between communication and sensing performance is also receiving much attention lately [162] [163], and it is discussed in more detail in section 5.2.5. RISs can also improve the performance of CF-mMIMO systems, in which each user simultaneously communicates with several APs (or BS), rather than with a single AP [165][166], as it will be elaborated in section 5.2.6.

After a brief review of the SoTA (section 5.2.1), the subsequent subsections summarize the main results obtained in the first year of 6G-SENSES in RIS-support for energy and spectrum efficiency (Task 3.3).

5.2.1 Background and State-of-the-Art

5.2.1.1 Communication systems

Experimentation with RIS prototypes has been intense in recent years, with even some commercial alternatives already available on the market, such as those from Greenerwave[10], TMYTEK[11], or NEC[12]. Probably, the world's first RIS prototypes in the sub-6 GHz band (2.3 GHz) and the mmWave FR2 band (28.5 GHz) were the 16x16 panels with cells composed of positive intrinsic-negative (PIN) diodes allowing 2-bit phase shifting for beamforming described in [167]. Each cell was composed of 5 PIN diodes. The prototype described in [168] is a 6x6 RIS panel working at sub-6 GHz (4.9 GHz to 5.1 GHz) with 3-bit resolution. Each of the RIS cells is composed of 4 varactor diodes. The RIS is capable of any phase rotation of the reflected

[10] https://greenerwave.com/

[11] https://www.tmytek.com/

[12] https://www.nec.com/

electromagnetic wave from 0º to 360º. A prototype of a 4 × 4-element RIS fabricated based on PIN diode switches allowing 4-bit phase resolution and operating at 2.4 GHz is described in [170]. The NEC panel developed within the EU Project MINTS [169] is a 10 x 10 RIS operating at 5.3 GHz and providing a resolution of 3 bits [171]. It comprises arrays of patch antennas, delay lines and programmable RF switches that enable almost-passive 3D beamforming. A 14 x 14 RIS based on varactor diodes, which allows continuous control of the phase shifts, working in the 5.15–5.75 GHz band is presented in [172]. The conventional architecture assumed for RIS is realized by reconfiguring each cell or element through a variable impedance, leading to diagonal scattering matrices whose elements are modeled as phase shifters. Moreover, the transmitter and receiver should be in the reflection space of conventional RISs.

Other architectures are currently being studied to improve the limited flexibility of conventional RISs. Simultaneously Transmitting and Reflecting RIS (STAR-RIS) is designed to provide full-space or 360º coverage by enabling simultaneous transmission and reflection of signals [173]. Thus, STAR-RIS can cover a wider area and is expected to improve the system performance especially when a regular RIS cannot cover all the users, for instance when the BS is located outdoors and supports both indoor and outdoor users. It has been shown that STAR-RIS provides higher average max-min rates compared to the reflective RIS. These passive architectures, to which transmissive RIS or reflectarrays also belong, are generically called hybrid RIS. The concept of beyond-diagonal RIS (BD-RIS) has been proposed as a generalization in which all RIS elements can be connected by variable reactances to each other, leading to fully-connected or group-connected scattering matrices [174]. According to network theory, when the impedance network is purely reactive the BD-RIS scattering matrix must be unitary and symmetric, which introduces new challenges in its optimization.

Although the interest of RISs lies mainly in the fact that they are virtually passive devices which means they can be deployed and operated autonomously, their passive nature also causes the received signal to suffer from the product/double path loss attenuation. Passive RISs must therefore be located close to either the transmitter (an extreme case being the transmissive RIS) or the receiver in the so-called area of influence [175]. To tackle this challenge and extend the RIS area of influence, the concept of active RIS has been proposed and investigated in [176]. Active RIS not only adjust the phase shifts but also amplify the received signal thus making them similar to the concept of instantaneous relays. Another RIS architecture that has recently been considered in the literature, called globally passive, constrains the RIS elements so that the power reflected by the surface is not greater than the incident power [177]. Some globally passive BD-RIS elements may amplify the signal while others may attenuate it. The globally passive BD-RIS architecture provides a higher design flexibility than a passive lossless or locally passive BD-RIS and, therefore, it provides an upper bound in any performance metric.

5.2.1.2 RIS-assisted ISAC

Recent publications on this particular topic have proven that the incorporation of RIS technology into ISAC not only favourably alters the wireless propagation environment, but also increases sensing performance, leading to improved SNR, estimation accuracy, and reliability.

To date, numerous works have proposed incorporating RIS into ISAC to increase SINR and target illumination power, particularly when the direct channel from the BS to the UEs or targets is blocked [182][183][184][185]. Transmit beamformers, and RIS phase shifts are typically engineered to achieve desired communication and sensing performance levels. The majority of the works consider relatively simple scenarios, like using only one antenna for communications [186], or single user multiple targets [187], or multiple users single target [188], [189]. In their most generic form, [182], [190], [193], [181] discusses the settings of RIS-assisted ISAC systems for multiple users and targets. In [182], information is communicated and sensed via a single dedicated transmit waveform. For an ISAC system with independent colocated subarrays for sensing and communication, the transmit beamformers and reflection coefficients are constructed in [190]. The signal received at the RIS will also take up a lot of radar waveforms because radar and communication subarrays are so close to one another. This will increase interference at the UEs but is ignored in [190].

5.2.1.3 RIS-assisted CF-mMIMO

A significant advancement in current research is the incorporation of RIS within CF-mMIMO architectures [203][204][205], which are generally positioned between the APs and UEs to reflect signals—the predominant mode of RIS deployment. RIS fundamentally enhances wireless networks by enabling dynamic control over the radio environment, facilitating effective switching between active and passive signal states. This capability is essential for improving both coverage and signal quality. In CF-mMIMO systems, where maintaining robust communication links across diverse environments is of paramount importance, the adaptability of RIS becomes invaluable [100][104].

The authors in [211] analyze an alternative architecture where an RIS is integrated into the antenna array at each access point and acts as an intelligent transmitting surface to expand the aperture area.

Additionally, recent innovations, such as the introduction of an RIS-based offset index modulation (RIS-OIM) scheme, further exemplify this integration. By organizing RIS elements into blocks and optimizing transmission strategies, RIS-OIM not only boosts the reliability of information transmission but also elevates data rates while minimizing operational complexity. This holistic approach underscores the potential of RIS to significantly enhance the performance of CF-mMIMO systems, making them more efficient and responsive to varying operational conditions [104].

5.2.2 BD-RIS-Assisted interference minimization

Most of the previous works studying the role of RIS in 6G communication systems mainly consider RIS-assisted point-to-point or MU-SIMO systems. However, works on the K-user MIMO interference channel (IC) – of relevance to the 6G-SENSES use cases – are scarcer and have been mostly limited to diagonal RIS. To achieve the maximum degrees of freedom (DoF) of the K-user IC, the interfering signals at each receiver must fall into a reduced-dimensional subspace, a technique called interference alignment (IA). The design of the IA multi-antenna precoders is done by adopting as the optimization criterion the sum of the power of the interference leaked in the receive subspaces of all users, a cost function that is known in the literature as *interference leakage* (IL) [178].

In 6G-SENSES we propose a two-stage approach for interference management in the K-user MIMO-IC assisted by an RIS or a BD-RIS. The IL is minimized in the first stage by the BD-RIS while the precoder design takes care in the second stage of the residual interference that the BD-RIS could not remove. In addition to the reduction in complexity resulting from decoupling the passive and active beamforming optimization problems, another motivation for the proposed two-stage framework is that considering the 6G-SENSES architecture of deliverable D2.1 [1], the BD-RIS infrastructure provider might be different from the RAN operator in charge of the users' resource allocation strategies.

Some reasons justify minimizing the IL in a RIS-assisted K-user MIMO-IC. First, for the K-user MIMO-IC the min-IL precoders attain (if the IA problem is feasible) the maximum DoF of the channel. Second, if an RIS can sufficiently suppress interference, the users could design their precoders independently treating the residual interference as noise (TIN). Finally, the IL yields quadratic functions which are usually easier to optimize than other cost functions commonly used such as the sum rate or the mean-squared error (MSE). Motivated by these considerations, we considered the IL a suitable metric for the design of the RIS. More specifically, in Stage I the BD-RIS is optimized to solve the problem

$$(\mathcal{P}_1): \max_{\mathbf{\Theta}} \sum_{l \neq k} \|\mathbf{H}_{lk} + \mathbf{F}_k \mathbf{\Theta} \mathbf{G}_l^H\|_F^2 \quad \text{s.t. } \mathbf{\Theta}^T = \mathbf{\Theta},\ \mathbf{\Theta}^H \mathbf{\Theta} = \mathbf{I}_M, \tag{5-1}$$

where $\mathbf{H}_{lk}$ is the (*l*,*k*) MIMO-IC, $\mathbf{G}_l$ is the channel from the *l*th transmitter to the BD-RIS, $\mathbf{F}_k$ is the channel from the BD-RIS to the kth receiver and $\mathbf{\Theta}$ is the MxM BD-RIS scattering matrix. The IL minimization problem (5-1) is non-convex and requires an iterative algorithm to find a (probably suboptimal) solution. We have proposed two algorithms to solve it. The first one is an optimization algorithm in the manifold of unitary matrices that can be applied to fully-connected BD-RIS. The second one is a greedy, computationally efficient algorithm, for group-connected BD-RIS. Details of these algorithms may be found at [179]. After the BD-RIS has been optimized, the users' precoders are optimized in Stage II according to one of the following criteria:

1. **Interference oblivious SVD-based precoders**. Each user independently optimizes its precoder by considering only the receiver noise and disregarding the residual interference not eliminated by the BD-RIS. If the BD-RIS designed in Stage I reduces the interference significantly below the noise level, the MIMO-IC channel decouples into K parallel MIMO Gaussian channels and the SVD-based precoders are capacity-achieving.
2. **Min-IL precoders**. The precoders and decoders are designed to minimize residual IL that the BD-RIS may not have eliminated. This approach can be considered as an altruistic design of the precoders in which each user tries to generate the least interference to other users. In contrast, SVD-based precoders can be considered a selfish design in which each user tries to maximize the rate over its direct channel without considering the interference it causes to (or receives from) other users.
3. **Max-SINR precoders**. The min-IL precoders do not consider direct channels. An alternative approach that gives better sum rate performance than min-IL precoders designs the precoders and decoders to maximize the SINR. The iterative algorithm for the design of Max-SINR precoders is very similar to that of Min-IL decoders.
4. **Max sum-rate precoders**. The precoders are designed to maximize the sum-rate over the MIMO-IC channel. This is the most computationally expensive approach, for which several algorithms exist in the literature.

For the evaluation of the proposed two-stage method, we have considered a simulation scenario with the parameters described in Table 5-1. The K =3 transmitters and receivers are regularly located in a square of 50 m. The coordinates (x,y,z) in meters [m] of the *k*th transmitter and the *k*th receiver are (0, $50(k-1)/(K-1)$,1.5) and (50, $50(k-1)/(K-1)$,1.5), $\mathrm{k} = 1, \dots, \mathrm{K}$, respectively. The BD-RIS located at (x, y,5) [m], where the (x,y) coordinates can vary between 5 and 45 m. Since the BD-RIS is located higher than the transmitters and receivers with a direct LoS to all of them, it is assumed that all transmitters and receivers are in the reflection space of the RIS. As a figure of merit, we use the difference in dBs between the interference leakage (IL) ratios with and without BD-RIS, which is also the difference in dBs between the interference-to-noise ratios (INR) with and without BD-RIS.

$$\Delta\mathrm{INR} = 10\log_{10}\left(\frac{\sum_{l\neq k}\|(\mathbf{H}_{lk} + \mathbf{F}_k\mathbf{\Theta}\mathbf{G}_l^H)\|_F^2}{\sum_{l\neq k}\|\mathbf{H}_{lk}\|_F^2}\right) \tag{5-2}$$

Table 5-1 Scenario parameters for the BD-RIS-assisted MIMO IC

Parameter	Value
Carrier frequency	2.4 GHz
Bandwidth	40 MHz

Number of users	3
MIMO links	3x3
Streams per user	2
Path Loss	$PL = -28 - 10\alpha log_{10} r$
Rayleigh NLoS direct links	$\alpha = 3.75$
Ricean LOS through RIS links	$\alpha = 2$
Noise variance	$\sigma^2 = -174(\text{dBm/Hz}) + 10\log_{10} B\,(\text{Hz}) + \text{F(dB)}$
Tx Power	$P_t = 10$ dBm

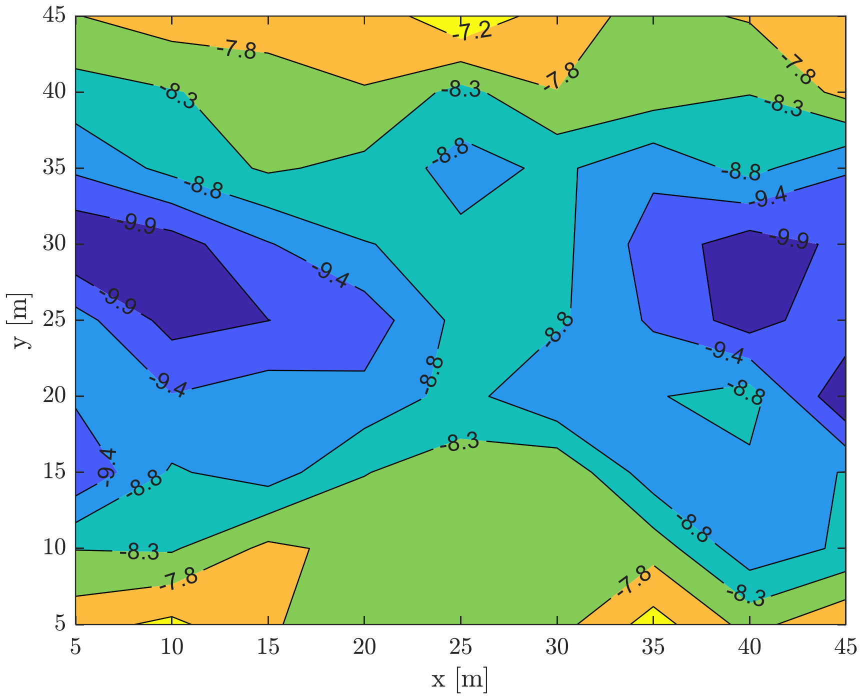

Figure 5-11 ΔINR as a function of the position of a BD-RIS with M=40 elements in a MIMO-IC.

Figure 5-11 shows the reduction in interference measured as in (5-2) achieved by varying the position in the (x,y) plane of a fully-connected BD-RIS with M=40 elements. The positions in the (x,y) plane vary on a grid of 5 [m] along each coordinate while the height remains fixed at z=5 [m]. We can observe two optimal positions or hot spots for the BD-RIS at approximately (10, 25, 5) [m] and (40,25,5) [m], where a reduction of about 10 dB in the interference level is achieved with respect to a scenario without BD-RIS

Figure 5-12 shows the sum rate obtained by different precoders designed in Stage II as a function of the number of BD-RIS elements for two transmission powers. When the power transmitted by the users is $P_t =$ 10 dBm, the interference level is not very high. Therefore, a BD-RIS with a moderate number of elements can eliminate much of this interference thus transforming the MIMO-IC into K=3 parallel MIMO Gaussian channels. This is why the differences between Max-SR, Max-SINR, and SVD-based precoders are negligible for $M \geq 60$. When the power transmitted by the users increases to $P_t = 20$ dBm, the residual interference not eliminated by the BD-RIS is higher and therefore the differences between the performance of the precoders are more remarkable. The Max-SR precoders provide the best performance as expected. When the precoders and BD-RIS are jointly designed to minimize IL, a BD-RIS with M=20 elements is capable of drowning out interference below the noise level, and hence increasing M does not translate into a sum rate improvement.

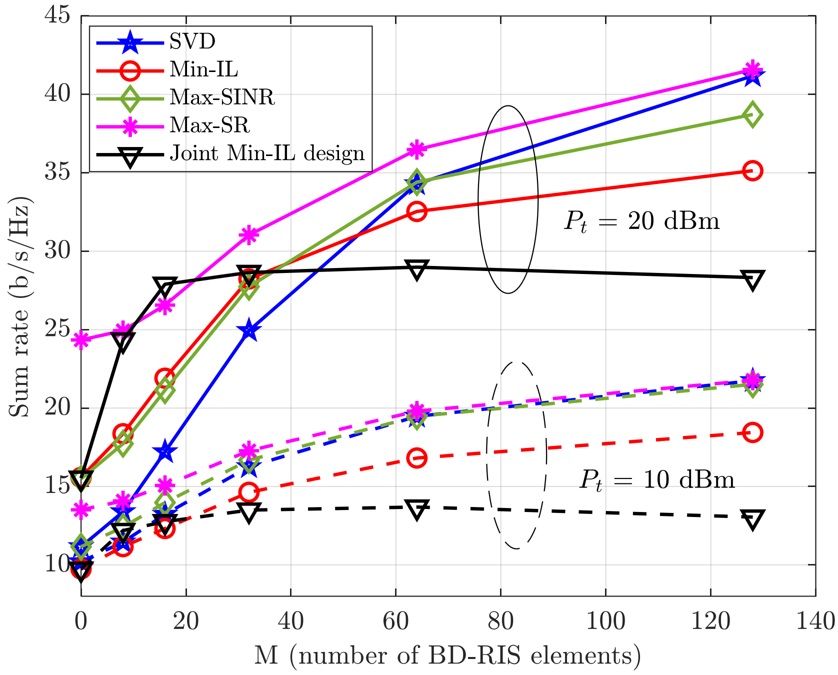

Figure 5-12 Sum rate vs. M for a BD-RIS assisted $(3 \times 3, 2)^2$ MIMO-IC with different precoders. The users transmit $P_t = 10$ dBm (dashed lines) or $P_t = 20$ dBm (solid lines).

5.2.3 RIS-Based Offset Index Modulation for MIMO Systems

The proposed RIS-OIM scheme introduces a novel offset mechanism and block selection strategies to enhance MIMO communication systems. This section elaborates on the system model, the offset design principles, block selection methods, and their implications for SE, EE, and reliability.

5.2.3.1 System Model

The system incorporates: Transmitting Antennas (TAs), RIS blocks, and Receiving Antennas (RAs). RIS is divided into G blocks, each containing S elements, making the total RIS elements:

$$N = G \times S \tag{5-3}$$

The cascaded channel is modeled as:

$$\Psi_g = D_g \Phi_g H_g \tag{5-4}$$

where H_g and D_g are the channel matrices from TAs to RIS blocks and RIS blocks to RAs, respectively, and Φ_g represents the RIS phase-shifter matrix.

The transmitted signal is expressed as:

$$x = [x_{g,1,\dots,} x_g, N_t]^T, g \in \{1, \dots, G\} \tag{5-5}$$

where x is offset to another RIS block j, yielding:

$$\bar{x} = [x_{j,1,\dots,} x_j, N_t]^T, j \in \{1, \dots, G\} \tag{5-6}$$

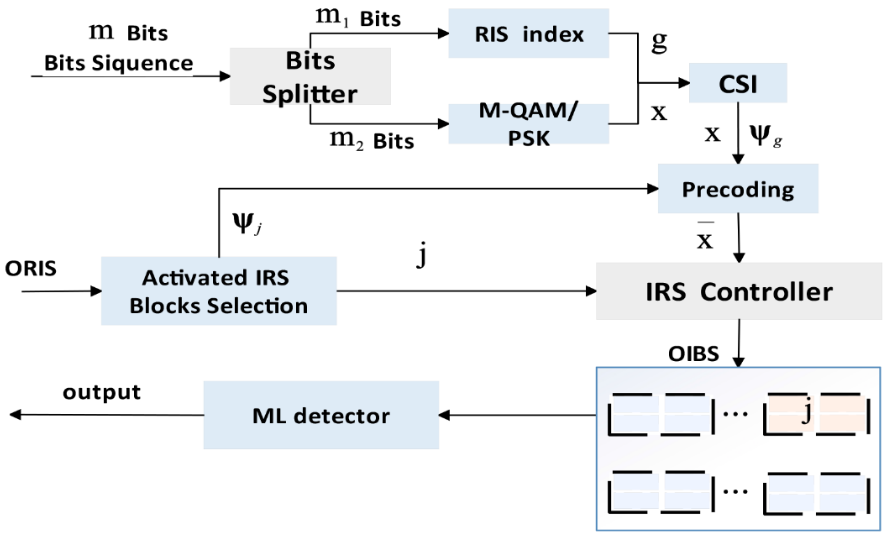

Figure 5-13 System model of the RIS-OIM scheme.

Figure 5-13 illustrates the system components, including the transmitting antennas, RIS blocks, receiving antennas, and the cascaded channel model. It visualizes how the signal propagates through the TAs, is reflected by selected RIS blocks, and finally reaches the RAs. The figure supports understanding of the mathematical model and how the offset modulation and block selection operate in the system.

5.2.3.2 Offset-Based Block Selection (OIBS) Methods

Three novel OIBS approaches are introduced to balance complexity and performance:

a) *Static OIBS (S-OIBS):* A fixed RIS block is selected, minimizing controller operations. Mathematically:

$$\bar{x} = \Psi_j^{-1}\Psi_g\beta_j x \tag{5-7}$$

where β_j normalizes transmit power.

b) Dynamic Optimal OIBS (DO-OIBS): The RIS block j is selected dynamically based on channel gain:

$$j = arg \max_{g\in\chi} \mid \delta g \mid, \delta g = (det(\Psi_g \Psi_g^T))^{1/2} \tag{5-8}$$

c) *Dynamic Multi-Activation OIBS (DMA-OIBS):*

Multiple RIS blocks are activated, enhancing the effective gain:

$$J = \{j_{1,\dots,}j_n\}, \bar{x} = \sum_{j\in J} \Psi_j^{-1}\Psi_g\beta_j x \tag{5-9}$$

5.2.3.3 Mathematical Analysis

a) Average Bit Error Probability (ABEP): The ABEP upper bound for RIS-OIM is derived as:

$$P_c \leq \frac{1}{\gamma 2\gamma} \sum_{i=1}^{\gamma} \sum_{j=1}^{\gamma} e_{i,j} \prod_{m=1}^{r_{i,j}} \left(\frac{8}{8+\rho\beta^2\lambda_{i,j,m}} \right)^{N_r} \tag{5-10}$$

b) Complexity Analysis

Floating-point operations for each scheme are detailed, showing that while RIS-OIM has higher complexity than RGB-IM, its BER performance is significantly improved.

5.2.3.4 Simulation Results

The proposed RIS-OIM scheme for MIMO systems was evaluated using extensive simulations. The results demonstrate the effectiveness of the novel offset-based block selection strategies (Static OIBS, Dynamic Optimal OIBS, and Dynamic Multi-Activation OIBS) in enhancing system performance. Key metrics include BER, SE, and computational complexity under various configurations.

Figure 5-14 presents the BER performance of RIS-OIM with the proposed block selection strategies (Static OIBS, Dynamic Optimal OIBS, and Dynamic Multi-Activation OIBS) compared to a benchmark scheme, RGB-IM.

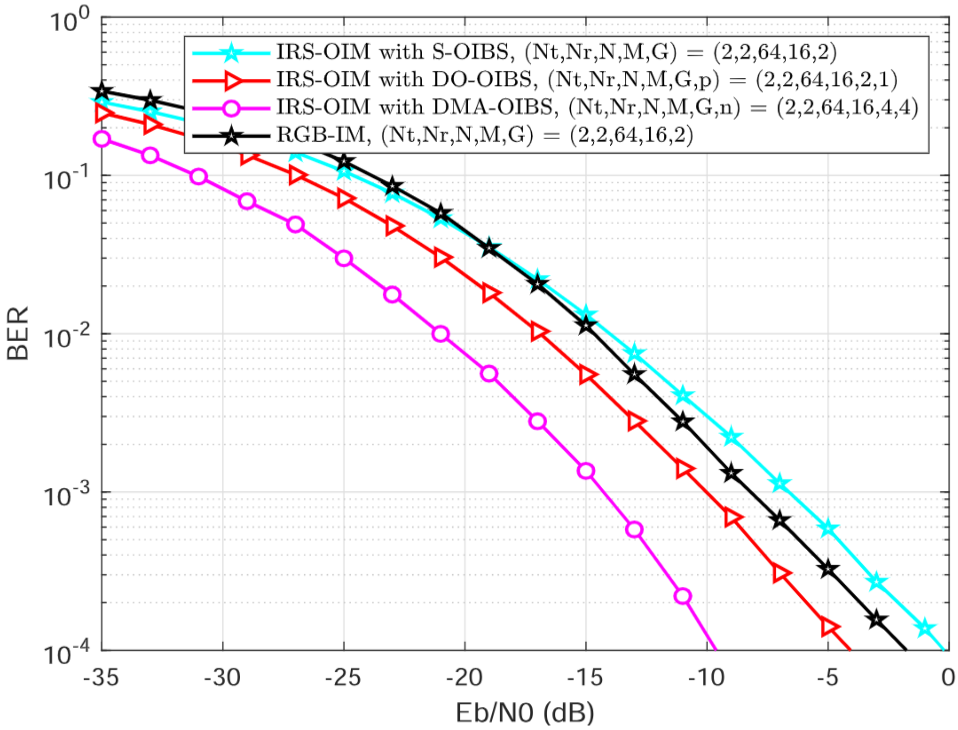

Figure 5-14 BER performance comparison of RIS-OIM with S-OIBS, DO-OIBS, and DMA-OIBS respectively, and RGB-IM.

Among the proposed schemes, Dynamic Multi-Activation OIBS demonstrates the lowest BER across all SNR values. For instance, at an SNR of 10 dB, it achieves a BER reduction of up to 7 dB compared to RGB-IM. The Dynamic Optimal OIBS strategy also shows significant improvements over RGB-IM, particularly in high-noise scenarios, due to its adaptive block selection mechanism based on channel gain. While Static OIBS provides comparable performance to RGB-IM, its fixed block selection approach limits its adaptability to dynamic channel conditions.

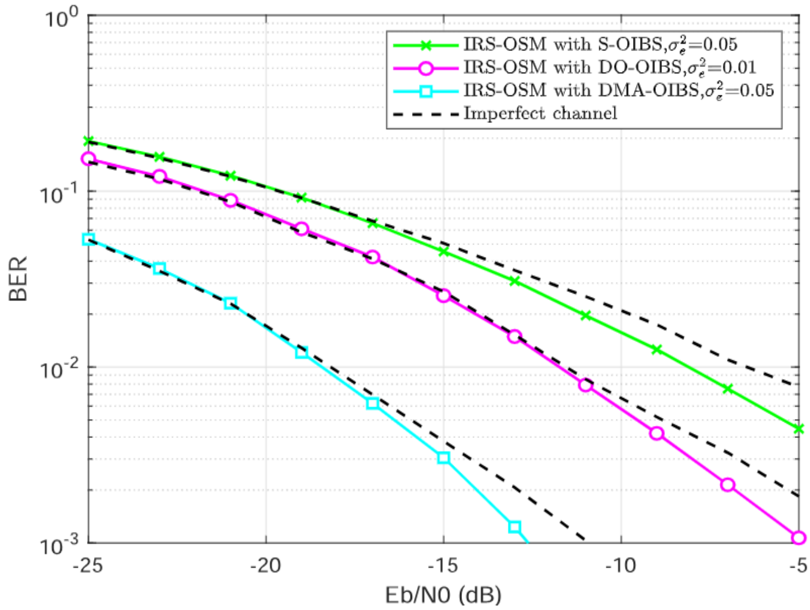

Figure 5-15 Comparison of perfect channel information and imperfect channel information of RIS-OIM with S-OIBS, DO-OIBS, and DMA-OIBS respectively.

Figure 5-15 highlights the trade-off between SE and computational complexity for the proposed RIS-OIM schemes under varying configurations of RIS elements and block sizes. Dynamic Multi-Activation OIBS achieves the highest SE among the schemes, leveraging the activation of multiple RIS blocks to maximize channel utilization. This improvement comes with a moderate increase in computational complexity. Static OIBS exhibits lower complexity due to its fixed block selection but achieves reduced SE compared to the dynamic strategies. Dynamic Optimal OIBS strikes a balance between SE and complexity, making it a suitable choice for scenarios requiring moderate performance gains with manageable computational demand. The simulation results validate the advantages of the proposed RIS-OIM schemes in enhancing the reliability and efficiency of MIMO systems. The key outcomes include:

- Lower BER: Up to 7 dB improvement over RGB-IM at high SNR values.
- Higher SE: Especially in Dynamic Multi-Activation OIBS, without significant sacrifices in complexity.
- Flexible Trade-Offs: Between performance and complexity, offering tailored solutions for various scenarios.

5.2.4 Active RIS in Digital Twin-Based URLLC IoT Networks

This part addresses the challenge of optimizing ultra-reliable and low-latency communications (URLLC) in DT-enabled IoT networks. By leveraging active RIS and MEC, the paper proposes and evaluates fully-connected and sub-connected active RIS architectures. The work focuses on minimizing total e2e latency under various constraints, such as power budgets, imperfect CSI, and computational capacity.

5.2.4.1 System Model

The study employs a DT-assisted MEC-enabled IoT network where IoT user nodes (UNs) communicate with a BS through an active RIS due to the lack of a direct communication link.

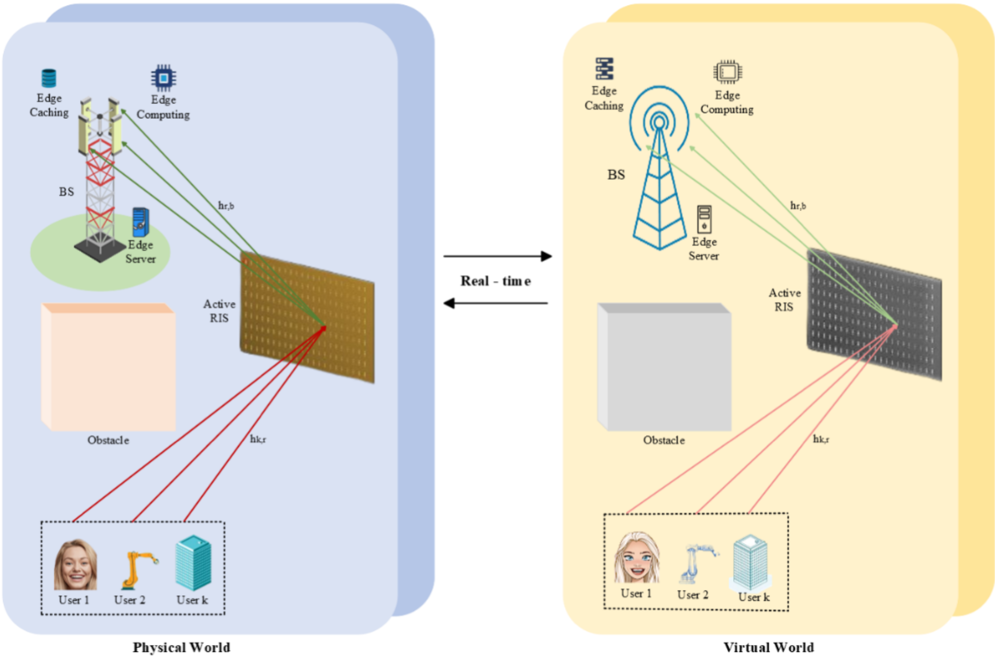

Figure 5-16 URLLC fully-connected active RIS-DT system.

Figure 5-16 depicts the DT-assisted IoT network with fully-connected and sub-connected active RIS configurations. It illustrates the flow of data from IoT UNs to the BS via the RIS, highlighting the system components and channel models.

Active RIS Elements: Each RIS element introduces a reflection coefficient:

$$\phi_n = \alpha_n n e^{j\theta_n} \tag{5-11}$$

where α_n is the amplitude and θ_n is the phase shift.

Channel Model:

- IoT UN to RIS Channel:

$$h_{r,k} = d_{r,k}^{\frac{-\gamma}{2}} \sqrt{\frac{Z_{r,k}}{1 + Z_{r,k}}} q_{LoS} + \sqrt{\frac{1}{1 + Z_{r,k}}} q_{NLoS} \tag{5-12}$$

where $d_{r,k}$ is the distance, $Z_{r,k}$ is the Rician factor, and q terms are LoS and Non-Line-of-Sight (NLoS) components.

RIS to BS Channel:

$$H_{b,r} = d_{b,r}^{\frac{-\gamma}{2}} \sqrt{\frac{Z_{b,r}}{1 + Z_{b,r}}} Q_{LoS} + \sqrt{\frac{1}{1 + Z_{b,r}}} Q_{NLoS} \tag{5-13}$$

Signal Reception:

- Effective Channel:

$$h_k = H_{b,r} \Phi h_{r,k} \tag{5-14}$$

- Received Signal:

$$y_b = w_k^H \left(h_k x_k + H_{b,r} \Phi z_0 + n_b \right) \tag{5-15}$$

where z_0 and $n_b$are noise terms.

5.2.4.2 Optimization Framework

The study formulates latency minimization problems for fully-connected and sub-connected architectures.

Latency Minimization:

- Fully-Connected Architecture:

$$\min_{\Phi,\beta k,\mu k} \sum_{k=1}^{K} T_k^{tot} \tag{5-16}$$

subject to constraints on power, caching, and latency.

Sub-Connected Architecture: Incorporates additional variables for power amplifiers:

$$\boldsymbol{\Phi} = diag(\phi_1, \dots, \phi_N), \Gamma = diag(\gamma_1, \dots, \gamma_L) \tag{5-17}$$

Optimization Variables:

- **Beamforming Design**: Optimized using MMSE: $w_k^* = (HH^H + \sigma^2 I)^{-1} H$
- **Caching and Offloading**: Modeled as:

$$T_k^{cache} = \frac{Data\ Size}{Caching\ Rate} \tag{5-18}$$

5.2.4.3 Simulation Results

The performance of the proposed fully-connected (FC) and sub-connected (SC) active RIS architectures was evaluated under various system configurations and compared against benchmark schemes, including Passive RIS with Optimal Beamforming (PRO) and Active RIS with Random Beamforming (ARR). Key metrics include total e2e latency, EE, and scalability, with a focus on scenarios involving imperfect CSI.

Figure 5-17 illustrates the convergence behavior of the Alternating Optimization (AO) algorithm for FC and SC active RIS configurations under both perfect and imperfect CSI conditions.

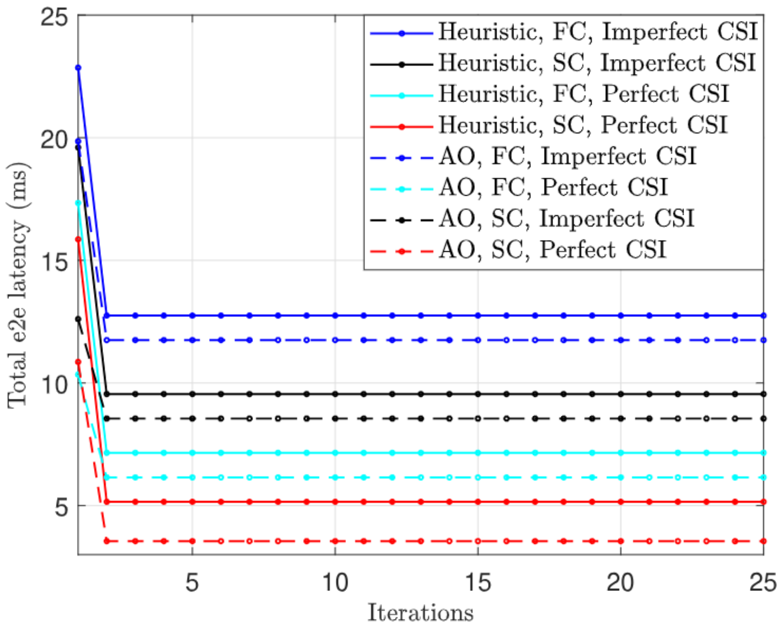

Figure 5-17 Convergence of the proposed Algorithm for two distinct cases: fully-connected and sub-connected RIS configurations.

The SC configuration consistently demonstrates lower E2E latency compared to the FC configuration. This is attributed to its reduced computational complexity and optimized signal path achieved through shared power amplifiers. Under imperfect CSI, the SC RIS maintains a steady performance with a latency reduction of approximately 11% compared to FC RIS. This indicates that SC RIS is less sensitive to channel estimation errors, a critical factor in real-world scenarios. The faster convergence of the AO algorithm for SC RIS reflects its lower overhead in controlling fewer active elements compared to FC RIS. The reduced convergence time highlights its suitability for real-time IoT applications requiring ultra-low latency.

Figure 5-18 examines the impact of the number of RIS elements (N) on E2E latency across different configurations, comparing FC and SC RIS with benchmark schemes such as PRO and ARR. As N increases, the SC RIS configuration shows a consistent reduction in latency, outperforming FC RIS and benchmark schemes. The latency reduction is primarily due to the intelligent phase and beamforming adjustments enabled by the SC architecture. SC RIS with Active RIS Optimal Beamforming (ARO) achieves up to 2.23 times lower latency compared to PRO schemes and a 2.38 times improvement compared to ARR schemes for higher values of N. This improvement reflects the ability of the SC RIS to balance computational efficiency and signal amplification. The SC RIS architecture scales effectively with the number of RIS elements, optimizing resource allocation and enhancing channel gain diversity. In contrast, the FC RIS architecture experiences higher latency due to the need for individually controlling a larger number of active elements.

In addition to latency improvements, the SC architecture achieves significant energy savings compared to the FC architecture. By sharing power amplifiers among groups of RIS elements, SC RIS reduces the total power consumption without compromising system performance. Moreover, the scalability of SC RIS ensures that its benefits extend to scenarios with a larger number of IoT devices and higher traffic loads.

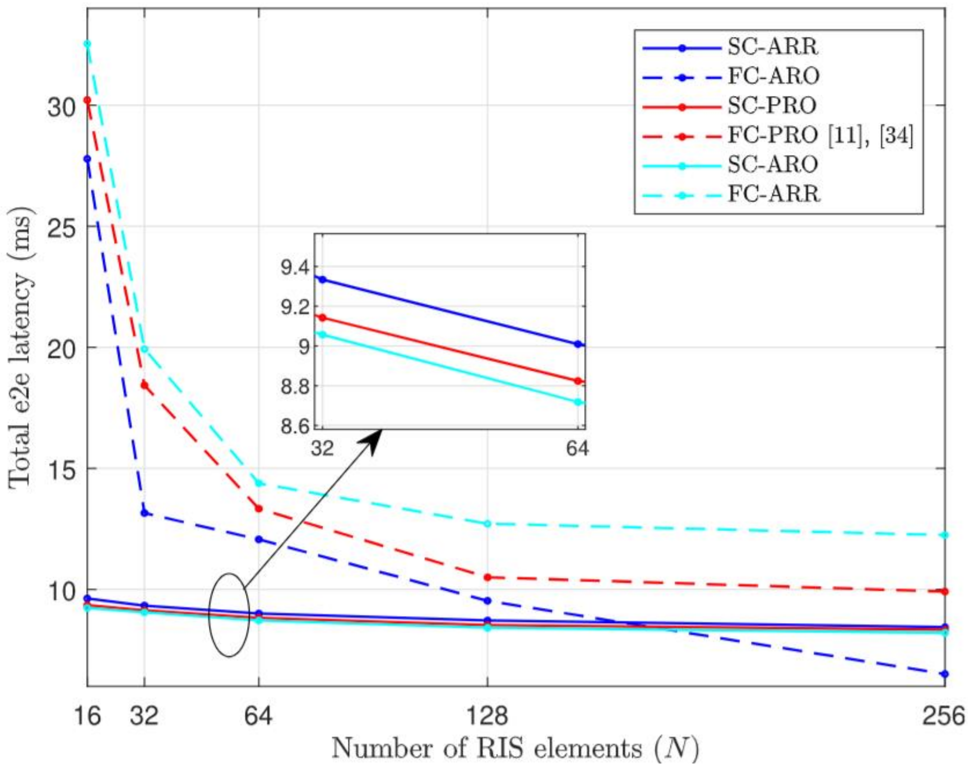

Figure 5-18 Effect of N.

5.2.5 RIS-assisted ISAC

5.2.5.1 State-of-the-art

To date, many publications have proposed the interplay of RISs and ISAC systems. The 3GPP Technical Specification Group Service and System Aspects Working Group 1 (SA1) has outlined some scenarios and requirements for ISAC. Following the outcomes of SA1, the channel model for ISAC is under intense discussion in RAN Working Group 1 (RAN1). Given the advantages of RIS in both communications and sensing functionalities, it can be envisaged that RIS-assisted ISAC will likely play an important role in the future generation wireless systems [192].

The goal is to increase SINR and target illumination power [180], mostly in NLoS scenarios [182], [183], [184], [185]. In this case, the degrees of freedom come from waveform design and RIS phase shifts to achieve the desired sensing and communication metrics.

Most works tackle relatively simple scenarios, e.g. single antenna for communications [186], or single user multiple targets [187], multiple users single target [188], [189]. In their most generic form, [182], [190], [193], [181] discuss the settings of RIS-assisted ISAC systems for multiple users and targets.

In [182], information is communicated and sensed via a single dedicated transmit waveform. For an ISAC system with independent colocated subarrays for sensing and communication, the transmit beamformers and reflection coefficients are constructed in [190]. The signal received at the RIS also takes up a lot of radar waveforms because radar and communication subarrays are so close to one another. This increases interference at the UEs but is ignored in [190]. Furthermore, target detection is impossible anytime the direct pathways to the targets are blocked because the DFBS senses the targets directly without any help from the RIS. A practical method for reducing mutual interference in wireless communication systems is to deploy RIS next to a communication device, as was done in the development of the dual-functional RIS-aided ISAC system [182]. When there is no direct path between the dual-functional radar and communication (DFRC) BS and the sensing target, the study mentioned in [184] uses RIS to achieve joint localization and communication. An algorithm for RIS passive beamforming as well as a target localization technique were recommended by the authors. In a more general scenario where the DFRC BS and target are in close contact, the authors of [185] suggested a revolutionary method that makes use of a single RIS for both sensing and communication needs. The coexistence of MIMO radar and multi-user communication systems in the shared spectrum presents an interference management challenge, as explored by [183] using RIS. The joint trajectory, sensing, and communication design of UAV were taken into consideration in [191]. Using RIS, the coexistence of multi-user communication systems and MIMO radar in the common spectrum was investigated in [183]. A radar-communication-coexistence (RCC) system with RIS assistance is considered in [193]. For sensing and communication, this system makes use of transceivers that are not dependent on geography. The goal of the study in [193] is limited to the communication interference minimization of the radar system; radar waveform design to attain a specific radar performance is not considered. The total radar SNR owing to multiple targets is the radar performance statistic that is used to build independent communication and sensor beamformers, according to [181]. One target may receive all of the power if the total radar SNR is utilized as a radar metric, which could result in one or more targets being completely missed by the radar system.

In [180] the performance improvement due to the joint use of RIS and ISAC is studied in different scenarios (comm enhancement only and dual-RIS assisted ISAC for both comms and radar improvement). The comm-RIS assisted ISAC system significantly raises the fairness SINR of the communication UEs while only slightly degrading the worst-case target illumination power.

5.2.5.2 6G-SENSES work on RIS-assisted ISAC

6G-SENSES will extend the SoTA in RIS through the development of realistic RIS and scalable models accounting for spatial correlation and the joint optimization of RIS and transceiver strategies for ISAC. RIS-assisted wideband wireless channels will be modelled based on measurements, ray-tracing and statistical models, taking hardware impairments and constraints into account.

A RIS panel will be leveraged to assess and compare the models with a real-world analysis in a lab environment. This panel will be used in the context of PoC#1. Based on these models, analytical investigations, optimization of RIS and transceiver strategies, and numerical assessments of the different KPIs are performed. Special focus lies on the novel aspect of joint optimization of RIS, including active, passive, beyond-diagonal (BD-RIS) phase shift matrices, and multi-sector RIS architectures for ISAC.

5.2.6 RIS-Assisted CF-mMIMO: Enhancing Performance Through Resource Optimization

6G-SENSES intends to bring new advancements to CF-mMIMO architectures thanks to the integration of RISs. This section describes some recent developments and reports on the WET, which brings additional synergies with the CF architecture and RIS-assisted wireless links.

In CF-mMIMO systems, the flexibility of RIS is particularly crucial, as it not only strengthens the reliability of communication links but also improves signal reception for UEs in complex environments through intelligent reflection mechanisms. Recent studies have demonstrated that RIS can also be integrated directly into the antenna arrays of APs, functioning as intelligent transmitting surfaces to expand the effective aperture area and further optimize system performance. Moreover, innovative approaches like RIS-based Offset Index Modulation (RIS-OIM) employ modular RIS design and optimized transmission strategies, significantly improving transmission reliability and data rates while reducing operational complexity.

These technological advancements highlight the substantial potential of RIS to enhance CF-mMIMO system performance, particularly in areas such as resource allocation, EE, and spectral utilization. The following sections will delve deeper into the performance optimization, EE improvements, and practical applications of RIS-assisted CF-mMIMO architectures, showcasing the innovative practices and research outcomes achieved in this domain.

RIS-assisted CF-mMIMO significantly outperforms traditional massive MIMO and pure CF-mMIMO. To fully exploit the performance gains, optimizing resource allocation in the distributed network is essential, with objectives varying based on QoS requirements. This section explores the interaction between RIS-assisted MIMO and wireless resource allocation across key communication metrics [212].

5.2.6.1 Energy Efficiency

RIS is highly valued in CF-mMIMO for its low cost and energy consumption. Studies show that iterative optimization of digital active beamforming at APs and RIS-based analogue passive beamforming can enhance EE by several orders of magnitude compared to conventional systems [215]. Replacing some APs with RISs can yield a twofold EE improvement over CF-mMIMO without RIS [216]. A fractional programming-based iterative algorithm proposed in [217] achieves at least 168% higher EE than traditional CF-mMIMO systems.

However, practical constraints like limited backhaul capacity are often overlooked. The study in [216] addresses this by designing an EE maximization framework under constraints such as per-AP transmit power, backhaul limitations, RIS nonconvexity, and minimum rate requirements. The proposed RIS-assisted CF-mMIMO system consistently outperformed centralized systems with or without RIS.

5.2.6.2 Spectral Efficiency

SE is another critical metric. By creating virtual LoS links, RIS improves user signals in dead zones or at cell edges, boosting the SE of CF MIMO.

The study in [218] introduces RIS-assisted CF MIMO to enhance network capacity and SE. The study proposes a general framework with multiple antennas, APs, users, RISs, and carriers. In each coherent timescale, a matching method pairs users with RISs, optimizing only matched channels while treating unmatched RISs as noise. The optimization problem is decoupled into two subproblems—active transmit precoding at APs and passive reflection precoding at RISs—solved iteratively for a suboptimal solution.

To address fronthaul constraints, the study in [219] proposed a decentralized cooperative framework based on alternating direction method of multipliers (ADMM). This method reduces backhaul overhead by incrementally updating and transmitting only a subset of variables, outperforming systems requiring full CSI exchange.

5.2.6.3 Applications of RIS-Assisted CF-mMIMO

This section discusses several emerging applications of RIS-assisted CF-mMIMO, such as WET. Integrating RIS with CF-mMIMO and these advanced technologies offers significant potential for beyond 5G networks. Below, we focus on RIS-assisted CF-mMIMO integration with WET and its impact on future wireless network services [212].

Many Internet of Everything (IoE) devices are energy-constrained due to their limited size and battery capacity. While frequent battery replacements could provide a temporary solution, the growing number of mobile devices in future communication systems like CF-mMIMO makes this option costly. To address this, WET has emerged as a promising solution. In this process, the RF energy emitted by the AP is captured by energy receivers through electromagnetic radiation, and this energy is then converted for use [212].

Despite the advantages of WET, challenges like signal attenuation and obstruction remain. RIS technology can help overcome these issues by enhancing the channel conditions via controlled signal reflection. In RIS-assisted CF MIMO systems, multiple cooperative APs transmit both information and energy-carrying signals to energy and information receivers, with RISs deployed to improve communication links [212].

Figure 5-19 shows the transmission flow in RIS-assisted CF-mMIMO system. Energy receivers first send energy demand signals to the APs through direct and RIS-assisted cascaded channels. The APs then forward these signals to the CPU, which allocates power and sends control signals back to the APs. Finally, the APs transmit energy to the energy receivers via downlink [212].

Figure 5-20 illustrates the system architecture, divided into four parts: energy receivers transmitting demand signals to APs via both direct and RIS-assisted channels; APs transmitting these signals to the CPU; the CPU allocating power and sending control signals to APs; and the APs transmitting wireless energy to the receivers.

Research has explored the integration of WET into RIS-assisted CF-mMIMO systems. The study in [218] examines deployment strategies, HW design, and operational modes, detailing the four-stage transmission process. The study in [219] investigates a weighted sum rate maximization problem under constraints including total power, energy harvesting, and RIS unit-modulus. Additionally, the study in [220] proposes a novel framework combining CF-mMIMO, RIS, and UAV technologies for RF energy transfer, showing superior energy harvesting performance compared to other benchmarks [212].

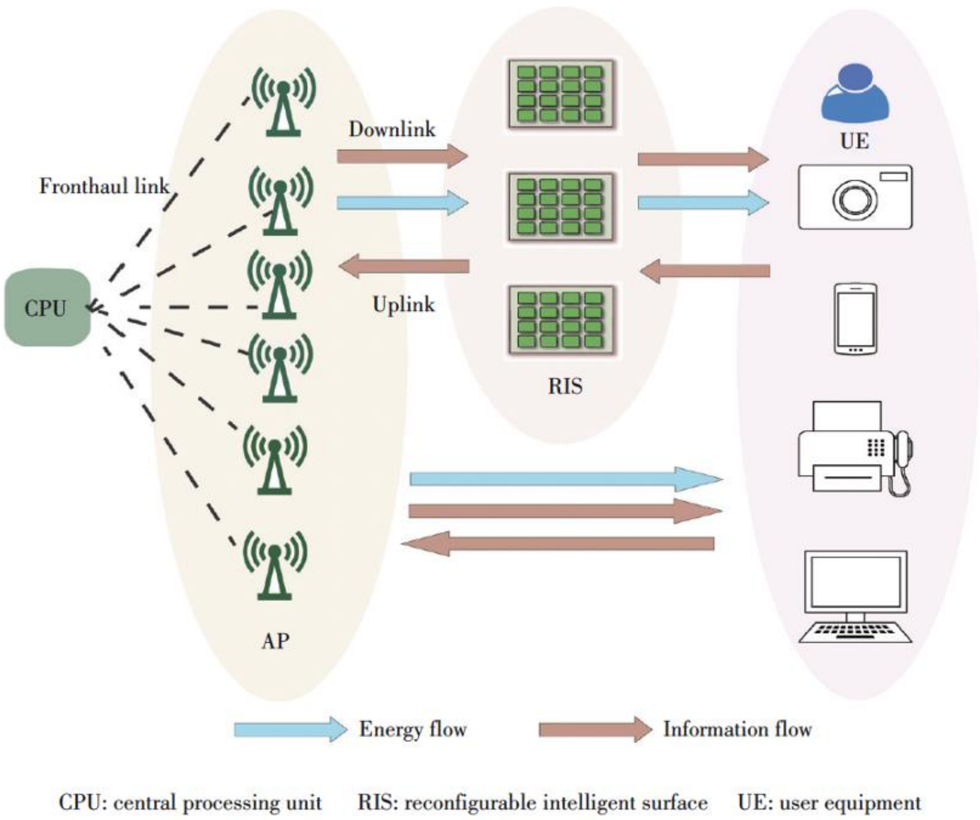

Figure 5-19 Transmission flow of RIS-assisted cell-free (CF) multiple-input multiple-output (MIMO) system with wireless energy transmission (WET) [212]

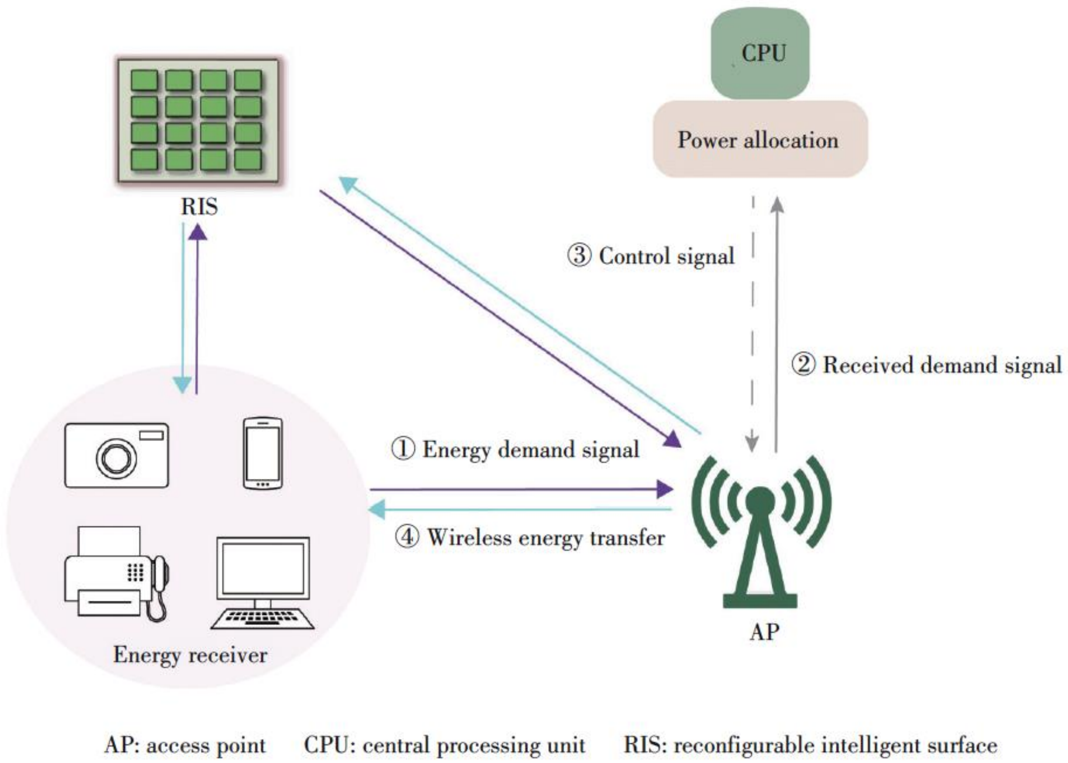

Figure 5-20 Architecture of RIS-assisted cell-free multiple-input multiple-output (CF MIMO) system with wireless energy transmission (WET) [212]

6 Conclusions

6G-SENSES has a bold vision for the future of wireless communication, seamlessly integrating sensing and communication to redefine the capabilities of 6G and beyond systems. By addressing the technical challenges of advanced frameworks such as ISAC and CF-mMIMO and harnessing the potential of emerging technologies like RIS, the initiative highlights a multifaceted approach to innovation. These efforts are not only aimed at improving technical efficiency but also at fostering human-centric, environmentally sustainable solutions that align with the needs of modern society.

6G-SENSES is developing a multi-technology/multi-layer platform able to support a large variety 6G services relying on a communication network infrastructure able to perform sensing. This deliverable is the first release of WP3 and promotes the research and development work carried out in the project during the first reporting period. Concretely, this deliverable: 1) provides a general vision of the data plane technologies (WATs) that are considered in the project; 2) investigates of waveforms and algorithms for ISAC to be used with 6G-SENSES technologies and to be implemented in the 6G-SENSES testbeds and PoCs; 3) proposes novel radio technologies for ISAC and design and development of energy aware O-RAN enabled control platforms for ISAC; 4) Includes the design and evaluation of signal processing techniques and algorithms to support efficient CF-mMIMO operation and tailor these implementations for deployment on HW for real-time operation; 5) provides a first version of the design, and implementation of mmWave MIMO transceivers for ISAC that are ultra-low power; and 6) contributes to extend the SoTA of novel radio technologies associated to RIS.

In this project, the emphasis on foundational research, practical testbed implementations, and cross-disciplinary collaborations which sets it apart as a leader in the development of 6G technologies. By focusing on applications ranging from smart environments to industrial automation and autonomous systems, 6G-SENSES aims to unlock transformative potential across diverse sectors. The integration of EE systems and adaptive communication strategies ensures that these advancements are not only high-performing but also sustainable.

Ultimately, the findings and implementations presented in this deliverable demonstrate the capacity of 6G-SENSES to pave the way for a truly connected future. By uniting SotA technologies, the initiative ensures that 6G wireless systems can meet the ever-growing demands of an increasingly digital world while addressing critical societal needs. The work conducted under 6G-SENSES serves as a blueprint for innovation, setting a benchmark for future developments in wireless communication and sensing systems.

7 References

[1] 6G-SENSES deliverable D2.1, “Report on 6G-SENSES use cases, requirements and KPIs, and key technological advancements”, September 2024, https://6g-senses.eu/wp-content/uploads/2024/10/2024-09-30-6G-SENSES_Deliverable_2_1_vf.pdf

[2] Z. Wei *et al.*, “Integrated sensing and communication signals toward 5G-A and 6G: A survey,” in *IEEE Internet of Things Journal*, vol. 10, no. 13, pp. 11068-11092, 1 July1, 2023, doi: 10.1109/JIOT.2023.3235618.

[3] 6G SNS White Paper, “RESEARCH PRIORITIES ON MICROELECTRONICS FOR 6G NETWORKS R&I ACTIVITIES”, https://6g-ia.eu/wp-content/uploads/2024/02/6g-ia-position-paper_microelectronics-final.pdf

[4] 6G SNS White Paper, “Open RAN and 6G Future Networks Development” https://6g-ia.eu/wp-content/uploads/2024/05/6g-ia-open-sns_open-networks-status-and-future-development_ran-final.pdf

[5] S. Buzzi and C. D’Andrea, "Cell-Free Massive MIMO: User-Centric Approach," in *IEEE Wireless Communications Letters*, vol. 6, no. 6, pp. 706-709, Dec. 2017, doi: 10.1109/LWC.2017.2734893.

[6] O-RAN Alliance Working Group 1 (Use Cases and Overall Architecture), “O-RAN Architecture Description”, O-RAN.WG1.OAD-R003-v12.00, June 2024.

[7] R. Beerten, A. Girycki, and S. Pollin, “User centric cell-free massive MIMO in the O-RAN architecture: Signalling and algorithm integration,” in *Proc. IEEE Conf. Standards Commun. Netw. (CSCN)*, Nov. 2022, pp. 181–187.

[8] V. Ranjbar, A. Girycki, M. A. Rahman, S. Pollin, M. Moonen, and E. Vinogradov, “Cell-free mMIMO support in the O-RAN architecture: A PHY layer perspective for 5G and beyond networks,” in *IEEE Commun. Standards Mag.*, vol. 6, no. 1, pp. 28–34, Mar. 2022.

[9] 5G PPP Technology Board, “On Board Procedure to 5G PPP Infrastructure Projects”, version 1.0, March 2020, https://5g-ppp.eu/wp-content/uploads/2020/04/On-Board-Procedure-to-5GPPP-Infrastructure-Projects-1.pdf

[10] IEEE P802.11.2/D1.01 – Draft Recommended Practice for the Evaluation of 802.11 Wireless Performance. February 2008.

[11] 6G-SENSES deliverable D2.2, “System architecture and preliminary evaluations”, (to appear) January 2025.

[12] X. Shao, C. You, W. Ma, X. Chen, and R. Zhang, “Target sensing with intelligent reflecting surface: Architecture and performance,” in *IEEE Journal on Selected Areas in Communications*, vol. 40, no. 7, pp. 2070–2084, Jul. 2022.

[13] M. Kamel, W. Hamouda, and A. Youssef, “Ultra-dense networks: A survey,” in *IEEE Commun. Surveys Tuts.*, vol. 18, no. 4, pp. 2522–2545, 4th Quart. 2016.

[14] H. Q. Ngo, G. Interdonato, E. G. Larsson, G. Caire and J. G. Andrews, "Ultradense Cell-Free Massive MIMO for 6G: Technical Overview and Open Questions," in *Proceedings of the IEEE*, vol. 112, no. 7, pp. 805-831, July 2024, doi: 10.1109/JPROC.2024.3393514.

[15] O. T. Demir, M. Masoudi, E. Bjornson, and C. Cavdar, “Cell-free massive MIMO in O-RAN: Energy-aware joint orchestration of cloud, fronthaul, and radio resources,” in *IEEE Journal on Selected Areas in Communications*, vol. 42, no. 2, pp. 356–372, Feb. 2024.

[16] F. Liu et al., “Joint Radar and Communication Design: Applications, State-of-the-Art, and the Road Ahead,” in *IEEE Transactions on Communications*, vol. 68, no. 6, June 2020, pp. 3834–62.

[17] F. Liu and Et. al., “Integrated sensing and communications: Toward dual-functional wireless networks for 6G and beyond,” in *IEEE Journal on Selected Areas in Communications*, vol. 40, no. 6, pp. 1728–1767, 2022.

[18] 3GPP TR 22.837 V19.4.0 (2024-06) Feasibility Study on Integrated Sensing and Communication (Release 19).

[19] Z. Behdad, Ö. T. Demir, K. W. Sung, E. Björnson and C. Cavdar, "Multi-Static Target Detection and Power Allocation for Integrated Sensing and Communication in Cell-Free Massive MIMO," in *IEEE Transactions on Wireless Communications*, vol. 23, no. 9, pp. 11580-11596, Sept. 2024, doi: 10.1109/TWC.2024.3383209.

[20] N. González-Prelcic et al., "The Integrated Sensing and Communication Revolution for 6G: Vision, Techniques, and Applications," in *Proceedings of the IEEE*, vol. 112, no. 7, pp. 676-723, July 2024, doi: 10.1109/JPROC.2024.3397609.

[21] ITU-R IMT towards 2030 and beyond, “New Recommendation ITU-R M.2160 on the “IMT-2030 Framework” (November 2023)”, URL: https://www.itu.int/en/ITU-R/study-groups/rsg5/rwp5d/imt-2030/Pages/default.aspx

[22] Z. Feng, Z. Fang, Z. Wei, X. Chen, Z. Quan, and D. Ji, “Joint radar and communication: A survey,” in *China Communications*, vol. 17, no. 1, pp. 1–27, Jan. 2020.

[23] C. B. Barneto, S. D. Liyanaarachchi, M. Heino, T. Riihonen, and M. Valkama, “Full duplex radio/radar technology: The enabler for advanced joint communication and sensing,” in *IEEE Wireless Communications*, vol. 28, no. 1, pp. 82–88, 2021.

[24] C. B. Barneto, T. Riihonen, M. Turunen, L. Anttila, M. Fleischer, K. Stadius, J. Ryynänen, and M. Valkama, “Full-duplex OFDM radar with LTE and 5G NR waveforms: Challenges, solutions, and measurements,” in *IEEE Transactions on Microwave Theory and Techniques*, vol. 67, no. 10, pp. 4042–4054, 2019.

[25] Y. Cui, X. Jing, and J. Mu, “Integrated Sensing and Communications Via 5G NR Waveform: Performance Analysis,” in *IEEE International Conference on Acoustics, Speech, and Signal Processing* (ICASSP), Singapore, Singapore, May 2022, pp. 8747–8751.

[26] D. Wen, Y. Zhou, X. Li, Y. Shi, K. Huang and K. B. Letaief, "A Survey on Integrated Sensing, Communication, and Computation," in *IEEE Communications Surveys & Tutorials*, doi: 10.1109/COMST.2024.3521498.

[27] A. Tang, S. Li, and X. Wang, “Self-interference-resistant IEEE 802.11adbased joint communication and automotive radar design,” in *IEEE Journal on Selected Topics in Signal Processing*, vol. 15, no. 6, pp. 1484–1499, 2021.

[28] C. Wu, F. Zhang, B. Wang, and K. J. R. Liu, “mmTrack: Passive multiperson localization using commodity millimeter wave radio,” in *Proc. IEEE INFOCOM*, April 27-30 2020.

[29] Y. Ge, H. Kim, L. Svensson, H. Wymeersch and S. Sun, "Integrated Monostatic and Bistatic mmWave Sensing," in *IEEE Global Communications Conference (GLOBECOM)*, Kuala Lumpur, Malaysia, 2023, pp. 3897-3903, doi: 10.1109/GLOBECOM54140.2023.10437391.

[30] V. Shatov et al., "Joint Radar and Communications: Architectures, Use Cases, Aspects of Radio Access, Signal Processing, and Hardware," in *IEEE Access*, vol. 12, pp. 47888-47914, 2024, doi: 10.1109/ACCESS.2024.3383771.

[31] N. Huang et al., "Edge Intelligence Oriented Integrated Sensing and Communication: A Multi-Cell Cooperative Approach," in *IEEE Transactions on Vehicular Technology*, vol. 73, no. 6, pp. 8810-8824, June 2024, doi: 10.1109/TVT.2024.3359094.

[32] X. Liu, H. Zhang, K. Sun, K. Long and G. K. Karagiannidis, "AI-Driven Integration of Sensing and Communication in the 6G Era," in *IEEE Network*, vol. 38, no. 3, pp. 210-217, May 2024, doi: 10.1109/MNET.2023.3326064.

[33] S. D. Liyanaarachchi, T. Riihonen, C. B. Barneto, and M. Valkama, "Optimized Waveforms for 5G–6G Communication with Sensing: Theory, Simulations and Experiments," in *IEEE Transactions on Wireless Communications*, vol. 20, no. 12, pp. 8301–8315, Dec. 2021.

[34] D. Ma, N. Shlezinger, T. Huang, Y. Liu, and Y. C. Eldar, "FRaC: FMCWBased Joint Radar-Communications System Via Index Modulation," in *IEEE Journal on Selected Topics in Signal Processing*, vol. 15, no. 6, pp. 1348–1364, Nov. 2021.

[35] F. Liu, Y. Cui, C. Masouros, J. Xu, T. X. Han, Y. C. Eldar, and S. Buzzi, "Integrated Sensing and Communications: Toward Dual-Functional Wireless Networks for 6G and Beyond," in *IEEE Journal on Selected Areas in Communications*, vol. 40, no. 6, pp. 1728–1767, Jun. 2022.

[36] W. Zhou, R. Zhang, G. Chen, and W. Wu, "Integrated sensing and communication waveform design: A survey," in *IEEE Open Journal of the Communications Society*, vol. 3, pp. 1930–1949, Oct. 2022.

[37] W. Zhou, R. Zhang, G. Chen, and W. Wu, "Integrated sensing and communication waveform design: A survey" in *IEEE Open Journal of the Communications Society*, 3, pp.1930-1949.

[38] Y. Li, F. Liu, Z. Du, W. Yuan, Q. Shi, and C. Masouros, "Frame Structure and Protocol Design for Sensing-Assisted NR-V2X Communications," in *IEEE Transactions on Mobile Computing*, Apr. 2024, Early access.

[39] H.-W. Hsu, M.-C. Lee, M.-X. Gu, Y.-C. Lin, and T.-S. Lee, "Analysis and Design for Pilot Power Allocation and Placement in OFDM Based Integrated Radar and Communication in Automobile Systems," in *IEEE Transactions on Vehicular Technology*, vol. 71, no. 2, pp. 1519–1535, Feb. 2022.

[40] K. Ji, Q. Zhang, Z. Wei, Z. Feng and P. Zhang, "Networking Based ISAC Hardware Testbed and Performance Evaluation," in *IEEE Communications Magazine*, vol. 61, no. 5, pp. 76-82, May 2023, doi: 10.1109/MCOM.005.2200440.

[41] K. Ji, Q. Zhang, Z. Wei, Z. Feng, and P. Zhang, "Networking Based ISAC Hardware Testbed and Performance Evaluation," in IEEE Communications Magazine, vol. 61, no. 5, pp. 76–82, May 2023.

[42] Z. Wei, Y. Wang, L. Ma, S. Yang, Z. Feng, C. Pan, Q. Zhang, Y. Wang, H. Wu, and P. Zhang, "5G PRS-Based Sensing: A Sensing Reference Signal Approach for Joint Sensing and Communication System," in *IEEE Transactions on Vehicular Technology*, vol. 72, no. 3, pp. 3250–3263, Mar. 2023.

[43] M. Lyu, H. Chen, D. Wang, G. Feng, C. Qiu and X. Xu, „Reference Signal-Based Waveform Design for Integrated Sensing and Communications System", https://arxiv.org/pdf/2411.07486

[44] K. V. Mishra, M. R. Bhavani Shankar, V. Koivunen, B. Ottersten and S. A. Vorobyov, "Toward Millimeter-Wave Joint Radar Communications: A Signal Processing Perspective," in *IEEE Signal Processing Magazine*, vol. 36, no. 5, pp. 100-114, Sept. 2019, doi: 10.1109/MSP.2019.2913173.

[45] C. De Lima et al., "Convergent Communication, Sensing and Localization in 6G Systems: An Overview of Technologies, Opportunities and Challenges," in *IEEE Access*, vol. 9, pp. 26902-26925, 2021, doi: 10.1109/ACCESS.2021.3053486.

[46] P. Sen, A. Harutyunyan, M. Umar, S. Kamal, "Joint Communication and Radar Sensing: RF Hardware Opportunities and Challenges—A Circuits and Systems Perspective", in *Sensor*, 23, 7673, 2023, https://doi.org/10.3390/s23187673

[47] M. Li, S. -L. Chen, Y. Liu and Y. J. Guo, "Wide-Angle Beam Scanning Phased Array Antennas: A Review," in *IEEE Open Journal of Antennas and Propagation*, vol. 4, pp. 695-712, 2023, doi: 10.1109/OJAP.2023.3296636.

[48] Y. Li, S. Xiao and J. Guo, "A Review of Wideband Wide-Angle Scanning 2-D Phased Array and its Applications in Satellite Communication," in *Journal of Communications and Information Networks*, vol. 3, no. 1, pp. 21-30, March 2018, doi: 10.1007/s41650-018-0001-x.

[49] E. Ali, et al., "Beamforming techniques for massive MIMO systems in 5G: overview, classification, and trends for future research," in *Frontiers Inf Technol Electronic Eng*, 18, 753–772 (2017). https://doi.org/10.1631/FITEE.1601817

[50] M. Umar, M. Laabs, N. Neumann and D. Plettemeier, "Bondwire Model and Compensation Network for 60 GHz Chip-to-PCB Interconnects," in *IEEE Antennas and Wireless Propagation Letters*, vol. 20, no. 11, pp. 2196-2200, Nov. 2021, doi: 10.1109/LAWP.2021.3108499.

[51] B. B. Adela, P. van Zeijl and A. B. Smolders, "Bondwire impedance compensation using a series transmission line section," in *European Conference on Antennas and Propagation (EuCAP)*, Davos, Switzerland, 2016, pp. 1-4, doi: 10.1109/EuCAP.2016.7481607.

[52] C. -H. Chan, C. -C. Chou and H. -R. Chuang, "Integrated Packaging Design of Low-Cost Bondwire Interconnection for 60-GHz CMOS Vital-Signs Radar Sensor Chip with Millimeter-Wave Planar Antenna," in *IEEE Transactions on Components, Packaging and Manufacturing Technology*, vol. 8, no. 2, pp. 177-185, Feb. 2018, doi: 10.1109/TCPMT.2017.2782342.

[53] W. -M. Wu, M. -C. Yu, C. -H. Li and C. -N. Kuo, "A low-cost DC-to-92 GHz broadband three-path bondwire interconnect," in *IEEE International Symposium on Radio-Frequency Integration Technology (RFIT)*, Sendai, Japan, 2015, pp. 34-36, doi: 10.1109/RFIT.2015.7377878.

[54] M. Umar, A. Schmidt, M. Laabs, N. Neumann and D. Plettemeier, "A 60-GHz Antenna-Duplexed Modular Front-End for Channel Sounding and Physical Layer Security," in *IEEE Transactions on Circuits and Systems*, vol. 71, no. 12, pp. 6152-6165, Dec. 2024, doi: 10.1109/TCSI.2024.3428609.

[55] P. Zetterberg and R. Fardi, "Open Source SDR Frontend and Measurements for 60-GHz Wireless Experimentation," in *IEEE Access*, vol. 3, pp. 445-456, 2015, doi: 10.1109/ACCESS.2015.2414815.

[56] R. Zhao, T. Woodford, T. Wei, K. Qian, and Z. Zhang, "M-Cube: A Millimeter-Wave Massive MIMO Software Radio," in the *26th Annual Conference in Mobile Computing and Communications (MobiCom'20)*, Sep. 2020, pp. 1–14.

[57] Z. Zhou, C. Zhang, and Y. Zeng, "Prototype of Real-time Integrated Sensing and Communication with Millimeter-Wave OFDM," in *IEEE/CIC International Conference on Communications in China (ICCC)*, Aug. 2023, pp. 1–2.

[58] P. Kumari, A. Mezghani, and R. Heath, "JCR70: A Low-Complexity Millimeter-Wave Proof-of-Concept Platform for a Fully-Digital SIMO Joint Communication-Radar," in *IEEE Open Journal of Vehicular Technology*, vol. PP, pp. 1–1, Mar. 2021.

[59] M. Neu, C. Karle, B. Nuss, P. Groeschel, and J. Becker, "A Scalable and Cost-Efficient Antenna Testbed Using FPGA-Server Compound Structures for Prototyping 6G Applications," in *19th International Conference on Distributed Computing in Smart Systems and the Internet of Things (DCOSS-IoT)*, Jun. 2023, pp. 171–178.

[60] M. Engelhardt, S. Giehl, M. Schubert, A. Ihlow, C. Schneider, A. Ebert, M. Landmann, G. Del Galdo, and C. Andrich, "Accelerating Innovation in 6G Research: Real-Time Capable SDR System Architecture for Rapid Prototyping," May 2024, preprint on arXiv at https://arxiv.org/abs/2402.06520.

[61] S. Wittig et al., "Demonstration of a Real-Time Testbed for D-Band Integrated Sensing and Communication," in *IEEE Military Communications Conference (MILCOM)*, Washington, DC, USA, 2024, pp. 641-642, doi: 10.1109/MILCOM61039.2024.10774050.

[62] M Petri, N. Maletic, "A mmWave JCAS System for Real-Time High-Data Rate Communication and RADAR Sensing", submitted to IEEE Access.

[63] K. I. Lee, J. Mung Shin, D. I. Kim and K. Won Choi, "An Experimental Proof of Concept for OFDM-based ISAC System Utilizing Stepped-Carrier and TDM MIMO scheme," in *IEEE 25th International Workshop on Signal Processing Advances in Wireless Communications (SPAWC)*, Lucca, Italy, 2024, pp. 601-605, doi: 10.1109/SPAWC60668.2024.10693992.

[64] C. Sturm and W. Wiesbeck, "Waveform Design and Signal Processing Aspects for Fusion of Wireless Communications and Radar Sensing," in *Proceedings of the IEEE*, vol. 99, no. 7, pp. 1236-1259, July 2011.

[65] Y. L. SIT, C. STURM, L. R. T. Z. W. W. "The OFDM joint radar-communication system: an overview", in Proc. 3rd Int. Conf. SPACOMM, pp. 69–74, Apr. 2011.

[66] BeGREEN SNS Phase 1 Project, https://www.sns-begreen.com/

[67] BeGREEN deliverable D3.2, "Initial Developments and Evaluation of the Proposed Enhancements and Optimisation Strategies", August 2024.

[68] N. Maletic, M. Petri, M. Appel, and E. Grass, "A Software-Defined Radio Solution for Integrated mmWave Communication and Sensing," in *IEEE Wireless Communications and Networking Conference (WCNC),* Workshop on Integrated Sensing-Communication-Computation for Intelligence of Everything, 2025.

[69] M. Petri and N. Maletic, "Demonstration: Real-Time mmWave Integrated Communication and Sensing," in *IEEE Wireless Communications and Networking Conference*, Demo Paper, 2025.

[70] Sivers Semiconductors AB, "BFM06010 data sheet," Available online: https://www.sivers-semiconductors.com/5g-millimeter-wave-mmwaveand-satcom/wireless-products/rf-modules/bfm06010-and-bfm06011/ [Accessed: December 18th, 2024], precursor BFM06005 not available online.

[71] Open6G-Hub project, "OpenLabs und Experimentierfelder - 6G für Mensch, Umwelt & Gesellschaft," Available online: https://www.open6ghub.de/project/openlabs-und-experimentierfelder/ [Accessed: December 18th, 2024].

[72] AMD, "AMD Zynq™ UltraScale+™ RFSoC," Available online: https://www.amd.com/de/products/adaptive-socs-and-fpgas/soc/zynqultrascale-plus-rfsoc.html [Accessed: December 16th, 2024].

[73] M. Piz, E. Grass, M. Marinkovic, and R. Kraemer, "Next-Generation Wireless OFDM System for 60-GHz Short-Range Communication at a Data Rate of 2.6 GBit/s," in *14th International OFDM-Workshop (InOWo'09)*, 2009.

[74] M. Petri, "Configurable, Modular and Scalable OFDM Baseband Processor for Data Rates up to 4 Gbps," in Wireless Communications. ACTA Press, Jun. 2011.

[75] M. Ehrig, M. Petri, V. Sark, J. G. Terán and E. Grass, "Combined high-resolution ranging and high data rate wireless communication system in the 60 GHz band," *in 11th Workshop on Positioning, Navigation and Communication (WPNC)*, Dresden, Germany, 2014, pp. 1-6, doi: 10.1109/WPNC.2014.6843304.

[76] ETSI, "Industry Specification Group (ISG) Integrated Sensing And Communications (ISAC)," 2024.

[77] K. Braun, “OFDM Radar Algorithms in Mobile Communication Network”s, Dissertation, KIT ISSN: 1433-3821, 2014.

[78] GNU Radio, https://www.gnuradio.org/

[79] ZeroMQ, https://zeromq.org/

[80] R. Vasist, V. Sark, M. Goodarzi, J. Gutiérrez and E. Grass, "Localization System Architecture for Enhanced Positioning in Industry 4.0 Applications," in *International Conference on Computing, Networking and Communications (ICNC)*, Honolulu, HI, USA, 2023, pp. 683-688, doi: 10.1109/ICNC57223.2023.10074001.

[81] A. Tzanakaki, M. P. Anastasopoulos and D. Simeonidou, "Converged optical, wireless, and data center network infrastructures for 5G services," in Journal of Optical Communications and Networking, vol. 11, no. 2, pp. A111-A122, Feb. 2019, doi: 10.1364/JOCN.11.00A111.

[82] M. Anastasopoulos, J. Gutierrez Teran, A. Tzanakaki, “Optical Transport Network Optimization Supporting Integrated Sensing and Communication Services”, in OFC 2025 (to appear).

[83] Sensing and Ranging in IMMW, IEEE 802.11-24/0723r0, May. 2024.

[84] Y. Zhu, Q. Zhang and T. Yang, "Low-Complexity Hybrid Precoding with Dynamic Beam Assignment in mmWave OFDM Systems," in *IEEE Transactions on Vehicular Technology*, vol. 67, no. 4, pp. 3685-3689, April 2018.

[85] IEEE Std 802.11™-2020 IEEE Standard for Information technology - Telecommunications and information exchange between systems - Local and metropolitan area networks - Specific requirements - Part 11: Wireless LAN Medium Access Control (MAC) and Physical Layer (PHY) Specifications.

[86] P. Kumari, J. Choi, N. González-Prelcic and R. W. Heath, "IEEE 802.11ad-Based Radar: An Approach to Joint Vehicular Communication-Radar System," in *IEEE Transactions on Vehicular Technology*, vol. 67, no. 4, pp. 3012-3027, April 2018.

[87] C. -X. Wang, J. Huang, H. Wang, X. Gao, X. You and Y. Hao, "6G Wireless Channel Measurements and Models: Trends and Challenges," in *IEEE Vehicular Technology Magazine*, vol. 15, no. 4, pp. 22-32, Dec. 2020, doi: 10.1109/MVT.2020.3018436.

[88] T. Wang, J. G. Proakis, E. Masry and J. R. Zeidler, "Performance degradation of OFDM systems due to Doppler spreading," in *IEEE Transactions on Wireless Communications*, vol. 5, no. 6, pp. 1422-1432, June 2006, doi: 10.1109/TWC.2006.1638663.

[89] M. Nauman et al., "Enhancing the WLAN OFDM-PHY by OTFS Precoding," in *Joint European Conference on Networks and Communications & 6G Summit (EuCNC/6G Summit)*, Antwerp, Belgium, 2024, pp. 451-456, doi: 10.1109/EuCNC/6GSummit60053.2024.10597133.

[90] A. Monk, R. Hadani, M. Tsatsanis, and S. Rakib, „OTFS - Orthogonal Time Frequency Space”, 2016.

[91] R. Hadani et al., "Orthogonal Time Frequency Space Modulation," 2017 *IEEE Wireless Communications and Networking Conference (WCNC)*, San Francisco, CA, USA, 2017, pp. 1-6, doi: 10.1109/WCNC.2017.7925924.

[92] P. Raviteja, K. T. Phan and Y. Hong, "Embedded Pilot-Aided Channel Estimation for OTFS in Delay–Doppler Channels," in *IEEE Transactions on Vehicular Technology*, vol. 68, no. 5, pp. 4906-4917, May 2019, doi: 10.1109/TVT.2019.2906357.

[93] H. Yi, T. Thaj, and E. Viterbo, “Delay-Doppler Communications: Principles and Applications”, *Elsevier*, 2022.

[94] T. Thaj, and E. Viterbo, “Low Complexity Iterative Rake Decision Feedback Equalizer for Zero-Padded OTFS Systems,” in *IEEE Transactions on Vehicular Technology*, 69(12), 15606–15622.

[95] M. Ouyang, Y. Wang, T. Zhang and F. Gao, "An RFSoC-Based Scalable ISAC Prototyping Platform with OTFS Waveform," in *IEEE Wireless Communications and Networking Conference (WCNC)*, Dubai, United Arab Emirates, 2024, pp. 1-5, doi: 10.1109/WCNC57260.2024.10571064.

[96] LTE; Evolved Universal Terrestrial Radio Access (E-UTRA); Base Station (BS) radio transmission and reception (3GPP TS 36.104 version 8.6.0 Release 8). (2009).

[97] S. Buzzi, C. D’Andrea and S. Liesegang, "Scalability and Implementation Aspects of Cell-Free Massive MIMO for ISAC," in *19th International Symposium on Wireless Communication Systems (ISWCS)*, Rio de Janeiro, Brazil, 2024, pp. 1-6, doi: 10.1109/ISWCS61526.2024.10639146

[98] H. Q. Ngo, A. Ashikhmin, H. Yang, E. G. Larsson and T. L. Marzetta, "Cell-Free Massive MIMO Versus Small Cells," in *IEEE Transactions on Wireless Communications*, vol. 16, no. 3, pp. 1834-1850, March 2017, doi: 10.1109/TWC.2017.2655515

[99] K. Xu, M. Huang, D. Zhang, X. Xia, W. Xie and N. Sha, "User Rate Optimization for Fronthaul-Constrained Cell-Free Massive MIMO-OFDM Systems: A Quadratic Transform-Based Approach," in *IEEE Open Journal of the Communications Society*, vol. 3, pp. 1244-1251, 2022, doi: 10.1109/OJCOMS.2022.3195756

[100] A. Amalia, Y. Pramitarini, R. H. Yoga Perdana, K. Shim and B. An, "Federated Learning-Enhanced QoS Multicast Routing to Support RIS and Edge Computing in IoT-Enabled MANETs with CF-mMIMO," 2024 *International Technical Conference on Circuits/Systems, Computers, and Communications (ITC-CSCC)*, Okinawa, Japan, 2024, pp. 1-6, doi: 10.1109/ITC-CSCC62988.2024.10628355.

[101] M. Bashar, K. Cumanan, A. G. Burr, H. Q. Ngo and M. Debbah, "Cell-Free Massive MIMO with Limited Backhaul," in *IEEE International Conference on Communications (ICC)*, Kansas City, MO, USA, 2018, pp. 1-7, doi: 10.1109/ICC.2018.8422865.

[102] O. A. Topal, Ö. T. Demir, E. Björnson, C. Cavdar, “Energy-Efficient Cell-Free Massive MIMO with Wireless Fronthaul”, https://arxiv.org/abs/2412.02771, 2024.

[103] A. E. Kalor et al., "Wireless 6G Connectivity for Massive Number of Devices and Critical Services," in *Proceedings of the IEEE*, doi: 10.1109/JPROC.2024.3484529.

[104] G. Zhang, X. -Q. Jiang, H. Hai, L. Xu and S. Mumtaz, "Intelligent Reflecting Surfaces Based Offset Index Modulation for MIMO Systems," in *IEEE Transactions on Vehicular Technology*, vol. 73, no. 8, pp. 11735-11742, Aug. 2024, doi: 10.1109/TVT.2024.3382310

[105] A. Lancho, G. Durisi and L. Sanguinetti, "Cell-Free Massive MIMO for URLLC: A Finite-Blocklength Analysis," in *IEEE Transactions on Wireless Communications*, vol. 22, no. 12, pp. 8723-8735, Dec. 2023, doi: 10.1109/TWC.2023.3265303.

[106] J. Zeng, T. Wu, Y. Song, Y. Zhong, T. Lv and S. Zhou, "Achieving Energy-Efficient Massive URLLC Over Cell-Free Massive MIMO," in *IEEE Internet of Things Journal*, vol. 11, no. 2, pp. 2198-2210, 15 Jan.15, 2024, doi: 10.1109/JIOT.2023.3293008.

[107] M. Elwekeil, A. Zappone and S. Buzzi, "Power Control in Cell-Free Massive MIMO Networks for UAVs URLLC Under the Finite Blocklength Regime," in *IEEE Transactions on Communications*, vol. 71, no. 2, pp. 1126-1140, Feb. 2023, doi: 10.1109/TCOMM.2022.3227230.

[108] S. R. Khosravirad, H. Viswanathan and W. Yu, "Exploiting Diversity for Ultra-Reliable and Low-Latency Wireless Control," in *IEEE Transactions on Wireless Communications*, vol. 20, no. 1, pp. 316-331, Jan. 2021, doi: 10.1109/TWC.2020.3024741.

[109] R. Hashemi, S. Ali, N. H. Mahmood and M. Latva-aho, "Average Rate and Error Probability Analysis in Short Packet Communications Over RIS-Aided URLLC Systems," in *IEEE Transactions on Vehicular Technology*, vol. 70, no. 10, pp. 10320-10334, Oct. 2021, doi: 10.1109/TVT.2021.3105878.

[110] E. Bjornson and L. Sanguinetti, "Scalable Cell-Free Massive MIMO Systems," in *IEEE Transactions on Communications*, vol. 68, no. 7, pp. 4247–4261, 2020.

[111] M. H. Lee, M. C. Ha, H. S. Yoon, C. W. Yun, C. W. Yu and K. W. Choi, "Demo: SDR Implementation of a Fully Distributed Cell-Free MIMO System," in *IEEE International Conference on Communications Workshops (ICC Workshops)*, Seoul, Republic of Korea, 2022, pp. 1-2.

[112] M. H. Lee, C. Yun, G. H. Kim, S. Y. Park, C. W. Yu and K. W. Choi, "Fully Distributed Cell-Free MIMO Systems: Architecture, Algorithm, and Testbed Experiments," in *IEEE Internet of Things Journal*, vol. 11, no. 5, pp. 7956-7973, 1 March1, 2024, doi: 10.1109/JIOT.2023.3317578.

[113] D. Wang, C. Zhang, Y. Du, J. Zhao, M. Jiang, and X. You, "Implementation of a Cloud-Based Cell-Free Distributed Massive MIMO System," in *IEEE Communications Magazine*, vol. 58, no. 8, pp. 61–67, 2020.

[114] H. Kamboj et al., "Hardware Implementation of Cell-Free MIMO and Dynamic TDD using the OAI 5G NR Codebase", in *Workshop on Smart Antennas (WSA)*, 2021.

[115] Y. Cao et al., "Experimental Performance Evaluation of Cell-Free Massive MIMO Systems Using COTS RRU With OTA Reciprocity Calibration and Phase Synchronization," in *IEEE Journal on Selected Areas in Communications*, vol. 41, no. 6, pp. 1620-1634, June 2023, doi: 10.1109/JSAC.2023.3276057.

[116] M. Polese, L. Bonati, S. D'Oro, S. Basagni and T. Melodia, "Understanding O-RAN: Architecture, Interfaces, Algorithms, Security, and Research Challenges," in *IEEE Communications Surveys & Tutorials*, vol. 25, no. 2, pp. 1376-1411, Secondquarter 2023, doi: 10.1109/COMST.2023.3239220.

[117] M. Polese et al., "Empowering the 6G Cellular Architecture With Open RAN," in *IEEE Journal on Selected Areas in Communications*, vol. 42, no. 2, pp. 245-262, Feb. 2024, doi: 10.1109/JSAC.2023.3334610.

[118] A. E. Gamal and Y.-H. Kim, "Network Information Theory". Cambridge, U.K.: Cambridge Univ. Press,2011.

[119] H. Zhao, G. J. Pottie and B. Daneshrad, "Reciprocity Calibration of TDD MIMO Channel for Interference Alignment," *in IEEE Transactions on Wireless Communications*, vol. 19, no. 5, pp. 3505-3516, May 2020, doi: 10.1109/TWC.2020.2974465.

[120] X. Jiang et. al. "A Framework for Over-The-Air Reciprocity Calibration for TDD Massive MIMO Systems", in *IEEE Transactions on Wireless Communications*, vol. 17, no. 9, pp. 5975-5990, Sept. 2018.

[121] H. Rogalin et. al, "Scalable Synchronization and Reciprocity Calibration for Distributed Multiuser MIMO," in *IEEE Transactions on Wireless Communications*, Vol. 13, no. 4, pp. 1815-1831, April 2014.

[122] E. A. Jorswieck, "Next-Generation Multiple Access: From Basic Principles to Modern Architectures," in *Proceedings of the IEEE*, vol. 112, no. 9, pp. 1149-1178, Sept. 2024, doi: 10.1109/JPROC.2024.3412423.

[123] A. Gharehgoli, A. Nouruzi, N. Mokari, P. Azmi, M. R. Javan and E. A. Jorswieck, "AI-Based Resource Allocation in End-to-End Network Slicing Under Demand and CSI Uncertainties," in *IEEE Transactions on Network and Service Management*, vol. 20, no. 3, pp. 3630-3651, Sept. 2023, doi: 10.1109/TNSM.2023.3243837.

[124] M. Simsek, T. Hößler, E. Jorswieck, H. Klessig and G. Fettweis, "Multiconnectivity in Multicellular, Multiuser Systems: A Matching- Based Approach," in Proceedings of the IEEE, vol. 107, no. 2, pp. 394-413, Feb. 2019, doi: 10.1109/JPROC.2018.2887265.

[125] S. Park, S. Jeong, J. Na, O. Simeone, and S. Shamai, "Collaborative cloud and edge mobile computing in C-RAN systems with minimal end-to-end latency," in *IEEE Transactions on Signal and Information Processing over Networks*, vol. 7, pp. 259–274, 2021.

[126] A. Checko et al., "Cloud RAN for mobile networks—A technology overview," in *IEEE Commun. Surveys Tuts.*, vol. 17, no. 1, pp. 405–426, 1st Quart., 2015.

[127] Y. Lin, L. Shao, Z. Zhu, Q. Wang, and R. K. Sabhikhi, "Wireless network cloud: Architecture and system requirements," IBM J. Res. Develop., vol. 54, no. 1, pp. 4:1–4:12, Jan. 2010.

[128] Emil Björnson; Eduard Jorswieck, Optimal Resource Allocation in Coordinated Multi-Cell Systems , now, 2013, doi: 10.1561/0100000069.

[129] N. Moosavi, M. Sinaie, P. Azmi, P.-H. Lin, and E. Jorswieck, "Cross layer resource allocation inH-CRAN with spectrum and energy cooperation," in *IEEE Transactions on Mobile Computing*, vol. 22, no. 1,pp. 145–158, Jan. 2023.

[130] A. H. Zarif, P. Azmi, N. M. Yamchi, M. R. Javana and E. A. Jorswieck, "AoI minimization in energyharvesting and spectrum sharing enabled 6Gnetworks," in *IEEE Transactions on Green Communication Networks*, vol. 6, no. 4, pp. 2043–2054, Dec. 2022.

[131] A. A. Ahmad, Y. Mao, A. Sezgin and B. Clerckx, "Rate Splitting Multiple Access in C-RAN," in *IEEE 31st Annual International Symposium on Personal, Indoor and Mobile Radio Communications*, London, UK, 2020, pp. 1-6, doi: 10.1109/PIMRC48278.2020.9217249.

[132] A. A. Ahmad, Y. Mao, A. Sezgin, and B. Clerckx, "Rate splitting multiple access in C-RAN: A scalable and robust design," in *IEEE Transactions on Communications*, vol. 69, no. 9, pp. 5727–5743, Sep. 2021.

[133] E. Nayebi, A. Ashikhmin, T. L. Marzetta, and H. Yang, "Cell-free massive MIMO systems," in *Proc. 49th Asilomar Conf. Signals, Syst. Comput.,* Nov. 2015, pp. 695–699.

[134] G. Interdonato, E. Björnson, H. Q. Ngo, P. Frenger, and E. G. Larsson, "Ubiquitous cell-free massive MIMO communications," EURASIP J. Wireless Commun. Netw., vol. 2019, no. 1, pp. 1–13, Dec. 2019.

[135] Ö. T. Demir, E. Björnson, and L. Sanguinetti, "Foundations of user-centric cell-free massive MIMO," Found. Trends Signal Process., vol. 14, nos. 3–4, pp. 162–472, 2021,

[136] E. Nayebi, A. Ashikhmin, T. L. Marzetta, H. Yang, and B. D. Rao, "Precoding and power optimization in cell-free massive MIMO systems," in *IEEE Transactions on Wireless Communications*, vol. 16, no. 7, pp. 4445–4459, Jul. 2017.

[137] M. Zaher, Ö. T. Demir, E. Björnson, and M. Petrova, "Learning-based downlink power allocation in cell-free massive MIMO systems", in IEEE Transactions on Wireless Communications, vol. 22, no. 1, pp. 174–188, Jan. 2023.

[138] T. C. Mai, H. Q. Ngo, and L.-N. Tran, "Energy efficiency maximization in large-scale cell-free massive MIMO: A projected gradient approach", in *IEEE Transactions on Wireless Communications*, vol. 21, no. 8, pp. 6357–6371, Aug. 2022.

[139] L. Miretti, R. L. G. Cavalcante, S. Stanczak, M. Schubert, R. Böhnke, and W. Xu, "Closed-form max-min power control for some cellular and cell-free massive MIMO networks," in *Proc. IEEE95th Veh. Technol. Conf. (VTC-Spring)*, Jun. 2022, pp. 1–7.

[140] A. R. Flores, R. C. De Lamare, and K. V. Mishra, “Rate-splitting meets cell-free MIMOcommunications,” in *Proc. IEEE Int. Conf.Commun. Workshops (ICC Workshops)*, May 2022, pp. 657–662.

[141] A. Mishra, Y. Mao, L. Sanguinetti and B. Clerckx, "Rate-Splitting Assisted Massive Machine-Type Communications in Cell-Free Massive MIMO," in IEEE Communications Letters, vol. 26, no. 6, pp. 1358-1362, June 2022, doi: 10.1109/LCOMM.2022.3160511.

[142] J. Zheng, J. Zhang, J. Cheng, V. C. M. Leung, D. W. K. Ng and B. Ai, "Asynchronous Cell-Free Massive MIMO With Rate-Splitting," in IEEE Journal on Selected Areas in Communications, vol. 41, no. 5, pp. 1366-1382, May 2023, doi: 10.1109/JSAC.2023.3240709.

[143] G. Interdonato, H. Q. Ngo and E. G. Larsson, "Enhanced Normalized Conjugate Beamforming for Cell-Free Massive MIMO," in IEEE Transactions on Communications, vol. 69, no. 5, pp. 2863-2877, May 2021, doi: 10.1109/TCOMM.2021.3055522.

[144] M. Attarifar, A. Abbasfar and A. Lozano, "Modified Conjugate Beamforming for Cell-Free Massive MIMO," in IEEE Wireless Communications Letters, vol. 8, no. 2, pp. 616-619, April 2019, doi: 10.1109/LWC.2018.2890470.

[145] G. Interdonato, M. Karlsson, E. Björnson and E. G. Larsson, "Local Partial Zero-Forcing Precoding for Cell-Free Massive MIMO," in IEEE Transactions on Wireless Communications, vol. 19, no. 7, pp. 4758-4774, July 2020, doi: 10.1109/TWC.2020.2987027.

[146] L. Miretti, E. Björnson and D. Gesbert, "Team MMSE Precoding With Applications to Cell-Free Massive MIMO," in IEEE Transactions on Wireless Communications, vol. 21, no. 8, pp. 6242-6255, Aug. 2022, doi: 10.1109/TWC.2022.3147895.

[147] Z. Li, F. Göttsch, S. Li, M. Chen and G. Caire, "Joint Fronthaul Load Balancing and Computation Resource Allocation in Cell-Free User-Centric Massive MIMO Networks," in *IEEE Transactions on Wireless Communications*, vol. 23, no. 10, pp. 14125-14139, Oct. 2024, doi: 10.1109/TWC.2024.3409609.

[148] A. Carleial, "Interference channels," in *IEEE Transactions on Information Theory*, vol. 24, no. 1, pp. 60-70, January 1978, doi: 10.1109/TIT.1978.1055812.

[149] Y. Polyanskiy, "A perspective on massive random-access," in *IEEE International Symposium on Information Theory (ISIT),* Aachen, Germany, 2017, pp. 2523-2527, doi: 10.1109/ISIT.2017.8006984.

[150] R. C. Yavas, V. Kostina and M. Effros, "Gaussian Multiple and Random Access Channels: Finite-Blocklength Analysis," in *IEEE Transactions on Information Theory*, vol. 67, no. 11, pp. 6983-7009, Nov. 2021, doi: 10.1109/TIT.2021.3111676.

[151] M. Effros, V. Kostina and R. C. Yavas, "Random Access Channel Coding in the Finite Blocklength Regime," in *IEEE International Symposium on Information Theory (ISIT)*, Vail, CO, USA, 2018, pp. 1261-1265, doi: 10.1109/ISIT.2018.8437831.

[152] X. Chen, T. -Y. Chen and D. Guo, "Capacity of Gaussian Many-Access Channels," in *IEEE Transactions on Information Theory*, vol. 63, no. 6, pp. 3516-3539, June 2017, doi: 10.1109/TIT.2017.2668391.

[153] S. S. Kowshik, K. Andreev, A. Frolov, andY. Polyanskiy, “Short-packet low-power codedaccess for massive MAC,” in Proc. 53rd AsilomarConf. Signals, Syst., Comput., Nov. 2019, pp. 827–832.

[154] S. Lu, F. Liu, L. Fan, Z. Yunxin, H. Kecheng, H. Huang, Z. Hongjia, J. Zou, X. Li, Y. Dong, F. Dong, J. Zhu, Y. Xiong, Y. Yifeng, C. Weijie, Y. Cui, L. Hanzo, “Integrated sensing and communications: recent advances and ten open challenges”, in *IEEE Internet of Things Journal*, 11 (11), 19094-19120, 2024.

[155] J. Navarro-Ortiz, P. Romero-Diaz, S. Sendra, P. Ameigeiras, J. J. Ramos Munoz and J. M. Lopez-Soler, “A Survey on 5G Usage Scenarios and Traffic Models," in IEEE Communications Surveys & Tutorials, vol. 22, no. 2, pp. 905-929, Secondquarter 2020, doi: 10.1109/COMST.2020.2971781.

[156] "IEEE Standard for Information technology-- Local and metropolitan area networks-- Specific requirements-- Part 11: Wireless LAN Medium Access Control (MAC)and Physical Layer (PHY) Specifications Amendment 5: Enhancements for Higher Throughput," in IEEE Std 802.11n-2009 (Amendment to IEEE Std 802.11-2007 as amended by IEEE Std 802.11k-2008, IEEE Std 802.11r-2008, IEEE Std 802.11y-2008, and IEEE Std 802.11w-2009), vol., no., pp.1-565, 29 Oct. 2009.

[157] E. Jorswieck, L. Kunz, R. Raghunath and B. Peng, "Rate-Splitting Downlink Transmission in Cell-Free Networks under Fronthaul Constraints," in *19th International Symposium on Wireless Communication Systems (ISWCS)*, Rio de Janeiro, Brazil, 2024, pp. 1-6, doi: 10.1109/ISWCS61526.2024.10639051.

[158] R. Raghunath, B. Peng and E. A. Jorswieck, "Energy-Efficient Power Allocation in Cell-Free Massive MIMO via Graph Neural Networks," in *IEEE International Conference on Machine Learning for Communication and Networking (ICMLCN)*, Stockholm, Sweden, 2024, pp. 31-37, doi: 10.1109/ICMLCN59089.2024.10625052.

[159] B. Clerckx et al., "A Primer on Rate-Splitting Multiple Access: Tutorial, Myths, and Frequently Asked Questions," in *IEEE Journal on Selected Areas in Communications*, vol. 41, no. 5, pp. 1265-1308, May 2023, doi: 10.1109/JSAC.2023.3242718

[160] M. Di Renzo *et al*, “Smart radio environments empowered by reconfigurable intelligent surfaces: How it works, state of research, and the road ahead,” in *IEEE Journal on Selected Areas in Communications*, vol. 38, no. 11, pp. 2450-2525, 2020.

[161] “Reconfigurable intelligent surfaces (RIS); use cases deployment scenarios and requirements,” Reconfigurable Intelligent Surfaces (RIS) ETSI Industry Specifications Group (ISG), DGR/IRS/001,2023.

[162] R. Liu, M. Li, H. Luo, Q. Liu, and A. L. Swindlehurst, "Integrated Sensing and Communication with Reconfigurable Intelligent Surfaces: Opportunities, Applications, and Future Directions," in *IEEE Wireless Communications*, vol. 30, no. 1, pp. 50-57, February 2023, doi: 10.1109/ MWC.002.2200206.

[163] A. M. Elbir, K. V. Mishra, M. R. B. Shankar, and S. Chatzinotas, “The rise of intelligent reflecting surfaces in integrated sensing and communications paradigms,” in *IEEE Network*, 2023.

[164] W. Xu, J. An, H. Li, L. Gan and C. Yuen, "Algorithm-Unrolling-Based Distributed Optimization for RIS-Assisted Cell-Free Networks," in IEEE Internet of Things Journal, vol. 11, no. 1, pp. 944-957, 1 Jan.1, 2024, doi: 10.1109/JIOT.2023.3288072.

[165] J. Yao, J. Xu, W. Xu, D. W. K. Ng, C. Yuen and X. You, "Robust Beamforming Design for RIS-Aided Cell-Free Systems With CSI Uncertainties and Capacity-Limited Backhaul," in *IEEE Transactions on Communications*, vol. 71, no. 8, pp. 4636-4649, Aug. 2023, doi: 10.1109/TCOMM.2023.3277539.

[166] W. Lyu, Y. Xiu, S. Yang, C. Yuen, and Z. Zhang, “Energy-efficient cell-free network assisted by hybrid RISs,” in *IEEE Wireless Communication Letters*, vol. 12, no. 4, pp. 718–722, 2023.

[167] L. Dai, *et al*, “Reconfigurable intelligent Surface-based wireless communications: Antenna design, prototyping, and experimental results”, in *IEEE Access*, vol. 8, pp. 45913-45923, 2020, doi: 10.1109/ACCESS.2020.2977772.

[168] S. Zhao, R. Langwieser, C. F. Mecklenbräuker, “Reconfigurable digital metasurface for 3-bit phase encoding,” *25th International ITG Workshop on Smart Antennas*, French Riviera, France, 2021, pp. 1-6.

[169] Marie-Curie EU Horizon 2020 MSCA-ETN "Millimeter-wave Networking and Sensing for Beyond 5G" (MINTS) project, https://b5g-mints.eu/

[170] J. Rao, *et al*, “A Novel Reconfigurable Intelligent Surface for Wide-Angle Passive Beamforming,” *IEEE Trans. Microw. Tech*. vol. 70, no. 12, pp. 5427-5439, 2022.

[171] M. Rossanese *et al*, “Designing, Building, and Characterizing RF Switch-based Reconfigurable Intelligent Surfaces,” in *ACM MobiCom*, 2022.

[172] R. Fara *et al*, “A Prototype of Reconfigurable Intelligent Surface with Continuous Control of the Reflection Phase”, in *IEEE Wireless Communications*, vol. 29, no. 1, pp. 70-77, February 2022, doi: 10.1109/MWC.007.00345.

[173] J. Xu, Y. Liu, X. Mu, R. Schober and H. V. Poor, "STAR-RISs: A Correlated T&R Phase-Shift Model and Practical Phase-Shift Configuration Strategies," in IEEE Journal of Selected Topics in Signal Processing, vol. 16, no. 5, pp. 1097-1111, Aug. 2022, doi: 10.1109/JSTSP.2022.3175030.

[174] H. Li, S. Shen, and B. Clerckx, “Beyond diagonal reconfigurable intelligent surfaces: From transmitting and reflecting modes to single-, group-, and fully-connected architectures,” in *IEEE Transactions on Wireless Communications*, vol. 22, no. 4, pp. 2311-2324,2022.

[175] C. G. Alexandropoulos, et al “RIS-enabled smart wireless environments: deployment scenarios, network architecture, bandwidth and area of influence, in *EURASIP Journal on Wireless Communications and Networking*, 2023.

[176] R. K. Fotock, A. Zappone, and M. Di Renzo, “Energy efficiency optimization in RIS-aided wireless networks: Active versus nearly passive RIS with global reflection constraints,” in *IEEE Transactions on Communications*, vol. 72, no. 1, pp. 257-272, Jan. 2024, doi: 10.1109/TCOMM.2023.3320700.

[177] Z. Zhang *et al*., "Active RIS vs. Passive RIS: Which Will Prevail in 6G?", in *IEEE Transactions on Communications*, vol. 71, no. 3, pp. 1707-1725, March 2023, doi: 10.1109/TCOMM.2022.3231893.

[178] K. Gomadam, V. R. Cadambe, S. A. Jafar, “A Distributed Numerical Approach to Interference Alignment and Applications to Wireless Interference Channels,” in *IEEE Transactions on Information Theory*, vol. 57, no. 6, pp. 3309-3322, 2011.

[179] I. Santamaria, M. Soleymani, E. Jorswieck, J. Gutiérrez, “Interference minimization in Beyond-diagonal RIS-assisted MIMO Interference Channels,” submitted to *IEEE Transactions on Communications*, 2024.

[180] M. I. Ismail, A. M. Shaheen, M. M. Fouda and A. S. Alwakeel, "RIS-Assisted Integrated Sensing and Communication Systems: Joint Reflection and Beamforming Design," in *IEEE Open Journal of the Communications Society*, vol. 5, pp. 908-927, 2024, doi: 10.1109/OJCOMS.2024.3353770.

[181] M. Hua, Q. Wu, C. He, S. Ma, and W. Chen, “Joint active and passive beamforming design for IRS-aided radar-communication,” in *IEEE Transactions on Wireless Communications*, vol. 22, no. 4, pp. 2278–2294, Apr. 2023.

[182] X. Wang, Z. Fei, Z. Zheng, and J. Guo, “Joint waveform design and passive beamforming for RIS-assisted dual-functional radar communication system,” in *IEEE Transactions on Vehicular Technology*, vol. 70, no. 5, pp. 5131–5136, May 2021.

[183] X. Wang, Z. Fei, J. Guo, Z. Zheng, and B. Li, “RIS-assisted spectrum sharing between MIMO radar and MU-MISO communication systems,” in *IEEE Wireless Communication Letters*, vol. 10, no. 3, pp. 594–598, Mar. 2021.

[184] R. S. Prasobh Sankar, B. Deepak, and S. P. Chepuri, "Joint communication and radar sensing with reconfigurable intelligent surfaces," in *Proc. IEEE 22nd Int. Workshop Signal Process. Adv. Wireless Commun. (SPAWC)*, 2021, pp. 471–475.

[185] Z. -M. Jiang et al., "Intelligent Reflecting Surface Aided Dual-Function Radar and Communication System," in *IEEE Systems Journal*, vol. 16, no. 1, pp. 475-486, March 2022, doi: 10.1109/JSYST.2021.3057400.

[186] Y. He, Y. Cai, H. Mao and G. Yu, "RIS-Assisted Communication Radar Coexistence: Joint Beamforming Design and Analysis," in *IEEE Journal on Selected Areas in Communications*, vol. 40, no. 7, pp. 2131-2145, July 2022, doi: 10.1109/JSAC.2022.3155507.

[187] X. Song, D. Zhao, H. Hua, T. X. Han, X. Yang and J. Xu, "Joint Transmit and Reflective Beamforming for IRS-Assisted Integrated Sensing and Communication," in *IEEE Wireless Communications and Networking Conference (WCNC)*, Austin, TX, USA, 2022, pp. 189-194, doi: 10.1109/WCNC51071.2022.9771801.

[188] R. Liu, M. Li and A. L. Swindlehurst, "Joint Beamforming and Reflection Design for RIS-assisted ISAC Systems," in *30th European Signal Processing Conference (EUSIPCO)*, Belgrade, Serbia, 2022, pp. 997-1001, doi: 10.23919/EUSIPCO55093.2022.9909807.

[189] R. Liu, M. Li, Y. Liu, Q. Wu and Q. Liu, "Joint Transmit Waveform and Passive Beamforming Design for RIS-Aided DFRC Systems," in *IEEE Journal of Selected Topics in Signal Processing*, vol. 16, no. 5, pp. 995-1010, Aug. 2022, doi: 10.1109/JSTSP.2022.3172788.

[190] Z. Zhu et al., "Intelligent reflecting surface assisted integrated sensing and communications for mmWave channels," 2022, arXiv:2202.00552.

[191] X. Wang, Z. Fei, J. A. Zhang, J. Huang, and J. Yuan, "Constrained utility maximization in dual-functional radar-communication multiUAV networks," in IEEE Transactions on Communications, vol. 69, no. 4, pp. 2660–2672, Apr. 2021.

[192] J. Lou, C. Jiang, X. Han and X. Wang, "A Standardization Framework for Channel Modeling in RIS-Assisted Integrated Sensing and Communication Systems," in *IEEE Communications Standards Magazine*, vol. 8, no. 4, pp. 48-53, December 2024, doi: 10.1109/MCOMSTD.0001.2400033.

[193] E. Shtaiwi, H. Zhang, A. Abdelhadi and Z. Han, "Sum-rate Maximization for RIS-assisted Radar and Communication Coexistence System," in *IEEE Global Communications Conference (GLOBECOM)*, Madrid, Spain, 2021, pp. 01-06, doi: 10.1109/GLOBECOM46510.2021.9685312.

[194] C. Shepard, H. Yu, N. Anand, E. Li, T. Marzetta, R. Yang, and L. Zhong, "Argos: practical many-antenna base stations". In *Proceedings of the 18th annual international conference on Mobile computing and networking (Mobicom '12)*, 2012.

[195] U. K. Ganesan, R. Sravendranath, E. G. Larsson, "BeamSync: Over-The-Air Synchronization for Distributed Massive MIMO Systems," in *IEEE Transactions on Wireless Communications*, 2024, doi:10.1109/TWC. 2023.3335089.

[196] V. S. Asadchy, M. S. Mirmoosa, A. Díaz-Rubio, S. Fan and S. A. Tretyakov, "Tutorial on Electromagnetic Nonreciprocity and its Origins," in *Procedings of the IEEE*, vol. 108, no. 10, pp. 1684-1727, Oct. 2020, doi: 10.1109/JPROC.2020.3012381.

[197] Y. Polyanskiy, "A perspective on massive random-access," in *IEEE International Symposium on Information Theory (ISIT)*, Aachen, Germany, 2017, pp. 2523-2527, doi: 10.1109/ISIT.2017.8006984.

[198] A. Vem, K. R. Narayanan, J. -F. Chamberland and J. Cheng, "A user-independent successive interference cancellation-based coding scheme for the unsourced random access Gaussian channel," in IEEE Transactions on Communications, vol. 67, no. 12, pp. 8258-8272, Dec. 2019.

[199] M. Ozates, M. Kazemi and T. M. Duman, “Unsourced random access using ODMA and polar codes,” in *IEEE Wireless Communication Letters*, vol. 13, no. 4, pp. 1044-1047, Apr. 2024.

[200] E. Nassaji, M. Bashir and D. Truhachev, “Unsourced random access over fading channels via data repetition, permutation, and scrambling,” in *IEEE Transactions on Communications*, vol. 70, no. 2, pp. 1029-1042, Feb. 2022.

[201] M. Ozates, M. Kazemi and T. M. Duman, “A slotted pilot-based unsourced random access scheme with a multiple-antenna receiver,” in *IEEE Transactions on Wireless Communications*, vol. 23, no. 4, pp. 3437-3449, Apr. 2024.

[202] 3GPP, Further advancements for E-UTRA physical layer aspects (Release 9). 3GPP TS 36.814, Mar. 2017.

[203] T. Van Chien, H. Q. Ngo, S. Chatzinotas, M. Di Renzo, and B. Ottersten, “Reconfigurable intelligent surface-assisted cell-free massive MIMO systems over spatially-correlated channels,” in *IEEE Transactions on Wireless Communications*, vol. 21, no. 7, pp. 5106–5128, 2022.

[204] B. Al-Nahhas, M. Obeed, A. Chaaban, and M. J. Hossain, “RIS-aided cell-free massive MIMO: Performance analysis and competitiveness,” in *IEEE International Conference on Communications Workshops (ICC Workshops)*, 2021, pp. 1–6.

[205] M. Bashar, K. Cumanan, A. G. Burr, P. Xiao, and M. Di Renzo, “On the performance of reconfigurable intelligent surface-aided cellfree massive MIMO uplink,” in GLOBECOM 2020 - 2020 IEEE Global Communications Conference, 2020, pp. 1–6.

[206] 5G-PPP White Paper, “Whitepaper Beyond 5G/6G EMF Considerations”, 2023, https://5g-ppp.eu/wp-content/uploads/2023/07/EMF-TF-white-paper_v1.2__.pdf

[207] 6G-IA Position Paper, “RESEARCH PRIORITIES ON MICROELECTRONICS FOR 6G NETWORKS R&I ACTIVITIES”, January 2024, https://6g-ia.eu/wp-content/uploads/2024/02/6g-ia-position-paper_microelectronics-final.pdf

[208] H. J. Ng, M. Kucharski, W. Ahmad and D. Kissinger, "Multi-Purpose Fully Differential 61- and 122-GHz Radar Transceivers for Scalable MIMO Sensor Platforms," in *IEEE Journal of Solid-State Circuits*, vol. 52, no. 9, pp. 2242-2255, Sept. 2017, doi: 10.1109/JSSC.2017.2704602.

[209] George et al., "Over-the-air 26GHz Receiver Hardware-Software Evaluation towards Joint Communication and Radar Sensing," in *54th European Microwave Conference (EuMC)*, Paris, France, 2024, pp. 509-512, doi: 10.23919/EuMC61614.2024.10732620.

[210] B. Sutbas, H. J. Ng, M. H. Eissa and G. Kahmen, "A Low-Power V-Band Radar Transceiver Front-End Chip Using 1.5 V Supply in 130-nm SiGe BiCMOS," in *IEEE Transactions on Microwave Theory and Techniques*, vol. 71, no. 11, pp. 4855-4868, Nov. 2023, doi: 10.1109/TMTT.2023.3269519.

[211] Ö. T. Demir and E. Björnson, "User-Centric Cell-Free Massive MIMO with RIS-Integrated Antenna Arrays," in *IEEE 25th International Workshop on Signal Processing Advances in Wireless Communications (SPAWC)*, Lucca, Italy, 2024, pp. 546-550, doi: 10.1109/SPAWC60668.2024.10694297.

[212] Y. Zhao, H. Ke, W. Xu, X. Ye, Y. Chen, “RIS-Assisted Cell-Free MIMO: A Survey”, [J]. ZTE Communications, 2024, 22(1): 77-86.

[213] Y. Zhang et al., "Beyond Cell-Free MIMO: Energy Efficient Reconfigurable Intelligent Surface Aided Cell-Free MIMO Communications," in *IEEE Transactions on Cognitive Communications and Networking*, vol. 7, no. 2, pp. 412-426, June 2021, doi: 10.1109/TCCN.2021.3058683.

[214] Q. N. Le, V. -D. Nguyen, O. A. Dobre and R. Zhao, "Energy Efficiency Maximization in RIS-Aided Cell-Free Network With Limited Backhaul," in *IEEE Communications Letters*, vol. 25, no. 6, pp. 1974-1978, June 2021, doi: 10.1109/LCOMM.2021.3062275.

[215] H. Lu, D. Zhao, Y. Wang, C. Kong and W. Chen, "Joint Power Control and Passive Beamforming in Reconfigurable Intelligent Surface Assisted User-Centric Networks," in *IEEE Transactions on Communications*, vol. 70, no. 7, pp. 4852-4866, July 2022, doi: 10.1109/TCOMM.2022.3174071.

[216] Z. Zhang and L. Dai, "A Joint Precoding Framework for Wideband Reconfigurable Intelligent Surface-Aided Cell-Free Network," in *IEEE Transactions on Signal Processing*, vol. 69, pp. 4085-4101, 2021, doi: 10.1109/TSP.2021.3088755.

[217] S. Huang, Y. Ye, M. Xiao, H. V. Poor and M. Skoglund, "Decentralized Beamforming Design for Intelligent Reflecting Surface-Enhanced Cell-Free Networks," in *IEEE Wireless Communications Letters*, vol. 10, no. 3, pp. 673-677, March 2021, doi: 10.1109/LWC.2020.3045884.

[218] E. Shi et al., "Wireless Energy Transfer in RIS-Aided Cell-Free Massive MIMO Systems: Opportunities and Challenges," in *IEEE Communications Magazine*, vol. 60, no. 3, pp. 26-32, March 2022, doi: 10.1109/MCOM.001.2100671.

[219] Z. Yang and Y. Zhang, "Beamforming optimization for RIS-aided SWIPT in cell-free MIMO networks," in *China Communications*, vol. 18, no. 9, pp. 175-191, Sept. 2021, doi: 10.23919/JCC.2021.09.014.

[220] A. A. Khalil, M. Y. Selim and M. A. Rahman, "CURE: Enabling RF Energy Harvesting Using Cell-Free Massive MIMO UAVs Assisted by RIS," in *IEEE 46th Conference on Local Computer Networks (LCN)*, Edmonton, AB, Canada, 2021, pp. 533-540, doi: 10.1109/LCN52139.2021.9524984.

8 Acronyms

Acronym	Description
2D	Two-Dimensional
3GPP	3rd Generation Partnership Project
5GC	5G Core Network
5GNR	5G New Radio
6G-IA	6G Infrastructure Association
A/D	Analog-to-Digital
ABEP	Average Bit Error Probability
ADMM	Alternating Direction Method of Multipliers
AiP	Antenna in Package
AO	Alternating Optimization
AoI	Age-of-Information
AP	Access Point
API	Application Programming Interface
BER	Bit Error Rate
BPSK	Binary Phase-Shift Keying
BI	*Barkhausen Institut* (6G-SENSES Beneficiary)
BR	BubbleRAN (6G-SENSES Beneficiary)
BS	Base Station
CAPEX	CAPital EXpenditures
CCC	Cell Configuration and Control
CCWD	Communication-Centric Waveform Design
CEF	Channel Estimation Field
CF	Cell-Free
CFAR	Constant False Alarm Rate
CFO	Carrier Frequency Offset
CF-mMIMO	Cell-Free massive MIMO
CIR	Channel Impulse Response
CoMP-JT	Coordinated Multi-point Joint Transmission
COTS	Commercial Off-The-Shelf
CPO	Carrier Phase Offset
CPU	Central Processing Unit
CRB	Cramér-Rao Bound
CSI	Channel State Information
CSP	Communication Service Provider
CW	Continuous Wave
D/A	Digital-to-Analog
DMRS	Demodulation Reference Signal
DoW	Description of Work

DCSP	DataCenter Service Provider
DNN	Deep Neural Network
DoA	Direction of Arrival
DoW	Description of Work
DT	Digital Twin
DZT	Discrete Zak Transform
e2e	End-to-End
EA	Ethics Advisor
EC	European Commission
EDMG	Enhanced directional multi-gigabit
EE	Energy Efficiency
eMBB	enhanced Mobile BroadBand
EMF	Electromagnetic field
ESPRIT	Estimation of signal parameters via rotational invariant techniques
EVM	Error Vector Magnitude
FDSOI	Fully Depleted Silicon on Insulator
FMCW	Frequency-Modulated Continuous Wave
FoV	Field of View
GA	Grant Agreement
GPSDO	GPS Disciplined Oscillator
HW	Hardware
IASA	Institute of Accelerating Systems and Applications (6G-SENSES Beneficiary)
IBFD	In-Band Full Duplex
IC	Integrated Circuit
ICT	Information and Communication Technology
IFFT	Inverse Fast Fourier Transform
IHP	*IHP – Leibniz Institut für innovative Mikroelektronik* (6G-SENSES Beneficiary)
IMT	International Mobile Telecommunications
INT	*Intel Deutschland GmbH* (6G-SENSES Beneficiary)
IoE	Internet of Everything
IoT	Internet of Things
IQ	In-Phase and Quadrature
ISAC	Integrated Sensing and Communication
ISFT	Inverse Symplectic Fourier Transform
ISM	Industrial, Scientific and Medical
IT	Information Technology
ITU	International Telecommunications Union
JWOD	Joint Waveform Optimization and Design
KPI	Key Performance Indicator
KV	Key Value
KVI	Key Value Indicator

LMF	Location Management Function
LMMSE	Linear Minimum Mean-Square Error
LO	Local Oscillator
LoS	Line-of-Sight
LTF	Long Training Field
m/eMTC	massive/enhanced Machine Type Communications
MAC	Medium Access Control
MEC	Multi-access Edge Computing
MGA	Model Grant Agreement
MIMO	Multiple-Input Multiple-Output
MLO	Multi-Link Operation
mMIMO	Massive MIMO
MNO	Mobile Network Operator
MP	Message Passing
MRT	Maximum-Ratio Combining
MUI	MultiUser Interference
MX	Multi-x (i.e. multi-vendor, multi-version, multi-node, multi-distribution, multi-runtime, multi-cloud, and multi-instance)
MUSIC	MUltiple SIgnal Classification
nGRG	O-RAN next Generation Research Group
NFV	Network Function Virtualization
NLoS	Non-Line-of-Sight
NN	Neural Network
NOP	Network Operator
NR	New Radio
NSaaS	Network Security as a Service
NTU	Nottingham Trent University
OAI	OpenAirInterface
OAM	Operations And Management
OCXO	Oven Controlled Crystal Oscillator
OIBS	Offset-Based Block Selection
OIM	Offset Index Modulation
OPEX	OPerational EXpenditures
OS	Operating System
OSS	Operations Support System
OTA	Over-The-Air
OTFS	Orthogonal Time Frequency Space
QM	Quality Manager
PBCH	Physical Broadcast Channel (PBCH)
PCA	Principal Component Analysis
PCB	Printed Circuit Board

PCT	Printed Circuit Technology
PDSCH	Physical Downlink Shared Channel
PHY	Physical
PoC	Proof-of-Concept
PRS	Positioning Reference Signal
PTP	Precision Time Protocol
PUPE	Per-User Probability of Error
PUSCH	Physical Uplink Shared Channel
RAN	Radio Access Network
RB	Resource Block
RC	RAN Control
RF	Radio Frequency
RIS	Reconfigurable Intelligent Surface
RL	Reinforcement Learning
RRM	Radio Resource Management
RU	Radio Unit
SA	Stand Alone
SBA	Service-Based Architecture
SCWD	Sensing-Centric Waveform Design
SDC	Software-Defined Communications
SDG	Sustainable Development Goal
SDK	Software Development Kit
SDN	Software Defined Networking
SDR	Software Defined Radio
SE	Spectral Efficiency
SFFT	Symplectic Fast Fourier Transform
SFO	Sampling Frequency Offset
SiGe	Silicon-Germanium
SINR	Signal-to-Interference-plus-Noise Ratio
SM	Service Model
SMO	Service Management and Orchestration
SNS JU	Smart Networks and Services Joint Undertaking
SOF	Start Of Frame
SRL	Society Readiness Level
SRS	Sounding Reference Signal
SS	Synchronization Signal
STAR-RIS	Simultaneously Transmitting and Reflecting RIS
STFT	Short-Time Fourier Transform
STO	Sampling Time Offset
SW	Software
TDD	Time Division Duplex

TDM	Time-Division Multiplexing
THz	Terahertz
TL	Task Leader
TM	Technical Manager
TRL	Technology Readiness Level
TSDB	TimeScale DataBase
TUBS	*Technische Universität Braunschweig* (6G-SENSES Beneficiary)
UAV	Unmanned Aerial Vehicles
UC	University of Cantabria (6G-SENSES Beneficiary)
UHD	USRP Hardware Driver
ULA	Uniform Linear Array
UN	United Nations
URA	Unsourced Random Access
URLLC	Ultra-Reliable and Low-Latency Communications
USRP	Universal Software Radio Peripheral
UWB	Ultra-Wideband
V2X	Vehicle-to-Everything
VISP	Virtualization Infrastructure Service Provider
WAT	Wireless Access Technology
WG	Work Group
WR	White Rabbit
Wi-Fi	Wireless-Fidelity
WLAN	Wireless Local Area Network
WP	Work Package